ŁÓDŹ UNIVERSITY OF TECHNOLOGY
Faculty of Electrical, Electronic, Computer and
Control Engineering

Co-Simulation of Transient Effects in Superconducting Accelerator Magnets

mgr inż. Michał Maciejewski

Łódź University of Technology Supervisor
prof. dr hab. inż. Andrzej Bartoszewicz

CERN Supervisor
Bernhard Auchmann, PhD

Łódź, October 2018

To my family

Abstract

Numerical modeling of complex physical systems involving several coupled physical domains, so called multi-domain and multi-physics systems, poses considerable challenges w.r.t. consistency of the formulation and selection of a suitable representation. The landscape is further complicated in case these phenomena occur at a wide range of temporal (multi-rate) and spatial (multi-scale) scales. Resolving all in one scale may result in unacceptable computational time.

Recent development in port-based modeling techniques, in particular the port-Hamiltonian framework originating from control theory, made it possible to model complex multi-domain and multi-physics phenomena represented by means of both ordinary and partial differential equations in a generic and consistent way. The port-Hamiltonian models capture in an elegant way the internal energy flow, storage, dissipation as well as interaction through lumped, distributed, and boundary ports. In the thesis, we employ the port-Hamiltonian formalism to characterize the coupling between the electromagnetic and thermodynamic systems in a superconducting magnet along with an accompanying electrical circuit. In addition, we employ bond graph modeling to graphically represent the energy flow in the considered systems. These methods allow to study the model consistency as well as the computational causality.

Similarly, the advances in cooperative simulation, in particular the application of the waveform relaxation algorithm to field/circuit coupling along with the use of pre-conditioners for field models allowed to achieve satisfactory convergence rates and accurate results. This method is particularly suited to approach multi-rate and multi-scale problems such as the simulation of a superconducting magnet and circuit. In this thesis, an architecture, data structures, and algorithms for automatic handling of hierarchical co-simulation are presented. The resulting framework supports four main co-simulation algorithms (one-way coupling, weak coupling, strong coupling, and waveform relaxation). Furthermore, the evolution of a transient in a co-simulation scenario may call for the adjustment of the model fidelity in order to accurately reproduce a given phenomenon. This is achieved by switching models and coupling algorithms during the co-simulation execution.

The performance of the presented co-simulation framework is illustrated with several relevant examples of transient effects in accelerator magnets. The studied co-simulation scenarios involve superconducting accelerator magnets, circuits, and controllers of power converters in nominal and failure conditions. The developed energy-based models support the analysis of the performance of the co-simulation scenarios.

Acknowledgements

At the end of this scientific journey, I can only quote a sentence of Mr. Nelson Mandela "It only seems impossible until it's done". In fact, the feeling of difficulty followed me like a shadow in the initial part of the research work. However, on the way I was assisted by experienced and inspiring people whom I owe a great debt of gratitude for believing in me and making what once seemed impossible possible.

First and foremost, I would like to thank my supervisor at CERN, Dr Bernhard Auchmann for proposing an interesting and relevant research topic as well as incredible support while performing the research work. His passion to science and endless enthusiasm were invigorating to me in tough moments while the admiration for simplicity and elegance were setting the direction for the work. I am also grateful for being given a lot of freedom, while my progress was closely followed in countless discussions. Working with Bernhard was an amazing opportunity for not only scientific development but also for personal growth.

I would like to also express words of gratitude to my supervisor at the Łódź University of Technology, prof. Andrzej Bartoszewicz for careful evaluation of my progress as well as multiple suggestions while carrying out my PhD studies. I am also grateful for his trust and effort in establishing good communication necessary while working abroad.

One of the most exciting part of this work, was being part of a team composed of experienced colleagues. I would like to say *grazie mille* to Lorenzo Bortot and Dr Marco Prioli, with whom I shared ups and downs of the STEAM development as well as countless discussions. I would like to thank TE-MPE-PE section leader Dr Arjan Verweij, who was supporting various ideas and providing valuable feedback. I am also happy to have worked with Jonas Blomberg Ghini and would like to thank him for sharing the complexities of superfluid helium and valuable comments on my writing. Working with younger colleagues was also an enriching experience, I would like to express my gratitude towards Deepak Paudel, Maurice Baveco, Tina Griesemer, Michał Wilczek, and Sara Ambjörndalen.

I am also grateful to prof. Sebastian Schöps and Idoia Cortes-Garcia (Technical University of Darmstadt) for introducing me to the universe of cooperative simulations and mathematical analysis as well as many consultations on the way. In addition, many thanks to prof. Herbert De Gersem and prof. Stefan Kurz for keen interest in and support to our work.

I would like to acknowledge continuous support of Kamil Król, Jean-Christophe Garnier, and Mateusz Koza from TE-MPE-MS, who provided multiple suggestions and support in the software development. My gratitude extends to Dr Sven Friedel (COMSOL Multiphysics Switzerland), and Dr Klaus Wolf and Pascal Bayrasy (Fraunhofer Institute SCAI) for patience in solving simulation challenges.

Last but not least I am grateful to my family and friends for continuous and unconditional support. In particular, to my parents and grandparents for being great mentors and sources of inspiration as well as my brothers who I could always count on. To my best friend Julian for countless, inspiring brainstorming sessions and energizing trips; to Mateusz and Lukas for being great flatmates with whom I explored the neighboring mountains hiking, biking, running, and cross-country skiing.

I don't like work - no man does - but I like what is in the work - the chance to find yourself.
-JOSEPH CONRAD

Contents

Chapter 1

Introduction

Modern high-energy particle accelerators demand high magnetic fields in order to steer the trajectory of charged particles traveling at nearly the speed of light. Superconducting magnets fulfill this requirement and are one of the main components of particle accelerators. In circular accelerators, the particles travel in opposite directions and are accelerated over multiple turns (a circular accelerator is also called a storage ring). Once the particles reach the desired energy, while bunched together as a beam, they are made to collide. As a first approximation, the center-of-mass energy of a particle is proportional to the circumference of the accelerator and the magnetic field of the bending magnets. The larger the beam energy during collisions, the deeper we can probe the fundamental constituents of the colliding particles. Analysis of the resulting particle showers created during a collision provides insights into the structure of matter, as well as the forces governing it.

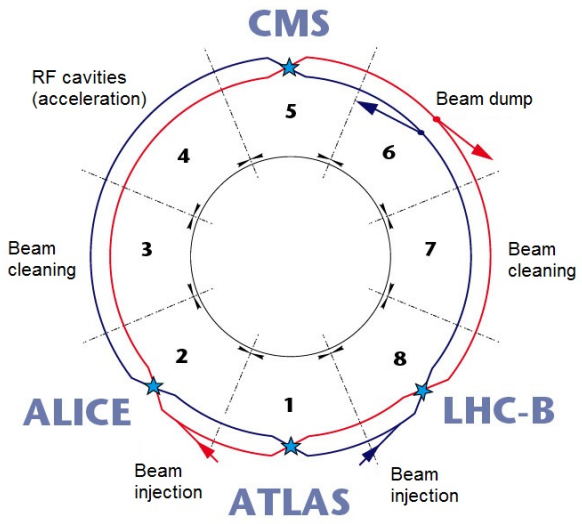

Figure 1.1: Schematic representation of the LHC. [1]

The European Organization for Nuclear Research (CERN) operates the largest circular particle accelerator in the world, the Large Hadron Collider (LHC). The LHC has a circumference of 27 km and is located about 100 m below the French-Swiss border. It consists of over 1500 dipole and quadrupole superconducting magnets, operated at cryogenic temperatures ($1.9-4.2$ K), and several other components, such as accelerating cavities, beam transfer lines, and beam control equipment. As shown in Fig. 1.1, the LHC is composed of 8 sectors, each made up of an arc and a straight section. Arcs are filled with 154 15-meter-long dipole magnets needed to bend the trajectory of particles, as well as tens of several-meter-long quadrupole magnets providing

the necessary focusing for the beam of particles (there are also additional corrector magnets to account for magnetic field imperfections). Straight sections are dedicated to injection of the beam from the Super Proton Synchrotron (SPS), the smaller, preceding accelerator in the chain of accelerators in the CERN accelerator complex, acceleration with radio-frequency (RF) cavities, beam cleaning with a dedicated collimation system, beam dump system[1], and detectors. A detector records traces left by secondary particles generated during a collision. The traces are then used to validate models, such as the Standard Model, representing our understanding of the particle physics. There are four detectors analyzing collisions in the LHC; ATLAS, CMS, ALICE, LHCb. [2]

1.1 Superconducting Accelerator Magnets and Circuits

Superconductivity, discovered by the Dutch physicist Kamerling Ohnes in 1911, is a property of matter characterized by a lack of electrical resistance. The superconductive phase may only persist within a so-called critical surface, given in a coordinate system determined by the temperature, current density, and magnetic field. As long as the operating point of a magnet is below the critical surface, a material is in the superconducting state. Outside the critical surface, the material reverts to normal, resistive conductivity. A sudden transition from the superconducting to the normal conducting state is called a quench.

There are two types of superconductors: low and high temperature superconductors, LTS and HTS, respectively. Niobium-titanium (Nb-Ti) and Niobium-tin (Nb_3Sn) are examples of LTS, which require liquid helium to operate. The LHC dipole magnets are operated at 1.9 K. Nb-Ti is an alloy widely used in accelerator magnets due to its ductility, which facilitates the coil winding process. Nb_3Sn offers larger operational margins (distance from the operating point to the critical surface), however, this material is brittle, which complicates the manufacturing of these magnets. In fact, the coils are made from filaments where Nb and Sn are separate, and only create the superconducting compound Nb_3Sn after a lengthy process (lasting for several days) of reacting at relatively high temperatures ($650 - 700°C$). This process is also referred to as "wind and react".

Another type of superconductors are HTS, such as copper oxide ReBCO (Rare earth - Barium - Copper Oxide), which can operate in temperatures of the liquid nitrogen (77 K). HTS-based magnets feature large magnetic flux densities and operational margins (in order to achieve larger operational margin magnets operate at low temperatures in the order of 4 K). However, the HTS cables are formed as tapes. This translates into a non-uniform current distribution which complicates the control of the magnetic field.

Fig. 1.2 shows the cross-section of an LHC main dipole magnet. A magnet is composed of a coil consisting of many turns of a superconducting cable. The coil is usually clamped in a steel collar to counteract large electrodynamic forces. Then, the steel collar is surrounded by an iron yoke in the form of a hollow cylinder. Eventually, the assembly of the coil, steel collar and iron yoke is embedded in a so-called outer shell (typically made of steel), which provides a container for a static bath of helium (there are heat exchange tubes with helium in the iron yoke).

The smallest component of a superconducting cable is a filament. A filament is a single thread of a superconductor with a diameter optimized toward performance improvements as well as reduction of persistent magnetization and flux jumps. Persistent magnetization currents arise due to variations of the magnetic field. Unlike in normal conducting magnets, these bipolar magnetization currents do not decay but persist for long periods of time (in the order of hundreds of thousands of years). Flux jumps are related to a decrease in the critical current density as a response to an increase in operating temperature of the magnet in the presence of an external magnetic field (this field is usually the field created by the magnet itself). As the critical current density decreases, the screening currents in the superconductor are reduced, which lets the

[1] In case of failures, the high-energy beam of particles has to be safely extracted from an accelerator and dumped on a graphite block. Particle beams are also dumped in case their quality deteriorates below a certain value as a result of multiple collisions.

magnetic field penetrate deeper into the bulk of the superconductor. This increased penetration is equivalent to motion of flux, which induces voltage, that translates into heat generation in the superconductor. [3, Section 2.4] [4, Chapter 7]

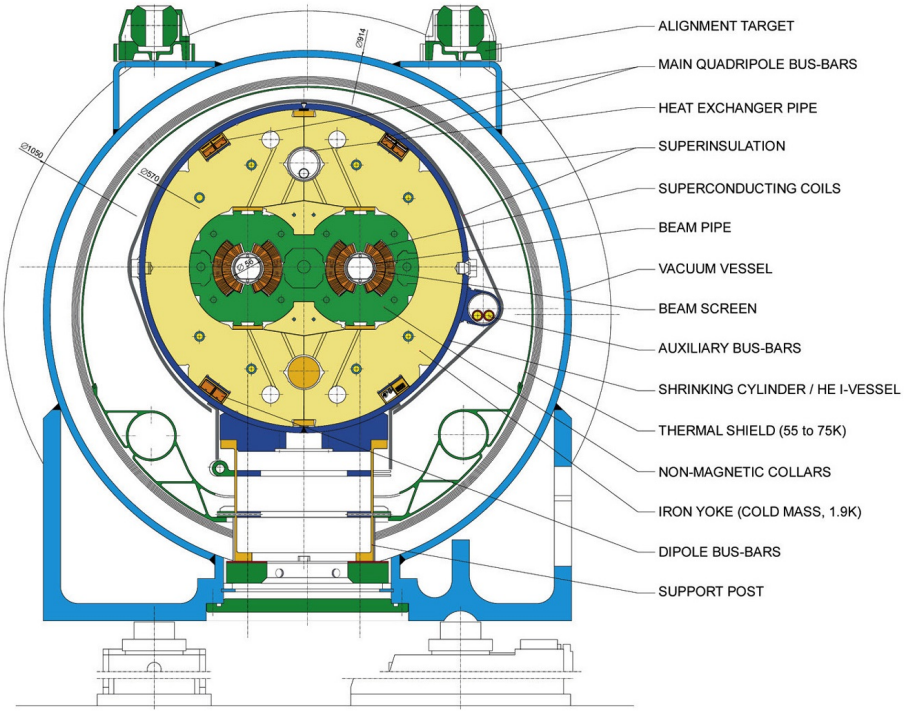

Figure 1.2: Cross-section of the LHC main dipole magnet with description of main components. [5]

Filaments are twisted and embedded in a stabilizing material (usually copper) making a superconducting strand. The stabilizer provides mechanical support as well as a heat sink in case of local depositions of energy in filaments, which could lead to the undesirable loss of superconductivity. In case of a quench, the current flowing in a superconducting filament is ejected to the stabilizer, which has lower resistivity as compared to the superconductor in the normal conducting state. As a result, after a quench less heat is generated in the stabilizer as compared to the superconductor.

A superconducting cable for accelerator magnets is typically composed of fully transposed strands, usually about 20-40, arranged in layers to form a high-aspect ratio rectangular cross-section. Such a cable is called a Rutherford type; see Fig. 1.3. This allows for obtaining high operating current densities and low cable eddy currents.

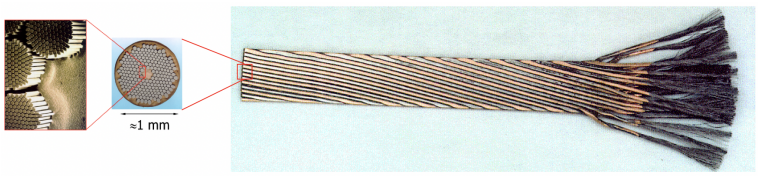

Figure 1.3: Rutherford cable composed of multi-filament strands. [6]

The superconducting filaments are coupled through the surrounding stabilizer matrix. In this setup any magnetic field change will induce eddy currents in a loop composed partly of superconductor and partly of stabilizer. The resulting current flow through the stabilizer generates Ohmic loss, heating up the superconductor. In order to reduce the size of the loop and

consequently the heat deposition, the filaments are twisted. A similar phenomenon occurs between strands within the fully-transposed Rutherford cable. Loops are created in cross-over points between the strands. In the presence of a time-varying magnetic field, voltage is induced in the loop and current starts to flow through the stabilizer also in this case. In fact, the cross-contact resistance between the strands is an important parameter determining the magnitude of the induced Ohmic losses. These two types of cable eddy currents typically have different time constants and both must be considered when determining the maximum ramp rate of the current increase in the magnet. The current ramp-rate is related to the rate of increase in the beam energy as an accelerator can not immediately start operating at the maximum energy. As we shall see later, the cable eddy currents can support the protection system activated in case of a quench to discharge the energy stored in the magnetic field (this is called a quench back).

A cable is wrapped with insulation to separate the windings from one another. The insulation material has to fulfill three main requirements in a wide range of operating temperatures [3]: (i) withstand high radiation doses due to beam losses in the accelerator; (ii) provide sufficient electrical insulation (above 1 kV); (iii) ensure good mechanical properties (elasticity, yield strength). Insulation composed of polymide satisfies these requirements. The insulation for Nb-Ti-based cables is made of several layers with gaps providing channels for the liquid helium to penetrate the cable. This solution is not suitable for Nb_3Sn coils, which undergo a thermal treatment which would deteriorate, maybe even ruin, the properties of polymide. Instead, Nb_3Sn magnets are impregnated with epoxy, which improves the mechanical properties and introduces a barrier for liquid helium. [3]

It can be shown that to generate a perfect dipole field in the center of an aperture, where the beam is located, the current density across the magnet cross-section must be proportional to the cosine of the angle between the midplane of the magnet and the line from magnet cross-section center and a given point on the magnet cross-section periphery. A magnet with this target in mind is often called a cos-theta-magnet (see Fig. 1.4). However, such a distribution

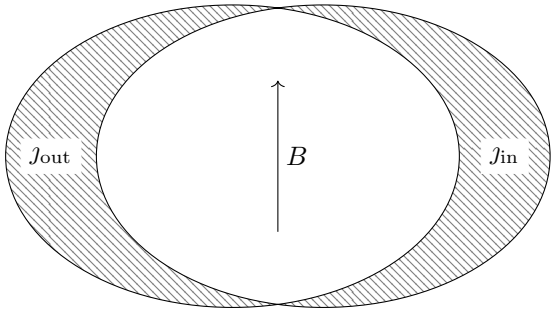

Figure 1.4: Current distribution in cos-theta magnets explained with the intersecting ellipses model.

of current is unfeasible in practice. An approximation is to organize the windings in blocks separated by azimuthally spaced copper wedges. This approximation gives rise to multipole components (such as quadrupole, sextupole, etc.). Multipoles can lead to beam instabilities and therefore the magnet design is optimized with dedicated software (e.g., ROXIE) to reduce their contribution to an acceptable magnitude. Other relevant magnet geometries are block coils and canted-cosine-theta. [4]

Once a magnet is powered, it experiences large Lorentz forces as a consequence of the large current density and magnetic flux density. As a result, the turns can displace, which will cause changes in the magnetic field distribution in the magnet aperture. In addition, the frictional heat generated due to the movement of turns, can cause a quench. In order to reduce the displacement, the steel collar mentioned earlier encloses the coil with a certain pre-stress. The iron yoke surrounding the steel collar in superconducting accelerator magnets has three main roles: (i) support the mechanical structure in order to ensure the coil remains properly compressed during operation; (ii) shield the magnetic field in order to avoid interference with the electronic equipment in the accelerator; (iii) improve the field quality and increase the peak magnetic flux

density. The mechanical structure is subject to an optimization procedure carried out with dedicated simulation software.

Since the heat capacity of considered materials is low at cryogenic temperatures, superconducting magnets are prone to quench by local energy depositions (mechanical movement, coupling losses in the superconducting cable, cryogenic malfunction, beam losses, etc.). With the considerable energy stored in the magnetic field, the quench of a magnet may result in an uncontrolled release of the energy as Ohmic losses. This translates into an increase in the maximum temperature (so called hot-spot temperature), and, possibly, in catastrophic damage of the magnet and electrical circuit. In order to prevent this scenario, there are dedicated magnet and circuit protection systems put in place in order to quickly dissipate the stored energy in the magnetic field. An electrical circuit can be protected with active energy extraction system. The system introduces an additional resistance in the circuit, which reduces the current discharge constant. In addition, there are passive diodes, parallel resistors, and active crowbar switches, which provide an additional path for the current discharge and dissipate some energy as Ohmic loss. The active protection systems such as heaters [7] and CLIQ (Coupling Loss-Induced Quench) [8] are depositing energy in the magnet coils to quench a large fraction of its volume within a short time in order to dissipate uniformly the energy stored in the magnetic field. The heaters, thin, insulated metallic strips attached to the coil heat-up subject to capacitor discharge. The generated heat propagates to the coil, which results in the temperature increase and a quench in the magnet. The CLIQ system is composed of a charged capacitor bank attached to the magnet. Once the system is triggered, the capacitive discharge introduces current oscillations, which provoke inter-filament and inter-strand eddy currents. The eddy currents generate heat inside the magnet and cause a quench.

1.2 Simulation of Transient Effects in Accelerator Magnets

To properly understand a protection scenario, a thorough study of electro-thermal transients in a superconducting magnet, such as quench initiation, longitudinal and transverse propagation, interaction with electrical circuits and accompanying powering control systems, etc., has to be performed. Such a study poses a challenge in terms of the number of coupled physical domains (electric, magnetic, thermal, mechanical, fluid dynamics, etc.), their highly nonlinear behavior, their geometric scales, and their vastly varying time constants.

1.2.1 Magnet

Numerical models play an important role in the design and performance evaluation of a superconducting magnet. Even more important are physical models, built in order to verify the design in practice and validate the numerical models.

A consistent simulation of a wide range of transient effects in accelerator magnets such as: (i) the optimization of the magnetic field; (ii) AC losses; (iii) magneto-thermal phenomena during quench; (iv) mechanical response to large electromagnetic forces and temperature differences, all pose considerable challenges. First of all, a superconducting magnet model consists of several coupled physical domains, i.e., thermal, electrical, magnetic, and mechanical, all characterized by highly nonlinear material properties. Second of all, the dynamic behavior of the coupled physical domains is represented by time constants ranging from microseconds (quench initiation) to minutes (current discharge in a large circuit). Third of all, the transient phenomena occur at a wide range of geometric scales, from sub-millimeter resolution required to accurately track the quench propagation in a superconducting cable, to 15-meter-long magnets.

One of the most important transient effect, due to its potential to damage the magnet and/or cause considerable machine downtime is a quench. Initially, the quench occurs in a small volume of the cable due to a local heat deposition. A 1D model suffices to capture the initial quench propagation along the cable. However, with certain delay, turn-to-turn heat transfer also

becomes important to determine how the quench propagates through the coil. Upon detection, the magnet's power supply is switched off and the energy stored in the magnetic field (represented by either a 2D or 3D magnet model) is being discharged in the internal resistance of the magnet.

1.2.2 Circuit

Magnets are typically connected in series to form a circuit consisting of a power converter, a low-pass filter, and circuit protection systems. A numerical model consists of nonlinear switches, diodes, thyristors, as well as multiple voltage and current sources, and RLC elements. An electrical circuit can consist of several thousand of elements representing phenomena ranging from centimeters to kilometers characterized by large time constants (from milliseconds to minutes).

The energy stored in a superconducting circuit is equal to the sum of energies stored in the magnetic field of each magnet. The total energy can be enormous for the LHC main dipole circuit (> 1 GJ) and dedicated circuit and magnet protection system must be put in place [9].

1.2.3 Controller

The current supplied by a power converter follows a prescribed profile in time. The profile is continuous (at least twice differentiable) in order to avoid introducing electromagnetic waves traveling along the circuit. The ramp rate is usually constrained to limit eddy current losses. The increase of current results in higher bending force for the dipole magnets, which allows for an increase of the beam energy. At the same time, in order to achieve a stable circulation of the beam in an accelerator, the magnetic field has to be of high quality. This means that magnets must be fed with a low ripple current. Therefore, a dedicated controller is put in place to ensure good accuracy in providing the reference current profile. A controller operates with a fixed frequency and is implemented as a digital system.

1.2.4 Multi-domain, Multi-physics, Multi-rate, Multi-scale

We consider three coupled domains: a superconducting magnet, the accompanying circuit, and the power converter controller. Each domain in turn can represent several coupled physical phenomena. These are characterized by a highly nonlinear behavior with a wide range of time constants occurring at geometric scales spanning several orders of magnitude. In summary, the simulation of transient effects in accelerator magnets is a multi-domain, multi-physics, multi-rate, and multi-scale problem.

Simulation of such a system in a single tool poses several challenges w.r.t. the computational complexity. The equations representing the model would need to be discretized at a large scale. On top of that, various physical phenomena may require custom discretization. In addition, the time integration would need to deal with various transients by choosing the time step capable of reproducing the fastest time constant in the system. And, depending on the studied operational scenario, the physical phenomena are represented with different models in particular phases. In fact, depending on the desired model fidelity, there is a need for switching the models from the available collection thereof. Since the coupled problem is non-tractable in a monolithic sense, we employ the divide and conquer philosophy. Following this approach the coupled problem is subdivided into smaller parts which are solved independently, though they are allowed to exchange information at discrete points in time. This approach, however, brings several research questions to mind:

- How to divide the coupled problem into subproblems?
- What quantities should be exchanged between the subproblems?
- In what order should the subproblems be solved?
- How to re-establish the link between subproblems in order to recover the solution to the original coupled problem?

- How to ensure that the results of the coupled system are consistent?

1.3 Research Theses

The motivation of the research work was to provide answers to these questions. As a result, the following theses were formulated and will be outlined in the remainder of the treatise

1. it is possible, by employing the port-Hamiltonian formalism, to develop a consistent mathematical formulation of magneto-thermal phenomena occurring in the superconducting accelerator magnets and circuits, which will be used to analyze cooperative simulations of these systems;

2. it is possible to develop an architecture, algorithms, and data structures in order to automatically perform hierarchical cooperative simulations of superconducting accelerator magnets, circuits, and controllers in order to solve the formulation given in (1).

The analysis of the coupling between the considered systems should provide insights into how they would need to be partitioned in order to improve computational performance. The analysis framework should provide a unified treatment of various physical domains as well as support both distributed and lumped representations of these domains. The port-Hamiltonian formalism along with graphical representation by means of bond graphs promises to support this type of analysis.

1.4 State of the Art

Several approaches have been undertaken in order to tackle multi-* problems. Port-Hamiltonian models were already developed in several areas. Trang has developed a port-Hamiltonian model of thermo-magneto-hydrodynamics of plasma in a tokamak of the International Thermonuclear Experimental Reactor (ITER)[10]. The model was used to design a controller for plasma, whose stability is one of the most critical aspects of the tokamak operation. The bond graph framework was applied to modeling and validation of electro-thermal behavior in semiconductor switches [11]. Due to its modular structure, the bond graph model can be extended and connected to an electrical machine such as a three-phase induction motor [12].

Hamada et al. have developed a monolithic quench and arc model for simulation of ITER superconducting coils [13]. The ANSYS model is representing the 3D geometry of the superconducting coils and allows simulating electro-thermal phenomena occurring during quenching and arcing. The distributed model contains nonlinear relationships while the model of the electrical network is linear. The Routine for the Optimization of magnet X-sections, Inverse field computation and coil End design (ROXIE) is a FEM-BEM (Finite Element Method - Boundary Element Method) code dedicated to the design and optimization of the magnet's geometry in order to generate a high-quality magnetic field in accelerator magnets [14]. In addition, ROXIE is equipped with a module for monolithic quench simulation as well as interfaces to CAD (Computer Aided Design) software and other simulation tools (geometry and Lorentz force export to ANSYS). Caspi and Ferracin have proposed an integrated approach to electrical, thermal, and mechanical analysis of the accelerator magnet design process bringing together several CAD and simulation tools [15].

Another class of solution methods to the coupled problem involve cooperative simulations (co-simulations for short). Following this approach, a coupled problem can be regarded as a combination of dedicated models of a particular part of the problem. Using suitable algorithms, the link between the different models is reestablished, and a consistent solution is obtained. An advantage of this method is that each subproblem can be solved with appropriate physics-specific discretization and time steps distribution driven by its dynamics. However, co-simulation introduces challenges w.r.t. the convergence of the coupled system. This aspect has to be studied in order to ensure consistency of the obtained solution, in particular for non-linear systems.

The waveform relaxation algorithm has been successfully applied to the field-circuit coupling problem, especially for systems characterized by multi-scale and multi-rate behavior [16]. Schöps has shown that a reduced-order representation of the field model on a circuit side (differential inductance evaluated at the operating point), also referred to as a pre-conditioner, enhances the convergence rate [16]. For linear problems, the waveform relaxation guarantees convergence for an arbitrary duration of time window for which the coupled models are solved. However, for nonlinear problems, an excessive time window can lead to divergence. When using the weak coupling algorithm, for which only single data points are transferred, the energy exchanged between the coupled models can be used to control the duration of the time window [17]. FMI (Functional Mock-up Interface) is a simulation software agnostic standard for model exchange and cooperative simulation. The FMI interface supports many solvers however is based on the weak coupling algorithm and does not support waveform relaxation technique [18]. SuperMagnet suite for simulating superconducting magnets provides a coupling of several tools: THEA (Thermal-Electric Hydraulic Analysis) to simulate quench propagation in superconducting cables, FLOWER to model cryogenic circuits, POWER to simulate electrical circuits and HEATER to account for the heat conduction in a coil and surrounding structures [19].

1.5 Thesis Outline

The thesis is organized as follows. Chapter 2 provides a compact introduction to energy-based modeling of lumped and distributed phenomena with bond graphs and port-Hamiltonian equations. Then, bond graph and port-Hamiltonian models of superconducting magnets are developed starting from the Maxwell equations and the entropy balance equation. Energy based modeling is also applied to the case of superconducting circuits represented by means of the modified nodal analysis.

Chapter 3 deals with cooperative simulations of superconducting accelerator circuits. A description of the main co-simulation algorithms is provided. The architecture of the co-simulation framework implementing the algorithms is discussed. Afterwards, the framework is applied to the simulation of relevant transient effects in superconducting circuits. Properties and the performance of the algorithms are also outlined.

Chapter 4 extends the architecture given in Chapter 3 to allow for hierarchical co-simulation. The extension is based on an observation that a given simulation scenario can consist of several coupled models active only during certain intervals of the considered scenario.

The thesis ends with a conclusion and a list of main contributions of the thesis. The conclusion comes with an outlook for potential future research in the field of co-simulation as well as numerical modeling of superconducting magnets in general.

Appendix A provides a brief introduction to the differential forms which are used in the thesis to represent physical quantities. The fundamental relationships representing electromagnetism and thermodynamics are summarized in Appendices B and C, respectively. Deterministic Finite Automata are presented in a compact form in Appendix D.

The work was carried out in the TE-MPE-PE[2] section at CERN within the scope of the STEAM (Simulation of Transient Effects in Accelerator Magnets) project. The goal of the project is to provide a high-fidelity simulation framework to study existing and design future accelerator magnets and circuits. The foundation of the simulation environment is a set of dedicated field and circuit models. These models are generated by automated workflows and then solved with appropriate proprietary and in-house solvers independently or in a co-simulation.

The main contribution of the work presented in this thesis to the STEAM project has been the theoretical study of magneto-thermal coupling in superconducting magnets, as well as electrical phenomena in superconducting circuits. Another relevant contribution has been the design and analysis of the architecture, algorithms, and data structures for the co-simulation framework. Given the complexity of the subject matter, some individual applications of the framework are a result of cooperation of a team of engineers.

[2]Technology Department, Machine Protection and Electrical Integrity Group, Performance Evaluation Section

Chapter 2

Port-Hamiltonian Modelling of Controlled Coupled Problems

In this chapter we derive a bond graph representation and the corresponding port-Hamiltonian model of a superconducting circuit. The circuit is composed of a superconducting magnet and elements used for powering and protection. The superconducting magnet model consists of electromagnetic and thermal domains originating from, respectively, the Maxwell equations and the laws of thermodynamics. Thus, the superconducting magnet is represented as a distributed-parameter model for which differential forms are employed. The superconducting circuit model is represented as a lumped-parameter network by means of the Modified Nodal Analysis (MNA).

Bond graph and port-Hamiltonian modeling are complementary, domain-independent techniques allowing for a consistent modeling of energy flow in physical systems. They are particularly useful to represent multi-physical systems for which a generic representation is important. A bond graph model is a decomposition of a physical system into consecutive stages of the energy flow, storage, and dissipation. Such a bond graph model serves as a good starting point to derive a port-Hamiltonian representation of the system by aggregating subsystems together. In fact, the bond graph framework serves as a visualization of the mathematical structure given by the port-Hamiltonian system. A port-Hamiltonian model is suitable for analysis of internal energy variation in the entire system due to dissipation and/or interaction through the boundary and distributed ports. Furthermore, these modeling tools can be used to represent both, lumped and distributed parameter systems as well as their combination. Another relevant area of application is the control of multi-physical dynamical systems.

2.1 Dirac Structure

Power-conservation is a fundamental property of mathematical models describing physical phenomena. Modeling consistency can be ensured if each building block fulfills this requirement. Furthermore, it is important to ensure that the combination of these blocks still maintains this property. A Dirac structure describes a general class of power-continuous subsystems characterized by a linear space of conjugate power-continuous variables.

First, let us introduce a finite dimensional linear space of flows $\mathcal{F}$, and its dual linear space of efforts $\mathcal{E} = \mathcal{F}^*$. Then, we introduce the duality inner product between elements of these spaces as

$$\langle f|e\rangle = f^\top e, f \in \mathcal{F}, e \in \mathcal{E}. \tag{2.1}$$

The result of the duality inner product (2.1) is the net power in the system characterized by flows and efforts. With the definitions of spaces of conjugate variables and the duality inner product one can define a Dirac structure.

Definition 2.1 (Definition 2.1 in [20]) *A Dirac structure on $\mathcal{F} \times \mathcal{E}$ is a subspace $\mathcal{D} \in \mathcal{F} \times \mathcal{E}$ characterized by the following two properties*

$$\langle f|e\rangle = f^\top e = 0, \forall (f,e) \in \mathcal{D}, \tag{2.2a}$$

$$\dim \mathcal{D} = \dim \mathcal{F}. \tag{2.2b}$$

Thus, a Dirac structure is a subspace of maximal dimension (2^{nd} property) which satisfies power-continuity (1^{st} property). Dirac structure in Fig. 2.1 is represented as a junction connecting three pairs of conjugate variables. The arrow indicates the orientation of the product of flow and effort variables such that the positive product indicates the outgoing power. Note that this does not determine the sign of conjugate variables.

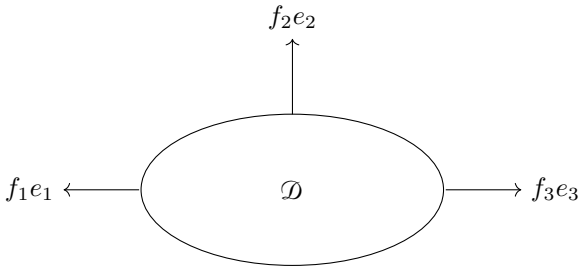

Figure 2.1: Dirac structure as a junction connecting three pairs of conjugate variables (f_1, e_1), (f_2, e_2), (f_3, e_3).

Another definition of a Dirac structure arises with $\mathcal{D}^\perp$ as the orthogonal complement of $\mathcal{D}$ with respect to the bilinear form on the space of conjugate variables $\mathcal{F} \times \mathcal{E}$

$$\langle\langle (f,e), (\hat{f},\hat{e})\rangle\rangle := \langle e|\hat{f}\rangle + \langle \hat{e}|f\rangle, \tag{2.3}$$

where $(f,e), (\hat{f},\hat{e}) \in \mathcal{F} \times \mathcal{E}$.

Definition 2.2 (Proposition 2.1 in [20] and Section 2 in [21]) *A Dirac structure on $\mathcal{F} \times \mathcal{E}$ is a subspace $\mathcal{D} \subset \mathcal{F} \times \mathcal{E}$ such that $\mathcal{D} = \mathcal{D}^\perp$, with $\mathcal{D}^\perp$ given as*

$$\mathcal{D}^\perp = \left\{ (f,e) \in \mathcal{F} \times \mathcal{E} : \langle e|\hat{f}\rangle + \langle \hat{e}|f\rangle = 0, \forall (\hat{f},\hat{e}) \in \mathcal{D} \right\}. \tag{2.4}$$

Def. 2.2 is also suited for infinite dimensional vector spaces and is therefore more fundamental and is equivalent only in the finite-dimensional case to Def. 2.1. We note that the bilinear form (2.3) becomes equivalent, up to a factor, to the duality inner product (2.1) for a pair of the same flows and efforts $(f^a, e^a) = (f^b, e^b) = (f,e) \in \mathcal{D}$

$$\langle\langle (f,e), (f,e)\rangle\rangle = 2\langle f|e\rangle = 0. \tag{2.5}$$

From (2.5) we conclude that the bilinear form (2.3) can be used to verify whether power conservation is satisfied and the considered structure is a Dirac structure. For the former purpose it is sufficient to verify whether the duality inner product (2.1) is vanishing.

2.1.1 Bond Graphs

Introduced by Henry Paynter [22], the bond graph technique provides a generic framework for representing power-continuous models of multi-physical systems. The framework is based on bonds carrying a pair of flow and effort variables. The product of flow and effort variables in each bond describes the power flow. A model can be represented at two levels of abstraction connecting together either large units (so-called word bond graphs) or regular bond graphs composed of single-, two-, and multi-port elements. As a result, a bond graph model represents the flow of energy in the considered system. The elements used to create bond graphs consist of: (i) a group of power-continuous structures such as 0- and 1- junctions, transformers, gyrators; (ii) sources of flow and effort; (iii) energy storage elements; (iv) dissipative elements.

2.1.2 Bilateral Bonds

A bond is a pair of power variables, namely flow $f \in \mathcal{F}$ and its dual complement effort $e \in \mathcal{E} = \mathcal{F}^*$. The graphical representation of a bond is a half-arrow (also referred to as a harpoon) with the flow variable on the side with a half-arrow and the effort variable on the other side. The orientation of the half-arrow denotes the sign convention of the model, which is needed to calculate the power-balance equations. A bond $\longrightarrow\!\!\!\!\!\!\nearrow$ means flow to the right is positive and power is counted positive if it flows to the right as well. An important concept is a computational causality assignment reflected by a causal stroke attached to either end of a bond. Causality determines which of the nodes is setting the effort and which is setting the flow. For example, in Fig. 2.2 System 1 has effort-out causality, i.e., the effort variable is calculated from the flow, which is set by System 2 and *vice versa*. In contrast to standard arrows representing the flow of information in block diagrams, bonds are bilateral w.r.t. the power exchange. In other words, a bond represents the bilateral exchange of flow and effort signals. To pass the same information, an equivalent block diagram requires two information arrows and a sign convention for the power flow.

Figure 2.2: Representation of power exchange between two systems by means of a word bond graph (left) and a block diagram (right). Note that the block diagram does not indicate the direction of the power flow.

It is possible to combine both types of diagrams to represent controlled bond graph models. In this case, the input of a controller can be obtained with a sensor of flow or effort and the control signal can be implemented as a source of flow or effort, or as a modulation of transformers or gyrators as we will see later in Section 2.1.8.

2.1.3 Examples of Dirac Structures and their Bond Graphs

In this Section we introduce 0- and 1-junctions, a transformer, and a gyrator. It will be shown, that these structures, relating pairs of conjugate power variables, have a power-conservation property and can be represented as Dirac structures. For completeness, it is assumed that the output power is positive and the input power is negative, which is relevant for the power balance equations.

0-junction

A 0-junction is one of the basic building blocks in the bond graph theory. The 0-junction relates flows and efforts such that the flows add up to zero and all efforts across the bonds are equal. An example of a 0-junction with three output power bonds reads

$$\mathcal{D}_0 = \left\{ \begin{array}{l} (f_1, f_2, f_3, e_1, e_2, e_3) \in \mathcal{F}_0 \times \mathcal{E}_0 : \\ \begin{bmatrix} f_2 \\ e_1 \\ e_3 \end{bmatrix} = \begin{bmatrix} 0 & -1 & -1 \\ 1 & 0 & 0 \\ 1 & 0 & 0 \end{bmatrix} \begin{bmatrix} e_2 \\ f_1 \\ f_3 \end{bmatrix} \end{array} \right\}. \tag{2.6}$$

A bond graph depicting a 0-junction is shown in Fig. 2.3. Notation adopted in (2.6) reflects the causality assignment, i.e., variables of bonds on the left hand side have out causality, respectively f_2 has flow-out causality, and e_1 and e_3 have effort-out causality w.r.t. the 0-junction. As a result of this convention, in the thesis, the structural matrix is characterized by the skew-symmetry property. From (2.6) it follows that in a 0-junction only one bond can have effort-in

causality attached to the junction, and as a consequence the remaining bonds have fixed effort-out causalities.

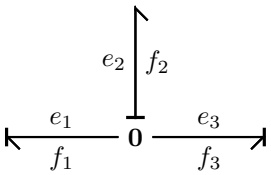

Figure 2.3: Bond graph representation of a 0-junction with three output power bonds. Bond (f_2, e_2) is establishing the effort for the junction.

With the adopted power sign convention, it is immediate to show that a 0-junction in Fig. 2.3 is a Dirac structure

$$\begin{aligned}&\left\langle\left\langle(f_1,f_2,f_3,e_1,e_2,e_3),(\hat{f}_1,\hat{f}_2,\hat{f}_3,\hat{e}_1,\hat{e}_2,\hat{e}_3)\right\rangle\right\rangle = f_1\hat{e}_1 + f_2\hat{e}_2 + f_3\hat{e}_3 + \\ &+ \hat{f}_1 e_1 + \hat{f}_2 e_2 + \hat{f}_3 e_3 = f_1\hat{e}_2 + f_2\hat{e}_2 + f_3\hat{e}_2 + \hat{f}_1 e_2 + \hat{f}_2 e_2 + \hat{f}_3 e_2 = \\ &(f_1 + f_2 + f_3)\hat{e}_2 + (\hat{f}_1 + \hat{f}_2 + \hat{f}_3)e_2 = 0.\end{aligned} \tag{2.7}$$

Let us now consider a case for which, the bond (f_1, e_1) in (2.6) denotes input power. As a consequence, the corresponding 0-junction is given as

$$\mathscr{D}_0 = \left\{ \begin{array}{l}(f_1,f_2,f_3,e_1,e_2,e_3) \in \mathscr{F}_0 \times \mathscr{E}_0 : \\ \begin{bmatrix} f_2 \\ e_1 \\ e_3 \end{bmatrix} = \begin{bmatrix} 0 & -1 & -1 \\ 1 & 0 & 0 \\ 1 & 0 & 0 \end{bmatrix} \begin{bmatrix} e_2 \\ -f_1 \\ f_3 \end{bmatrix} \end{array} \right\}. \tag{2.8}$$

The change of the power flow is represented by the sign change of f_1 in (2.8). From the bond graph representation standpoint, the change of the power flow is reflected by a change of the (f_1, e_1) bond orientation as depicted in Fig. 2.4. Note that the computational causality assignment of the bonds did not change. In other words, computational causality of bonds is independent from the direction of the power flow.

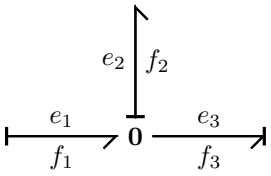

Figure 2.4: Bond graph representation of a 0-junction with a single input power bond (f_1, e_1) and two output power bonds (f_2, e_2) and (f_3, e_3).

The Kirchhoff Current Law stating that the sum of currents in a node of a circuit is equal to zero is a 0-junction.

Example: Fig. 2.5 shows an exemplary parallel RLC circuit with a current source. Due to the resulting causality assignment, the Ohm law of the resistor reads $f_2 = Ge_2$.

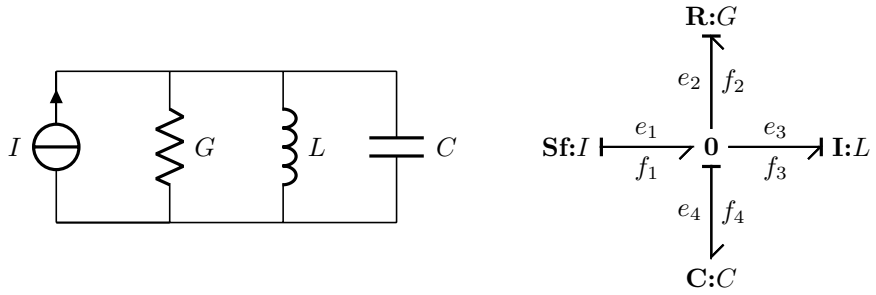

Figure 2.5: Parallel RLC circuit powered by an ideal current source depicted as an electrical schematic (left) and a bond graph (right).

As we shall see later, a current source, conductance, capacitance and inductance, are modelled as, respectively, a source of flow **Sf** (Section 2.1.4), dissipative element **R** (Section 2.1.6), **C**- and **I**-type storage elements (Section 2.1.5). The 0-junction representing the parallel RLC circuit is represented in the matrix form as

$$\mathscr{D}_0 = \left\{ \begin{array}{l} (f_1, f_2, f_3, f_4, e_1, e_2, e_3, e_4) \in \mathscr{F}_0 \times \mathscr{E}_0 : \\ \begin{bmatrix} f_4 \\ e_1 \\ e_2 \\ e_3 \end{bmatrix} = \begin{bmatrix} 0 & -1 & -1 & -1 \\ 1 & 0 & 0 & 0 \\ 1 & 0 & 0 & 0 \\ 1 & 0 & 0 & 0 \end{bmatrix} \begin{bmatrix} e_4 \\ -f_1 \\ f_2 \\ f_3 \end{bmatrix} \end{array} \right\}. \tag{2.9}$$

1-junction

A complementary structure to the 0-junction (2.6) is a 1-junction relating pairs of flows and efforts according to

$$\mathscr{D}_1 = \left\{ \begin{array}{l} (f_1, f_2, f_3, e_1, e_2, e_3) \in \mathscr{F}_1 \times \mathscr{E}_1 : \\ \begin{bmatrix} e_2 \\ f_1 \\ f_3 \end{bmatrix} = \begin{bmatrix} 0 & -1 & -1 \\ 1 & 0 & 0 \\ 1 & 0 & 0 \end{bmatrix} \begin{bmatrix} f_2 \\ e_1 \\ e_3 \end{bmatrix} \end{array} \right\}. \tag{2.10}$$

Fig. 2.6 presents a graphical representation of the 1-junction (2.10) in the form of a bond graph.

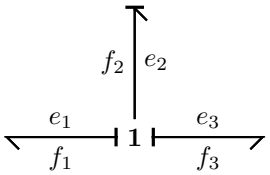

Figure 2.6: Bond graph representation of the 1-junction (2.10).

Following the orientation of the half-arrows in Fig. 2.6, the bilinear form for the considered 1-junction reads

$$\begin{aligned} &\Big\langle\Big\langle (f_1, f_2, f_3, e_1, e_2, e_3), (\hat{f}_1, \hat{f}_2, \hat{f}_3, \hat{e}_1, \hat{e}_2, \hat{e}_3) \Big\rangle\Big\rangle = f_1\hat{e}_1 + f_2\hat{e}_2 + f_3\hat{e}_3 \\ &+ \hat{f}_1 e_1 + \hat{f}_2 e_2 + \hat{f}_3 e_3 = f_2\hat{e}_1 + f_2\hat{e}_2 + f_2\hat{e}_3 + \hat{f}_2 e_1 + \hat{f}_2 e_2 + \hat{f}_2 e_3 = \\ &= f_2(\hat{e}_1 + \hat{e}_2 + \hat{e}_3) + \hat{f}_2(e_1 + e_2 + e_3) = 0. \end{aligned} \tag{2.11}$$

which leads to a conclusion that, indeed, a 1-junction is a Dirac structure.

The 1-junction is a generalization of the Kirchhoff Voltage Law in circuit theory, which expresses that the algebraic sum of voltages around a closed loop is zero.

Example: An example of a 1-junction is a series RLC circuit with a voltage source (Fig. 2.7).

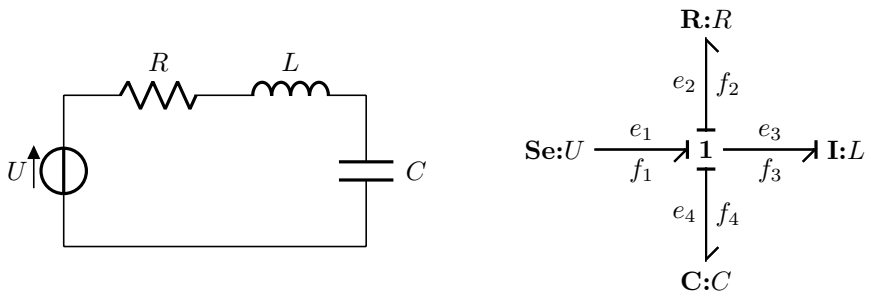

Figure 2.7: A bond graph model (right) of an electrical circuit (left) composed of a series connection of RLC elements and an ideal voltage source.

The voltage source in 2.7 is represented as a source of effort **Se** (cf. Section 2.1.4). As one can notice, in the 1-junction in Fig. 2.7 there is only one bond with flow-in causality. This is a general property of a 1-junction, as only one bond can set the flow for the remaining ones.

Transformer

A transformer links a pair of flow and effort variables according to the transformer ratio n_{TF} as

$$\mathscr{D}_{\mathrm{TF}} = \left\{ \begin{array}{l} (f_1, f_2, e_1, e_2) \in \mathscr{F}_{\mathrm{TF}} \times \mathscr{E}_{\mathrm{TF}} : \\ \begin{bmatrix} e_1 \\ f_2 \end{bmatrix} = \begin{bmatrix} 0 & n_{\mathrm{TF}} \\ -n_{\mathrm{TF}} & 0 \end{bmatrix} \begin{bmatrix} -f_1 \\ e_2 \end{bmatrix} \end{array} \right\}. \tag{2.12}$$

Fig. 2.8 depicts a bond graph representation of a transformer with the computational causality determined from (2.12).

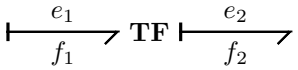

Figure 2.8: Bond graph representation of a transformer.

The power balance equation of a transformer reads

$$\langle f | e \rangle = f^{\top} e = -f_1 e_1 + f_2 e_2 = -f_1 n_{\mathrm{TF}} e_2 + n_{\mathrm{TF}} f_1 e_2 = 0. \tag{2.13}$$

It is immediate to show that a transformer is not only power-continuous, but also forms a Dirac structure as the bilinear form (2.3) is vanishing

$$\begin{aligned} &\Big\langle \Big\langle (f_1, f_2, e_1, e_2), (\hat{f}_1, \hat{f}_2, \hat{e}_1, \hat{e}_2) \Big\rangle \Big\rangle = -f_1 \hat{e}_1 + f_2 \hat{e}_2 - \hat{f}_1 e_1 + \hat{f}_2 e_2 = \\ &= -f_1 n_{\mathrm{TF}} \hat{e}_2 + n_{\mathrm{TF}} f_1 \hat{e}_2 - \hat{f}_1 n_{\mathrm{TF}} e_2 + n_{\mathrm{TF}} \hat{f}_1 e_2 = 0. \end{aligned} \tag{2.14}$$

Transformers are used in electrical engineering to adjust the amplitude of an AC voltage and introduce a galvanic separation between the input and the output.

Gyrator

A gyrator is used to represent an exchange of flow and effort variables with the gyrator ratio n_{GY}. Its constitutive relation reads

$$\mathscr{D}_{\mathrm{GY}} = \left\{ \begin{array}{l} (f_1, f_2, e_1, e_2) \in \mathscr{F}_{\mathrm{GY}} \times \mathscr{E}_{\mathrm{GY}} : \\ \begin{bmatrix} e_1 \\ e_2 \end{bmatrix} = \begin{bmatrix} 0 & n_{\mathrm{GY}} \\ -n_{\mathrm{GY}} & 0 \end{bmatrix} \begin{bmatrix} -f_1 \\ f_2 \end{bmatrix} \end{array} \right\}. \tag{2.15}$$

From (2.15) effort-out computational causality is deduced as shown in Fig. 2.9.

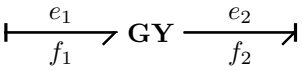

Figure 2.9: Schematic representation of a gyrator.

Similarly, as in the case of a transformer, we demonstrate that a gyrator is a Dirac structure

$$\Big\langle\Big\langle (f_1, f_2, e_1, e_2), (\hat{f}_1, \hat{f}_2, \hat{e}_1, \hat{e}_2) \Big\rangle\Big\rangle = -f_1\hat{e}_1 + f_2\hat{e}_2 + -\hat{f}_1 e_1 + \hat{f}_2 e_2 =$$
$$- f_1 n_{\mathrm{GY}} \hat{f}_2 + f_2 n_{\mathrm{GY}} \hat{f}_1 - \hat{f}_1 n_{\mathrm{GY}} f_2 + \hat{f}_2 n_{\mathrm{GY}} f_1 = 0.$$

The symplectic gyrator is a unit gyrator with $n_{\mathrm{GY}} = 1$. The symplectic gyrator can be used to swap flow and effort variables without introducing a gain.

Example: An example of a gyrator is a DC electric motor relating the motor's angular velocity ω_{M} and the voltage U_{M} as well as the torque T_{M} and the current I_{M} (see Fig. 2.10). With k_{M} being the motor speed constant, a gyrator representing the motor reads

$$\mathcal{D}_{\mathrm{GY_M}} = \left\{ \begin{matrix} (f_1, f_2, e_1, e_2) \in \mathcal{F}_{\mathrm{GY_M}} \times \mathcal{E}_{\mathrm{GY_M}} : \\ \begin{bmatrix} -f_1 \\ f_2 \end{bmatrix} = \begin{bmatrix} 0 & -k_{\mathrm{M}} \\ k_{\mathrm{M}} & 0 \end{bmatrix} \begin{bmatrix} e_1 \\ e_2 \end{bmatrix} \end{matrix} \right\}. \tag{2.16}$$

For the considered DC motor, the gyrator (2.16) is parametrized as

$$(I_{\mathrm{M}}, \omega_{\mathrm{M}}, U_{\mathrm{M}}, T_{\mathrm{M}}) = (f_1, f_2, e_1, e_2) \in \mathcal{D}_{\mathrm{GY_M}} \subset \mathcal{F}_{\mathrm{GY_M}} \times \mathcal{E}_{\mathrm{GY_M}}. \tag{2.17}$$

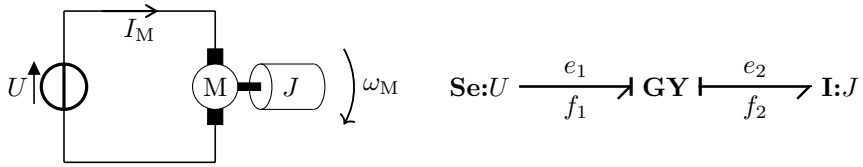

Figure 2.10: Left: Schematic representation of a DC motor with a moment of inertia J, modelled as an **I**-type storage, powered from a voltage source. Right: Equivalent bond graph model.

To conclude the example, from Fig. (2.9) and (2.10) we observe that a gyrator can have input and output bonds with either both effort-in or both flow-in computational causalities.

2.1.4 Sources

The bond graph modeling framework is also equipped with sources of flow and effort. As depicted in Fig. 2.11 the source of flow has flow-out causality, whereas the source of effort has effort-out causality. In both cases, the computational causality is fixed. From that, we note that it is not possible to connect k flow sources to a k-port 1-junction, where k is an integer number. By analogy, it is prohibited to attach k effort sources to a k-port 0-junction.

Figure 2.11: Source of flow (left) and source of effort (right).

2.1.5 Storage Elements

The dynamics of the system is determined by the evolution of a conserved quantity $x \in \mathcal{X}$ with $\mathcal{X}$ being a smooth manifold[1]. The conserved quantity is associated with an energy function, also referred to as the Hamiltonian energy function $\mathcal{H}(x)$. The flow variables are defined as the time derivative of the conserved quantity $f_\mathrm{s} = \partial_t x$. The effort variables are derived from the Hamiltonian function as

$$e_\mathrm{s} = \partial_x \mathcal{H}(x) = \delta_x H \left(\int f_\mathrm{s} \mathrm{d}t + x_0 \right). \tag{2.18}$$

The variation of the internal energy yields

$$\partial_t \mathcal{H} = \langle \partial_x \mathcal{H}(x) | \partial_t x \rangle = \left(\partial_x \mathcal{H} \left(\int f_\mathrm{s} \mathrm{d}t + x_0 \right) \right)^\top \partial_t x = e_\mathrm{s} (f_\mathrm{s})^\top f_\mathrm{s}, \tag{2.19}$$

which is interpreted as the integral causality. For the case of the derivative causality one should consider co-energy $\mathcal{H}^*(e_\mathrm{s})$ given as a Legendre transformation of $\mathcal{H}(x)$, i.e., $\mathcal{H}^*(e_\mathrm{s}) = e_\mathrm{s}^\top x - \mathcal{H}(x)$. In this setup, the state variable is derived from the co-energy as $x = \partial_{e_\mathrm{s}} \mathcal{H}^*(e_\mathrm{s})$, so that the flow variable is defined as

$$f_\mathrm{s} = \partial_t x = \partial_t \partial_{e_\mathrm{s}} \mathcal{H}^*(e_\mathrm{s}). \tag{2.20}$$

Then, the variation of the internal energy yields

$$\partial_t \mathcal{H} = \langle \partial_x \mathcal{H}(x) | \partial_t x \rangle = \partial_x \mathcal{H}(x)^\top \partial_t x = e_\mathrm{s}^\top \partial_t \partial_{e_\mathrm{s}} \mathcal{H}^*(e_\mathrm{s}) = e_\mathrm{s}^\top f_\mathrm{s}(e_\mathrm{s}). \tag{2.21}$$

In bond graph theory, the storage elements are grouped into I- and C-type storage elements, for which effort and flow variables are integrated, respectively. In electrical engineering, an example of an I-type storage is an inductor with inductance L and a constitutive relation $f_\mathrm{s} = 1/L \int e_\mathrm{s} \mathrm{d}t$ with $f_\mathrm{s} = I$ and $e_\mathrm{s} = U$ being, respectively, voltage and current. By analogy, a capacitor characterized by capacitance C is a C-type storage governed by $e_\mathrm{s} = 1/C \int f_\mathrm{s} \mathrm{d}t$.

Thus, the I-type storage has a preferred effort-in causality and the C-type prefers flow-in causality as shown in Fig. 2.12.

Figure 2.12: Bond graph representation of an I-type (left) and C-type (right) storage in preferred (integral) causality.

Note that in this connection positive power increases the stored energy; see also (2.19) and (2.21). The integral computational causality as compared to the differential one is preferred from the numerical implementation standpoint as it leads to more stable computation schemes.

2.1.6 Dissipation

Dissipative phenomena are represented by means of resistive elements. The dissipated energy is irreversibly lost in the form of generated heat. Depending on the considered modeling requirements and operating conditions, the generated heat can be a source term in the thermal system.

[1] Manifold is a topological space which locally behaves like $\mathbb{R}^n$ with n independent coordinates. A manifold can also be infinitely dimensional in order to describe continuous fields.

Resistor

In case the resulting temperature variation is negligible, a resistor is represented as a single-port element. Let R be a positive, in general nonlinear, function characterizing a resistor and (f, e) be a corresponding pair of flow and effort. Then, the governing equation of a resistor is given as either $e = Rf$ or $f = R^{-1}e = Ge$, where G is the conductance. If R is a function, more complex relationships between e and f are possible. The appropriate representation is determined by the resulting causality of the dissipative system (see Fig. 2.13). Thus, a resistor accepts both, effort-out and effort-in computational causality. In other words, a resistor has an arbitrary causality.

Figure 2.13: Bond graph representation of a resistor with an effort-out (left) and effort-in (right) causality.

Power flowing into a resistor is either lost or increases entropy of the system, see below.

Irreversible Entropy Source

In some simulation scenarios the thermal domain has to be considered in order to account for the temperature variation due to energy dissipation. For an electrical resistor characterized by a resistance R, the flow of current $I = f_1$ results in a voltage drop across its terminals $U = RI = e_1$. Furthermore, Ohmic loss is generated according to $q_R = RI^2 = e_1 f_1$. Thus, a resistor can be considered as an irreversible transducer, i.e., the power flow is one-directional as the energy is dissipated. A resistor acts as an irreversible entropy source $\sigma_R = f_2$, so called resistive source (RS); see Fig. 2.14. The entropy source is connected to the thermal domain, from which temperature $T = e_2$ is deduced. The equation governing this 2-port element reads

$$\mathcal{G}_{\mathrm{RS}} = \left\{ \begin{array}{c} (f_1, f_2, e_1, e_2) \in \mathcal{F}_{\mathrm{RS}} \times \mathcal{E}_{\mathrm{RS}} : \\ \begin{bmatrix} e_1 \\ f_2 \end{bmatrix} = \begin{bmatrix} 0 & -\mathrm{e}_R(f_1, e_2) \\ \mathrm{e}_R(f_1, e_2) & 0 \end{bmatrix} \begin{bmatrix} -f_1 \\ e_2 \end{bmatrix} \end{array} \right\}, \tag{2.22}$$

where $\mathrm{e}_R(f_1, e_2) = -\frac{1}{T}RI$. The RS source has fixed flow-out computational causality on the thermal side, but with the adopted Ohm law the electrical side has an arbitrary causality.

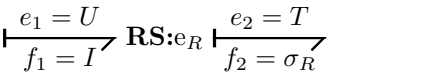

Figure 2.14: Bond graph representation of a resistive source that relates electric and thermal domains.

The RS source is characterized by the power-conservation property (2.14).

$$\langle f | e \rangle = f^\top e = -f_1 e_1 + f_2 e_2 = f_1 \mathrm{e}_R(f_1, e_2) e_2 - \mathrm{e}_R(f_1, e_2) f_1 e_2 = 0. \tag{2.23}$$

However, the structural matrix is nonlinear, and therefore the RS source is not a Dirac structure, i.e., the bilinear pairing (2.3) is nonzero

$$\begin{aligned} &\Big\langle \Big\langle (f_1, f_2, e_1, e_2), (\hat{f}_1, \hat{f}_2, \hat{e}_1, \hat{e}_2) \Big\rangle \Big\rangle = -f_1 \hat{e}_1 + f_2 \hat{e}_2 - \hat{f}_1 e_1 + \hat{f}_2 e_2 = \\ &f_1 \mathrm{e}_R(\hat{f}_1, \hat{e}_2) \hat{e}_2 - \mathrm{e}_R(f_1, e_2) f_1 \hat{e}_2 + \hat{f}_1 \mathrm{e}_R(f_1, e_2) e_2 - \mathrm{e}_R(\hat{f}_1, \hat{e}_2) \hat{f}_1 e_2 \neq 0. \end{aligned} \tag{2.24}$$

With regard to Def. 2.1, we note that $\mathcal{G}_{\mathrm{RS}}$ is not a linear space of $\mathcal{F} \times \mathcal{E}$.

2.1.7 Multiport Bond Graphs

So far, we only considered bond graph elements connected via scalar bonds, i.e., the bonds that carry a single pair of flow and effort. In certain applications, such as multi-body dynamics in mechanical engineering, scalar pairs of flow and effort variables are grouped into vectors in order to avoid clutter in the graphical representation of a system. These vectors of conjugate power variables form multiport (or vector) bond graphs and are represented as two parallel lines with a single half-arrow as depicted in Fig. 2.15 [23]. We use double-struck letters to denote symbols of multiport bond graph elements.

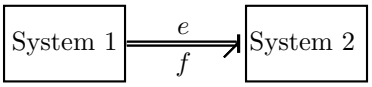

Figure 2.15: Word bond graph with a multiport bond connecting two arbitrary systems.

In the remainder of this Section we introduce the multiport transformer and gyrator, which will be employed in the modeling of superconducting magnets. A more detailed treatment of multiport bond graphs including a discussion on I-, C-, and R-fields can be found in [23].

Multiport Transformer

A multiport transformer relates vectors of flows and efforts with a matrix $N_{\mathbb{TF}}$ being the transformer ratio, as given by the following relation

$$\mathcal{D}_{\mathbb{TF}} = \left\{ \begin{array}{c} (f_1, f_2, e_1, e_2) \in \mathcal{F}_{\mathbb{TF}} \times \mathcal{E}_{\mathbb{TF}} : \\ \begin{bmatrix} e_1 \\ f_2 \end{bmatrix} = \begin{bmatrix} 0 & N_{\mathbb{TF}} \\ -N_{\mathbb{TF}}^\top & 0 \end{bmatrix} \begin{bmatrix} -f_1 \\ e_2 \end{bmatrix} \end{array} \right\}. \tag{2.25}$$

The multiport transformer representation in terms of multiport bond graphs with the computational causality determined from (2.25) is shown in Fig. 2.16.

Figure 2.16: Bond graph representation of a multiport transformer.

Unless the transformer ratio matrix is invertible the computational causality is fixed. An analysis of the causality assignment in multiport bond graphs is carried out in [24], [23]. It can be demonstrated, that a multiport transformer is a Dirac structure

$$\begin{aligned} &\Big\langle\Big\langle (f_1, f_2, e_1, e_2), (\hat{f}_1, \hat{f}_2, \hat{e}_1, \hat{e}_2) \Big\rangle\Big\rangle = -f_1^\top \hat{e}_1 + f_2^\top \hat{e}_2 - \hat{f}_1^\top e_1 + \hat{f}_2^\top e_2 = \\ &- f_1^\top N_{\mathbb{TF}} \hat{e}_2 + (N_{\mathbb{TF}}^\top f_1)^\top \hat{e}_2 - \hat{f}_1^\top N_{\mathbb{TF}} e_2 + (N_{\mathbb{TF}}^\top \hat{f}_1)^\top e_2 = \\ &- f_1^\top N_{\mathbb{TF}} \hat{e}_2 + f_1^\top N_{\mathbb{TF}} \hat{e}_2 - \hat{f}_1^\top N_{\mathbb{TF}} e_2 + \hat{f}_1^\top N_{\mathbb{TF}} e_2 = 0. \end{aligned} \tag{2.26}$$

Multiport Gyrator

Similarly to the case of a multiport transformer, a multiport gyrator is characterized by a gyrator ratio matrix $N_{\mathbb{GY}}$. The governing equation of a multi-port gyrator reads

$$\mathcal{D}_{\mathbb{GY}} = \left\{ \begin{array}{c} (f_1, f_2, e_1, e_2) \in \mathcal{F}_{\mathbb{GY}} \times \mathcal{E}_{\mathbb{GY}} : \\ \begin{bmatrix} -f_1 \\ f_2 \end{bmatrix} = \begin{bmatrix} 0 & -N_{\mathbb{GY}} \\ N_{\mathbb{GY}}^\top & 0 \end{bmatrix} \begin{bmatrix} e_1 \\ e_2 \end{bmatrix} \end{array} \right\}. \tag{2.27}$$

Fig. 2.17 shows a bond graph representation of the multiport gyrator (2.27) with effort-in causalities.

Figure 2.17: Bond graph representation of a multiport gyrator.

We carry out an analogous proof that a multiport gyrator is a Dirac structure. For that purpose we exploit a property of the transposition of two matrices stating that $A^\top B^\top = (BA)^\top$ and the commutativity of the scalar product, i.e., $e^\top f = f^\top e$. The bilinear product reads

$$\begin{aligned}&\Big\langle\Big\langle (f_1, f_2, e_1, e_2), (\hat{f}_1, \hat{f}_2, \hat{e}_1, \hat{e}_2)\Big\rangle\Big\rangle = -f_1^\top \hat{e}_1 + f_2^\top \hat{e}_2 - \hat{f}_1^\top e_1 + \hat{f}_2^\top e_2 = \\ &(-N_{\mathbb{GY}} e_2)^\top \hat{e}_1 + (N_{\mathbb{GY}}^\top e_1)^\top \hat{e}_2 + (-N_{\mathbb{GY}} \hat{e}_2)^\top e_1 + (N_{\mathbb{GY}}^\top \hat{e}_1)^\top e_2 = \\ &- e_2^\top N_{\mathbb{GY}}^\top \hat{e}_1 + \hat{e}_2^\top N_{\mathbb{GY}}^\top e_1 - \hat{e}_2^\top N_{\mathbb{GY}}^\top e_1 + e_2^\top N_{\mathbb{GY}}^\top \hat{e}_1 = 0.\end{aligned} \tag{2.28}$$

Multiport Injector

The injector is an element mapping from a lumped bond into a distributed one. Its structure resembles a transformer, albeit an injector has a fixed computational causality for both, input and output bond, which can not be reverted (as for a transformer).

$$\mathscr{D}_{\mathbb{INJ}} = \left\{ \begin{array}{l} (f_1, f_2, e_1, e_2) \in \mathscr{F}_{\mathbb{INJ}} \times \mathscr{E}_{\mathbb{INJ}} : \\ \begin{bmatrix} e_1 \\ f_2 \end{bmatrix} = \begin{bmatrix} 0 & N_{\mathbb{INJ}} \\ -N_{\mathbb{INJ}}^\top & 0 \end{bmatrix} \begin{bmatrix} -f_1 \\ e_2 \end{bmatrix} \end{array} \right\}. \tag{2.29}$$

Fig. 2.18 presents a bond graph representation of the multiport injector (2.29) with flow-in, effort-in computational causalities.

Figure 2.18: Bond graph representation of a multiport injector mapping a lumped bond into a distributed one.

Hereunder, we carry out a proof similar to (2.26) that a multiport injector is a Dirac structure

$$\begin{aligned}&\Big\langle\Big\langle (f_1, f_2, e_1, e_2), (\hat{f}_1, \hat{f}_2, \hat{e}_1, \hat{e}_2)\Big\rangle\Big\rangle = -f_1^\top \hat{e}_1 + f_2^\top \hat{e}_2 - \hat{f}_1^\top e_1 + \hat{f}_2^\top e_2 = \\ &- f_1^\top N_{\mathbb{INJ}} \hat{e}_2 + (N_{\mathbb{INJ}}^\top f_1)^\top \hat{e}_2 - \hat{f}_1^\top N_{\mathbb{INJ}} e_2 + (N_{\mathbb{INJ}}^\top \hat{f}_1)^\top e_2 = \\ &- f_1^\top N_{\mathbb{INJ}} \hat{e}_2 + f_1^\top N_{\mathbb{INJ}} \hat{e}_2 - \hat{f}_1^\top N_{\mathbb{INJ}} e_2 + \hat{f}_1^\top N_{\mathbb{INJ}} e_2 = 0.\end{aligned} \tag{2.30}$$

2.1.8 Interconnection of Dirac Structures

An important property of a Dirac structure is a possibility to interconnect them. It can be shown that the resulting composition of two (or more) Dirac structure makes again a Dirac structure. We will consider a composition of two Dirac structures via an open port, which can be extended to an arbitrary number of interconnected structures. An open port is characterized by interaction variables over which the power is exchanged with an external system. First, we split the pairs of flow and effort variables into ones denoting the internal energy exchange and the interaction with other systems. Then, we introduce a Dirac structure $\mathscr{D}_A$ with a pair of internal flow and effort variables $(f_\mathrm{A}, e_\mathrm{A}) \in \mathscr{F}_\mathrm{A} \times \mathscr{E}_\mathrm{A}$ and an open port. The open port is identified and characterized by the power variables $(f_{\mathrm{A,p}}, e_{\mathrm{A,p}}) \in \mathscr{F}_\mathrm{p} \times \mathscr{E}_\mathrm{p}$

$$\mathscr{D}_\mathrm{A} = \left\{ (f_\mathrm{A}, f_{\mathrm{A,p}}, e_\mathrm{A}, e_{\mathrm{A,p}}) \in \mathscr{F}_\mathrm{A} \times \mathscr{E}_\mathrm{A} \times \mathscr{F}_\mathrm{p} \times \mathscr{E}_\mathrm{p} \right\} \tag{2.31}$$

This Dirac structure is connected to another one, $\mathscr{D}_B$. By analogy, $\mathscr{D}_B$ is given as

$$\mathscr{D}_\mathrm{B} = \left\{ (f_\mathrm{B}, f_{\mathrm{B,p}}, e_\mathrm{B}, e_{\mathrm{B,p}}) \in \mathscr{F}_\mathrm{B} \times \mathscr{E}_\mathrm{B} \times \mathscr{F}_\mathrm{p} \times \mathscr{E}_\mathrm{p} \right\} \tag{2.32}$$

We note that the incoming power in $\mathcal{D}_A$ should be equal to the outgoing power in $\mathcal{D}_B$. Thus, the interconnection of $\mathcal{D}_\mathrm{A}$ and $\mathcal{D}_\mathrm{B}$ is characterized by the following two conditions

$$\begin{bmatrix} f_{\mathrm{A,p}} \\ e_{\mathrm{B,p}} \end{bmatrix} = \begin{bmatrix} 0 & -1 \\ 1 & 0 \end{bmatrix} \begin{bmatrix} e_{\mathrm{A,p}} \\ f_{\mathrm{B,p}} \end{bmatrix} \quad \text{or} \quad \begin{bmatrix} f_{\mathrm{A,p}} \\ e_{\mathrm{B,p}} \end{bmatrix} = \begin{bmatrix} 0 & 1 \\ -1 & 0 \end{bmatrix} \begin{bmatrix} e_{\mathrm{A,p}} \\ f_{\mathrm{B,p}} \end{bmatrix}. \tag{2.33}$$

Let $\mathcal{D}_\mathrm{A}||\mathcal{D}_\mathrm{B}$ be the interconnection of the Dirac structures $\mathcal{D}_\mathrm{A}$ and $\mathcal{D}_\mathrm{B}$. Then, following the adopted convention, we consider the first condition of (2.33), obtaining $\mathcal{D}_{\mathrm{A}||\mathrm{B}}$ defined as

$$\mathcal{D}_{\mathrm{A}||\mathrm{B}} = \left\{ \begin{matrix} f_\mathrm{A}, f_\mathrm{B}, e_\mathrm{A}, e_\mathrm{B} \in \mathcal{F}_\mathrm{A} \times \mathcal{F}_\mathrm{B} \times \mathcal{E}_\mathrm{A} \times \mathcal{E}_\mathrm{B} : \exists (f_\mathrm{p}, e_\mathrm{p}) \in \mathcal{F}_\mathrm{p} \times \mathcal{E}_\mathrm{p} \\ \text{s.t. } (f_\mathrm{A}, f_\mathrm{p}, e_\mathrm{A}, e_\mathrm{p}) \in \mathcal{D}_\mathrm{A} \text{ and } (f_\mathrm{B}, -f_\mathrm{p}, e_\mathrm{B}, e_\mathrm{p}) \in \mathcal{D}_\mathrm{B} \end{matrix} \right\}. \tag{2.34}$$

A corresponding bond graph representation of $\mathcal{D}_{\mathrm{A}||\mathrm{B}}$ is shown in Fig. 2.19.

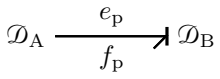

Figure 2.19: Bond graph representation of $\mathcal{D}_\mathrm{A}||\mathcal{D}_\mathrm{B}$.

A detailed proof that a composition of any number of Dirac structures is again a Dirac structure is reported in [25].

Procedure for Interconnection of Two Dirac Structures

Below we present a procedure for deriving the interconnection of two Dirac structures by eliminating common bonds. Let $\mathcal{D}_\mathrm{V}$ denote the first Dirac structure and vector V contain internal flow and effort variables. Then, V^* denotes a vector of conjugate effort and flow variables. In addition, the interaction port is given as a pair $(f_{\mathrm{V,p}}, e_{\mathrm{V,p}})$. The Dirac structure $\mathcal{D}_V$ is characterized by

$$\mathcal{D}_\mathrm{V} = \left\{ \begin{bmatrix} V^* \\ e_{\mathrm{V,p}} \end{bmatrix} = \begin{bmatrix} J_{\mathrm{V,i}} & J_{\mathrm{V,p}} \\ -J_{\mathrm{V,p}}^\top & 0 \end{bmatrix} \begin{bmatrix} V \\ f_{\mathrm{V,p}} \end{bmatrix} \right\}, \tag{2.35}$$

where $J_{\mathrm{V,i}}$ is a matrix representing the interconnection map between V and V^* and $J_{\mathrm{V,p}}$ is a column vector representing input map. Since the structural matrix representing a Dirac structure is skew-symmetric, $-J_{\mathrm{V,p}}^\top$ is the output map. The second Dirac structure, $\mathcal{D}_\mathrm{W}$, is given in an analogous way as

$$\mathcal{D}_\mathrm{W} = \left\{ \begin{bmatrix} W^* \\ f_{\mathrm{W,p}} \end{bmatrix} = \begin{bmatrix} J_{\mathrm{W,i}} & J_{\mathrm{W,p}} \\ -J_{\mathrm{W,p}}^\top & 0 \end{bmatrix} \begin{bmatrix} W \\ e_{\mathrm{W,p}} \end{bmatrix} \right\}, \tag{2.36}$$

Fig. 2.20 shows $\mathcal{D}_\mathrm{V}$ and $\mathcal{D}_\mathrm{W}$ with outward oriented interconnection bonds and causality determined from corresponding constitutive relationships

Figure 2.20: Word bond graph representation of $\mathcal{D}_\mathrm{V}$ and $\mathcal{D}_\mathrm{W}$.

The concatenated system is given as

$$\mathcal{D}_{\mathrm{V}||\mathrm{W}} = \left\{ \begin{bmatrix} V^* \\ e_{\mathrm{V,p}} \\ W^* \\ f_{\mathrm{W,p}} \end{bmatrix} = \begin{bmatrix} J_{\mathrm{V,i}} & J_{\mathrm{V,p}} & 0 & 0 \\ -J_{\mathrm{V,p}}^\top & 0 & 0 & 0 \\ 0 & 0 & J_{\mathrm{W,i}} & J_{\mathrm{W,p}} \\ 0 & 0 & -J_{\mathrm{W,p}}^\top & 0 \end{bmatrix} \begin{bmatrix} V \\ f_{\mathrm{V,p}} \\ W \\ e_{\mathrm{W,p}} \end{bmatrix} \right\}. \tag{2.37}$$

From (2.37) we note that the port variables are duplicated and will be removed in the following steps. First, we recall the interconnection relationship for the input port variables on the right hand side of (2.37)

$$\begin{bmatrix} f_{\mathrm{V,p}} \\ e_{\mathrm{W,p}} \end{bmatrix} = \begin{bmatrix} 0 & -1 \\ 1 & 0 \end{bmatrix} \begin{bmatrix} e_{\mathrm{V,p}} \\ f_{\mathrm{W,p}} \end{bmatrix}. \tag{2.38}$$

Second, we find the expression characterizing the output flow $e_{\mathrm{V,p}}$ and $f_{\mathrm{W,p}}$ from (2.35) and (2.36), respectively, as

$$\begin{bmatrix} e_{\mathrm{V,p}} \\ f_{\mathrm{W,p}} \end{bmatrix} = \begin{bmatrix} -J_{\mathrm{W,p}}^{\top} & 0 \\ 0 & -J_{\mathrm{V,p}}^{\top} \end{bmatrix} \begin{bmatrix} V \\ W \end{bmatrix}. \tag{2.39}$$

Combining (2.38) and (2.39), the input port variables are expressed in terms of internal variables as

$$\begin{bmatrix} f_{\mathrm{V,p}} \\ e_{\mathrm{W,p}} \end{bmatrix} = \begin{bmatrix} 0 & -1 \\ 1 & 0 \end{bmatrix} \begin{bmatrix} -J_{\mathrm{W,p}}^{\top} & 0 \\ 0 & -J_{\mathrm{V,p}}^{\top} \end{bmatrix} \begin{bmatrix} V \\ W \end{bmatrix} = \begin{bmatrix} 0 & J_{\mathrm{W,p}}^{\top} \\ -J_{\mathrm{V,p}}^{\top} & 0 \end{bmatrix} \begin{bmatrix} V \\ W \end{bmatrix}. \tag{2.40}$$

Eventually, we substitute the input port variables (2.40) into (2.37) and eliminate both ports, which results in the following relationship

$$\mathscr{D}_{\mathrm{V||W}} = \left\{ \begin{bmatrix} V^* \\ W^* \end{bmatrix} = \begin{bmatrix} J_{\mathrm{V,i}} & J_{\mathrm{V,p}} J_{\mathrm{W,p}}^{\top} \\ -J_{\mathrm{W,p}}^{\top} J_{\mathrm{V,p}} & J_{\mathrm{W,i}} \end{bmatrix} \begin{bmatrix} V \\ W \end{bmatrix} \right\}. \tag{2.41}$$

From (2.41) it immediately follows that the obtained interconnection map for the ensemble Dirac structure maintains the skew-symmetry property.

To conclude, the procedure of the interconnection of two Dirac structures represented in matrix form takes the following steps

1. Represent both Dirac structures with outward oriented interaction bonds;

2. Shuffle rows and columns in constitutive relationships such that the interaction variables occupy the last row;

3. Choose the system order according to the input causality, i.e., the first system has flow-in causality while the second system has effort-in causality;

4. Identify blocks in the structural matrices;

5. Apply the formula given in (2.41).

We note that this procedure can be applied to an interconnection of an arbitrary number of Dirac structures by sequentially connecting two Dirac structures at a time. The procedure, however, is not applicable for resistive elements given by a diagonal interconnection matrix.

Example: The interconnection of Dirac structures is illustrated with an adopted example 1.8.2 in [20] of a DC motor with inertia powered by an AC\DC converter connected to an AC source. The AC\DC converter is a thyristor rectifier bridge operated with the AC source frequency and controlled firing angle. The firing angle is determined by a PI controller designed to track the reference velocity ω_{ref} (for the sake of simplicity the motor current is assumed to be continuous). Fig. 2.21 represents the electrical circuit and the bond graph representation of the controlled DC motor.

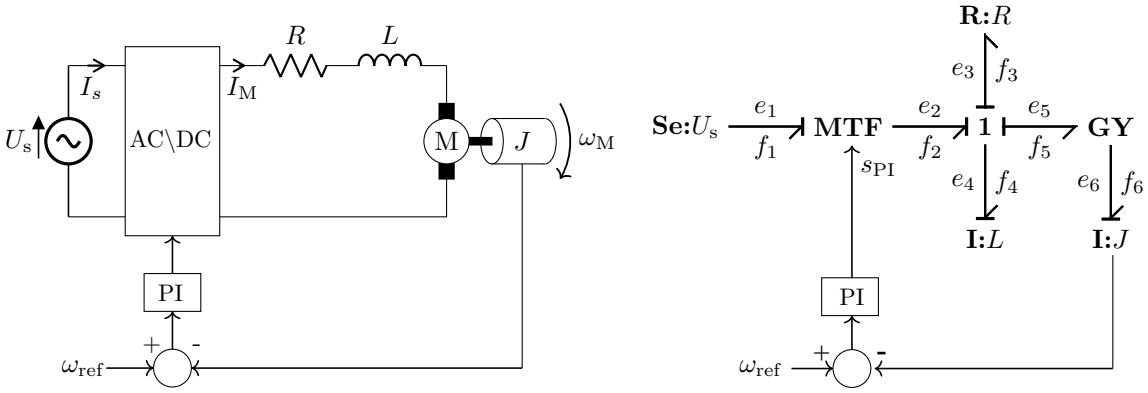

Figure 2.21: A schematic representing the velocity control of a DC motor (left) and a corresponding bond graph representation (right).

The AC source is connected to the AC\DC converter via a bond (I_s, U_s). The converter is modeled as a modulated transformer

$$\mathcal{D}_{\text{MTF}} = \left\{ \begin{array}{c} (f_1, f_2, e_1, e_2) \in \mathcal{F}_{\text{MTF}} \times \mathcal{D}_{\text{MTF}} : \\ \begin{bmatrix} -f_1 \\ e_2 \end{bmatrix} = \begin{bmatrix} 0 & -n_{\text{TF}}(s_{\text{PI}}) \\ n_{\text{TF}}(s_{\text{PI}}) & 0 \end{bmatrix} \begin{bmatrix} e_1 \\ f_2 \end{bmatrix} \end{array} \right\}, \tag{2.42}$$

and with $(f_1, f_2, e_1, e_2) = (I_s, I_M, U_s, U_{\text{DC}})$. The transformer ratio n_{TF} is modulated by the output of the PI controller s_{PI}. The output voltage of the modulated transformer is connected to the DC motor. With R, L, and DC denoting, respectively, the DC motor resistance, inductance, and the motor itself, from the Kirchhoff Voltage Law we derive the following relation

$$\mathcal{D}_1 = \left\{ \begin{array}{c} (f_2, f_3, f_4, f_5, e_2, e_3, e_4, e_5) \in \mathcal{F}_1 \times \mathcal{E}_1 : \\ \begin{bmatrix} e_4 \\ -f_2 \\ f_3 \\ f_5 \end{bmatrix} = \begin{bmatrix} 0 & 1 & -1 & -1 \\ -1 & 0 & 0 & 0 \\ 1 & 0 & 0 & 0 \\ 1 & 0 & 0 & 0 \end{bmatrix} \begin{bmatrix} f_4 \\ e_2 \\ e_3 \\ e_5 \end{bmatrix} \end{array} \right\}. \tag{2.43}$$

where $(f_2, f_3, f_4, f_5, e_2, e_3, e_4, e_5) = (I_M, I_M, I_M, I_M, U_{\text{DC}}, U_R, U_L, U_M)$. The DC motor is represented as a gyrator **GY**, which relates the motor voltage e_5 with the angular velocity f_6 and the current f_5 with the torque e_6.

$$\mathcal{D}_{\text{GY}} = \left\{ \begin{array}{c} (f_5, f_6, e_5, e_6) \in \mathcal{F}_{\text{GY}} \times \mathcal{E}_{\text{GY}} : \\ \begin{bmatrix} e_5 \\ e_6 \end{bmatrix} = \begin{bmatrix} 0 & n_{\text{GY}} \\ -n_{\text{GY}} & 0 \end{bmatrix} \begin{bmatrix} -f_5 \\ f_6 \end{bmatrix} \end{array} \right\}. \tag{2.44}$$

The gyrator (2.44) maps pairs of conjugate power variables onto physical quantities according to $(f_5, f_6, e_5, e_6) = (I_M, \omega_M, U_M, T_M) \in \mathcal{D}_{\text{GY}}$. Additionally, there is a moment of inertia J attached to the motor shaft. For $\mathcal{D}_{\text{MTF}} || \mathcal{D}_1 || \mathcal{D}_{\text{GY}}$, we identify (f_2, e_2) and (f_5, e_5) as the interconnection pairs of power variables linking, respectively, the AC\DC converter **MTF** with the motor circuit (1-junction), and the motor circuit with the motor **GY** (see Fig. 2.21). The ensemble system is obtained by applying the procedure in two steps.

The first step involves the interconnection of the modulated transformer and 1-junction. As a result, the bond (f_2, e_2) is eliminated leading to the following set of equations

$$\mathcal{D}_{\text{MTF}||1} = \left\{ \begin{array}{c} (f_1, f_3, f_4, f_5, e_1, e_3, e_4, e_5) \in \mathcal{F}_{\text{MTF}||1} \times \mathcal{E}_{\text{MTF}||1} : \\ \begin{bmatrix} f_1 \\ e_4 \\ f_3 \\ f_5 \end{bmatrix} = \begin{bmatrix} 0 & n_{\text{TF}} & 0 & 0 \\ -n_{\text{TF}} & 0 & -1 & -1 \\ 0 & 1 & 0 & 0 \\ 0 & 1 & 0 & 0 \end{bmatrix} \begin{bmatrix} e_1 \\ f_4 \\ e_3 \\ e_5 \end{bmatrix} \end{array} \right\}. \tag{2.45}$$

The second step is to connect (2.45) with the gyrator in order to eliminate the interconnection bond (f_5, e_5)

$$\mathcal{D}_{\mathrm{MTF||1||GY}} = \left\{ \begin{array}{c} (f_1, f_3, f_4, f_6, e_1, e_3, e_4, e_6) \in \mathcal{F}_{\mathrm{MTF||1||GY}} \times \mathcal{E}_{\mathrm{MTF||1||GY}} : \\ \begin{bmatrix} e_6 \\ f_1 \\ e_4 \\ f_3 \end{bmatrix} = \begin{bmatrix} 0 & 0 & n_{\mathrm{GY}} & 0 \\ 0 & 0 & n_{\mathrm{TF}} & 0 \\ -n_{\mathrm{GY}} & -n_{\mathrm{TF}} & 0 & -1 \\ 0 & 0 & 1 & 0 \end{bmatrix} \begin{bmatrix} e_6 \\ e_1 \\ f_4 \\ e_3 \end{bmatrix} \end{array} \right\}. \tag{2.46}$$

The pair (f_3, e_3) is finally eliminated by introducing the resistive relationship, eliminating the last row and column, and generating a diagonal entry in the column and row of f_4 and e_4, respectively

$$\mathcal{G}_{\mathrm{MTF||1||GY||R}} = \left\{ \begin{array}{c} (f_1, f_3, f_4, f_6, e_1, e_3, e_4, e_6) \in \mathcal{F}_{\mathrm{MTF||1||GY||R}} \times \mathcal{E}_{\mathrm{MTF||1||GY||R}} : \\ \begin{bmatrix} e_6 \\ f_1 \\ e_4 \end{bmatrix} = \begin{bmatrix} 0 & 0 & n_{\mathrm{GY}} \\ 0 & 0 & n_{\mathrm{TF}} \\ -n_{\mathrm{GY}} & -n_{\mathrm{TF}} & -R \end{bmatrix} \begin{bmatrix} e_6 \\ e_1 \\ f_4 \end{bmatrix} \end{array} \right\}. \tag{2.47}$$

The final form of a power-continuous structure representing the considered example (2.47) contains only an input bond and two storage bonds.

2.2 Distributed Parameter Systems

In this Section we consider a class of power-continuous systems characterized by distributed variables on an n-dimensional space $\Omega \subset \mathbb{R}^n$ with a smooth boundary $\Gamma = \partial\Omega$. Concepts such as bonds, junctions, single- and two-port elements already discussed for the lumped-parameter setting have qualitative equivalents for the distributed-parameter systems. We will also introduce a Dirac structure with a dedicated boundary port, the so called Stokes-Dirac structure.

Differential forms are employed to describe the distributed-parameter systems (for a brief introduction please refer to Appendix A). In this setting, a non-degenerate bilinear product takes the following form

$$\langle \alpha | \beta \rangle = \int_{\Omega} \alpha \wedge \beta, \tag{2.48}$$

where $\alpha \in \Lambda^k$ and $\beta \in \Lambda^{n-k}$ form a pair of conjugate vector spaces [26], Λ is a differential form space, and k is an integer number. The result of the product (2.48) is an integral power quantity in Ω.

2.2.1 Distributed Dirac Structure

The concept of a power-continuous Dirac structure can be applied to infinite-dimensional linear spaces of power variables. In this case, we consider a linear space of flows $\mathcal{F}$ with elements $f \in \mathcal{F}$ and a linear space of efforts $\mathcal{E}$ with elements given as $e \in \mathcal{E}$. With a bilinear product given in (2.48), Def. 2.2 characterizes an infinite-dimensional Dirac structure. This definition gives a basis for distributed 0- and 1-junctions, gyrators, transformers as well as storage and dissipative elements.

2.2.2 Stokes-Dirac Structure

In case of distributed systems, the spaces of flows and efforts can be extended to account for boundary power conjugate variables [20]. Such an extension gives rise to an additional structure within the framework of port-based modeling, a Stokes-Dirac structure. Hereunder, we provide a formal definition of a Stokes-Dirac structure along with its bond graph representation. We consider a system of two conservation laws with canonical inter-domain coupling [27]. The first

conservation law combines the time derivative of state variables and the spatial derivative of flux variables

$$\partial_t \begin{bmatrix} \alpha_p \\ \alpha_q \end{bmatrix} + \mathrm{d} \begin{bmatrix} \beta_p \\ \beta_q \end{bmatrix} = 0, \tag{2.49}$$

where $\alpha_p \in \Lambda^p(\Omega)$ and $\alpha_q \in \Lambda^q(\Omega)$ are the conserved quantities being differential forms of degree respectively p and q on the n-dimensional domain Ω, $q = n - p + 1$. The flux variables $\beta_p \in \Lambda^{p-1}(\Omega)$ and $\beta_q \in \Lambda^{q-1}(\Omega)$ are defined by the second conservation law

$$\begin{bmatrix} \beta_p \\ \beta_q \end{bmatrix} = \iota \begin{bmatrix} 0 & (-1)^r \\ 1 & 0 \end{bmatrix} \begin{bmatrix} e_p \\ e_q \end{bmatrix}, \tag{2.50}$$

with $r = pq + 1$ and $\iota = \{-1, 1\}$ depending on the sign convention of the considered physical domain. Considering the internal flow and effort variables as well as the boundary ones, the total space of flow variables is given as

$$\mathcal{F} = \left\{ f = \begin{bmatrix} f_p \\ f_q \\ f_\mathrm{b} \end{bmatrix} \in \Lambda^p(\Omega) \times \Lambda^q(\Omega) \times \Lambda^{n-q}(\Gamma) \right\}, \tag{2.51}$$

and, by analogy, the space of effort variables is defined as

$$\mathcal{E} = \left\{ e = \begin{bmatrix} e_p \\ e_q \\ e_\mathrm{b} \end{bmatrix} \in \Lambda^{n-p}(\Omega) \times \Lambda^{n-q}(\Omega) \times \Lambda^{n-p}(\Gamma) \right\}. \tag{2.52}$$

These spaces are endowed with a non-degenerated bilinear product

$$\left\langle \begin{bmatrix} f_p \\ f_q \\ f_\mathrm{b} \end{bmatrix} \middle| \begin{bmatrix} e_p \\ e_q \\ e_\mathrm{b} \end{bmatrix} \right\rangle = \int_\Omega (e_p \wedge f_p + e_q \wedge f_q) + \int_\Gamma e_\mathrm{b} \wedge f_\mathrm{b}. \tag{2.53}$$

Considering definitions (2.51 - 2.53) and the Stokes theorem one can define a Stokes-Dirac structure representing a system of two conservation laws.

Definition 2.3 (Proposition 4.1 in [20]) *The linear subset $\mathcal{D} \subset \mathcal{F} \times \mathcal{E}$ defined by*

$$\mathbb{D} = \left\{ \left(\begin{bmatrix} f_p \\ f_q \\ f_\mathrm{b} \end{bmatrix}, \begin{bmatrix} e_p \\ e_q \\ e_\mathrm{b} \end{bmatrix} \right) \in \mathcal{F} \times \mathcal{E} : \begin{bmatrix} f_p \\ f_q \end{bmatrix} = \iota \begin{bmatrix} 0 & (-1)^r \mathrm{d} \\ \mathrm{d} & 0 \end{bmatrix} \begin{bmatrix} e_p \\ e_q \end{bmatrix}, \begin{bmatrix} f_\mathrm{b} \\ e_\mathrm{b} \end{bmatrix} = \begin{bmatrix} 0 & 1 \\ 1 & 0 \end{bmatrix} \begin{bmatrix} e_p|_\Gamma \\ e_q|_\Gamma \end{bmatrix} \right\} \tag{2.54}$$

is a Stokes-Dirac structure w.r.t. the following pairing

$$\left\langle \left\langle \begin{bmatrix} f \\ e \end{bmatrix}, \begin{bmatrix} \hat{f} \\ \hat{e} \end{bmatrix} \right\rangle \right\rangle = \langle e | \hat{f} \rangle + \langle \hat{e} | f \rangle, \begin{bmatrix} f \\ e \end{bmatrix}, \begin{bmatrix} \hat{f} \\ \hat{e} \end{bmatrix} \in \mathcal{F} \times \mathcal{E} \tag{2.55}$$

with $\langle \cdot | \cdot \rangle$ being the bi-linear product as defined in (2.53).

For (2.55) we calculate the bilinear pairing of the internal flow and effort variables. For the sake of saving space, we neglect the boundary term, which yields

$$\begin{aligned} \langle\langle (f_p, f_q, e_p, e_q), (\hat{f}_p, \hat{f}_q, \hat{e}_p, \hat{e}_q) \rangle\rangle &= \iota \int_\Omega \left[e_p \wedge \hat{f}_p + \hat{e}_q \wedge f_q \right] + \iota \int_\Omega \left[\hat{e}_p \wedge f_p + \hat{e}_q \wedge f_q \right] = \\ &= \iota \int_\Omega \left[e_p \wedge (-1)^r \mathrm{d}\hat{e}_q + \hat{e}_q \wedge \mathrm{d}e_p \right] + \iota \int_\Omega \left[\hat{e}_p \wedge (-1)^r \mathrm{d}e_q + e_q \wedge \mathrm{d}\hat{e}_p \right]. \end{aligned} \tag{2.56}$$

Considering the property of the exterior derivation, we can reformulate (2.56) as

$$\langle\langle (f_p, f_q, e_p, e_q), (\hat{f}_p, \hat{f}_q, \hat{e}_p, \hat{e}_q) \rangle\rangle = -\iota \int_\Omega \mathrm{d} \left(e_p \wedge \hat{e}_q \right) - \iota \int_\Omega \mathrm{d} \left(\hat{e}_p \wedge e_q \right), \tag{2.57}$$

which exploiting the Stoke theorem yields

$$\langle\langle(f_p, f_q, e_p, e_q), (\hat{f}_p, \hat{f}_q, \hat{e}_p, \hat{e}_q)\rangle\rangle = -\iota \int_\Gamma e_p \wedge \hat{e}_q - \iota \int_\Gamma \hat{e}_p \wedge e_q. \tag{2.58}$$

As a result, the input power through the boundary remained, which would vanish provided that boundary flow and effort are considered in (2.56).

A detailed proof showing that the bilinear product (2.53) vanishes for a linear space of flow and efforts defined by a Stokes-Dirac structure is reported in [20] after Proposition 4.3. From (2.54) we note that a Stokes-Dirac structure is a special type of a gyrator providing a mapping between vectors of distributed flow and effort variables. The graphical representation resembles a gyrator with an additional boundary-port bond as shown in Fig. 2.22.

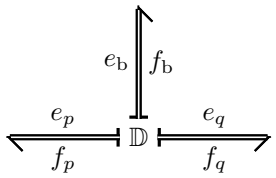

Figure 2.22: Bond graph representation of a Stokes-Dirac structure.

A Stokes-Dirac structure enables interaction across boundaries of the modeled systems and as such provides a link to port-Hamiltonian systems introduced in the following.

2.3 Port-Hamiltonian Systems

In this Section we present general, implicit port-Hamiltonian systems as well as a corresponding explicit representation based on the skew-symmetry interconnection map for a system of two conservation laws as discussed in Sec. 2.2.2.

Hamiltonian density function $\hbar : \Lambda^p(\Omega) \times \Lambda^q(\Omega) \mapsto \Lambda^n(\Omega)$ represents energy stored in the system, so that the total Hamiltonian is defined as

$$\mathcal{H} = \int_\Omega \hbar. \tag{2.59}$$

The total Hamiltonian function is a basis for the definition of implicit Hamiltonian systems and implicit port-Hamiltonian systems. Another relevant function is the variational derivative of Hamiltonian function $\delta_\alpha \mathcal{H}$ at $\alpha \in \Lambda^p(\Omega)$ defined as follows [26]. For any α, $\Delta\alpha \in \Lambda^p(\Omega)$ it can be shown that

$$\mathcal{H}(\alpha + \Delta\alpha) = \int_\Omega \hbar(\alpha + \Delta\alpha) = \int_\Omega \hbar(\alpha) + \int_\Omega \delta_\alpha \mathcal{H} \wedge \Delta\alpha + O(\Delta\alpha^2) \tag{2.60}$$

the variational derivative of Hamiltonian function $\delta_\alpha \mathcal{H}$ is the only function satisfying this equation.

Example: To illustrate the variational derivative, consider the Maxwell equations in Hamiltonian form (for more details on the Maxwell equations represented in terms of differential forms see Appendix B)

$$\mathcal{H}(B, D) = \frac{1}{2} \int_\Omega *_\nu B \wedge B + *_{\frac{1}{\epsilon}} D \wedge D. \tag{2.61}$$

Then, the variational derivative of the Hamiltonian (2.61) w.r.t. B reads

$$\begin{aligned}\mathcal{H}(B+\Delta B)-\mathcal{H}(B) =& \frac{1}{2}\int_\Omega *_\nu (B+\Delta B)\wedge(B+\Delta B) - \frac{1}{2}\int_\Omega *_\nu B\wedge B = \frac{1}{2}\int_\Omega *_\nu B\wedge B \\ &+\frac{1}{2}\int_\Omega *_\nu \Delta B\wedge B + \frac{1}{2}\int_\Omega *_\nu B\wedge \Delta B + \frac{1}{2}\int_\Omega *_\nu \Delta B\wedge \Delta B \\ &-\frac{1}{2}\int_\Omega *_\nu B\wedge B = \int_\Omega *_\nu B\wedge \Delta B + \frac{1}{2}\int_\Omega *_\nu \Delta B\wedge \Delta B\end{aligned} \tag{2.62}$$

By comparing (2.61) and (2.62) we observe that $\delta_B\mathcal{H}(B) = *_\nu B = H$. On a basis of the same argument, the variational derivative w.r.t. D yields a 1-form

$$\delta_D\mathcal{H}(B,D) = *_{\frac{1}{\epsilon}} D = E \tag{2.63}$$

Provided that the density function $\hbar$ does not depend on the derivatives of α, we note that the variational derivative becomes equal to the derivation of the density function w.r.t. the conserved quantity α

$$\delta_\alpha\mathcal{H} = \partial_\alpha\mathcal{H}. \tag{2.64}$$

Definition 2.4 (Definition 2 in [21]) *Let $\mathcal{X}$ be a manifold with (generalized) Dirac structure $\mathcal{D}$, and let $\mathcal{H}:\mathcal{X}\mapsto\mathbb{R}$ be a smooth function (the Hamiltonian). The implicit (generalized) Hamiltonian system corresponding to $(\mathcal{X},\mathcal{D},\mathcal{H})$ is given by*

$$(\partial_t x, \delta_x\mathcal{H}(x))\in\mathcal{D}, x\in\mathcal{X} \tag{2.65}$$

By substituting $e=\delta_x\mathcal{H}(x)$ and $f=\partial_t x$, we note that the implicit Hamiltonian system indeed forms a Dirac structure (2.2). Let $J:\mathcal{E}\mapsto\mathcal{F}$ be the following map

$$J = \iota\begin{bmatrix}0 & (-1)^r\mathrm{d}\\ \mathrm{d} & 0\end{bmatrix}, \tag{2.66}$$

where $f=\begin{bmatrix}f_p & f_q\end{bmatrix}^\top$ and $e=\begin{bmatrix}e_p & e_q\end{bmatrix}^\top$ are, respectively, flow and effort vectors. Then, the system introduced in Def. 2.4 can be represented in an explicit form as

$$f = Je, \tag{2.67}$$

with $f_p=\partial_t x_p\in\Lambda^p(\Omega)$, $f_q=\partial_t x_q\in\Lambda^q(\Omega)$ and $e_p=\delta_{x_p}\mathcal{H}\in\Lambda^{n-p}(\Omega)$, $e_q=\delta_{x_q}\mathcal{H}\in\Lambda^{n-q}(\Omega)$. The time variation of the Hamiltonian of the system (2.67) reads

$$\partial_t\mathcal{H} = \int_\Omega (e_p\wedge f_p + e_q\wedge f_q) = 0. \tag{2.68}$$

As the next step, we extend the definition of the implicit Hamiltonian system by introducing boundary port variables. As a result we obtain port-Hamiltonian systems capable of interacting with other systems and/or the environment.

Definition 2.5 (Definition 2 in [21]) *Let $\mathcal{X}$ be a manifold with (generalized) Dirac structure $\mathcal{D}$, and let $\mathcal{H}:\mathcal{X}\mapsto\mathbb{R}$ be a smooth function (the Hamiltonian). The implicit port-Hamiltonian system with boundary external variables corresponding to $(\mathcal{X},\mathcal{D},\mathcal{H})$ is given by*

$$(\partial_t x, f_\mathrm{b}, \delta_x\mathcal{H}(x), e_\mathrm{b})\in\mathcal{D}, x\in\mathcal{X}, \tag{2.69}$$

where $e_\mathrm{b}, f_\mathrm{b}$ denote the boundary port variables.

The system (2.69) is an example of an explicit boundary port-Hamiltonian system given by

$$\begin{bmatrix} f_p \\ f_q \end{bmatrix} = \iota \begin{bmatrix} 0 & (-1)^r \mathrm{d} \\ \mathrm{d} & 0 \end{bmatrix} \begin{bmatrix} e_p \\ e_q \end{bmatrix}, \begin{bmatrix} f_\mathrm{b} \\ e_\mathrm{b} \end{bmatrix} = \begin{bmatrix} 0 & 1 \\ 1 & 0 \end{bmatrix} \begin{bmatrix} e_p|_\Gamma \\ e_q|_\Gamma \end{bmatrix} \tag{2.70}$$

From (2.58) we find that the energy supply rate is equal to the product of the boundary flow and effort

$$\partial_t \mathcal{H} = \langle e|f\rangle = \langle e_p|f_p\rangle + \langle e_q|f_q\rangle = -\int_\Gamma e_\mathrm{b} \wedge f_\mathrm{b}. \tag{2.71}$$

The variation of the energy on the domain Ω is only due to the energy supply through the system boundary Γ. Source or dissipative terms can be added to the system through the boundary ports.

Now we will further extend Def. 2.5 in order to account for distributed port variables.

Definition 2.6 (Proposition 2.2 in [28]) *Let $\mathcal{X}$ be a manifold with (generalized) Dirac structure $\mathcal{D}$, and let $\mathcal{H} : \mathcal{X} \mapsto \mathbb{R}$ be a smooth function (the Hamiltonian). The implicit port-Hamiltonian system with boundary and distributed ports corresponding to $(\mathcal{X}, \mathcal{D}, \mathcal{H})$ is given by*

$$(\partial_t x, f_\mathrm{b}, f_\mathrm{p}, \delta_x \mathcal{H}(x), e_\mathrm{b}, e_\mathrm{p}) \in \mathcal{D}, x \in \mathcal{X}, \tag{2.72}$$

where $e_\mathrm{p}, f_\mathrm{p}$ denote the distributed port variables.

For superconducting magnet modeling purposes, we recall an input-state-output representation of a port-Hamiltonian system with dissipation as given in [29]

$$\begin{aligned} \partial_t x &= J(x)\delta_x \mathcal{H}(x) + g(x)u \\ y &= g^\top(x)\delta_x \mathcal{H}(x), \end{aligned} \tag{2.73}$$

where $x \in \mathcal{X}$ is the state vector, $J(x)$ is an interconnection linear map $J(x) : \mathcal{E} \mapsto \mathcal{F}$, and $g(x)$ is the input map.

An explicit representation of a port-Hamiltonian system with distributed port variables is thoroughly discussed in Section 4.2.6.1 of [20].

Assuming that both ports supply power to the system, the power balance reads

$$\partial_t \mathcal{H} = -\int_\Gamma e_\mathrm{b} \wedge f_\mathrm{b} - \int_\Omega e_\mathrm{p} \wedge f_\mathrm{p}, \tag{2.74}$$

from which we note that the power is provided not only by the boundary port but also by the distributed one.

Starting from Definition 2.6 one can terminate some of the open bonds with a resistive relation in order to account for dissipative phenomena [28]. Let us consider a resistive map $R : \Lambda^{n-k} \to \Lambda^k : e_p \mapsto f_p$ such that

$$\int_\Omega e_\mathrm{p} \wedge f_\mathrm{p} \geq 0, \quad \forall e_\mathrm{p} \in \Lambda^{n-k}, \tag{2.75}$$

where $f_\mathrm{p} = R(e_\mathrm{p})$. In the case of the obtained dissipative port-Hamiltonian system with distributed variables, the energy variation is given as

$$\partial_t \mathcal{H} = -\int_\Gamma e_\mathrm{b} \wedge f_\mathrm{b} + \int_\Omega e_\mathrm{p} \wedge R(e_\mathrm{p}) \geq -\int_\Gamma e_\mathrm{b} \wedge f_\mathrm{b}. \tag{2.76}$$

Eventually, we recall a complete input-state-output equation for explicit dissipative port-Hamiltonian systems

$$\begin{aligned} \partial_t x &= [J(x) - R(x)]\delta_x \mathcal{H}(x) + g(x)u \\ y &= g^\top(x)\delta_x \mathcal{H}(x) + S(x)u, \end{aligned} \tag{2.77}$$

where $R(x)$ is a symmetric linear mapping corresponding to the resistive port $R(x) : \mathcal{E} \mapsto \mathcal{F}$ and $S(x)$ is a direct feed-through map representing dissipation in the system.

An implicit port-Hamiltonian system can be expressed as a set of differential-algebraic equations by means of several equivalent relations. The skew-symmetric interconnection between the flow and effort variables is only one of the available choices. Another relation suitable for certain types of applications include a generalized Poisson bracket and the image and kernel representation of spaces of flow and effort variables. A complete overview is presented in [25] and [28]. In the remainder of this chapter, we will employ explicit port-Hamiltonian systems characterized by a skew-symmetric interconnection mapping.

2.4 Superconducting Magnet

In this Section we consider energy-based modeling of magneto-thermal phenomena occurring in superconducting magnets for the nominal operation (steady-state and transient effects) and protection scenarios (e.g., quench). The model consists of electromagnetic and thermal systems linked through a common energy reservoir and the irreversible entropy creation due to dissipative phenomena occurring in the former system. For modeling purposes we will employ both, bond graph modeling and the port-Hamiltonian formalism. Firstly, we will employ the former to represent energy flow in each system by means of power-continuous structures. (Note that the structures and corresponding bonds in each domain are numbered such that the link between the domains can be established by equating the indices of bonds.) Secondly, we will use the resulting model decomposition into consecutive stages of power flow to derive a port-Hamiltonian model for the considered subsystems. Thirdly, we construct a resulting bond graph (see Fig. 2.39) and port-Hamiltonian models of a superconducting magnet. As a convention, we will present each bond graph with numbered bonds accompanied with a corresponding bond with variables denoting physical quantities. With the bond graph model we will demonstrate the computational causality and with the port-Hamiltonian model the variation of the Hamiltonian energy function controlled by the input circuit port as well as boundary ports.

2.4.1 Bond Graph Model of the Electromagnetic Domain

We consider a current-driven distributed model of a superconducting magnet. The current profile can be either an arbitrary function of time or a waveform obtained as a solution of a superconducting circuit model. Thus, the port voltage U_{mag} is determined from the electromagnetic field solution, which indicates effort-out computational causality.

Voltage across a magnet U_{mag} comprises: (i) the resistive voltage U_{res} accounting for the resistance variation after a quench, and (ii) the dynamic voltage U_{dyn} representing the derivative of the induced magnetic flux linkage, influenced by the iron yoke saturation, eddy currents, the inter-filament and the inter-strand coupling currents, as well as persistent magnetization currents,

$$U_{\mathrm{mag}} = U_{\mathrm{res}} + U_{\mathrm{dyn}}. \tag{2.78}$$

Equation (2.78) forms a 1-junction representing the voltage division U_{mag} with the common flow equal to the source current I_{s}

$$\mathcal{D}_1 = \left\{ \begin{array}{l} (f_1, f_2, f_3, e_1, e_2, e_3) \in \mathcal{F}_1 \times \mathcal{E}_1 : \\ \begin{bmatrix} e_1 \\ f_2 \\ f_3 \end{bmatrix} = \begin{bmatrix} 0 & 1 & 1 \\ -1 & 0 & 0 \\ -1 & 0 & 0 \end{bmatrix} \begin{bmatrix} -f_1 \\ e_2 \\ e_3 \end{bmatrix} \end{array} \right\}. \tag{2.79}$$

with $(f_1, f_2, f_3, e_1, e_2, e_3) = (I_{\mathrm{s}}, I_{\mathrm{s}}, I_{\mathrm{s}}, U_{\mathrm{mag}}, U_{\mathrm{res}}, U_{\mathrm{dyn}})$ and $\mathcal{F}_1 = \mathbb{R} \times \mathbb{R} \times \mathbb{R}$, $\mathcal{E}_1 = \mathbb{R} \times \mathbb{R} \times \mathbb{R}$. The bond graph representation of the 1-junction (2.79) with flow-in causality on the input power bond $(U_{\mathrm{mag}}, I_{\mathrm{s}})$.

Figure 2.23: 1-junction representing a voltage divider of the input port voltage U_{mag}.

A multiport injector distributes the input current in the magnet domain. In addition, the injector allows obtaining lumped voltage of the resistive U_{res} and dynamic U_{dyn} components from their distributed representation in the magnet domain. With the winding density function χ, the injector is given by the following relation

$$\mathcal{D}_2 = \left\{ \begin{array}{l} (f_a, f_b, e_a, e_b) \in \mathcal{F}_2 \times \mathcal{E}_2 : \\ \begin{bmatrix} e_a \\ f_b \end{bmatrix} = \begin{bmatrix} 0 & \chi^\top \\ \chi & 0 \end{bmatrix} \begin{bmatrix} -f_a \\ e_b \end{bmatrix} \end{array} \right\} \tag{2.80}$$

with $\mathcal{F}_2 = \mathbb{R} \times \Lambda^2(\Omega)$, $\mathcal{E}_2 = \mathbb{R} \times \Lambda^1(\Omega)$. Pairs of conjugate flow and effort variables of the multiport transformer (see Fig. 2.24) representing the resistive voltage are given as $(I_{\mathrm{s}}, \jmath_{\mathrm{s}}, U_{\mathrm{res}}, -\mathrm{d}\varphi) = (f_a, f_b, e_a, e_b) \in \mathcal{D}_2$, with $a = 2, b = 4$. For the dynamic voltage as $(I_{\mathrm{s}}, \jmath_{\mathrm{s}}, U_{\mathrm{dyn}}, \partial_t A) = (f_a, f_b, e_a, e_b) \in \mathcal{D}_2$, where $a = 3, b = 5$.

Figure 2.24: Bond graph representation of a multiport injector relating lumped and distributed voltage and current for resistive (middle) and inductive (right) components.

The output of the injection $\mathcal{D}_2$ for the resistive voltage is terminated with the distributed resistivity of the magnet. Effort-out causality is assigned to that bond, as the effort

$$e_b = -\mathrm{d}\varphi = *_\rho \jmath_{\mathrm{s}} \tag{2.81}$$

is deduced from the flow $f_b = \jmath_{\mathrm{s}}$. As long as a magnet is in the superconducting state, the resistivity ρ is equal to zero. In the normal conducting state, the resistivity is non-zero and acts as an irreversible entropy source. Thus, in order to study the temperature distribution after a quench, this open port has to be terminated with an appropriate distributed RS element and connected to the thermal domain.

The source current density $\jmath_{\mathrm{s}}$ contains a contribution from the induced eddy currents in copper wedges calculated as

$$\jmath_{\mathrm{ind}} = - *_\kappa \partial_t A. \tag{2.82}$$

This contribution is captured by means of a 0-junction at a certain effort $\partial_t A$

$$\mathcal{D}_3 = \left\{ \begin{array}{l} (f_5, f_6, f_7, e_5, e_6, e_7) \in \mathcal{F}_3 \times \mathcal{E}_3 : \\ \begin{bmatrix} f_7 \\ e_5 \\ e_6 \end{bmatrix} = \begin{bmatrix} 0 & -1 & -1 \\ 1 & 0 & 0 \\ 1 & 0 & 0 \end{bmatrix} \begin{bmatrix} e_7 \\ -f_5 \\ f_6 \end{bmatrix} \end{array} \right\} \tag{2.83}$$

with $(f_5, f_6, f_7, e_5, e_6, e_7) = (\jmath_{\mathrm{s}}, \jmath_{\mathrm{ind}}, \jmath_{\mathrm{s}} - \jmath_{\mathrm{ind}}, \partial_t A, \partial_t A, \partial_t A)$ and $\mathcal{F}_3 = \Lambda^2(\Omega) \times \Lambda^2(\Omega) \times \Lambda^2(\Omega)$, $\mathcal{E}_3 = \Lambda^1(\Omega) \times \Lambda^1(\Omega) \times \Lambda^1(\Omega)$. The bond graph representation of the 0-junction (2.83) is shown in Fig. 2.25.

Figure 2.25: Bond graph representation of the 0-junction (2.83) representing distribution of the source current density $\jmath_\mathrm{s}$.

The 0-junction has an open port representing eddy currents (f_6, e_6). The open port can be terminated with an irreversible entropy creation element and linked to the thermal domain. The open port has effort-in causality as the flow is determined from (2.82). Thus, the second output power port has effort-in causality at the side of the 0-junction.

The coupling currents, representing losses occurring in superconducting cables, are modeled as equivalent magnetization M_cc following the formula proposed in [30]

$$\mathrm{d}M_\mathrm{cc} = -\mathrm{d}(*_{\nu\tau}\mathrm{d}\partial_t A) \tag{2.84}$$

with τ the equivalent time constant of the coupling currents. The coupling currents contribution is represented as a a 0-junction at a certain effort $\partial_t A$

$$\mathcal{D}_4 = \left\{ \begin{array}{l} (f_7, f_8, f_9, e_7, e_8, e_9) \in \mathcal{F}_4 \times \mathcal{E}_4 : \\ \begin{bmatrix} f_9 \\ e_7 \\ e_8 \end{bmatrix} = \begin{bmatrix} 0 & -1 & -1 \\ 1 & 0 & 0 \\ 1 & 0 & 0 \end{bmatrix} \begin{bmatrix} e_9 \\ -f_7 \\ f_8 \end{bmatrix} \end{array} \right\} \tag{2.85}$$

with $(f_7, f_8, f_9, e_7, e_8, e_9) = (\jmath_\mathrm{s} - \jmath_\mathrm{ind}, \mathrm{d}M_\mathrm{cc}, \jmath_\mathrm{s} - \jmath_\mathrm{ind} - \mathrm{d}M_\mathrm{cc}, \partial_t A, \partial_t A, \partial_t A)$ and $\mathcal{F}_4 = \Lambda^2(\Omega) \times \Lambda^2(\Omega) \times \Lambda^2(\Omega)$, $\mathcal{E}_4 = \Lambda^1(\Omega) \times \Lambda^1(\Omega) \times \Lambda^1(\Omega)$. The bond graph representation of (2.85) along with the corresponding causality assignment is depicted in Fig. 2.26.

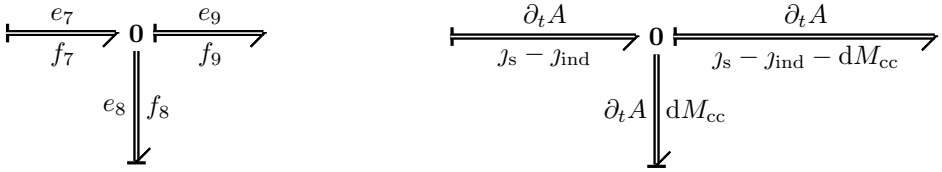

Figure 2.26: Bond graph model of the 0-junction given in (2.85).

Similarly as in the case of eddy currents, the coupling currents flowing in the stabilizer matrix are generating losses. The resulting irreversible entropy source plays an important role in the development of a quench in the superconducting magnet and has to be considered in order to study these phenomena. Thus, this port should be connected with the thermal domain.

The model also accounts for persistent eddy currents flowing in superconducting filaments. These currents are modeled by means of the equivalent persistent magnetization M_pc [4], [31]. Unlike the eddy and coupling currents, the persistent currents do not depend on the time derivative of the magnetic flux density but on the direction of the magnetic field. The persistent magnetization is composed of two contributions, i.e., reversible $M_\mathrm{pc,r}$ and irreversible $M_\mathrm{pc,ir}$ magnetization

$$M_\mathrm{pc} = M_\mathrm{pc,r} + M_\mathrm{pc,ir}. \tag{2.86}$$

We note that the reversible part is much smaller than the dissipative one. However, as we shall see later, the reversible magnetization forms an interesting coupling to the thermal domain. The adopted relationship describing the irreversible persistent magnetization reads

$$M_\mathrm{pc,ir} = -\frac{2}{3\pi} d_\mathrm{f} \jmath_\mathrm{c} \left(1 - \frac{|\jmath_\mathrm{s}|^2}{\jmath_\mathrm{c}^2}\right) v_B, \tag{2.87}$$

where d_f is the diameter of a superconducting filament, $\jmath_\mathrm{c}$ is the critical current density at the operating point, and v_B is the versor of the magnetic flux density. The versor and $\jmath_\mathrm{c}$ can be calculated from the magnetic vector potential, i.e., $M_\mathrm{pc,ir} = F_\mathrm{pc,ir}(\mathrm{d}A)$.

The total current density $\jmath_\mathrm{tot}$ is obtained from

$$\jmath_\mathrm{tot} = \jmath_\mathrm{s} - \jmath_\mathrm{ind} - \mathrm{d}M_\mathrm{cc} - \mathrm{d}M_\mathrm{pc,ir}. \tag{2.88}$$

We note that (2.88) defines a 0-junction with common effort $\partial_t A$ as

$$\mathcal{D}_5 = \left\{ \begin{array}{c} (f_9, f_{10}, f_{11}, e_9, e_{10}, e_{11}) \in \mathcal{F}_5 \times \mathcal{E}_5 : \\ \begin{bmatrix} f_{11} \\ e_9 \\ e_{10} \end{bmatrix} = \begin{bmatrix} 0 & -1 & -1 \\ 1 & 0 & 0 \\ 1 & 0 & 0 \end{bmatrix} \begin{bmatrix} e_{11} \\ -f_9 \\ f_{10} \end{bmatrix} \end{array} \right\} \tag{2.89}$$

with $(f_9, f_{10}, f_{11}, e_9, e_{10}, e_{11}) = (\jmath_\mathrm{s} - \jmath_\mathrm{ind} - \mathrm{d}M_\mathrm{cc}, \mathrm{d}M_\mathrm{pc,ir}, \jmath_\mathrm{tot}, \partial_t A, \partial_t A, \partial_t A)$ and $\mathcal{F}_5 = \Lambda^2(\Omega) \times \Lambda^2(\Omega) \times \Lambda^2(\Omega)$, $\mathcal{E}_5 = \Lambda^1(\Omega) \times \Lambda^1(\Omega) \times \Lambda^1(\Omega)$. The bond graph representation of (2.89) along with the corresponding causality assignment is depicted in Fig. 2.27.

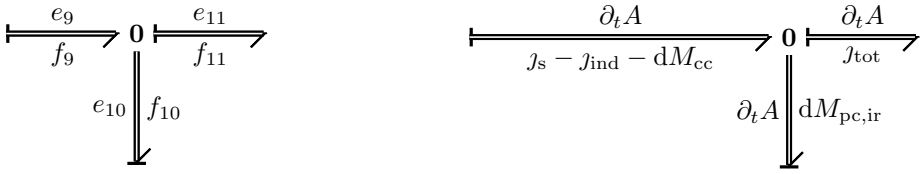

Figure 2.27: Bond graph model of the 0-junction given in (2.89).

Eventually, the power supplied by the total current density $\jmath_\mathrm{tot}$ and the variation of the magnetic vector potential $\partial_t A$ is linked to a Stokes-Dirac structure. The Stokes-Dirac structure $\mathcal{D}_5$ represents the interconnection in the magnetic domain and the interaction through the boundary. The governing equation of $\mathcal{D}_6$ reads

$$\mathcal{D}_6 = \left\{ \begin{array}{c} (f_{11}, f_{12}, f_\mathrm{b}, e_{11}, e_{12}, e_\mathrm{b}) \in \mathcal{F}_6 \times \mathcal{E}_6 : \\ \begin{bmatrix} f_{12} \\ f_{11} \end{bmatrix} = \begin{bmatrix} 0 & -\mathrm{d} \\ \mathrm{d} & 0 \end{bmatrix} \begin{bmatrix} e_{12} \\ e_{11} \end{bmatrix}, \begin{bmatrix} f_\mathrm{b} \\ e_\mathrm{b} \end{bmatrix} = \begin{bmatrix} 0 & -1 \\ 1 & 0 \end{bmatrix} \begin{bmatrix} e_{11}|_\Gamma \\ e_{12}|_\Gamma \end{bmatrix} \end{array} \right\}, \tag{2.90}$$

where $(f_{11}, f_{12}, f_\mathrm{b}, e_{11}, e_{12}, e_\mathrm{b}) = (\mathrm{d}(H - M_\mathrm{pc,r}), \partial_t B, \partial_t A|_\Gamma, \partial_t A, H - M_\mathrm{pc,r}, (H - M_\mathrm{pc,r})|_\Gamma)$ and $\mathcal{F}_6 = \Lambda^2(\Omega) \times \Lambda^2(\Omega) \times \Lambda^1(\Gamma)$, $\mathcal{E}_6 = \Lambda^1(\Omega) \times \Lambda^1(\Omega) \times \Lambda^1(\Gamma)$. For the Stokes-Dirac structure (2.90) we calculate the bilinear pairing (2.3) of internal flow and effort variables as

$$\langle\langle f | e \rangle\rangle = \int_\Omega f \wedge e = \int_\Omega (f_{11} \wedge e_{11} + f_{12} \wedge e_{12}) = \int_\Omega (\mathrm{d}e_{12} \wedge e_{11} - \mathrm{d}e_{11} \wedge e_{12}) \tag{2.91}$$

with $p = \deg(\mathrm{d}e_{11}) = 2$ and $q = \deg(e_{12}) = 1$ we find

$$\langle\langle f | e \rangle\rangle = \int_\Omega (\mathrm{d}e_{12} \wedge e_{11} - (-1)^{pq} e_{12} \wedge \mathrm{d}e_{11}) = \int_\Omega \mathrm{d}(e_{12} \wedge e_{11}) = \int_\Gamma (e_{12} \wedge e_{11}). \tag{2.92}$$

Application of the Stokes theorem to the power balance confirms, that in case of Stokes-Dirac structures, the power flow occurs through the boundary.

With appropriate homogeneous boundary conditions, the bond graph model of the Stokes-Dirac structure is depicted in Fig. 2.28.

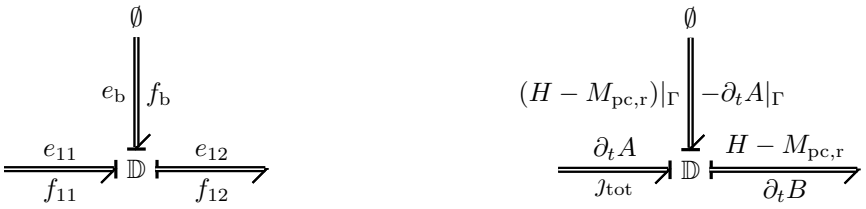

Figure 2.28: Bond graph representation of a Stokes-Dirac structure.

The reversible persistent magnetization $M_{\mathrm{pc,rev}}$ with time-variation of the magnetic field $\partial_t B$ represents the magneto-caloric effect and reversible energy flow from the magnetic storage to the internal energy. To represent the split of the flow of magnetic energy, we introduce a 1-junction given as

$$\mathscr{D}_7 = \left\{ \begin{array}{c} (f_{12}, f_{13}, f_{14}, e_{12}, e_{13}, e_{14}) \in \mathscr{F}_7 \times \mathscr{E}_7 : \\ \begin{bmatrix} e_{12} \\ f_{13} \\ f_{14} \end{bmatrix} = \begin{bmatrix} 0 & 1 & 1 \\ -1 & 0 & 0 \\ -1 & 0 & 0 \end{bmatrix} \begin{bmatrix} -f_{12} \\ e_{13} \\ e_{14} \end{bmatrix} \end{array} \right\} \tag{2.93}$$

with $(f_{12}, f_{13}, f_{14}, e_{12}, e_{13}, e_{14}) = (\partial_t B, \partial_t B, \partial_t B, H - M_{\mathrm{pc,r}}, M_{\mathrm{pc,r}}, H)$ and $\mathscr{F}_7 = \Lambda^2(\Omega) \times \Lambda^2(\Omega) \times \Lambda^2(\Omega)$, $\mathscr{E}_7 = \Lambda^1(\Omega) \times \Lambda^1(\Omega) \times \Lambda^1(\Omega)$. The bond graph representation of (2.93) along with the corresponding causality assignment is depicted in Fig. 2.29. In the electromagnetic domain, we distinguish two C-type storage elements, one for the energy stored in the magnetic field and another for the internal energy.

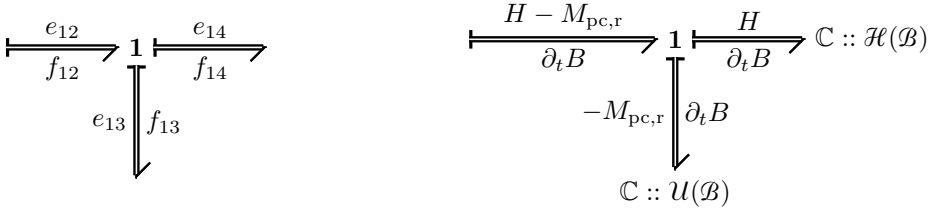

Figure 2.29: Bond graph model of the 1-junction given in (2.93).

The assembly of the structures discussed in this section is obtained by equating the bond indices and shown in Fig. 2.30. Comparing Fig. 2.27 and 2.28 we find that there is a causal conflict for the bond (f_{11}, e_{11}). The Stokes-Dirac structure (2.90) has fixed flow-out causality while according to (2.89) the same bond has effort-out causality. The fixed causality of the Stokes-Dirac structure will propagate backwards the causality change into structures (2.89)-(2.79). As a result, there is a causal conflict on the injector (2.80) and 0-junction (2.83) which does not contain an effort-establishing bond.

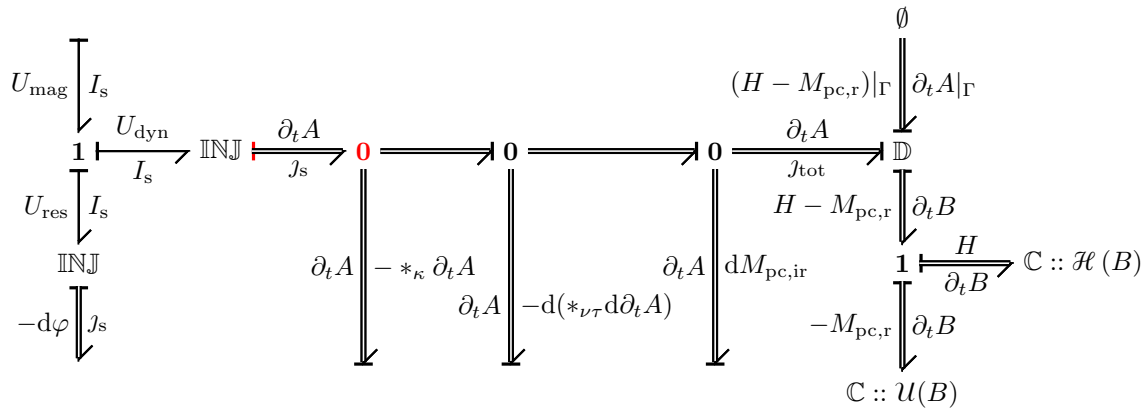

Figure 2.30: Bond graph representing energy flow in the electromagnetic domain of a superconducting magnet. Causal conflicts are indicated in red.

This concludes the description of the energy flow in the electromagnetic domain of a superconducting magnet. An assembly of the power-continuous structures (2.79) - (2.90) and the derivation of a port-Hamiltonian model is presented in the following.

2.4.2 Port-Hamiltonian Model of the Electromagnetic Domain

The aim of port-Hamiltonian modeling is to obtain a consistent representation of the internal connection between energy storage, dissipation, and interaction with the environment via the boundary and the open port. Once the port-Hamiltonian model of the electromagnetic domain is obtained, we will study factors influencing the variation of the energy function.

Let $x = [B, D]^\top$ be the state vector composed of the energy variables for a general electromagnetic model. For the sake of simplicity, linear material properties are assumed. Considering the magnetoquasistatic setup ($\partial_t D = 0$), the Hamiltonian function is defined as the total magnetic and electric energy, respectively, $\mathcal{H}(B)$ and $\mathcal{H}(D)$, in the domain Ω obtained by integration of the energy density $\hbar = \frac{1}{2}[*_\nu B \wedge B + *_{\frac{1}{\epsilon}} D \wedge D]$. The integral is given as

$$\mathcal{H}(B, D) = \frac{1}{2} \int_\Omega *_\nu B \wedge B + *_{\frac{1}{\epsilon}} D \wedge D \tag{2.94}$$

with the variational derivative being the magnetic field strength $\delta_B \mathcal{H} = H$ and the electric field strength $\delta_D \mathcal{H} = E$. However, for the considered magnetoquasistatic setting ($\epsilon \to 0$), the Hamiltonian shall stay bounded ($D \to 0$), that is

$$\lim_{\epsilon \to 0} \frac{1}{\epsilon} D = \frac{0}{0}. \tag{2.95}$$

With E not constrained by $\delta_D \mathcal{H}$, we define it via the local Faraday law $E = -\partial_t A$. In addition, to account for the reversible phenomena, we consider the internal energy $\mathcal{U}(B)$ for which the variational derivative w.r.t. the magnetic flux density is $\delta_B \mathcal{U} = -M_{\mathrm{pc,r}}$.

The first state equation is obtained from the Stokes-Dirac structure (2.90). The second state equation stems from the Kirchhoff Current Law given by (2.83), (2.85) and (2.89). The output equation is given by (2.79) and multiport injectors (2.80). We now present the state and output equations in a compact form as

$$\begin{aligned}
\begin{bmatrix} \partial_t B \\ 0 \end{bmatrix} &= \left(\begin{bmatrix} 0 & \mathrm{d} \\ -\mathrm{d} & 0 \end{bmatrix} - \begin{bmatrix} 0 & 0 \\ 0 & *_\kappa + \mathrm{d} *_{\nu\tau} \mathrm{d} + F_{\mathrm{pc,ir}}(\cdot) \end{bmatrix} \right) \begin{bmatrix} H - M_{\mathrm{pc,r}} \\ \partial_t A \end{bmatrix} + \begin{bmatrix} 0 \\ \chi \end{bmatrix} I_{\mathrm{s}} \\
U_{\mathrm{mag}} &= \begin{bmatrix} 0 & \chi^\top \end{bmatrix} \begin{bmatrix} H - M_{\mathrm{pc,r}} \\ \partial_t A \end{bmatrix} + \begin{bmatrix} 0 & \chi^\top \end{bmatrix} \begin{bmatrix} 0 & 0 \\ 0 & *_\rho \end{bmatrix} \begin{bmatrix} 0 \\ \chi \end{bmatrix} I_{\mathrm{s}},
\end{aligned} \tag{2.96}$$

which is recognized as an input-state-output port-Hamiltonian system

$$\begin{aligned} \partial_t x &= (J(x) - R(x))\, \delta_x(\mathcal{H}(x) + \mathcal{U}(x)) + gu \\ y &= g^\top \delta_x(\mathcal{H}(x) + \mathcal{U}(x)) + Su, \end{aligned} \tag{2.97}$$

with appropriate boundary conditions and the effort vector composed of the variational derivative of the Hamiltonian[2]. The obtained Hamiltonian structure satisfies the following dissipativity relation [29]

$$\begin{aligned} \partial_t(\mathcal{H}(x) + \mathcal{U}(x)) =& \delta_x(\mathcal{H}(x) + \mathcal{U}(x))^\top \partial_t x = \\ =& \delta_x(\mathcal{H}(x) + \mathcal{U}(x))^\top \left((J(x) - R(x))\, \delta_x(\mathcal{H}(x) + \mathcal{U}(x)) + gu\right) = \\ =& \delta_x(\mathcal{H}(x) + \mathcal{U}(x))^\top J(x) \delta_x(\mathcal{H}(x) + \mathcal{U}(x)) \\ & - \delta_x(\mathcal{H}(x) + \mathcal{U}(x))^\top R(x) \delta_x(\mathcal{H}(x) + \mathcal{U}(x)) \\ & + \delta_x(\mathcal{H}(x) + \mathcal{U}(x))^\top gu. \end{aligned} \tag{2.98}$$

We note, that the interconnection map $J(x)$ in $\delta_x(\mathcal{H}(x) + \mathcal{U}(x))^\top J(x) \delta_x(\mathcal{H}(x) + \mathcal{U}(x))$ leads to a boundary term as shown in (2.92)

$$\begin{aligned} \delta_x(\mathcal{H}(x) + \mathcal{U}(x))^\top J(x) \delta_x(\mathcal{H}(x) + \mathcal{U}(x)) &= \int_\Omega \begin{bmatrix} H - M_{\mathrm{pc,rev}} & \partial_t A \end{bmatrix} \begin{bmatrix} 0 & \mathrm{d} \\ -\mathrm{d} & 0 \end{bmatrix} \begin{bmatrix} H - M_{\mathrm{pc,r}} \\ \partial_t A \end{bmatrix} = \\ &= \int_\Omega (-\mathrm{d}\partial_t A \wedge (H - M_{\mathrm{pc,r}}) + \mathrm{d}(H - M_{\mathrm{pc,r}}) \wedge \partial_t A) = \\ &= \int_\Omega (-(H - M_{\mathrm{pc,r}}) \wedge \mathrm{d}\partial_t A + \mathrm{d}(H - M_{\mathrm{pc,r}}) \wedge \partial_t A) = \\ &= \int_\Omega \mathrm{d}((H - M_{\mathrm{pc,r}}) \wedge \partial_t A) = \int_\Gamma (H - M_{\mathrm{pc,r}}) \wedge \partial_t A \end{aligned} \tag{2.99}$$

so that the variation of the Hamiltonian becomes

$$\begin{aligned} \partial_t(\mathcal{H}(x) + \mathcal{U}(x)) = & \int_\Gamma H \wedge \partial_t A - \delta_x(\mathcal{H}(x) + \mathcal{U}(x))^\top R(x) \delta_x(\mathcal{H}(x) + \mathcal{U}(x)) \\ & + \int_\Gamma \delta_x(\mathcal{H}(x) + \mathcal{U}(x))^\top gu. \end{aligned} \tag{2.100}$$

With $y^\top = \delta_x(\mathcal{H}(x) + \mathcal{U}(x))^\top g + u^\top S^\top$ we can rewrite (2.100) as

$$\begin{aligned} \partial_t(\mathcal{H}(x) + \mathcal{U}(x)) = & \int_\Gamma (H - M_{\mathrm{pc,r}}) \wedge \partial_t A - \delta_x(H - M_{\mathrm{pc,r}})^\top R(x) \delta_x(\mathcal{H}(x) + \mathcal{U}(x)) \\ & + y^\top u - u^\top S^\top u \leq \int_\Gamma (H - M_{\mathrm{pc,r}}) \wedge \partial_t A + y^\top u. \end{aligned} \tag{2.101}$$

For the considered system, with $y^\top u = U_{\mathrm{mag}} I_{\mathrm{s}}$ and $u^\top S^\top u = U_{\mathrm{res}} I_{\mathrm{s}}$, the time-evolution of the

[2]Note that (2.96) could also be derived with only $\mathcal{H}(B)$ as a constrained port-Hamiltonian system with a Lagrange multiplier $\partial_t A$.

Hamiltonian reads

$$\begin{aligned}\partial_t(\mathcal{H}(x)+\mathcal{U}(x)) &= \int_\Gamma (H-M_{\mathrm{pc,r}})\wedge\partial_t A - \delta_x\mathcal{H}(x)^\top R(x)\delta_x(\mathcal{H}(x)+\mathcal{U}(x)) + y^\top u - u^\top S^\top u \\ &= \int_\Gamma (H-M_{\mathrm{pc,r}})\wedge\partial_t A \\ &\quad - \int_\Omega \begin{bmatrix} H-M_{\mathrm{pc,r}} & \partial_t A\end{bmatrix}\begin{bmatrix}0 & 0\\ 0 & *_\kappa + \mathrm{d}*_{\nu\tau}\mathrm{d} + F_{\mathrm{pc,ir}}(\cdot)\end{bmatrix}\begin{bmatrix} H-M_{\mathrm{pc,r}}\\ \partial_t A\end{bmatrix} \\ &\quad + U_{\mathrm{mag}}I_{\mathrm{s}} - U_{\mathrm{res}}I_{\mathrm{s}} = \\ &= U_{\mathrm{dyn}}I_{\mathrm{s}} + \int_\Gamma (H-M_{\mathrm{pc,rev}})\wedge\partial_t A - \int_\Omega (\partial_t A\wedge(*_\kappa + \mathrm{d}*_{\nu\tau}\mathrm{d} + F_{\mathrm{pc,ir}}(\cdot))\partial_t A)\,.\end{aligned} \tag{2.102}$$

From (2.102) we note that: (i) only the dynamic component U_{dyn} of the input port $(U_{\mathrm{mag}}, I_{\mathrm{s}})$ supplies the power to the magnetic system; (ii) power is also supplied via the boundary port $((H-M_{\mathrm{pc,r}})|_\Gamma, \partial_t A|_\Gamma)$; (iii) the energy stored in the magnetic field is dissipated due to the eddy, coupling, and persistent magnetization current losses. Thus, the Ohmic losses do not contribute directly to the magnetic energy dissipation in the distributed model but are exchanged through a port and dissipated elsewhere, e.g., circuit resistance. The dissipation term is considered by means of a lumped resistance through the common port in the circuit. Only then, the lumped resistance reduces current flowing through the superconducting magnet in the circuit.

2.4.3 Irreversible Entropy Creation

Entropy creation accounts for energy dissipation in the electromagnetic domain, i.e., Ohmic losses due to current flowing through the resistive matrix of a cable after a quench, eddy currents in copper wedges, persistent magnetization currents, and coupling currents in the coil.

Ohmic Loss

After a quench, a resistive voltage is present as given in (2.81). Consequently, an Ohmic loss $q_\rho = *_\rho \jmath_{\mathrm{s}} \wedge \jmath_{\mathrm{s}}$ is generated. An RS source representing Ohmic losses generated after a quench in the coil has a similar structure to (2.22) and is given as

$$\mathcal{J}_\rho = \left\{ \begin{bmatrix} e_4\\ f_{15}\end{bmatrix} = \begin{bmatrix} 0 & -\mathrm{e}_\rho(f_4,e_{15})\\ \mathrm{e}_\rho(f_4,e_{15}) & 0\end{bmatrix}\begin{bmatrix}-f_4\\ e_{15}\end{bmatrix} \;\middle|\; \begin{array}{c}(f_4,f_{15},e_4,e_{15})\in\mathcal{F}_\rho\times\mathcal{E}_\rho:\\ \end{array}\right\} \tag{2.103}$$

with $(f_4,f_{15},e_4,e_{15}) = (\chi I_{\mathrm{s}}, \sigma_\rho, -\mathrm{d}\varphi, T)$, $\mathrm{e}_\rho(f_4,e_{15}) = -\frac{1}{T}*_\rho \chi I_{\mathrm{s}}$ and $\mathcal{F}_\rho = \Lambda^2(\Omega)\times\Lambda^3(\Omega)$, $\mathcal{E}_\rho = \Lambda^1(\Omega)\times\Lambda^0(\Omega)$. A bond graph representation of the RS source (2.103) with appropriate causality assignment is shown in Fig. 2.31.

Figure 2.31: Bond graph representation of an RS source that relates electric and thermal domains.

Even though, the structure of the RS source and its bond graph representation resemble a transformer (2.12), we note that the power flow is one-directional and cannot be reverted. The distributed bond $(-\mathrm{d}\phi, \jmath_{\mathrm{s}})$ has a flow-in, effort-out causality since the distributed resistive voltage is calculated as the resistivity operating on the current density. It is particularly important in the superconducting state, while the resistance is equal to zero and current density can not be determined from the distributed resistive voltage. Furthermore, as it was demonstrated in Section 2.1.6, the RS source is not a Dirac structure.

Eddy and Persistent Currents

The variation of the magnetic field in conducting materials is introducing eddy currents. For superconducting cables, a special type of eddy currents, so called coupling currents, is present (2.84). In addition, we consider the persistent eddy currents flowing in the superconducting filaments. These three types of induced currents flow through a conducting material and generate losses. A similarity in the origin of these phenomena is reflected in their mathematical representation. They are represented by means of an RS source as

$$\mathcal{J}_\natural = \left\{ \begin{array}{c} (f_a, f_b, e_a, e_b) \in \mathcal{F}_\natural \times \mathcal{E}_\natural : \\ \begin{bmatrix} -f_a \\ f_b \end{bmatrix} = \begin{bmatrix} 0 & -\mathrm{e}_\natural(f_a, e_b) \\ \mathrm{e}_\natural(f_a, e_b) & 0 \end{bmatrix} \begin{bmatrix} e_a \\ e_b \end{bmatrix} \end{array} \right\} \quad \natural = \{\kappa, \nu\tau, \mathrm{pc}\}, \tag{2.104}$$

where $\mathcal{F}_\natural = \Lambda^2(\Omega) \times \Lambda^3(\Omega)$, $\mathcal{E}_\natural = \Lambda^1(\Omega) \times \Lambda^0(\Omega)$. Pairs of conjugate flow and effort variables of the eddy currents (κ) are given as $(-*_\kappa \partial_t A, \sigma_\kappa, \partial_t A, T) = (f_a, f_b, e_a, e_b) \in \mathcal{J}_\kappa$, with $a = 6, b = 16$. The coupling currents ($\nu\tau$) are characterized by flow and efforts as $(-\mathrm{d} *_{\nu\tau} \mathrm{d}\partial_t A, \sigma_{\nu\tau}, \partial_t A, T) = (f_a, f_b, e_a, e_b) \in \mathcal{J}_{\nu\tau}$, where $a = 8, b = 17$. The coefficients linking flow and effort variables are given as $\mathrm{e}_\kappa(f_a, e_b) = -\frac{1}{T} *_\kappa \partial_t A$, $\mathrm{e}_{\nu\tau}(f_a, e_b) = -\frac{1}{T}\mathrm{d} *_{\nu\tau} \mathrm{d}\partial_t A$,

Figure 2.32: Bond graph representation of an RS source for eddy (middle) and coupling (right) currents.

The persistent magnetization currents (pc) are given by $(\mathrm{d}M_{\mathrm{pc,ir}}, \sigma_{\mathrm{pc,ir}}, \partial_t A, T) = (f_a, f_b, e_a, e_b) \in \mathcal{J}_{\mathrm{pc,ir}}$, where $a = 10, b = 18$. The structural matrix is characterized by $\mathrm{e}_{\mathrm{pc,ir}}(f_a, e_b) = -\frac{1}{T}\mathrm{d}M_{\mathrm{pc,ir}}$. Fig. 2.32 presents a bond graph model of the RS source (2.104).

Figure 2.33: Bond graph representation of an RS source for persistent magnetization currents.

Note that the persistent magnetization loss is not explicitly dependent on the time derivative of the magnetic vector potential but on the direction of the magnetic field and therefore involves the functional $F_{\mathrm{pc,ir}}(\partial_t A)$.

We note that for all the discussed loss generation mechanisms, the causality of the distributed thermal bond is the same. The temperature is set by the thermal system on the basis of the irreversible entropy creation term, i.e., effort-out, flow-in causality from the point of view of the thermal system.

0-junction for Irreversible Entropy Creation

The irreversible entropy sources can be merged together and form a 0-junction. As a result, a single source term will be provided to the thermal domain. The 0-junction reads

$$\mathcal{D}_8 = \left\{ \begin{array}{c} (f_{15}, f_{16}, f_{17}, f_{18}, f_{19}, e_{15}, e_{16}, e_{17}, e_{18}, e_{19}) \in \mathcal{F}_8 \times \mathcal{E}_8 : \\ \begin{bmatrix} f_{19} \\ e_{15} \\ e_{16} \\ e_{17} \\ e_{18} \end{bmatrix} = \begin{bmatrix} 0 & -1 & -1 & -1 & -1 \\ 1 & 0 & 0 & 0 & 0 \\ 1 & 0 & 0 & 0 & 0 \\ 1 & 0 & 0 & 0 & 0 \\ 1 & 0 & 0 & 0 & 0 \end{bmatrix} \begin{bmatrix} e_{19} \\ -f_{15} \\ -f_{16} \\ -f_{17} \\ -f_{18} \end{bmatrix} \end{array} \right\}, \tag{2.105}$$

where $(f_{15}, f_{16}, f_{17}, f_{18}, f_{19}, e_{15}, e_{16}, e_{17}, e_{18}, e_{19}) = (\sigma_\rho, \sigma_\kappa, \sigma_{\nu\tau}, \sigma_{\mathrm{pc,ir}}, \sigma_{\mathrm{ext}}, T, T, T, T, T)$. Substituting corresponding expressions for irreversible entropy creation from (2.103) and (2.104) to

(2.105) yields

$$\sigma_{\text{ext}} = \frac{1}{T}(*_\rho \jmath_{\text{s}} \wedge \jmath_{\text{s}} + \partial_t A \wedge *_\kappa \partial_t A + \partial_t A \wedge \mathrm{d} *_{\nu\tau} \mathrm{d}\partial_t A + \partial_t A \wedge \mathrm{d}M_{\text{pc,ir}}). \tag{2.106}$$

Fig. (2.34) shows the bond-graph representation of the 0-junction with appropriate computational causality derived from (2.103) and (2.104).

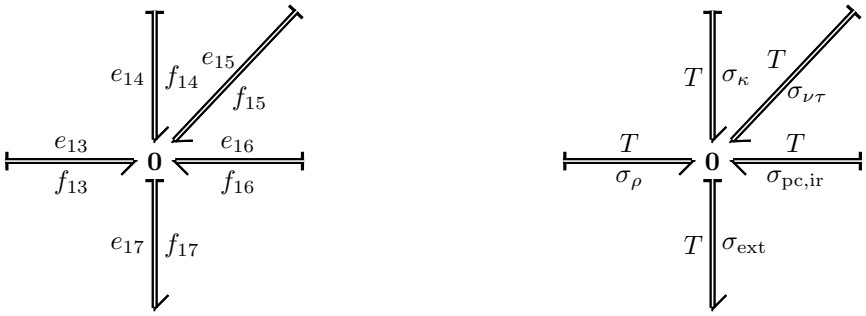

Figure 2.34: Bond graph representation of the 0-junction (2.105) for the irreversible entropy creation in the electromagnetic domain.

The next Section introduces the thermodynamic domain in order to account for the temperature changes due to these dissipative phenomena.

2.4.4 Bond Graph Model of the Thermodynamic Domain

The heat balance equation

$$C_V(T,B)\partial_t T = q_0 + \mathrm{d} *_{k(T)} \mathrm{d}T \tag{2.107}$$

is usually used to characterize the temperature variation of a system with given heat capacity $C_V(T,B)$ subject to the input heat flux q_0 and thermal conduction expressed as the Fourier law $J_{\text{Q}} = - *_{k(T)} \mathrm{d}T$ with $k(T)$ being a temperature-dependent heat conduction coefficient. However, it is not explicitly expressed in terms of a balance of two conjugate power variables and therefore can not be used directly to obtain a bond graph model.

For the purpose of the power-based modeling, we start the derivation from the internal energy (please refer to Appendix C for a brief summary to the thermodynamic constitutive relations expressed in terms of differential forms). Conservation of the internal energy in thermodynamic systems can be expressed as

$$\partial_t \mathcal{U} = -\mathrm{d}\jmath_{\text{Q}}, \tag{2.108}$$

where $\jmath_{\text{Q}}$ is the energy flow density. Differentiation of internal energy $\mathrm{d}\mathcal{U} = T\mathrm{d}s$ in time yields an expression for the variation of the entropy density

$$\partial_t s = -\frac{1}{T}\mathrm{d}\jmath_{\text{Q}}. \tag{2.109}$$

Then, by applying the exterior product rule and introducing the entropy flow $\jmath_{\text{S}} = \frac{\jmath_{\text{Q}}}{T}$ one obtains Jaumann's entropy balance [26]

$$\mathrm{d}\jmath_{\text{Q}} = \mathrm{d}(T\jmath_{\text{S}}) = T\mathrm{d}\jmath_{\text{S}} + \mathrm{d}T \wedge \jmath_{\text{S}} \tag{2.110}$$

leading to an expression characterizing the entropy variation

$$\partial_t s = -\frac{1}{T}\mathrm{d}T \wedge \jmath_{\text{S}} - \mathrm{d}\jmath_{\text{S}} = \frac{*_{k(T)}}{T^2}\mathrm{d}T \wedge \mathrm{d}T + \mathrm{d}\frac{*_{k(T)}}{T}\mathrm{d}T = \sigma_{\text{S}} - f_{\text{S}}, \tag{2.111}$$

with σ_{S} and f_{S} being irreversible and reversible entropy flow, respectively.

We will derive the heat balance equation for type II superconductors. In this type of superconductors, the entropy does not only depend on the temperature, but also is a function of the magnetic field due to the magnetocaloric effect [32]. The magnetocaloric effect demonstrates itself in the superconducting state while isentropicly increasing or decreasing the magnetic field, the temperature, respectively, decreases or increases. A reciprocal effect while changing temperature also takes place. In other words, the internal energy of the system U is a function of both, the entropy and the magnetic field (only the reversible magnetization). Hence, for an isolated and isothermal system, the variation of the entropy reads

$$\partial_t s = \partial_t T \partial_T s + \partial_t B \partial_B s. \tag{2.112}$$

Then, with $G(T)$ being the Gibbs free energy as the thermodynamic potential and Legendre transformation of the internal energy $\mathcal{U}^*$ we find

$$s = \partial_T \mathcal{U}^* = -\partial_T G(T). \tag{2.113}$$

Taking into account that $\partial_T s = -\partial_T^2 G(T) = C_V/T$, the entropy variation (2.112) takes the following form

$$\partial_t s = \frac{C_V}{T}\partial_t T + \frac{\lambda_B}{T}\partial_t B, \tag{2.114}$$

where $\lambda_B = \partial_B s \wedge T$ is the magnetocaloric coefficient. By comparing (2.111) and (2.112), and multiplying both sides by temperature, the heat balance equation for type-II superconductors reads

$$C_V \partial_t T = -\lambda_B \partial_t B + \frac{*_{k(T)}}{T}\mathrm{d}T \wedge \mathrm{d}T + \mathrm{d} *_{k(T)} \mathrm{d}T. \tag{2.115}$$

The magnetocaloric effect provides a link between the variation of the magnetic field and the temperature. However, the effect is generally small as compared to the external heat sources. The magnetocaloric coefficient is related to the reversible magnetization according to

$$\frac{\lambda_B}{T} = \partial_T \partial_B G = \lambda_T M_{\mathrm{pc,r}} = \partial_B S. \tag{2.116}$$

Considering the thermal domain, we formulate the power balance obtained with (2.111) as a 0-junction representing the entropy variation $\partial_t s$ at the temperature T

$$\mathcal{D}_9 = \left\{ \begin{array}{c} (f_{22}, f_{23}, f_{24}, e_{22}, e_{23}, e_{24}) \in \mathcal{F}_9 \times \mathcal{E}_9 : \\ \begin{bmatrix} f_{22} \\ e_{23} \\ e_{24} \end{bmatrix} = \begin{bmatrix} 0 & -1 & -1 \\ 1 & 0 & 0 \\ 1 & 0 & 0 \end{bmatrix} \begin{bmatrix} e_{22} \\ -f_{23} \\ f_{24} \end{bmatrix} \end{array} \right\} \tag{2.117}$$

with $(f_{22}, f_{23}, f_{24}, e_{22}, e_{23}, e_{24}) = (\partial_t s, \sigma_{\mathrm{s}}, \mathrm{d}\jmath_{\mathrm{s}}, T, T, T)$ and $\mathcal{F}_9 = \Lambda^3(\Omega) \times \Lambda^3(\Omega) \times \Lambda^3(\Omega)$, $\mathcal{E}_9 = \Lambda^0(\Omega) \times \Lambda^0(\Omega) \times \Lambda^0(\Omega)$. The power flow of the 0-junction (2.117) is modelled as a bond graph (see Fig. 2.35). The entropy variation bond $(\partial_t s, T)$ is attached to the internal energy storage.

Figure 2.35: Bond graph representation of the entropy variation (2.117).

The bond $(\mathrm{d}\jmath_{\mathrm{S}}, T)$ is connected to a Stokes-Dirac structure representing the interconnection in the thermal domain and the interaction via the domain boundary. The Stokes-Dirac structure

representing the reversible entropy flow $f_\mathrm{s} = \mathrm{d}\jmath_\mathrm{S}$ and the effort T along with the entropy flux $\jmath_\mathrm{S}$ and the temperature gradient $\mathrm{d}T$ within the thermal domain reads

$$\mathcal{D}_{10} = \left\{ \begin{array}{c} (f_{24}, f_{25}, f_\mathrm{b}, e_{24}, e_{25}, e_\mathrm{b}) \in \mathcal{F}_{10} \times \mathcal{E}_{10} : \\ \begin{bmatrix} -f_{24} \\ f_{25} \end{bmatrix} = \begin{bmatrix} 0 & -\mathrm{d} \\ \mathrm{d} & 0 \end{bmatrix} \begin{bmatrix} e_{24} \\ e_{25} \end{bmatrix}, \begin{bmatrix} f_\mathrm{b} \\ e_\mathrm{b} \end{bmatrix} = \begin{bmatrix} 0 & 1 \\ 1 & 0 \end{bmatrix} \begin{bmatrix} e_{24}|_\Gamma \\ e_{25}|_\Gamma \end{bmatrix} \end{array} \right\} \tag{2.118}$$

with $(f_{24}, f_{25}, f_\mathrm{b}, e_{24}, e_{25}, e_\mathrm{b}) = (\mathrm{d}\jmath_\mathrm{S}, \mathrm{d}T, \jmath_\mathrm{S}|_\Gamma, T, \jmath_\mathrm{S}, T|_\Gamma)$ and $\mathcal{F}_{10} = \Lambda^3(\Omega) \times \Lambda^1(\Omega) \times \Lambda^2(\Gamma)$, $\mathcal{E}_{10} = \Lambda^0(\Omega) \times \Lambda^2(\Omega) \times \Lambda^0(\Gamma)$. With regard to (2.50) we note that, $p = \deg(f_{24}) = 3$ and $q = \deg(f_{25}) = 1$, so that $r = pq + 1 = 4$, which confirms that the interconnection map has a symmetric structure. A bond graph representation of the Stokes-Dirac structure with the adiabatic boundary conditions is depicted in Fig. 2.36.

Figure 2.36: Bond graph representation of the Stokes-Dirac structure (2.118).

The bilinear pairing for the Stokes-Dirac structure (2.3) reads

$$\begin{aligned} \langle f|e\rangle = \int_\Omega f \wedge e = \int_\Omega (-f_{24} \wedge e_{24} + f_{25} \wedge e_{25}) + \int_\Gamma f_\mathrm{b} \wedge e_\mathrm{b} = \\ = \int_\Omega (\mathrm{d}e_{25} \wedge e_{24} + \mathrm{d}e_{24} \wedge e_{25}) + \int_\Gamma f_\mathrm{b} \wedge e_\mathrm{b} = 0. \end{aligned} \tag{2.119}$$

With $p = \deg(e_{24}) = 0$ and $q = \deg(\mathrm{d}e_{25}) = 3$ we obtain

$$\int_\Omega ((-1)^{pq} e_{24} \wedge \mathrm{d}e_{25} + \mathrm{d}e_{24} \wedge e_{25}) = \int_\Omega \mathrm{d}(e_{24} \wedge e_{25}) = \int_\Gamma (e_{24} \wedge e_{25}). \tag{2.120}$$

The heat conduction in the thermal domain is based on the Fourier law and represented as an irreversible entropy source

$$\mathcal{G}_k = \left\{ \begin{array}{c} (f_{23}, f_{25}, e_{23}, e_{25}) \in \mathcal{F}_k \times \mathcal{E}_k : \\ \begin{bmatrix} e_{25} \\ f_{23} \end{bmatrix} = \begin{bmatrix} 0 & -\mathrm{e}_k \\ \mathrm{e}_k & 0 \end{bmatrix} \begin{bmatrix} -f_{25} \\ e_{23} \end{bmatrix} \end{array} \right\} \tag{2.121}$$

with an exterior derivative operator $\mathrm{e}_k = \frac{*_{k(T)}}{T^2} \mathrm{d}T \wedge \cdot$. The spaces of flow and effort variables involved in the heat conduction are defined as $\mathcal{F}_k = \Lambda^3(\Omega) \times \Lambda^1(\Omega)$ and $\mathcal{E}_k = \Lambda^0(\Omega) \times \Lambda^2(\Omega)$, respectively. The RS source depicted in Fig. 2.37 connects the Stokes-Dirac structure (Fig. 2.36) and the 0-junction (Fig. 2.35).

Figure 2.37: Bond graph representation of an RS source for the heat conduction.

To conclude, the developed bond graph model accounts for the storage of the thermal energy and interaction through the model boundary as well as input port with the source of flow **Sf**. Additionally, the model considers reversible and irreversible entropy flow. The latter are modeled by means of an RS source. Furthermore, as it will be demonstrated in the following,

the 0-junction (2.117) can be extended and account for irreversible entropy sources, which stem from the electromagnetic domain.

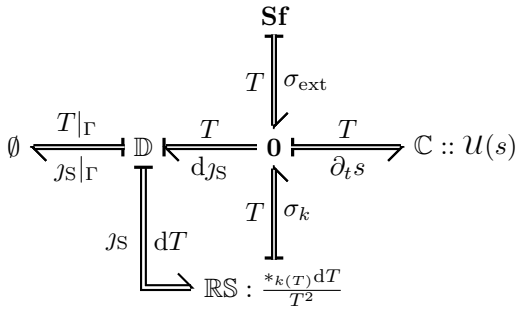

Figure 2.38: Bond graph representing energy flow in the thermal subsystem of a superconducting magnet.

2.4.5 Port-Hamiltonian Model of the Thermodynamic Domain

In case of the considered thermodynamic domain, let $\mathcal{U}$ be the Hamiltonian function given as the integral of the internal energy in the domain Ω. Similarly as for the electromagnetic domain, we construct a port-Hamiltonian model from the bond graph model developed in the prior Section. Starting from the already defined set of pairs of conjugate variables (f_i, e_i) for $i = \{22, 23, 24, 25\}$, we will construct a set of equations describing the thermodynamic domain.

Firstly, following the procedure outlined in Section 2.1.8, we combine the Stokes-Dirac structure (2.118) and the RS source (2.121). As a result, the interconnection port (f_{25}, e_{25}) is removed leading to the following set of equations

$$\mathcal{G}_{10||k} = \left\{ \begin{array}{c} (f_{23}, f_{24}, e_{23}, e_{24}) \in \mathcal{F}_{10||k} \times \mathcal{E}_{10||k} : \\ \begin{bmatrix} f_{23} \\ f_{24} \end{bmatrix} = \begin{bmatrix} 0 & -\mathrm{e}_k\mathrm{d} \\ \mathrm{d}\mathrm{e}_k & 0 \end{bmatrix} \begin{bmatrix} e_{23} \\ e_{24} \end{bmatrix} \end{array} \right\}. \tag{2.122}$$

Note that due to the adopted adiabatic boundary conditions, we neglect the boundary term of the Stokes-Dirac structure (2.118), which otherwise has to be considered.

Second, we combine the result from (2.122) and the 0-junction 2.117 with the interconnection port (f_{24}, e_{24}) as

$$\mathcal{G}_{10||k||1} = \left\{ \begin{array}{c} (f_{22}, f_{23}, e_{22}, e_{23}) \in \mathcal{F}_{10||k||1} \times \mathcal{E}_{10||k||1} : \\ \begin{bmatrix} f_{23} \\ e_{23} \\ f_{23} \end{bmatrix} = \begin{bmatrix} 0 & -1 & \mathrm{e}_k\mathrm{d} \\ 1 & 0 & 0 \\ -\mathrm{d}\mathrm{e}_k & 0 & 0 \end{bmatrix} \begin{bmatrix} e_{23} \\ f_{23} \\ e_{23} \end{bmatrix} \end{array} \right\}. \tag{2.123}$$

Equation (2.123) contains duplicated variables denoting the interconnection relationship. In fact, (2.123) contains a circular reference due to a loop in Fig. 2.38. From (2.123) we obtain

$$f_{23} = \mathrm{e}_k\mathrm{d}e_{23} - f_{23} = \mathrm{e}_k\mathrm{d}e_{23} + \mathrm{d}\mathrm{e}_k e_{23} = (\mathrm{e}_k\mathrm{d} + \mathrm{d}\mathrm{e}_k)e_{23}. \tag{2.124}$$

Now, we substitute the thermodynamic quantities with the flow and effort variables

$$\partial_t s = (\mathrm{e}_k\mathrm{d} + \mathrm{d}\mathrm{e}_k)T. \tag{2.125}$$

So far, the description of the thermal system given in (2.123) is self-contained and accounts only for the internal flow of heat due to the temperature gradients.

To construct an irreversible port-Hamiltonian model, let the entropy be the state variable $x = s$. Then, the variational derivative of the Hamiltonian function $\mathcal{U}$ w.r.t. the state is the temperature $\delta_x \mathcal{U} = T$. We also denote the source terms from the irreversible entropy creation

(2.106) discussed in Section 2.4.3 as the input $u = \sigma_{\text{ext}}$. Equation (2.125) can be rewritten in a compact form as

$$\begin{aligned} \partial_t x &= (\mathrm{d}\mathrm{e}_k + \mathrm{e}_k\mathrm{d})\delta_x \mathcal{U} + u \\ y &= \delta_x \mathcal{U}. \end{aligned} \tag{2.126}$$

Equation (2.126) forms a distributed irreversible port-Hamiltonian system. The variation of the internal energy of the thermodynamic domain reads

$$\partial_t \mathcal{U} = \delta_x \mathcal{U} \partial_t x = \int_\Omega T \wedge (\mathrm{d}\mathrm{e}_k T + \mathrm{e}_k \mathrm{d}T) + \int_\Omega T \wedge \sigma_{\text{ext}}. \tag{2.127}$$

We consider the first term in (2.127). With the Stokes theorem and $\mathrm{e}_k T = -\jmath_{\mathrm{S}}$ we obtain

$$\begin{aligned} \int_\Omega T \wedge (\mathrm{d}\mathrm{e}_k T + e_k \mathrm{d}T) = \int_\Omega (\mathrm{d}\mathrm{e}_k T \wedge T + e_k \mathrm{d}T \wedge T) = \int_\Omega (\mathrm{d}\jmath_{\mathrm{S}} \wedge T + \jmath_{\mathrm{S}} \wedge \mathrm{d}T) = \\ = -\int_\Omega \mathrm{d}(\jmath_{\mathrm{S}} \wedge T) = -\int_\Gamma \jmath_{\mathrm{S}} \wedge T. \end{aligned} \tag{2.128}$$

With adiabatic boundary conditions $\int_\Gamma \jmath_{\mathrm{S}} \wedge T = 0$ in (2.128) we get

$$\partial_t \mathcal{U} = \int_\Omega T \wedge \sigma_{\text{ext}}. \tag{2.129}$$

From (2.129) we note that, with the adopted adiabatic boundary conditions, the variation of the internal energy is due to the irreversible entropy creation (source term).

2.5 Bond Graph Model of a Superconducting Magnet

After separately discussing the port-based modeling of electromagnetic and thermal phenomena occurring in superconducting magnets, we construct an ensemble of the developed bond graph models. The resulting bond graph is shown in Fig. 2.39 and composed of three parts. The top part is devoted to the electromagnetic phenomena (2.78-2.93), the middle part represents the irreversible entropy creation due to the electromagnetic losses with RS sources (2.103-2.104), and the bottom part depicts the thermodynamic domain (2.117-2.121).

For the considered setup, on the electromagnetic side, we consider a source of flow **Sf** to impose the flow via an open port $(I_{\mathrm{s}}, U_{\mathrm{mag}})$. The open port is connected to a 1-junction representing the voltage divider (2.79). The output bonds of the 1-junction are attached to distributed injectors (2.80). For superconducting magnets the causality for the resistance is fixed as voltage can be determined from current and the opposite is not generally possible (in the superconducting state any current density less or equal to the critical current density can flow in a material resulting in the voltage drop across the material equal to zero). The distributed resistive voltage is terminated with an RS source that irreversibly generates entropy after a quench in the magnet. The output of the distributed injector for the inductive voltage is attached to a series connection of three 0-junctions, which represent the division of the total current density into several contributions. (Note that the three 0-junctions can be merged into one, however, for the sake of readability they are separated.) As a result, three bonds are established for: (i) the eddy currents $(\jmath_{\mathrm{ind}}, \partial_t A)$; (ii) the coupling currents $(\mathrm{d}M_{\mathrm{cc}}, \partial_t A)$; and (iii) the persistent magnetization currents $(\mathrm{d}M_{\mathrm{pc,ir}}, \partial_t A)$. These bonds are terminated with dedicated RS sources. The remaining power represented by the bond $(\jmath_{\mathrm{tot}}, \partial_t A)$ is connected to the Stokes-Dirac structure (2.90). The Stokes-Dirac structure provides a boundary port allowing the assignment of the appropriate boundary conditions and a distributed port $(\partial_t B, H - M_{\mathrm{pc,r}})$ connected to a 1-junction. The 1-junction splits the energy flow into the internal energy storage $(\partial_t B, -M_{\mathrm{pc,r}})$ and the magnetic energy reservoir $(\partial_t B, H)$.

For the current-driven case, the causality assignment determined by the fixed causalities of the input port, Stokes-Dirac structure as well as preferred causalities of bonds related to RS

sources, lead to a causality conflict in the injector related with the dynamic voltage. The injector has two effort-out causalities. The conflict translates into a need to invert that relationship which is confirmed by the numerical finite element formulation of the curl-curl equation for the magnetoquasistatic setup where each step in the time integration requires an inversion of the system matrix. We note also that the storage elements from the magnetoquasistatic perspective have preferred, integral causalities.

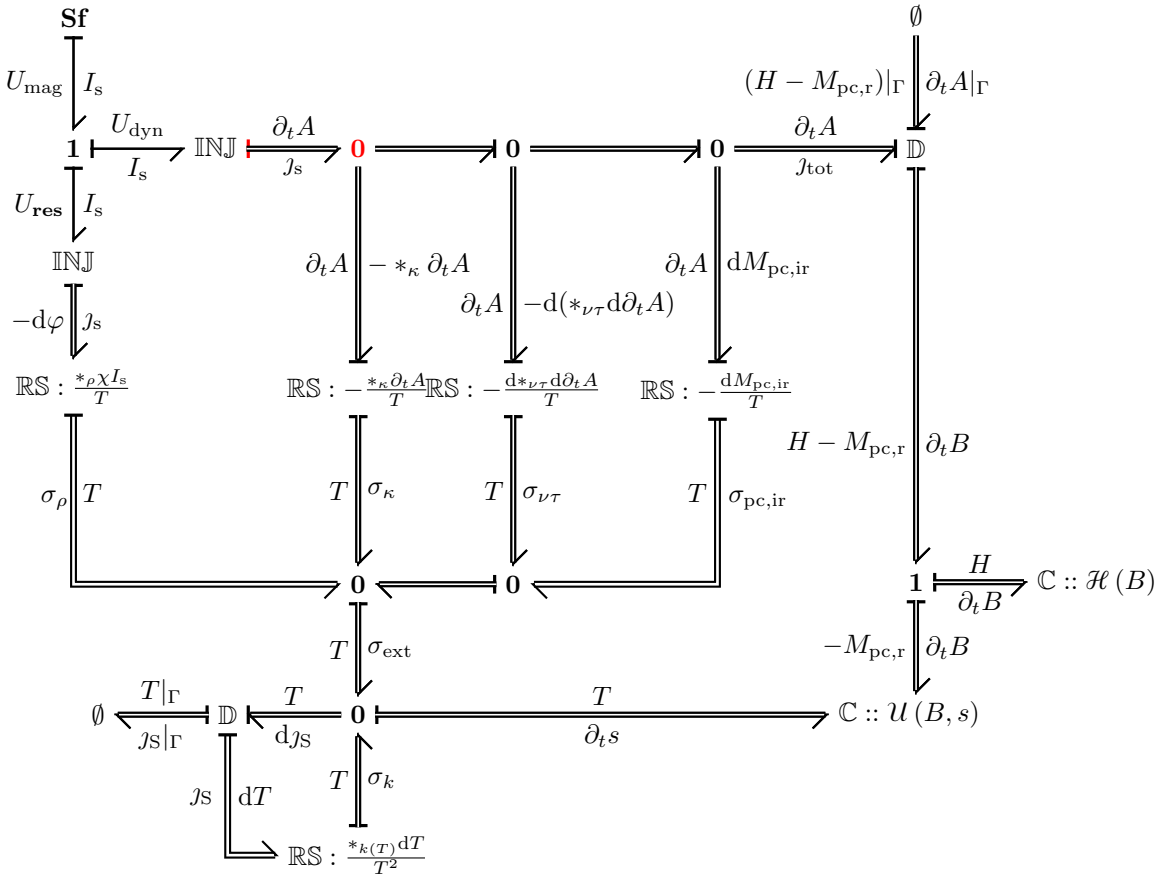

Figure 2.39: Bond graph representing energy flow in a superconducting magnet.

For the voltage-driven case, the input port has effort-out causality, seen from the 1-junction perspective, as shown in Fig. 2.40. This translates into a causal conflict at the 1-junction as each input bond is setting effort. This conflict requires an additional equation to resolve the voltage distribution as will be shown for the field/circuit coupling in Chapter 3. The remaining causality assignment is the same as for the current-driven case.

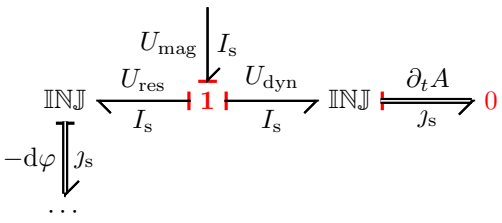

Figure 2.40: Voltage-driven case with effort-in causality on the input 1-junction.

The power dissipated due to the Ohmic loss (2.103), eddy-current, coupling-current, and persistent magnetization currents (2.104) is represented by means of RS sources with appropriate ratios. The resulting irreversible entropy creation is merged together into a 0-junction (2.105) and provided as a load to the thermal domain; for the sake of readability a superfluous 0-junction is added. The thermodynamic model accounts for the entropy variation due to the source term as well as reversible and irreversible processes. The entropy variation is represented by a 0-junction. In addition, the bond $(\partial_t s, T)$ is linked to the energy storage. Furthermore, with the Stokes-Dirac structure it is possible to account for the adiabatic boundary conditions and heat conduction in the thermal domain. We note that the causality assignment in the thermal domain leads to a preferred integral causality on the storage element. As a result of the preferred causality, the solution of the thermal problem does not require inversion of the system matrix and only involves integration of the system of equations.

The developed bond graph model of a superconducting magnet provides several relevant pieces of information regarding the modeling process. Firstly, the computational causality assignment indicates what are the numerical implications of the selected input port causality. Secondly, we identified two boundary ports, for electromagnetic and thermal domains, respectively. These ports provide an interface to link with external sources of the magnetic field (e.g., absorption coils [33]) and temperature (e.g., modelling of the helium bath surrounding the magnet [34] or heater-based protection [35]). The model can be further developed to account for other relevant physical domains, e.g., the mechanical and the fluid dynamics domains.

2.6 Port-Hamiltonian Model of a Superconducting Magnet

In order to study the properties of the ensemble model composed of electromagnetic and thermodynamic domains interconnected via irreversible entropy creation, we combine corresponding constitutive input-state output equations (2.96) and (2.126). Let the state vector be $x = \begin{bmatrix} B & D & s \end{bmatrix}^\top$, and the Hamiltonian function

$$\mathcal{U}(B,s) + \mathcal{H}(B,D) = \mathcal{U}(B,s) + \frac{1}{2}\int_\Omega (*_\nu B \wedge B + *_{\frac{1}{\epsilon}} D \wedge D, \tag{2.130}$$

so that $e = \delta_x(\mathcal{H}(x) + \mathcal{U}(x)) = \begin{bmatrix} H - M_{\mathrm{pc,r}} & \partial_t A & T \end{bmatrix}^\top$. Assuming that the boundary terms are set to 0, the state of a superconducting magnet is characterized by

$$\begin{aligned}
\begin{bmatrix} \partial_t B \\ 0 \\ \partial_t s \end{bmatrix} &= \left(\begin{bmatrix} 0 & \mathrm{d} & 0 \\ -\mathrm{d} & 0 & \mathrm{e}_\kappa + \mathrm{e}_{\nu\tau} + \mathrm{e}_{\mathrm{pc}} \\ 0 & -\mathrm{e}_\kappa - \mathrm{e}_{\nu\tau} - \mathrm{e}_{\mathrm{pc}} & 0 \end{bmatrix} + \begin{bmatrix} 0 & 0 & 0 \\ 0 & 0 & 0 \\ 0 & 0 & -\mathrm{d}\mathrm{e}_k - \mathrm{e}_k \mathrm{d} \end{bmatrix} \right) \begin{bmatrix} H - M_{\mathrm{pc,r}} \\ \partial_t A \\ T \end{bmatrix} \\
&\quad + \begin{bmatrix} 0 \\ \chi \\ \mathrm{e}_\rho \chi \end{bmatrix} I_{\mathrm{s}} \\
U_{\mathrm{mag}} &= \begin{bmatrix} 0 & \chi^\top & \chi^\top \mathrm{e}_\rho \end{bmatrix} \begin{bmatrix} H - M_{\mathrm{pc,r}} \\ \partial_t A \\ T \end{bmatrix}.
\end{aligned} \tag{2.131}$$

We arrange (2.131) into a more compact form as

$$\begin{aligned}
\partial_t x &= \left(J_{\mathrm{em}}(x) + J_{\mathrm{th}}(x)\right) e + g u \\
y &= g^\top e,
\end{aligned} \tag{2.132}$$

where $J_{\mathrm{em}}(x) : e \mapsto f$ is an interconnection map between the electromagnetic and thermal domains, $J_{\mathrm{th}}(x) : e \mapsto f$ is a map between efforts and flows in the thermal domain. We use

(2.132) to study factors influencing the Hamiltonian variation

$$\begin{aligned}\partial_t \left(\mathcal{U}(x)+\mathcal{H}(x)\right) &= \delta_x \left(\mathcal{U}(x)+\mathcal{H}(x)\right)^\top \partial_t x = e^\top \left\{\left(J_{\mathrm{em}}(x)+J_{\mathrm{th}}(x)\right)e+gu\right\} = \\ &= e^\top J_{\mathrm{em}}(x)e + e^\top J_{\mathrm{th}}(x)e + e^\top gu.\end{aligned} \tag{2.133}$$

We find that $e^\top J_{\mathrm{em}}(x)e = \int_\Gamma (H - M_{\mathrm{pc,r}}) \wedge \partial_t A$ and $y^\top = e^\top g$ in order to simplify (2.133) into

$$\begin{aligned}\partial_t \left(\mathcal{U}(x)+\mathcal{H}(x)\right) &= \int_\Gamma (H - M_{\mathrm{pc,r}}) \wedge \partial_t A + e^\top J_{\mathrm{th}}(x)e + y^\top u = \\ &= \int_\Gamma (H - M_{\mathrm{pc,r}}) \wedge \partial_t A + \int_\Omega T \wedge (\mathrm{d}e_k T + e_k \mathrm{d}T) + U_{\mathrm{mag}} I_{\mathrm{s}} = \\ &= \int_\Gamma (H - M_{\mathrm{pc,r}}) \wedge \partial_t A - \int_\Gamma \jmath_{\mathrm{S}} \wedge T + U_{\mathrm{mag}} I_{\mathrm{s}}.\end{aligned} \tag{2.134}$$

The time derivative of the Hamiltonian function representing electromagnetic and thermal phenomena occurring in superconducting accelerator magnets is driven by the power delivered due to the common port $(U_{\mathrm{mag}}, I_{\mathrm{s}})$ and via the thermal and magnetic boundary ports, respectively, $(T|_\Gamma, \jmath_{\mathrm{S}}|_\Gamma)$ and $((H - M_{\mathrm{pc,r}})|_\Gamma, -\partial_t A|_\Gamma)$.

2.7 Superconducting Circuit

A superconducting accelerator circuit consists of a single magnet or a series connection of multiple superconducting magnets. In addition, a superconducting circuit comprises equipment dedicated to powering, measurements, and protection. There is a relevant reciprocal influence of a superconducting magnet on a circuit and vice versa. Resistance growth in a coil following a quench event is detected with a dedicated measurement system and results in triggering the protection systems for the magnet and the circuit. Active magnet protection aims at transitioning large fractions of the coil volume into the normal conducting state. As a result, the coil resistance grows and affects the distribution of voltages and currents in the circuit. In this Section, we study the model of superconducting circuits based on the Modified Nodal Analysis (MNA) and its port-based representation by means of a Kirchhoff-Dirac structure.

2.7.1 Modified Nodal Analysis

We consider an electrical network composed of n_n nodes with ϕ_j denoting the j-th nodal potential with respect to a grounded node representing an algebraic condition, and n_b branches with I_i and U_i being, respectively, the current through the i-th branch and the voltage across the i-th branch. The circuit topology is represented by the incidence matrix A, with non-zero elements $A_{i,j}$ equal to either -1 or 1 depending on the assumed direction of branch i with respect to node j (branch orientation from -1 to 1).

With the incidence matrix A, the Kirchhoff Current Law is written as $AI = 0$, where I is a vector of branch currents. What is more, the vector of nodal voltages ϕ is related to the vector of branch voltages U by $-A^\top \phi = U$.

In case of a superconducting accelerator circuit only linear capacitors, inductors, nonlinear resistors, and time-dependent voltage and current sources are considered. Thus, the incidence matrix A can be decomposed into a block form

$$A = [A_{\mathrm{C}}|A_{\mathrm{R}}|A_{\mathrm{L}}|A_{\mathrm{U}}|A_{\mathrm{I}}], \tag{2.135}$$

where A_{C} is the capacitance incidence matrix, A_{R} is the resistance incidence matrix, A_{L} is the inductance incidence matrix, A_{U} is the voltage source incidence matrix, and A_{I} is the current source incidence matrix. Based on these matrices, a so-called charge/flux oriented formulation

of the MNA [36] is expressed as

$$A_{\mathrm{C}}\partial_t Q + A_{\mathrm{L}} I_{\mathrm{L}} + A_{\mathrm{R}} G(t) A_{\mathrm{R}}^\top \phi + A_{\mathrm{U}} I_{\mathrm{U}} + A_{\mathrm{I}} I_{\mathrm{s}}(t) = 0, \tag{2.136a}$$

$$\partial_t \Psi - A_{\mathrm{L}}^\top \phi = 0, \tag{2.136b}$$

$$A_{\mathrm{U}}^\top \phi = U_{\mathrm{U}}(t), \tag{2.136c}$$

$$R\partial_t I_{\mathrm{R}} - A_{\mathrm{R}}^\top \phi = 0 \tag{2.136d}$$

where C, L, and G denote capacitance, inductance, and conductance matrices, respectively. We also introduce resistance R that in case of a quench is equal to zero (the conductance of a superconductor is infinite). The unknowns of the system are the vector of charges Q and fluxes Ψ, node potentials ϕ, and currents through the inductors I_{L}, voltage sources I_{U}, and resistors I_{R}. In order to obtain a unique solution, a grounding node is selected and an additional equation for the voltage sources' unknown current in terms of the applied voltage drop is added.

2.7.2 Port-Based Model

Energy of an electrical circuit is stored in the electric field of capacitors and the magnetic field of inductors whereas resistors dissipate the energy. The power is supplied by means of current and voltage sources. The energy stored in a linear electrical circuit is expressed as

$$\mathcal{H}(Q, \Psi) = \frac{1}{2} C^{-1} Q^2 + \frac{1}{2} L^{-1} \Psi^2. \tag{2.137}$$

These lumped elements are governed by constitutive relations relating voltage across the component with the current flowing through it [37]. We recall that in case of an electrical circuit the flow and effort variables are associated with the currents and voltages, respectively. For a capacitor with charge Q, the current is given as $\dot{Q} = I_{\mathrm{C}}$, and the constitutive relation reads

$$U_{\mathrm{C}} = \partial_Q \mathcal{H}(Q). \tag{2.138}$$

In case of an inductor with a flux linkage Ψ, the induced voltage is the time derivative of Ψ, i.e., $\dot{\Psi} = U_{\mathrm{L}}$, and the constitutive equation is given as

$$I_{\mathrm{L}} = \partial_\Psi \mathcal{H}(\Psi). \tag{2.139}$$

The dissipative relation of a resistor $R = G^{-1}$ is represented as

$$U_{\mathrm{R}} = R I_{\mathrm{R}} \quad \text{or} \quad I_R = G U_R \quad \text{with} \quad U_{\mathrm{R}} I_{\mathrm{R}} \geq 0. \tag{2.140}$$

In the remainder of the Section we will construct a Kirchoff-Dirac structure representing the MNA. To this end, we adopt a convention with a superscript denoting the order of a complex. Let f^1 and e^1 be, respectively, the current flowing through, and the voltage across all branches of the circuit. Furthermore, $f^0 = \partial_t q^0$ is the time variation of the nodal charge, and e^0 is the nodal potential (w.r.t. the ground). Then, in the context of algebraic topology [38, Chapter 12] we note that $f^1 \in \mathcal{C}_1$ are 1-chains, $e^1 \in \mathcal{C}^1$ are 1-cochains, $f^0 \in \mathcal{C}_0$ are 0-chains, and $e^0 \in \mathcal{C}^0$ are 0-cochains. The boundary operator ∂ (represented in MNA as the incidence matrix A) is defined as a linear map

$$\partial : \mathcal{C}_1 \to \mathcal{C}_0. \tag{2.141}$$

Then, f^1 is characterized by

$$f^1 \in \ker \partial, \tag{2.142}$$

so that $\partial f^1 = 0$, as defined by the Kirchhoff Current Law. The kernel of the boundary operator is the cycle space $\mathcal{Z}_1 = \ker \partial \subset \mathcal{C}_1$, i.e., $\mathcal{Z}_1$ is the subspace of the 1-chains in the kernel of the boundary operator. The coboundary operator is an adjoint transformation to ∂ acting on the space of 0-cochains

$$\mathrm{d} : \mathcal{C}^0 \to \mathcal{C}^1. \tag{2.143}$$

The vector space of voltage 1-cochains is expressed as

$$e^1 \in \operatorname{im} \mathrm{d} \tag{2.144}$$

and $e^1 = -\mathrm{d}e^0$, which satisfies the Kirchhoff Voltage Law. The image of the coboundary operator is the coboundary space $\mathcal{B}^1 = \operatorname{im} \mathrm{d} \subset \mathcal{C}^1$. The vector spaces of the 1-cycles and 1-coboundaries form an implicit Kirchhoff-Dirac structure

$$\mathcal{K} : \left\{ (f^1, e^1) = \left(\bigtimes_\lambda f^1_\lambda, \bigtimes_\lambda e^1_\lambda \right) \in \mathcal{Z}_1 \times \mathcal{B}^1 \right\}, \tag{2.145}$$

with $\mathcal{C}_1 = \bigtimes_\lambda \mathcal{C}^\lambda_1$ and $\mathcal{C}^1 = \bigtimes_\lambda \mathcal{C}^1_\lambda$, where $\bigtimes_\lambda$ is the Cartesian product of the respective vector spaces over each branch element type λ, for $\lambda = \{R, L, C, e, f\}$. It can be shown, following the Tellegen theorem, that the Kirchhoff-Dirac structure is power-continuous

$$e^1(f^1) = -\mathrm{d}e^0(f^1) = -e^0(\partial f^1) = 0. \tag{2.146}$$

From (2.146) we note, that the branch current is dual to the branch voltage. In other words, the coboundary space $\mathcal{B}^1$ is the anihilator space for the cycle space $\mathcal{Z}_1$. The Kirchhoff-Dirac structure (2.145) representing MNA is depicted in Fig. 2.41.

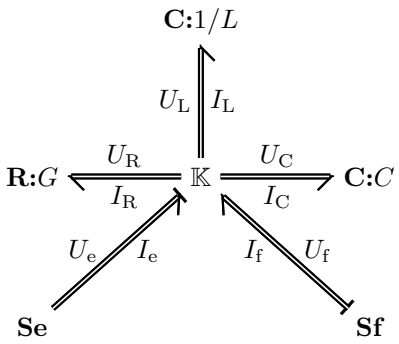

Figure 2.41: Bond graph representing energy flow in an electric circuit.

At this moment, the implicit Kirchhoff-Dirac structure is defined. However, in order to obtain a more practical representation we will introduce an explicit Kirchhoff-Dirac structure defined on a subset of branches of type λ. As a result, the explicit Kirchhoff-Dirac structure will be represented in terms of the MNA. In order to provide an explicit basis of the spaces $\mathcal{Z}_1$ and $\mathcal{B}^1$, we introduce dedicated boundary ∂^λ and coboundary d^λ operators for each branch type. In the matrix notation of the MNA, the boundary operator is expressed as the incidence matrix A_λ, such that the coboundary operator is given as the transpose $A^\top_\lambda$. It shall be noted that the coboundary operator d^λ acts as a surjection, i.e., the coboundary operator maps from the vector space of 0-cochains to the vector subspace of 1-coboundaries composed of a given type of the branch elements

$$\mathrm{d}^\lambda : \mathcal{C}^0 \to \mathcal{B}^1_\lambda \subset C^1_\lambda. \tag{2.147}$$

Furthermore, the boundary operator ∂^λ is an injective map of the space of branch type λ 1-chains to the 0 boundary chains

$$\partial^\lambda : \mathcal{C}^\lambda_1 \to \mathcal{B}_0. \tag{2.148}$$

To complete the overview of operators and spaces needed for the network modelling, we note that $\operatorname{im} \mathrm{d}^\lambda = \mathcal{B}^1_\lambda$ and $\operatorname{im} \partial^\lambda = \mathcal{B}^\lambda_0 \subset \mathcal{B}_0 \subset \mathcal{C}_0$. Considering branch types λ, the relations between 0-, 1-chains and cochains are given as an explicit Kirchhoff-Dirac structure defined on a subset of branches of type λ.

$$\mathcal{K}_\lambda : \left\{ (f^1_\lambda, f^0_\lambda, e^1_\lambda, e^0_\lambda) \in \mathcal{C}^\lambda_1 \times \mathcal{B}_0 \times \mathcal{B}^1_\lambda \times C^0 | f^0_\lambda = \partial^\lambda f^1_\lambda, e^1_\lambda = -\mathrm{d}^\lambda e^0_\lambda \right\}, \tag{2.149}$$

which is represented in a matrix form as

$$\begin{bmatrix} f_\lambda^0 \\ e_\lambda^1 \end{bmatrix} = \begin{bmatrix} 0 & \partial^\lambda \\ -\mathrm{d}^\lambda & 0 \end{bmatrix} \begin{bmatrix} e_\lambda^0 \\ f_\lambda^1 \end{bmatrix}. \tag{2.150}$$

Note that $\partial^\lambda f_\lambda^1$ is different from 0 only on branches incident with type λ branches and 0 everywhere else. This implies that the power-continuity of $\mathscr{K}_\lambda$ is fulfilled.

The explicit type-λ Kirchhoff-Dirac structures are related together via a 0-junction in order to get a bond graph which defines all nodal potentials and branch currents of the entire network.

$$\mathscr{D}_1 = \left\{ \begin{array}{l} (f_1, f_2, f_3, f_4, f_5, e_1, e_2, e_3, e_4, e_5) \in \mathscr{F} \times \mathscr{E} : \\ \begin{bmatrix} f_1 \\ e_2 \\ e_3 \\ e_4 \\ e_5 \end{bmatrix} = \begin{bmatrix} 0 & -1 & -1 & -1 & -1 \\ 1 & 0 & 0 & 0 & 0 \\ 1 & 0 & 0 & 0 & 0 \\ 1 & 0 & 0 & 0 & 0 \\ 1 & 0 & 0 & 0 & 0 \end{bmatrix} \begin{bmatrix} e_1 \\ f_2 \\ f_3 \\ -f_4 \\ -f_5 \end{bmatrix} \end{array} \right\} \tag{2.151}$$

with $(f_1, f_2, f_3, f_4, f_5, e_1, e_2, e_3, e_4, e_5) = (\partial_t q_\mathrm{R}, \partial_t q_\mathrm{L}, \partial_t q_\mathrm{C}, \partial_t q_\mathrm{f}, \partial_t q_\mathrm{e}, \phi, \phi, \phi, \phi, \phi)$. The spaces of flow and effort are given as $\mathscr{F} = C_0$ and $\mathscr{E} = C^0$, respectively. Based on the definitions of the power-continuous Kirchhoff-Dirac structure (2.149-2.150) and 0-junction (2.151), a bond graph is constructed as depicted in Fig. 2.42.

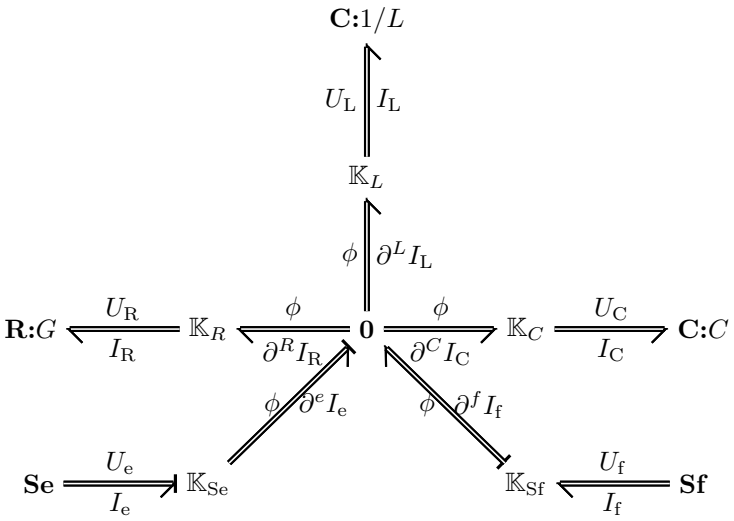

Figure 2.42: Multi-bond graph representing energy flow in an electrical circuit.

It is noteworthy that an alternative way of deriving an explicit formulation of the Kirchhoff-Dirac structure is given in [39] in terms of bases of homology- and cohomology of the network, i.e., loop currents and cut-set voltages.

In Fig. 2.42 only fixed computational causalities are depicted, i.e. the causalities of sources of flow and effort. For storage and resistive elements it is not possible to assign causality for an entire multibond as it depends on the circuit topology. For multiport bond graphs in general it is not always possible to assign a homogeneous causality and provides some choice as it might not hold for all the elements in the bond. For example, for a multiport C-type storage and a given circuit topology, some C-type elements can have preferred (integral) causality, while others can have non-preferred (derivative) causality. The Kirchhoff-Dirac structure can be interpreted as a 0-junction given by equation (2.136a). In this case each row of the respective incidence matrix has its own causality assignment. Thus, for a given circuit topology, some rows have the preferred causality assignment, while for others there could be a causality conflict. A discussion on causality in multiport bond graphs is presented in [24].

2.8 Control of Port-Hamiltonian Systems

The port-Hamiltonian framework originated from the need to control lumped and distributed multi-physical systems. At an abstract level, a port-Hamiltonian system is represented by the geometric structure with ports representing storage, dissipation, interconnection with other systems and control. For the control port, there are several relevant approaches studied in the literature. The input-state-output port-Hamiltonian systems (2.77) are well suited for the control purposes. In fact, the structure resembles a control theory's State-Space Representation of dynamical systems. Additionally, the input-state-output representation provides a direct access to conjugate input-output pairs of control, dissipative, and interaction ports. An overview of various control techniques applied to the port-Hamiltonian systems is reported in Chapters 5 and 6 of [20].

There are several strategies to the control of finite-dimensional port-Hamiltonian systems. Firstly, since a port-Hamiltonian system is based on the energy function, the impedance control, for which energy transfer from the controller to the plant is considered, is a suitable strategy [40]. The control laws for port-Hamiltonian systems reflect the geometrical structure of the port-Hamiltonian systems. In particular, a controller can also be represented as a port-Hamiltonian system in the framework of control by interconnection. This gives a benefit of the resulting system being a port-Hamiltonian system and by the virtue of the interconnection of Dirac structures, the sum of the Hamiltonian functions and dissipative elements still maintain the power-continuity property. One of the goals of a port-Hamiltonian-based control algorithm is to shape the energy function of a given system. As a result one can establish a desired equilibrium point as well as the trajectory of a system towards that point. An example of this control technique is the passivity-based control which introduces a feedback action such that the energy function of the system reaches its minimum at the desired equilibrium point.

For infinite-dimensional system similar control techniques are being studied [41]. However, the infinite-dimensional setup is more complex as compared to the finite-dimensional one since the system is characterized by partial-differential equations. In fact, the control of distributed parameter systems is an active research field focusing among others on the stability criteria. The Lyapunov theory of stability indicates that the energy function is a good candidate for a stability function [20]. Thus, an infinite-dimensional port-Hamiltonian system appears to be a suitable representation of a system for stability analysis.

In the treatise we are considering an implicit control of the port-Hamiltonian system through a power converter of an electrical circuit. A superconducting circuit is powered by a controlled-voltage source which is responsible for shaping the current evolution according to the desired profile. Typically, proportional-integral-differential (PID) controllers are considered in practice. The governing equation of a continuous PID controller is given as

$$U_{\mathrm{con}}(t) = k_{\mathrm{p}} E(t) + k_{\mathrm{i}} \int_0^t E(\tau) d\tau + k_{\mathrm{d}} \partial_t E(t), \tag{2.152}$$

with $E(t) = Y_{\mathrm{ref}}(t) - Y_{\mathrm{meas}}(t)$ being the error given as a difference between the reference profile Y_{ref} and its actual, measured waveform Y_{meas}. The parameters of the controller k_{p}, k_{i}, and k_{d} are the proportional, integral, and differential gains, respectively.

Chapter 3

Algorithms for Cooperative Simulations

A consistent analysis of electro-thermal transient effects occurring in superconducting magnets, such as quench initiation, propagation, and protection as well as their interaction with the powering control systems poses several challenges in terms of consistency and computational performance.

In the previous chapter, three domains were characterized, namely the distributed field model along with the lumped electrical and controller models. The field model comprises coupled magnetoquasistatic and thermodynamic systems. In addition, the mechanical response due to electrodynamic forces and temperature differences is relevant for the analysis of the magnet behavior. These distributed multi-physical systems are governed by nonlinear equations with highly nonlinear material properties. Furthermore, the transient effects span over a wide range of temporal and spatial scales.

Monolithic simulation of multi-domain, multi-physics, multi-scale, and multi-rate behavior of superconducting circuits requires unacceptable computational times and demands considerable computational resources. In order to avoid this scenario we follow an approach based on the concept of cooperative simulations (co-simulations for short). The STEAM co-simulation framework is capable of tackling these challenges. The main contribution of this work is the design of the architecture, algorithms, and data structures required to perform co-simulations. The foundation of the proposed co-simulation framework is a set of dedicated models implemented with appropriate proprietary solvers, namely, network models for electrical circuits and control algorithms as well as FEM models for 1D and 2D field problems. These solvers are optimized towards accurately solving particular problems while minimizing the computation cost. Once such a heterogeneous domain decomposition is performed, the next step is to introduce dedicated co-simulation algorithms in order to restore the coupling between the models given by the governing equations of the coupled problem. The co-simulation framework provides several features: (i) an inheritance structure to accommodate each simulation tool; (ii) algorithms implementing four co-simulation schemes; (iii) data structures and algorithms for signal exchange.

The Model-Based System Engineering (MBSE) approach is followed in the development of the framework [42]. This approach introduces a set of characteristics of high-fidelity models (obtained by means of thorough validation and verification) such as modularity, consistency, and availability of interfaces. Furthermore, MBSE provides a syntax and a set of diagrams based on the SySML language in order to represent system architecture along with relevant relationships between main components (see Section 3.2).

The remainder of this chapter is organized as follows. First, we recall four well-established algorithms for cooperative simulations and discuss their properties. Then, we present the STEAM architecture allowing to integrate these algorithms into a general purpose co-simulation framework. Finally, we present several relevant applications of the co-simulation framework to simulation of transient effects in accelerator magnets. These applications are aimed at illustrating

the features of the framework and properties of the coupling schemes.

3.1 Algorithms

In this Section we will discuss four algorithms dedicated to the coupling of numerical models. In particular, we will focus on: one-way coupling, weak coupling, strong coupling, and waveform relaxation. These algorithms can be grouped into non-iterative (one-way and weak coupling) and iterative (strong coupling and waveform relaxation) algorithms. In general, the co-simulation algorithms can be applied to any type of coupled models. Particularly, these algorithms apply to both, distributed and lumped-element models. Nonetheless, other types of models can be considered e.g., physical models coupled with numerical ones following HIL (Hardware In the Loop) approach. The choice of a particular algorithm depends on the nature of a considered coupled problem and the desired accuracy.

To illustrate these co-simulation schemes let us consider an arbitrary coupled system composed of two subsystems, namely S_1 and S_2. Without loss of generality, we assume that the subsystems are coupled through the state variables. We can represent the coupled system as, in general, a nonlinear state equation with algebraic constraints

$$\begin{aligned} \begin{bmatrix} \partial_t x_1 \\ \partial_t x_2 \end{bmatrix} &= \begin{bmatrix} A_{11}(x_1, x_2) & A_{12}(x_1, x_2) \\ A_{21}(x_1, x_2) & A_{22}(x_1, x_2) \end{bmatrix} \begin{bmatrix} x_1 \\ x_2 \end{bmatrix} + gu \\ \begin{bmatrix} 0 \\ 0 \end{bmatrix} &= \begin{bmatrix} B_{11}(x_1, x_2) & B_{12}(x_1, x_2) \\ B_{21}(x_1, x_2) & B_{22}(x_1, x_2) \end{bmatrix} \begin{bmatrix} x_1 \\ x_2 \end{bmatrix} + du \end{aligned} \tag{3.1}$$

where $A_{11}(x_1, x_2)$ and $A_{22}(x_1, x_2)$, respectively, characterize the dynamics of subsystems S_1 and S_2 considered independently. Off-diagonal entries $A_{12}(x_1, x_2)$ and $A_{21}(x_1, x_2)$ represent the coupling between both subsystems. Matrix g is the input matrix, and u is the input vector. Similarly, constraints of subsystems S_1 and S_2 are denoted, respectively, by $B_{11}(x_1, x_2)$ and $B_{22}(x_1, x_2)$. Cross-coupling is given by matrices $B_{12}(x_1, x_2)$ and $B_{21}(x_1, x_2)$; d is the input matrix. We note that, with an appropriate selection of variables, coupled problem (3.1) can be reformulated in terms of explicit port-Hamiltonian systems with constraints [20].

For the purpose of presenting co-simulation schemes in the following, we reformulate (3.1) as an abstract differential-algebraic initial value problem. For the sake of simplicity we neglect the input port u. The first subsystem, S_1, is given as

$$\begin{cases} F_1(x_1, \partial_t x_1, x_2, \partial_t x_2) = 0 \\ G_1(x_1, x_2) = 0 \end{cases}, \tag{3.2}$$

with the initial value $x_1(T_0) = x_{1,0}$, the unknown $x_1(t)$, and $x_2(t)$ the solution of the other subsystem. By analogy, the second subsystem, S_2, reads

$$\begin{cases} F_2(x_2, \partial_t x_2, x_1, \partial_t x_1) = 0 \\ G_2(x_2, x_1) = 0 \end{cases}, \tag{3.3}$$

where $x_2(T_0) = x_{2,0}$ is the initial value, $x_2(t)$ and $x_1(t)$ are the unknown and the solution of the other subsystem, respectively.

Co-simulation assumes that coupled subsystems exchange signals at discrete communication points and in between are solved independently with appropriate time-stepping schemes. Depending on the nature of a coupled problem, the communication should take place less or more frequently. Hence, let the overall simulation time $\mathcal{I} = \begin{bmatrix} T_0 & T_N \end{bmatrix} \subset \mathbb{R}$ be divided into N time windows $\mathcal{I}_j = (T_j, T_{j+1}]$ with $j = 0, ..., N-1$. In the remainder of this chapter we adopt the following convention in order to denote state variables, initial conditions, and indices for which state variables are exchanged. Single subscript represents an index of a state variable (e.g., x_1). The index followed by a comma and 0 denotes the subsystem's initial condition (e.g., $x_{1,0}$). An initial condition for a given time window j is given by a triplet of the subsystem index, j, and 0 separated by commas (e.g., $x_{1,j,0}$). Note that with this notation, $x_{1,0,0} = x_{1,0}$. The index that

follows by a comma the one denoting the subsystem in the case of a time-dependent state variable, denotes the time window for which the variable is obtained (e.g. $x_{1,j}(t) = x_1(t), t \in \mathcal{I}_j$). A superscript k for a state variable denotes an iteration index of the co-simulation algorithm for which the state variable is evaluated at a time window j (e.g., $x^k_{1,j}(t)$). As we will see in the coming sections, for signal exchange, variables can be provided either as a waveform evaluated at certain iteration k (e.g., $x^k_{1,j}(t)$) or as a data point obtained at communication point j (e.g., $x_{1,j}(T_j) = x_{1,j,0}$).

3.1.1 One-Way Coupling

One-way coupling (also referred to as parameter extraction) scheme assumes a unidirectional flow of signals between coupled models [43]. In other words the output of a model becomes an input to another as shown in Fig. 3.1. The scheme does not incorporate the feedback of the latter subsystem on the former one. The exchanged signal can be either a final state or a waveform of a coupled variable evaluated at communication points T_j.

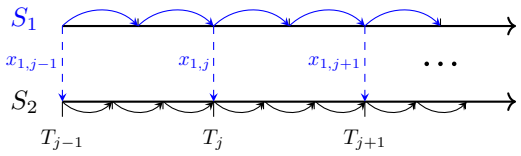

Figure 3.1: Schematic representation of a one-way coupling scheme.

This scheme is suited to couple subsystems, for which the input of one subsystem is known and/or has negligible influence on the second subsystem for a given simulation scenario. Considering a scalar variable transfered from S_1 to S_2 and obtained at each communication point T_j, the one-way coupling algorithm is taking steps outlined in Alg. 1.

Algorithm 1 One-way coupling

1: assume initial values $x_{1,0}$, $x_{2,0}$ to be known
2: assume input of S_1 from S_2 $\hat{x}_2(t)$ to be known for $t \in \mathcal{I}$
3: **for** $j = 0, 1, ..., N-1$ **do**
4: solve (3.2) for $x_{1,j}(t)$ on $\mathcal{I}_j$ with initial value $x_{1,j,0}$ and known input $\hat{x}_{2,j}(T_j)$
5: solve (3.3) on $\mathcal{I}_j$ with initial value $x_{2,j,0}$ and extrapolated input $\hat{x}_{1,j}(T_j)$
6: set final state of S_1 as initial value $x_{1,j+1,0} = x_{1,j}(T_{j+1})$
7: set final state of S_2 as initial value $x_{2,j+1,0} = x_{2,j}(T_{j+1})$

This algorithm can also be used to transfer distributed parameters from one distributed subsystem to another. However, in this case, a dedicated mesh-based interpolation algorithm has to be put in place in order to account for possible differences in mesh definitions between the coupled subsystems. Section 3.3.4 is devoted to one-way coupling of distributed magneto-thermal and mechanical models employing mesh-based interpolation.

An extreme case of the one-way coupling is a sequential execution of two models for which one model is solved first and provides an input to another one. In other words there is only single transfer of signals, i.e., $N = 1$. An exemplary application is the calculation of the magnetic field maps with a dedicated FEM software as an input to quench simulation codes based on equivalent electro-thermal network modeling [44], [45]. In the presence of a nonlinear iron yoke, this approach is only valid in a certain vicinity of the operating point. However, it serves as a good approximation for a quick exploration of the parameter space.

3.1.2 Weak Coupling

Provided that the reciprocal influence of coupled subsystems can not be neglected, weak coupling is a suitable extension of the one-way coupling scheme [43]. With this scheme, a bidirectional exchange of signals between coupled systems is considered. Since for a given communication point, the exchange is performed only once, there is no feedback mechanism in place to control the convergence of the scheme. In other words, without additional safeguards the algorithm can successfully exchange the signals for the overall simulation time $\mathcal{I}$ and lead to inconsistent results. An adaptive time-window algorithm, in analogy to adaptive integration schemes, could check convergence and ensure an optimal window size minimizing the error due to the coupling. Therefore, depending on the coupling strength between the models, the communication intervals have to be adaptively adjusted [17]. Whether or not the scheme converges for a given partition of $\mathcal{I}$ into time windows also depends on the extrapolation of input signals for the interval between communication points while subsystems are solved independently and the evolution of input signals is unknown [46].

Co-simulation with the weak coupling scheme provides a choice on the execution mode, i.e., the subsystems can be solved either sequentially or in parallel (see Fig. 3.2). In the former case, one subsystem is provided with a solution from the previous communication point T_j and the other one with a solution calculated in the current communication point T_{j+1}, whereas in the latter case both models are provided with results from the previous communication point T_j. The first method, called Gauss-Seidel scheme may still converge to a consistent solution for larger time windows compared to the other scheme [43] as one model receives an updated input. The second method, called Jacobi scheme provides faster execution of time windows as coupled subsystems can be executed simultaneously.

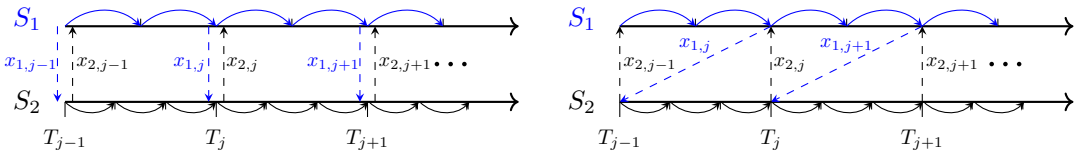

Figure 3.2: Schematic representation of a weak coupling algorithm with Jacobi (left) and Gauss-Seidel (right) schemes.

Provided that scalar values are exchanged at communication times T_j, the weak coupling algorithm takes steps given in Alg. 2.

Algorithm 2 Weak coupling

1: assume initial values $x_{1,0}$, $x_{2,0}$ to be known
2: (for the Gauss-Seidel scheme only $x_{2,0}$ has to be known)
3: **for** $j = 0, 1, ..., N-1$ **do**
4: set $\hat{x}_{2,j}(t)$ constant extrapolation of $x_{2,j,0}$ for $t \in \mathcal{I}_j$
5: solve (3.2) for $x_{1,j}(t)$ on $\mathcal{I}_j$ with initial value $x_{1,j,0}$ and input $\hat{x}_{2,j}(t)$
6: set $\hat{x}_{1,j}(t)$ constant extrapolation of $x_{1,j,0}$ (Jacobi) or $x_{1,j+1,0}$ (Gauss-Seidel) for $t \in \mathcal{I}_j$
7: solve (3.3) for $x_{2,j}(t)$ on $\mathcal{I}_j$ with initial value $x_{2,j,0}$ and input $\hat{x}_{1,j}(t)$
8: set final state of S_1 as initial value $x_{1,j+1,0} = x_{1,j}(T_{j+1})$
9: set final state of S_2 as initial value $x_{2,j+1,0} = x_{2,j}(T_{j+1})$

Subsystems coupled through the weak coupling algorithm are solved with individual time stepping regimes. Thus, the weak coupling scheme is suited to the coupling of subsystems with dynamics characterized by different time scales.

Weak coupling is often used for the co-simulation of multi-body system dynamics. A detailed discussion on the subject matter is provided in [47]. For distributed systems, similarly as for the one-way coupling scheme, mesh-based interpolation has to be considered.

3.1.3 Strong Coupling

In case subsystems are tightly coupled, i.e., there is a strong mutual dependence of one subsystem on the other, instead of using weak coupling one should consider an application of the strong coupling scheme. In the strong coupling information is exchanged iteratively between subsystems at each time step until convergence up to a certain tolerance is reached as depicted in Fig. 3.3.

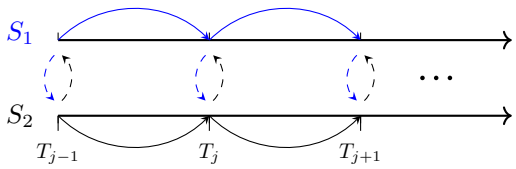

Figure 3.3: Strong coupling iteration of subsystems at discrete intervals.

Subsystems in the strong coupling scheme are solved in a segregated manner (Gauss-Seidel type) until convergence up to a certain tolerance is reached. For that reason we introduce a convergence indicator c_m which is evaluated for each subsystem S_m and is based on three assertions: (i) calculation of either absolute absTol

$$c_{m,1}(k) = \left(||x_m^k(T_j) - x_m^{k-1}(T_j)|| < \text{absTol} \right), \tag{3.4}$$

where $||\cdot||$ is an appropriate norm;
(ii) or relative relTol tolerance

$$c_{m,2}(k) = \left(\frac{||x_m^k(T_j) - x_m^{k-1}(T_j)||}{||x_m^k(T_j)||} < \text{relTol} \right); \tag{3.5}$$

(iii) attainment of maximum number of iterations

$$c_{m,3}(k) = \begin{cases} \text{true} & \text{if } k = k_{\max} \\ \text{false} & \text{otherwise.} \end{cases} \tag{3.6}$$

Convergence indicators (3.4) and (3.5) are evaluated for a given data point obtained from two consecutive iterations (k) and $(k-1)$ for $k \geq 1$ (for $k = 0$ the indicators return false) at a communication point T_j. Eventually, the convergence indicator is true if at least one condition is satisfied, i.e.,

$$c_m(k) = c_{m,1}(k) \vee c_{m,2}(k) \vee c_{m,3}(k). \tag{3.7}$$

The algorithm is represented as a sequence of steps as outlined in Alg. 3.

Algorithm 3 Strong Coupling

1: assume initial values $x_{1,0}$, $x_{2,0}$ to be known
2: assume input of S_1 from S_2, i.e., $x_{2,j}^0(t)$ to be known for $t \in \mathcal{I}_j$, $j = 0$
3: **for** $j = 0, 1, ..., N-1$ **do**
4: set $k = 0$
5: set $\hat{x}_{2,j}(t)$ constant extrapolation of $x_{2,j,0}$ for $t \in \mathcal{I}_j$
6: **while** $\exists m \in \{1, 2\} : c_m(k) = \text{false}$ **do**
7: solve (3.2) for $x_{1,j}^{k+1}(T_{j+1})$ with initial value $x_{1,j,0}$ and input $x_{2,j}^k(t)$ for $t \in \mathcal{I}_j$
8: solve (3.3) for $x_{2,j}^{k+1}(T_{j+1})$ with initial value $x_{2,j,0}$ and input $x_{1,j}^{k+1}(t)$ for $t \in \mathcal{I}_j$
9: set $k = k + 1$
10: set final state of S_1 as initial value $x_{1,j+1,0} = x_{1,j}^k(T_{j+1})$
11: set final state of S_2 as initial value $x_{2,j+1,0} = x_{2,j}^k(T_{j+1})$

Segregated solution of a coupled problem results in smaller dimensions of matrices being solved for each subsystem as compared to the set of equations for a monolithic approach. This coupling scheme is suited for both, distributed and lumped element models. Due to strong reciprocal influence of distributed electromagnetic and thermal subsystems representing a superconducting magnet, they are usually solved either as a monolithic or as a strongly coupled problem with commercial and in-house multi-physics software, among others, respectively [48], and [44], [45].

3.1.4 Waveform Relaxation

In case of a coupled problem which exchanges scalar variables between subsystems, a reasonable solution method is waveform relaxation (also called dynamic iteration) scheme. Both terms reveal the nature of the algorithm, i.e., it relies on an iterative exchange of scalar waveforms obtained for a given window until convergence is reached. With each iteration, the subsystems receive an update, which for a well-posed system leads to a solution satisfying tolerances of both subsystems. It is noteworthy that the updates take place only in discrete time instances and in between these points the coupled models are solved independently, each with an appropriate time stepping scheme. Unlike the weak coupling algorithm, the waveform relaxation method allows obtaining a converged solution up to a desired accuracy. In fact, the termination criterion for the iterations in time window $\mathcal{I}_j$ can be determined by applying an appropriate norm to measure the difference of two subsequent waveforms calculated from either one or both of the models. As in the weak coupling algorithm, waveform relaxation can be executed with either a Jacobi or a Gauss-Seidel scheme as shown in Fig. 3.4. We note that the Gauss-Seidel scheme yields faster convergence for the waveform relaxation algorithm [43] while Jacobi has the advantage that both systems can be computed out in parallel.

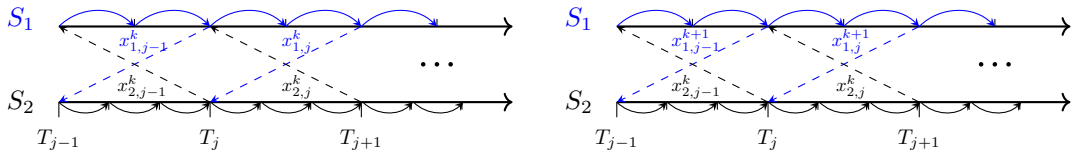

Figure 3.4: Schematic representation of a waveform relaxation algorithm with Jacobi (left) and Gauss-Seidel (right) schemes.

Similarly to the weak coupling algorithm, waveform relaxation is a reasonable choice to solve multi-rate coupled problems, i.e., problems composed of subsystems with distinct time constants, which would require distinct distributions of time steps per model representing given subsystem [16].

In order to terminate iterations of the waveform relaxation algorithm for a given time window, a convergence criterion is introduced. In analogy to the strong coupling algorithm, the convergence indicator c_m (3.7), where m is a counting index of subsystems, is evaluated for each subsystem S_m and is based on three assertions: (i) calculation of either absolute absTol (3.4); (ii) or relative relTol (3.5) tolerance for a given waveform obtained from two consecutive iterations (k) and $(k-1)$ for $k \geq 1$ with an appropriate norm $||\cdot||$ to measure the difference between these waveforms; (iii) attainment of maximum number of iterations in the same way as for the strong coupling scheme (3.6).

The waveform relaxation algorithm for two coupled systems exchanging scalar waveforms is summarized as shown in Alg. 4.

Algorithm 4 Waveform Relaxation

assume initial values $x_{1,0}$, $x_{2,0}$ to be known
for $j = 0, 1, ..., N-1$ **do**
    set $k = 0$
    set $x^0_{2,j}(t)$ constant extrapolation of $x_{2,j,0}$ for $t \in \mathcal{I}_j$
    for Jacobi Scheme set $x^0_{1,j}(t)$ constant extrapolation of $x_{1,j,0}$ for $t \in \mathcal{I}_j$
    while $\exists m \in \{1, 2\} : c_m(k) =$ false **do**
        solve (3.2) for $x^{k+1}_{1,j}(t)$, $t \in \mathcal{I}_j$ with initial value $x_{1,j,0}$ and input $x^k_{2,j}(t)$
        solve (3.3) for $x^{k+1}_{2,j}(t)$, $t \in \mathcal{I}_j$ with initial value $x_{2,j,0}$ and input $x^k_{1,j}(t)$ (Jacobi) or $x^{k+1}_{1,j}(t)$ (Gauss-Seidel)
        set $k = k + 1$
    set final state of S_1 as initial value $x_{1,j+1,0} = x^k_{1,j}(T_{j+1})$
    set final state of S_2 as initial value $x_{2,j+1,0} = x^k_{2,j}(T_{j+1})$

The waveform relaxation algorithm can be adopted to deal with exchange of distributed waveforms for distributed parameter systems. However, this setup can require considerable amounts of memory to handle the communication.

Waveform relaxation is particularly suited to solve field/circuit coupling problems. The field problem is usually represented with partial differential equations, while a circuit problem is modeled with a set of differential-algebraic equations. In this setup integral quantities of distributed variables, such as resistance, flux linkage, voltage, current, etc. are provided from the field solution, while the electric circuit provides either voltage or current [49]. A detailed description of the application of field/circuit coupling to the analysis of transient effects in superconducting magnets is presented in Section 3.3.3.

To conclude, we summarize the coupling schemes in Table 3.1 based on heuristics in using these algorithms. The reason for the use of heuristics is the lack of a formal definition of the coupling strength as a metric to discriminate between these algorithms. The coupling schemes are grouped depending on the coupling strength (strong or weak) and the signal type (lumped or distributed).

Table 3.1: Comparison of co-simulation algorithms.

Coupling Strength	Lumped (scalar/waveform)	Distributed
weak	one-way coupling weak coupling	one-way coupling weak coupling
strong	waveform relaxation	strong coupling

We note that these algorithms can be extended for the co-simulation of a coupled problem composed of an arbitrary number of subsystems. Furthermore, a combination of several coupling interfaces can be used to cover a co-simulation scenario.

3.2 Architecture

In this Section we present the architecture of the co-simulation framework STEAM. The architecture is composed of three layers. The bottom layer consists of numerical models solved with proprietary simulation tools. The middle layer provides a set of tool adapters capable of controlling the simulation tools and implicitly the models by means of tool-specific APIs (Application Programming Interface). The management of the co-simulation schemes, simulation time, convergence, and signal exchange is carried out by the top layer. The co-simulation framework architecture is represented in Fig. 3.5.

To describe the architecture let us consider a coupled problem composed of n_m models stored in an array $\mathscr{M}$, where $\mathscr{M}_m$ is the m-th model for $1 < m < n_\mathrm{m}$. A dedicated tool adapter is

assigned to each model m. The tool adapters are grouped in a tool adapter array $\mathscr{T}$ with n_{ta} being the length of $\mathscr{T}$. In general a co-simulation scenario can consist of several models solved with the same tool, however, there is a one to one relationship between models and tool adapters, i.e., $n_{\mathrm{m}} = n_{\mathrm{ta}}$.

With the proposed architecture, the tool adapters can form a co-simulation scenario employing one of the algorithms presented in the previous Section. Weak coupling and waveform relaxation schemes can incorporate either a Gauss-Seidel or a Jacobi method. For all the algorithms, we consider a fixed distribution of time windows.

The centralized main co-simulation algorithm orchestrates the co-simulation process and distributes instructions to each tool adapter independently. As a result there is a clear separation between the layers with a bidirectional flow of information through dedicated interfaces. The tool adapters are coupled only by means of a common signal exchange protocol.

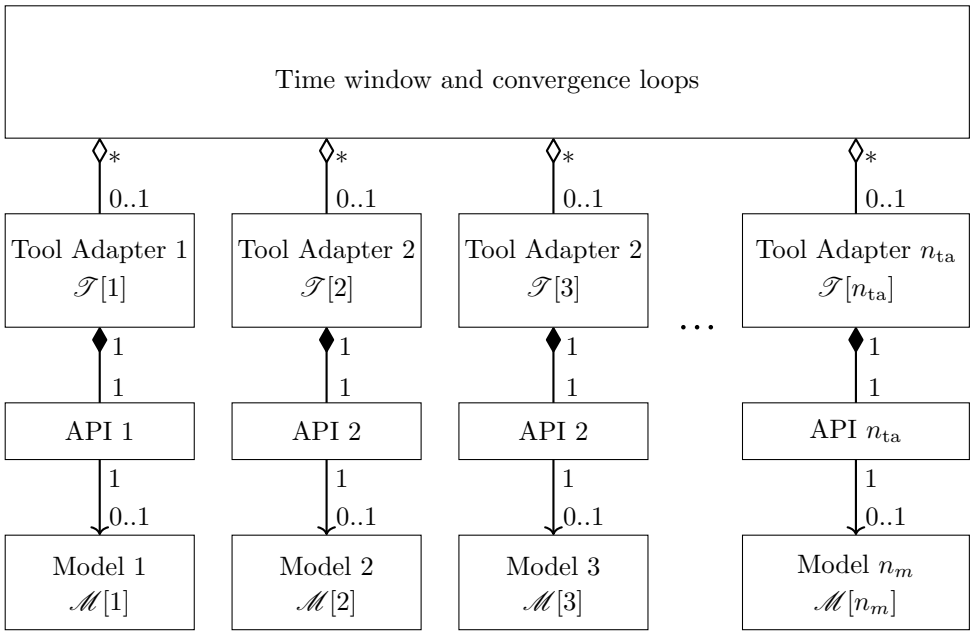

Figure 3.5: SysML structure diagram of the STEAM framework architecture with appropriate relationships between components and their cardinality.

The co-simulation framework is scalable and supports an arbitrary number of coupled tool adapters as long as sufficient computational resources and licenses are available. In addition, the tool adapters can be aligned with any execution order in the Gauss-Seidel case. The modularity and scalability has been achieved by means of inheritance outlined in the following.

3.2.1 Tool Adapters

For the implementation of the middle layer of the architecture we follow the object-oriented modeling (OOM) paradigm. The OOM conceptually resembles the port-based modeling approach based on encapsulating model dynamics and providing ports for the energy exchange. With the port-based approach, the coupled problem is represented by subsystems representing particular physical domains. The encapsulation of a physical domain dynamics simplifies the analysis of their behavior. The coupling between subsystems is obtained by means of port variables which can take lumped, distributed or boundary form. Similarly, following the OOM paradigm, the coupled problem is also subdivided into a set of models. Then, the models are represented by means of dedicated classes. These classes encapsulate the model properties which can be accessed and modified through a set of public methods. Furthermore, classes are equipped with methods to control execution of models and interfaces for data exchange with other objects

(instances of classes). With an appropriate selection of the signal exchange interface one can obtain equivalent representation of a port-based model.

Models participating in a co-simulation process are characterized by a set of shared properties and methods which form a tool adapter represented by a *ToolAdapter* abstract class. Among the properties there are an input/output signal port array and three arrays with elements corresponding to each time window with the following elements: (i) time window definitions (start and end time as well as the maximum time step for each solver); (ii) maximum number of iterations; (iii) values of relative and absolute tolerance. Additionally there is a label of a convergence signal for which tolerances are calculated.

The set of methods follows the sequence of operations needed to handle the simulation of a time window. Firstly, the simulation parameters are set and initial conditions are assigned. For the first iteration of the first time window, i.e., $j = 0$, $k = 0$, it might be necessary to execute a dedicated study in order to calculate appropriate initial conditions (e.g., magnetostatic study for a 2D field model). For the first iteration of the following time windows the initial conditions are restored as the final state of the last iteration from the previous time window. Secondly, the signals are exchanged (for detailed description see Section 3.2.3) and the inputs are written. Thirdly, the study is executed and output signals are retrieved. Finally, at the end of an iteration of a time window, for waveform relaxation and strong coupling, if iteration index $k \geq 1$ the convergence is checked.

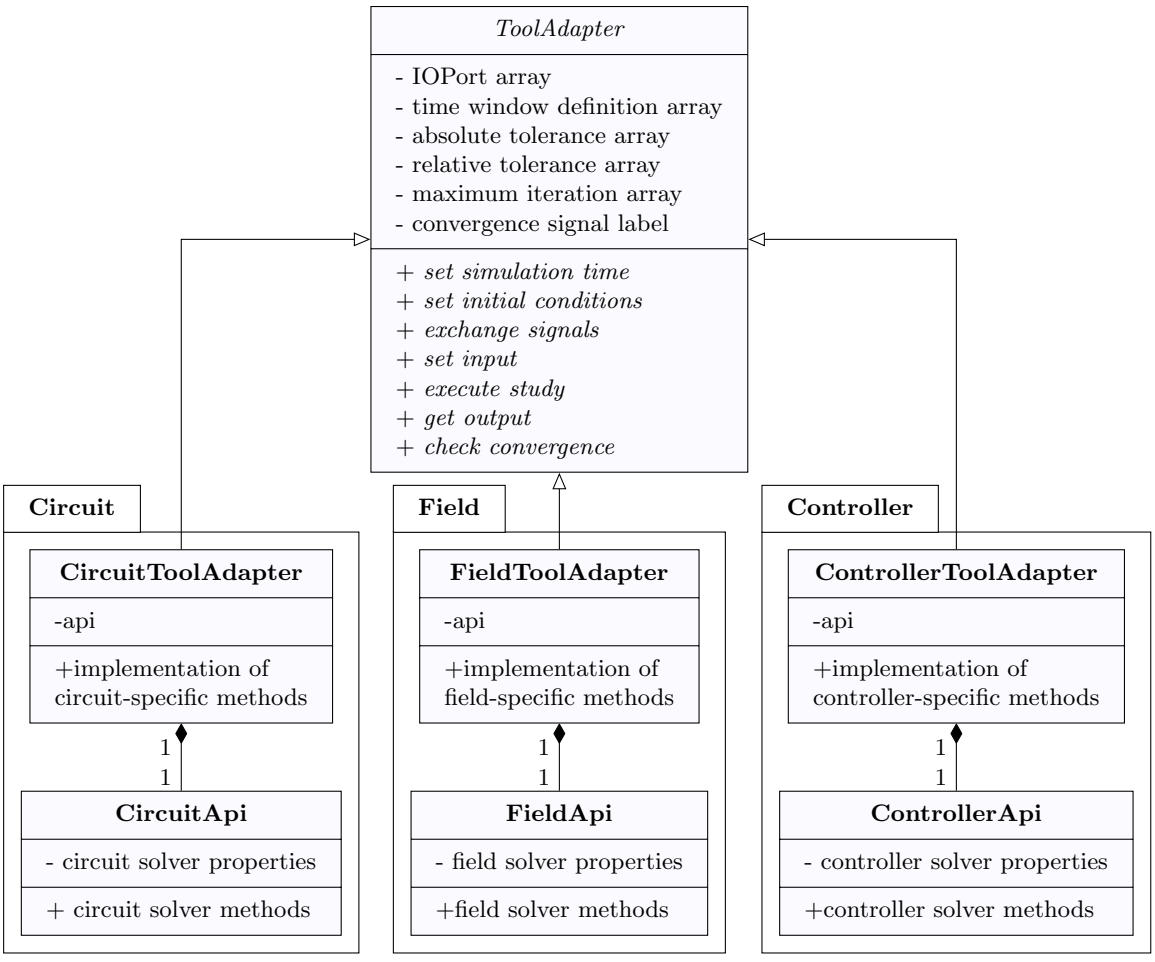

Figure 3.6: UML diagram of the inheritance structure for the tool adapters with exemplary implementations for Circuit, Field, and Controller classes.

In this Chapter we consider the co-simulation of superconducting circuits composed of circuit, field, and controller models. Insofar we introduce three classes, namely *CircuitToolAdapter*, *FieldToolAdapter*, and *ControllerToolAdapter*. As names indicate, these classes inherit from the *ToolAdapter* abstract class. Thus, each of them implements methods enforced by the superclass. Naturally, particular implementations may vary due to differences in corresponding APIs. The practical implementation in the STEAM co-simulation framework involves particular simulation tools for field, circuit, and controller models.

With this inheritance structure, the tool adapters can be conveniently assembled into an array to represent a given coupled problem. Since *a priori* the set of tool adapters is unknown, methods needed to control the co-simulation are executed for each tool adapter as described in the following.

3.2.2 Time Window and Convergence Loops

Since each tool adapter implements the same abstract class, they are stored in an array after the initialization process. As a consequence the framework is scalable w.r.t. the number of tool adapters used in the co-simulation and there is no predefined order of tools except the one indicated by a particular coupled problem. Thus, methods for time window execution are called for each tool adapter stored in the array $\mathscr{T}$ as given in Alg. 5.

The algorithm managing the time window, and convergence iterations is composed of several loops. The outermost for-each loop steps through time windows $\mathscr{I}_j \subset \mathscr{I}$. Execution of each time window starts with an initialization procedure. For each tool adapter a time window definition is provided and initial conditions are set. Afterwards, the tool adapters are executed in a loop until convergence is reached for each of them. For a convergence iteration tool adapters are called following their execution index $e = 1, 2, ..., n_{\mathscr{E}}$, where $n_{\mathscr{E}}$ is the maximum execution index. Tool adapters with the same index e are executed simultaneously. The execution of a tool adapter comprises several steps. First, the signals are exchanged, which is followed by setting of inputs into respective models. Second, simulations are executed, which may involve parallel processing in case of the Jacobi scheme. Lastly, the output is retrieved and stored for the post-processing. In order to achieve parallelization of the algorithm for a Jacobi-type co-simulation this operations are executed sequentially in a single for-each loop. Note that the execution order avoids race conditions, i.e., a situation when parallel execution of several processes may lead to mis-synchronization of communication due to the overwriting of shared resources; for a co-simulation the race condition might occur if an output signal is overwritten with a new value before being assigned to all inputs.

Algorithm 5 Main Time and Convergence Loops

```
1:  for each 𝒥_j ⊂ 𝒥 do
2:      for each 𝒯_m ∈ 𝒯 do
3:          set time window definition (start and end time, maximum time step)
4:          set initial conditions
5:      set k = 0
6:      set c_m(k) = false for m ∈ {1, ..., n_m}
7:      while ∃m ∈ {1, ..., n_m} : c_m(k) = false do
8:          for e = 1, 2, ..., n_ℰ do
9:              assign to 𝒯̂ a subset of tool adapters 𝒯 with execution index equal to e
10:             for each 𝒯̂_m ∈ 𝒯̂ do
11:                 exchange signals
12:                 set inputs
13:                 execute study
14:                 get outputs
15:                 check for convergence
16:         set k = k + 1
```

Now we focus on three relevant components of the algorithm: (i) execution order for selection of either a Jacobi or a Gauss-Seidel numerical schemes; (ii) convergence criteria which terminate the iterations of a time window; (iii) general purpose signal exchange algorithm which requires additional data structures to represent signals.

Execution Order

Execution order $\mathscr{E} = \{1, ..., n_{\mathscr{E}}\}$ as the name indicates, determines the order of execution for tool adapters in a given co-simulation scheme, i.e., $\dim \mathscr{E} = \dim \mathscr{M}$. The execution order is 1-based and the first index corresponds to a subset of tool adapters executed as the first ones. Several tool adapters can be assigned with the same execution index, i.e., $n_{\mathscr{E}} \leq n_{\mathscr{T}}$. In fact, $n_{\mathscr{E}}$ determines the maximum number of executions of tool adapters for a given iteration as the ones with the same execution index are parallelized.

The execution order determines whether a coupled problem will be solved according to a Jacobi (with all execution order indices equal to 1) or a Gauss-Seidel (with ascending order of indices from 1 to $n_{\mathscr{E}}$) scheme. The selected scheme indicates what signals should be extrapolated during the co-simulation process. With an appropriate assignment of the execution order it is also possible to obtain a mixed Jacobi/Gauss-Seidel scheme in a single co-simulation definition.

Convergence Criterion

Recall that the convergence loop is terminated if either convergence up to a certain tolerance is reached, or $k_{\max}$ is reached. This condition has to be satisfied for every element in an array of tool adapters $\mathscr{T}$

$$\forall \mathscr{T}_m \in \mathscr{T} : c_m(k) = \text{true}. \tag{3.8}$$

We note that the maximum number of iterations $k_{\max}$ equal to 1 results in selection of either the one-way or weak coupling algorithms (iteration index is 0-based). These two algorithms are discriminated through the definition of signal exchange (recall that weak coupling is based on bidirectional exchange); see next Section. These algorithms do not perform convergence check and, therefore, the convergence loop terminates after one iteration.

3.2.3 Signal Exchange

Signal exchange is at the heart of the co-simulation and each tool adapter participating in this process is equipped with an appropriate input/output interface. We propose a definition of data structures representing input and output signals along with an algorithm for signal exchange. With n_{I} and n_{O} being, respectively number of input and output signals, Fig. 3.7 presents data structures used to handle the exchange of coupled signals.

IOPort Array

Each tool adapter $\mathscr{T}_m$ contains an array of *IOPort* elements, the dimension of this array is equal to n_{P}. The port array is composed of a unique name and bundles of arrays for input and output signals as well as an array for definitions of bonds. Definition of either input or output signals are mandatory for a tool adapter to be coupled with other tool adapters. The list of bonds is optional and contains pairs of conjugate variables by matching inputs and outputs stored in an *IOPort* elements.

SignalBundle

A *SignalBundle* object is dedicated to store multiple time-series waveforms or data points with a single time vector, a unique name, and a signal type being either a waveform or a data point depending on the chosen co-simulation algorithm. Each waveform is characterized by a label which is used to interact with the model for setting input and retrieving output. Labels are introduced in order to follow the naming convention enforced by a particular tool which may

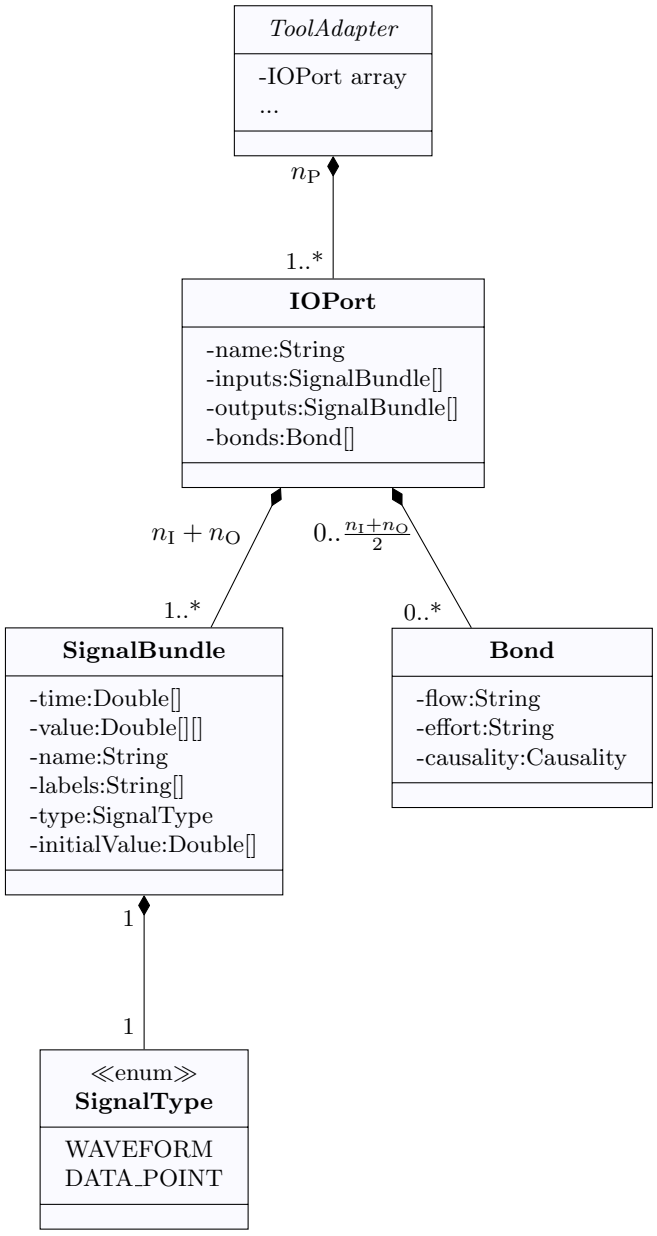

Figure 3.7: UML class diagram representing relationship between classes representing signals exchanged between the tools. Cardinality is also marked with appropriate multiplicity factors.

result in a conflict with the naming convention of another model. The name, however, allows to keep the same name of a coupled signal across different models. In this fashion, a *SignalBundle* contains a map from a generic name to a model-specific label. In addition, each signal can be provided with an initial value needed for the first iteration of the first time window.

Bond

Eventually, we introduce a *Bond* class, implementing a concept thoroughly discussed in the previous chapter, that allows to determine what input and output signals from the list of input and output signals form a pair of flow and effort variables for energy exchange. The causality is already determined by the choice of input and output signals. The bond definition is optional and provides an additional capability for the framework to calculate power exchanged between the coupled models. Nonetheless, the signals exchanged might not always form a pair of conjugate variables and calculation of the power exchanged between the subsystems of a coupled problem might not always be of interest.

Algorithm

The aforementioned data structures describe inputs and outputs of each tool adapter. Input and output signals are exchanged by means of a dedicated algorithm. The signal exchange algorithm is input-driven, i.e., the communication is determined only by input signals and is terminated if all inputs were successfully assigned (see Alg. 6). This algorithm is executed for each tool adapter $\mathcal{T}_m$ upon setting input and executing the corresponding model for a given time window (cf. Alg. 5). The algorithm iterates over all elements of the *IOPort* array. Next step is to loop over each input signal in the input signals array. For each input a tool adapter $\hat{m}$ with matching output signal is found. There is a two factor matching criterion: (i) *IOPort* elements of corresponding *IOPort* arrays have the same names; (ii) the coupling parameter name of the respective input is equal to the coupling parameter name of the output. Separation of the common port array name from the names of input and output signals facilitates grouping of signals related to a port array and reduces naming duplications in the signal definitions.

Once the output signal is retrieved, for the first iteration of each time window, extrapolation of output signal takes place and is based on the execution order. The output signals are extrapolated if the execution order of the receiving tool adapter is smaller than that of the providing tool adapter $e_m < e_{\hat{m}}$ (indicating Gauss-Seidel type co-simulation). If output signal type is DATA_POINT constant extrapolation is always performed in the current version of the STEAM co-simulation framework. Eventually, the output signal from $\hat{\jmath}$ is set as the input for $\jmath$.

Algorithm 6 Signal Exchange

1: **for each** *IOPort* in *IOPort* array of tool adapter m **do**
2: **for each** input signal in *IOPort* **do**
3: in tool adapter array $\mathcal{T}$ find a tool adapter $\hat{m}$ with matching *IOPort* name
4: in output signal array from found *IOPort* of $\hat{m}$ find a signal with matching signal name
5: get matching output signal from $\hat{m}$
6: **if** ($k = 1$ and $e_m < e_{\hat{m}}$) or output signal type is DATA_POINT **then**
7: constant extrapolation of output signal
8: set output signal from $\hat{m}$ as input for m

We note that the algorithm is scalable w.r.t. the number of elements of the *IOPort* array as well as the number of input signals per each element. Furthermore, the algorithm allows for a self-reference within a model, i.e., input and output signals may correspond to the same model.

3.3 Applications

In this Section we present several applications of the STEAM co-simulation framework. The applications are selected to demonstrate capabilities of the framework as well as the properties of the co-simulation schemes. Firstly, we consider various models to demonstrate that the proposed architecture supports multi-domain problems. Secondly, we study different co-simulation schemes. These applications are based on lumped variables, which are exchanged between the tools in order to tackle the multi-physics, multi-rate, and multi-scale behavior. We also present first attempts to include distributed variables and extend the framework to support distributed ports.

- The controller/circuit coupling is an application of a weak coupling and waveform relaxation scheme to a problem composed of two ordinary differential equations [50]. Properties of the waveform-relaxation algorithm's convergence, i.e., the minimum and maximum number of iterations, are studied.
- The 1D field/circuit coupling considers a 1D nonlinear thermal model characterized in terms of a partial differential equation coupled to an electrical circuit. This application aims at carrying out a comparison of weak coupling and waveform relaxation schemes.
- With field/circuit coupling we present an analysis of waveform relaxation scheme and two equivalent circuital representations of field models [51]. Several concepts for the convergence improvement and computational time reduction are also discussed.
- Eventually, we consider coupling of distributed magneto-thermal and mechanical models by means of mesh-based interpolation [52]. The goal of this study is to introduce distributed ports to the STEAM framework.

3.3.1 Controller/Circuit Coupling

In this Section, we study a PI power converter controller coupled to a linear electrical circuit. We consider a setting for treating PI controllers and linear circuits as ordinary differential equations (ODEs) and differential-algebraic equations (DAEs). Typically, the controller and circuit models are studied independently with different simulation solvers. The motivation for this choice is twofold. Firstly, the controller model is solved with fixed time steps, and the circuit model is computed with an adaptive time-stepping method in order to account for the transient effects. Secondly, the design of a controller typically involves an equivalent low-order model of an electrical circuit. Similarly, a circuit powered by an ideal current source (disregarding the controller action) is satisfactory for certain simulation scenarios [53].

In addition to the weak coupling scheme, we propose the application of the waveform relaxation algorithm [43], [54], [55] to controller/circuit coupling. Instead of sequentially executing the controller and circuit solver with the sampling frequency of the controller, the problem is translated into an iterative process on larger time windows equal to several sampling periods. This approach promises several benefits in terms of reduction of communication overhead and thus eventually computational time.

We consider a closed feedback system including a discrete ZOH element with a PI controller and an electrical circuit as shown in Fig. 3.8. The latter two are characterized, respectively, by transfer functions $G_{\mathrm{CON}}(\cdot)$ and $G_{\mathrm{CIR}}(\cdot)$.

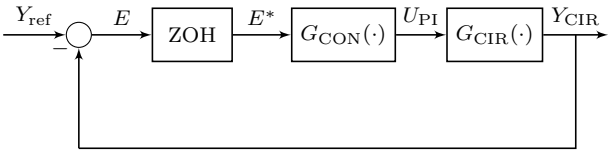

Figure 3.8: A block diagram representation of the closed loop feedback system with a series connection of a discrete zero order hold (ZOH), controller and circuit transfer function in the open loop.

PI Controller

For the scope of this Section we assume all signals to be differentiable ($C^1(\mathcal{I})$). The governing equation of a continuous PI controller, obtained from (2.152) by setting $k_\mathrm{d} = 0$, is given in the time domain as

$$U_\mathrm{con}(t) = k_\mathrm{p} E(t) + k_\mathrm{i} \int_0^t E(\tau) d\tau, \tag{3.9}$$

where $E(t) = Y_\mathrm{ref}(t) - Y_\mathrm{meas}(t)$ is the error obtained as a difference between the desired, reference signal Y_ref and its actual, measured waveform Y_meas. The transfer function of a PI controller (3.9), obtained as a Laplace transform, reads

$$G_\mathrm{CON}(s) = \frac{U_\mathrm{con}(s)}{E(s)} = k_\mathrm{p} + k_\mathrm{i} \frac{1}{s}. \tag{3.10}$$

Let $t_\mathrm{d} > 0$ denote the physical sampling period of the controller. The temporal discretization is given by times $t_l = l \Delta t_\mathrm{con}$ with $l = 1, \ldots, n_\mathrm{con}$, where Δt_con is the sampling period of the controller in simulation ($t_\mathrm{d} = \Delta t_\mathrm{con}$). Considering the rectangle method for quadrature as well as the Implicit-Euler scheme for differentiation yield

$$U_\mathrm{con}(t_j) = k_\mathrm{p} E(t_j - t_\mathrm{d}) + k_\mathrm{i} \Delta t_\mathrm{con} \sum_{i=1}^{j} E(t_i - t_\mathrm{d}). \tag{3.11}$$

Differentiating equation (2.152) results in the following (delay) differential equation

$$\partial_t U_\mathrm{con}(t) = k_\mathrm{p} \partial_t E(t - t_\mathrm{d}) + k_\mathrm{i} E(t - t_\mathrm{d}). \tag{3.12}$$

Equation (3.12) can be rewritten as

$$F_\mathrm{con}(\partial_t x_1, \partial_t x_2, x_2, u(t)) = 0, \tag{3.13}$$

with the initial values $\begin{bmatrix} x_2(t_0) & x_1(t_0) \end{bmatrix}$, the unknown $x_1(t) = U_\mathrm{con}(t)$, the excitation $x_2(t) = Y_\mathrm{meas}(t)$, and the reference signal $u(t) = Y_\mathrm{ref}(t)$.

Electrical Circuit

In analogy to (3.13), the system (2.136) is represented as an abstract differential-algebraic initial-value problem

$$F_\mathrm{cir}(\partial_t x_3, x_3, x_1(t)) = 0 \tag{3.14}$$

with the initial value $x_3(t_0)$ and unknowns $x_3 := \begin{bmatrix} \phi & I_\mathrm{L} & I_\mathrm{con} \end{bmatrix}^\top$. The external input function $x_1(t)$ is given in the considered case by the output voltage of the controller $U_\mathrm{con}(t)$. The controller output is obtained from $Y_\mathrm{meas}(t) = I_\mathrm{con}(t)$ with $I_\mathrm{con}(t)$ being the current flowing through the PI-controlled voltage source; see (3.13). Let us consider the simple case of a first-order, series RL network and a controller shown in Fig. 3.9 (left). (As we shall see later such a first-order model suffices to represent low frequency behavior of the LHC main dipole circuit.) Then, the incidence matrices representing the circuit are given as

$$A_\mathrm{R} = \begin{bmatrix} 1 \\ -1 \end{bmatrix}, \; A_\mathrm{L} = \begin{bmatrix} 0 \\ 1 \end{bmatrix}, \; A_\mathrm{CON} = \begin{bmatrix} -1 \\ 0 \end{bmatrix},$$

with the elements $L = L_\mathrm{eq}$ and $G = R_\mathrm{eq}^{-1}$. The application of MNA results in four DAEs in the (redundant) variables denoting nodal potentials ϕ_1, ϕ_2, and branch currents I_con, I_L. The DAEs are expressed by the mathematically equivalent ODE

$$\partial_t I_\mathrm{con} = -\frac{1}{L_\mathrm{eq}} U_\mathrm{con} - \frac{R_\mathrm{eq}}{L_\mathrm{eq}} I_\mathrm{con}. \tag{3.15}$$

The transfer function of the considered first-order circuit model reads

$$G_{\mathrm{CIR}}(s) = \frac{I_{\mathrm{con}}(s)}{U_{\mathrm{con}}(s)} = \frac{1}{sL_{\mathrm{eq}} + R_{\mathrm{eq}}}, \tag{3.16}$$

where $I_{\mathrm{con}}(s)$ and $U_{\mathrm{con}}(s)$ are, respectively, Laplace transforms of input and output signals.

Recovering the underlying ODE from the MNA representation is straightforward for relatively small systems, given that there are no CV loops or LI cutsets present in the circuit [56]. Causality assignment of bond graph model in Fig. 3.9 (right) indicates no causal conflicts for the considered model.

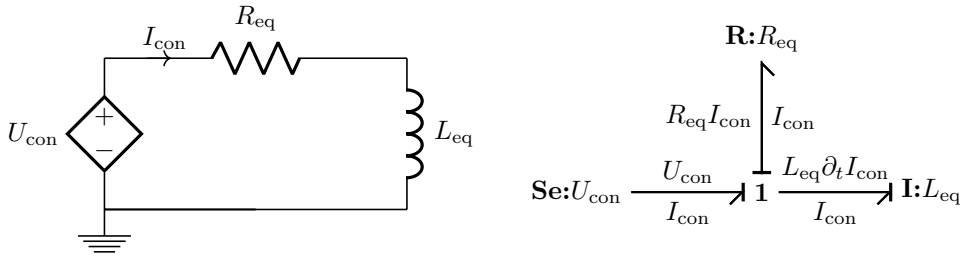

Figure 3.9: Left: First order RL model of the LHC main dipole circuit. Right: Equivalent bond graph model.

Weak Coupling

Hardware implementation of a PI controller resembles Gauss-Seidel type weak coupling scheme (cf. Section 3.1.2). In this setup the controller is solved as the first subsystem and provides input to the electrical circuit

$$F_{\mathrm{con}}(\partial_t x_{1,j+1}, \partial_t x_{2,j+1}, x_{2,j}, u(t)) = 0. \tag{3.17}$$

The controller algorithm calculates the control signal based on a data point of current signal calculated at the communication point

$$I_{\mathrm{con},j+1}(T_{j+1}) = I_{\mathrm{cir},j}(T_j). \tag{3.18}$$

The electrical circuit is solved as the second subsystem

$$F_{\mathrm{cir}}(\partial_t x_{2,j+1}, x_{2,j+1}, x_{1,j+1}(t)) = 0. \tag{3.19}$$

The controller output is provided as an input to the electrical circuit only at discrete communication points determined by the sampling frequency. For the duration of a time window, the control signal is kept constant following the ZOH component

$$U_{\mathrm{cir},j+1}(T_{j+1}) = U_{\mathrm{con},j+1}(T_{j+1}). \tag{3.20}$$

Waveform Relaxation

In practice, the electrical circuit model (3.14) is typically numerically solved with an adaptive time stepping method (e.g., trapezoidal rule or BDF (Backward Differentiation Formula) schemes, [57]). The controller model is computed with fixed time steps corresponding to its operating frequency. Co-simulation of both models with the waveform relaxation algorithm allows maintaining this setup, by exchanging waveforms at discrete communication time instants T_j. To this end, the total simulation time $\mathcal{I}$ is divided into N time windows $\mathcal{I}_j = (T_j, T_{j+1}]$ with $j = 0, ..., N-1$.

The Gauss-Seidel scheme is employed for the waveform relaxation method following the algorithm described in Section 3.1.4. At each time window, circuit and controller models are

solved sequentially as shown in Fig. 3.4 (right). The controller is solved as the first subsystem (S_1)

$$F_{\mathrm{con}}(\partial_t x_1^{k+1}, \partial_t x_2^{k+1}, x_2^k, u(t)) = 0 \tag{3.21}$$

with the coupling condition being the current of the PI-controlled voltage source obtained in the previous iteration

$$I_{\mathrm{con}}^{k+1} = I_{\mathrm{cir}}^{k}. \tag{3.22}$$

Then the calculated voltage is set as an input to the circuit model, which is solved as the second subsystem (S_2)

$$F_{\mathrm{cir}}(\partial_t x_2^{k+1}, x_2^{k+1}, x_1^{k+1}, u(t)) = 0. \tag{3.23}$$

with a coupling condition given as the PI-controlled voltage of the power converter

$$U_{\mathrm{cir}}^{k+1} = U_{\mathrm{con}}^{k+1}. \tag{3.24}$$

Proposition 1 *Given the proposed waveform relaxation algorithm coupling equations* (3.12) *and* (3.15) *with controller time step equal to the controller delay* $\Delta t_{\mathrm{con}} = t_{\mathrm{d}}$ *and disregarding the error of the adaptive time stepping scheme used to solve* (3.15)*, then*

$$I_{\mathrm{con}}^{k+1}(t) = I_{\mathrm{cir}}^{k}(t),\ t \in \mathcal{I}_j \tag{3.25}$$

for all iteration indices larger or equal to the number of controller steps within a given time window j*, i.e., for all* $k \geq n_{\mathrm{con}}$*.*

A proof of this proposition is reported in [50]. We note that an additional termination criterion can be considered. The convergence iterations are terminated when either (i) the convergence iteration index k reached n_{con}, or (i) a difference between two subsequent waveforms is below a certain tolerance. Unless the waveforms converged in fewer than n_{con} iterations, we can observe that the stopping criterion based on iterations requires one convergence iteration fewer as compared to the convergence criterion based on waveforms. Furthermore, if the time window size $H_j = T_{j+1} - T_j$ matches the controller sampling period, Δt_{con}, according to Proposition 1, the waveform relaxation algorithm reduces to a weak coupling scheme. In this case both models are solved only once ($n_{\mathrm{con}} = 1$) and the convergence check is not performed (the maximum number of iterations is set to 1).

Proposition 2 shows that for a certain class of open loop systems and reference current profiles, the number of iterations needed to reach convergence in the steady state is fewer than n_{con}.

Proposition 2 *For systems of type p, i.e., systems with p-fold pole equal to zero in the continuous open loop system transfer function, with the reference signal being a polynomial function of time of (p-1)-th order, and for a given time window in the steady state, the proposed waveform relaxation algorithm converges at* $k = 1$*.*

A proof of the second proposition is presented in [50]. To conclude, Proposition 2 indicates the minimum number of convergence iterations. Both Propositions determine the lower and upper bounds for the number of iterations during a co-simulation, i.e., $1 \leq k \leq n_{\mathrm{con}}$. The proposed weak coupling and waveform relaxation algorithms are now applied to a practical case of the co-simulation of an LHC main dipole circuit (RB) and its PI power converter controller.

Numerical Examples

The performance of the developed coupling algorithms is demonstrated with two simulation cases involving a simplified, first order model and a realistic model of the RB circuit. The simplified model is compared to a monolithic reference simulation of a controller and electrical circuit in order to verify the waveform relaxation algorithm. Once the performance and properties of the scheme are demonstrated with the simplified model, the realistic model can be used to study nominal current ramp-up in the RB circuit.

Powersim PSIM and ORCAD Cadence PSpice, are employed for controller and electrical circuit simulation, respectively. The monolithic simulation is obtained with Powersim PSIM. The controller gains are calculated following the procedure described in [50, Section IV]. The simulated controller sampling period is $t_\mathrm{d} = 0.04$ s and is chosen as a step size of the controller model $\Delta t_\mathrm{con} = t_\mathrm{d}$. The maximum time step size for the adaptive time-stepping method of the circuit simulation is equal to $\Delta t_\mathrm{cir} \leq 0.04$ s. An absolute error tolerance of the circuit model is set to 10^{-10} A.

Simplified First Order Model

The first case aims at verifying the algorithm operation and validating Propositions 1 and 2. We study a step response of the simplified, first-order model of the RB circuit. The schematic is given in Fig. 3.9 with $L_\mathrm{eq} = 15.4$ H and $R_\mathrm{eq} = 0.1\ \Omega$. The co-simulation time is equal to 2.4 s. The time interval $\mathcal{I}$ is divided into $N = 15$ windows of fixed length $H = 0.16$ s ($n_\mathrm{con} = 4$). Signal exchange between the solvers takes place at discrete time points $T_j = jH$. To demonstrate Propositions 1 and 2 we employ only the current-based stopping criterion. The termination criterion is based on the relative tolerance between two iterates of the current waveforms according to

$$c_\mathrm{cir}(k) = \frac{\int_{t_j}^{t_{j+1}} |I_\mathrm{cir}^k(\tau) - I_\mathrm{cir}^{k-1}(\tau)| \mathrm{d}\tau}{\int_{t_j}^{t_{j+1}} |I_\mathrm{cir}^k(\tau)| \mathrm{d}\tau} \leq 10^{-6}, \text{for} \quad k \geq 1.$$

Fig. 3.10 depicts the comparison of the reference step current profile and the current waveforms obtained with the co-simulation and monolithic simulation. The comparison indicates a very good agreement between the reference, monolithic study and co-simulation results.

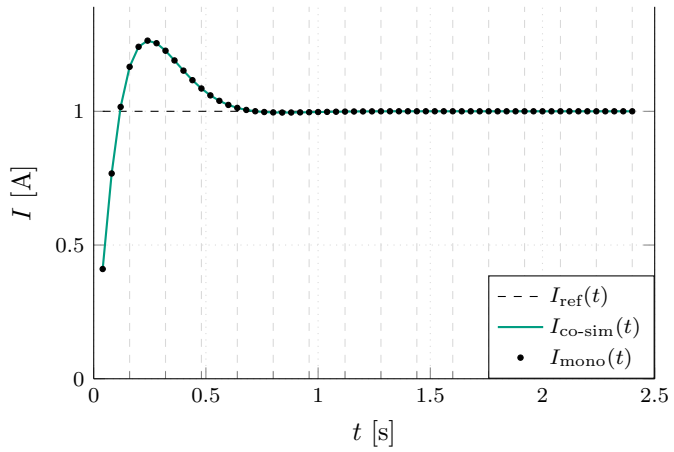

Figure 3.10: Current evolution in the first-order RB circuit for a step reference current profile.

Table 3.2 lists controller output voltage for the first time window. The first row contains the monolithic simulation and the remaining rows contain results of consecutive iterations of the waveform relaxation algorithm. With each iteration, the controller output $U_\mathrm{co\text{-}sim}^k(t)$ approaches the monolithic solution $U_\mathrm{mono}(t)$. In other words, each iteration k extends the period of time for which the controller output approaches, for the considered case is equal to, the monolithic, reference solution. This is an expected behavior of the waveform relaxation scheme [55]. The controller output for the last two convergence iterations is identical. This is due to the fact that the applied current-based convergence criterion (3.3.1) requires two consecutive iterations with the same input voltage in order to detect convergence.

Table 3.2: Comparison of the monolithic controller voltage with the co-simulated one for convergence iterations of the first time window.

t [s]	0.04	0.08	0.12	0.16
$U_{\text{mono}}(t)$ [V]	161.16	119.34	76.12	41.67
$U^0_{\text{co-sim}}(t)$ [V]	161.16	185.48	209.80	234.11
$U^1_{\text{co-sim}}(t)$ [V]	161.16	119.34	62.55	-14.95
$U^2_{\text{co-sim}}(t)$ [V]	161.16	119.34	76.12	44.45
$U^3_{\text{co-sim}}(t)$ [V]	161.16	119.34	76.12	41.67
$U^4_{\text{co-sim}}(t)$ [V]	161.16	119.34	76.12	41.67

The number of iterations for each time window is shown in Fig. 3.11. (Note that the iterations are 0-based.). In the initial transient phase, the number of iterations equals $n_{\text{con}}+1$. The number of iterations steadily decreases to two iterations until the integral part of the PI controller stabilises at the appropriate output for the excitation function and studied circuit topology. In case of the simplified model, the open loop system is of type 1 as one can observe from the series connection of transfer functions of the controller (3.10) and circuit (3.16).

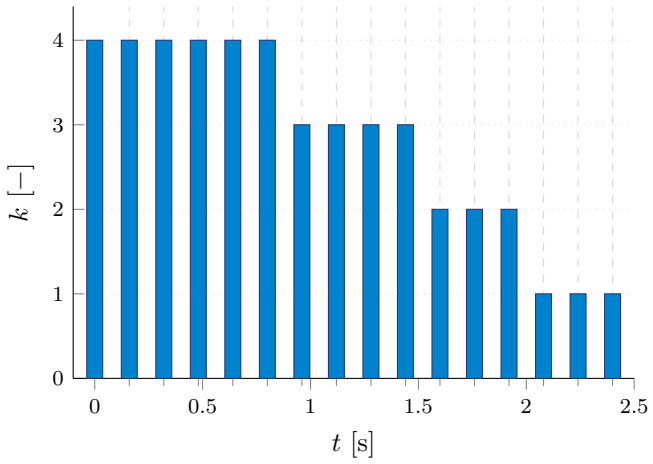

Figure 3.11: Number of iterations needed to reach convergence in each time window (0-based).

To conclude, the analysis of the simplified model confirmed the number of iterations predicted by Propositions 1 and 2.

Parabolic-Linear Response of a Realistic Model

Once the convergence properties and operation of the waveform relaxation coupling scheme are verified, the second scenario studies a controller/circuit coupling of the considerably more complex RB circuit. Fig. 3.12 shows the circuit composed of 154 equivalent lumped RLC models of a dipole magnet along with a power converter, a filter, and protection devices. The model parameters were identified to match the available frequency transfer function measurements [58].

In this study we leverage the immanent feature of the co-simulation, i.e., we will replace the simplified model used in the previous test with a more detailed model shown in Fig. 3.12. Moreover, we will not update neither the controller model nor the signal exchange definition.

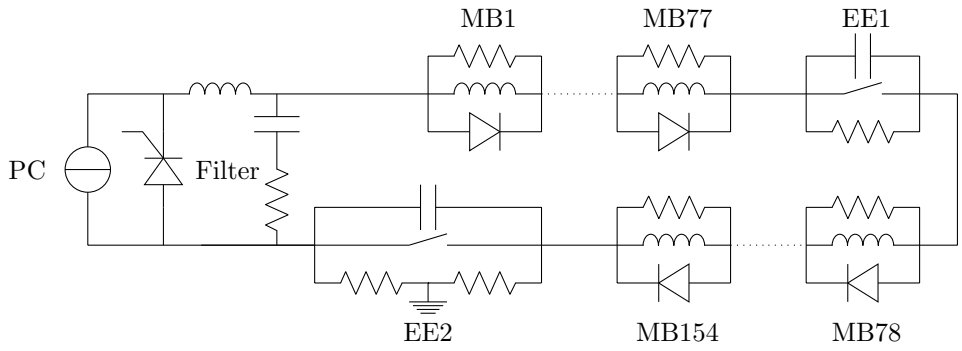

Figure 3.12: Schematic with the main components of a main dipole circuit of the LHC such as power converter (PC), RLC low-pass filter, 154 magnets (MB) represented as an inductor with parallel diode and resistor, and two energy extraction systems (EE).

The circuit model contains several thousand lumped components [53] and, therefore, the underlying ODE cannot be easily extracted. As a consequence this setup may not be easily covered by classical arguments of the waveform relaxation analysis. We assume nominal operation of the circuit during a ramp-up of the current with deactivated quench protection systems. The goal of this test is to verify the operation of the proposed algorithm in a weak coupling scheme. The total co-simulation time is 120 s and corresponds to the initial parabolic increase ($0\ \text{s} < t < 100\ \text{s}$) of the current profile followed by the linear increase ($t > 100$ s). The time interval $\mathcal{I}$ is divided into $N = 3000$ windows of fixed length $H = 0.04$ s ($n_{\text{con}} = 1$) corresponding to the controller sampling frequency of 25 Hz. The current response shown in Fig. 3.13 (left) reproduces the desired current profile with good accuracy. Fig. 3.13 (right) presents the PI controller output voltage.

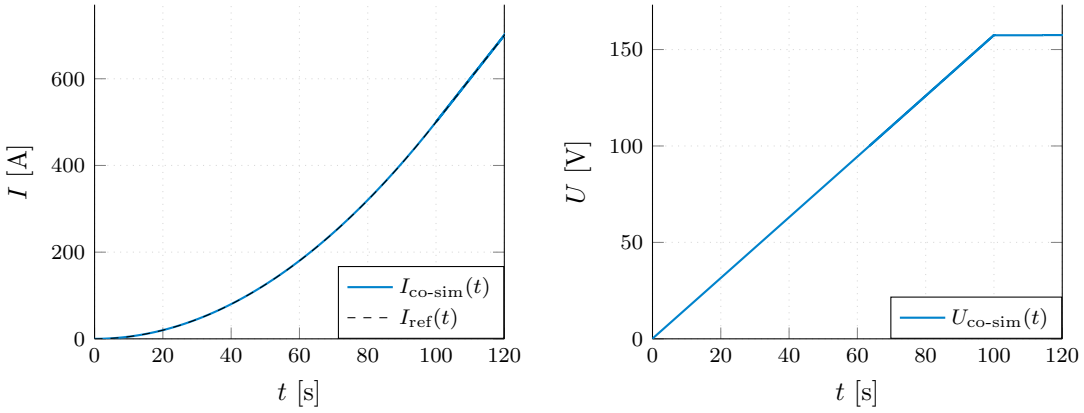

Figure 3.13: Left: Initial part of the parabolic-linear reference current profile compared to the solution of the co-simulation with the weak coupling scheme. Right: Output of the PI controller for the considered current profile.

During the first 100 seconds, the reference current profile has parabolic shape, which results in a linear increase of the controller voltage. For $100\ \text{s} < t < 120$ s the reference profile becomes linear and, therefore, the controller output has constant value. Since the linear ramp rate is equal to 10 A/s, the controller output in the second period is equal to about 154 V due to the inductive voltage with a linearly growing component accounting for the circuit resistance.

In this study we have shown that a simplified, first-order model is sufficient to design a PI controller (for more details see [50]). The controller model was applied to a more refined circuit model of the LHC main dipole chain. As a result, the reference linear-parabolic current profile was reproduced with a satisfactory accuracy. Moreover, the more refined model allows to

study the distribution of voltage across each magnet and propagation of voltage waves during the controller operation generating a stepwise output. The more refined model can be used to study operation of the controller in the case of failures occurring in the circuit, such as shorts to ground and/or quenches in superconducting busbars and magnets. In between the quench initiation and detection, the controller action would adjust the output in order to compensate for the resistance growth in the circuit. This might require taking into account either a 1D and/or 2D finite element models.

3.3.2 1D Thermal Field/Circuit Coupling

A quench usually occurs in a small volume of a superconducting magnet. If cooling is insufficient to absorb initial quench heating, the quench will propagate. Initially quench propagation takes place longitudinally along a superconducting cable and then with a certain delay introduced by the cable insulation, the so called turn-to-turn propagation occurs.

The study of quench initiation and propagation is aimed at estimating the velocity of the resistive-zone growth, which translates into the increase of the resistive voltage. The resistive voltage is compared to a threshold value which, once reached, indicates a quench in a superconducting magnet. Results of such a study allow adjusting detection threshold and validation times which translate into the delay of real-world quench protection triggering. If a protection system is triggered too late, then irreversible damages in a magnet could occur.

A quench is a sharp transition from the superconducting to the normal conducting state governed by highly nonlinear equations. Thus, a fine temporal and spatial resolution is necessary in order to accurately reproduce the quench propagation. A 3D model of a superconducting magnet fulfilling these requirements would lead to an unacceptable number of degrees of freedom. Furthermore, since a quench occurs locally in the initial phase, such a large model is not necessary. Instead, often 1D models are used to study quench initiation and propagation as a conservative assumption neglecting the turn-to-turn propagation.

In the remainder of this Section we will study a coupling of a 1D thermal model and an electrical circuit. Due to a nature of initial quench propagation characterized by a large time constant due to a relatively large inductance and small resistance we will consider two algorithms: (i) weak coupling; and (ii) waveform relaxation. The study will be illustrated with an academic example of the longitudinal quench propagation in an LHC main dipole.

1D Thermal Field Model

The 1D model representing a superconducting cable is composed of n_{N} nodes connected by $n_{\mathrm{N}} - 1$ edges. Nodes represent the thermal mass of fractions of cable while edges account for the heat conduction between them.

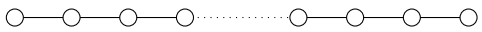

Figure 3.14: Sketch of a 1D model of a superconducting cable composed of nodes and edges.

The thermal model is represented in terms of the heat balance equation (2.107) [59]. The external heat source q_0 represents the Ohmic loss occurring after a quench

$$q_0 = \frac{\rho l}{S} I_{\mathrm{s}}^2, \tag{3.26}$$

where l is the length of an edge associated with a node for which the heat is applied and S is the cross-section of the turn. The resistivity ρ is nonlinearly dependent on the temperature and magnetic field. The magnetic field is calculated as $B = f_B I_{\mathrm{s}}$ with the linear scaling coefficient f_B extracted at the operating point $I_{\mathrm{s}}(t = 0)$. The lumped resistance representing the thermal model on the circuit side reads

$$R = \frac{1}{S} \int_{\Omega} f_{\mathrm{q}} \rho, \tag{3.27}$$

where f_{q} is a flag denoting whether or not a given node in the model is in either normal or superconducting state. The flag is a function of the operating point, i.e., the temperature, current density, and magnetic field.

The distributed model (2.107) is represented as an abstract differential-algebraic initial-value problem

$$F_{\mathrm{thermal}}(x_1, \partial_t x_1, y_1, u_1(t)) = 0 \tag{3.28}$$

with the unknown $x_1 = T$, temperature. The output variable y_1 is the resistance R. The input vector u_1 is the source current I_{s}.

Circuit Model

The topology of a superconducting circuit is described in terms of the current-voltage oriented MNA. An equivalent representation of the 1D thermal model on the circuit side is a time-varying resistance shown in Fig. 3.15.

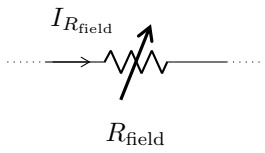

Figure 3.15: Schematic of an equivalent circuital representation of the 1D thermal model.

In analogy to (3.28) the network model is also characterized in terms of an initial value problem as

$$F_{\mathrm{circuit}}(x_2, \partial_t x_2, y_2, x_3, \partial_t x_3, y_3, u_2(t)) = 0 \tag{3.29}$$

with appropriate initial values and unknowns x_2 and x_3 being, respectively, the currents through the inductors and voltage sources, and nodal voltages. The output variable y_2 and y_3 are currents through the resistance representing the 1D field model $I_{R_{\mathrm{field}}}$ and the voltages across these resistors $U_{R_{\mathrm{field}}}$, respectively. The voltage across these resistors can be used as a port variable to a model of the quench detection system. The input signal u_2 is the field resistance R_{field}.

Weak Coupling

A Gauss-Seidel-type weak coupling algorithm as given in Section 3.1.2 is discussed in the first place. The circuit model is solved as the first subsystem

$$F_{\mathrm{circuit}}\left(x_{2,j+1}, \partial_t x_{2,j+1}, y_{2,j+1}, x_{3,j+1}, \partial_t x_{3,j+1}, y_{3,j+1}, u_{2,j}(t)\right) = 0 \tag{3.30}$$

with the following coupling condition

$$R_{\mathrm{field},j+1} = R_j. \tag{3.31}$$

The second subsystem is the field model (3.28) represented as

$$F_{\mathrm{field}}\left(x_{1,j+1}, \partial_t x_{1,j+1}, y_{1,j+1}, u_{1,j+1}(t)\right) = 0 \tag{3.32}$$

with a coupling condition given as

$$I_{\mathrm{s},j+1} = I_{R,j+1}. \tag{3.33}$$

For the weak coupling algorithm, we consider constant extrapolation of resistance and current.

Waveform Relaxation

As an alternative coupling scheme, we study the coupling of the 1D thermal model (3.28) and the electrical circuit (3.29) by means of a Gauss-Seidel-type scheme with waveform relaxation algorithm as given in Section 3.1.4. Similarly to the weak coupling scheme, the circuit model is solved as the first subsystem

$$F_{\text{circuit}}\left(x_2^{k+1}, \partial_t x_2^{k+1}, y_2^{k+1}, x_3^{k+1}, \partial_t x_3^{k+1}, y_3^{k+1}, u_2^k(t)\right) = 0 \tag{3.34}$$

with the following coupling condition

$$R_{\text{field}}^{k+1} = R^k. \tag{3.35}$$

The second subsystem is the field model (3.28) represented as

$$F_{\text{field}}\left(x_1^{k+1}, \partial_t x_1^{k+1}, y_1^{k+1}, u_1^{k+1}(t)\right) = 0 \tag{3.36}$$

with a coupling condition given as

$$I_{\text{s}}^{k+1} = I_{R_{\text{field}}}^{k+1}. \tag{3.37}$$

For the circuit model, we select the termination criterion of iterations of the waveform relaxation algorithm based on the relative tolerance given as

$$c_{\text{circuit}}(k) = \max_{t \in \mathcal{T}_j} \frac{|y_2^k(t) - y_2^{k-1}(t)|}{|y_2^k(t)|} < \text{relTol}. \tag{3.38}$$

The coupling of the 1D thermal field and circuit models is illustrated with a case of quench propagation in a superconducting cable of an LHC main dipole. The superconducting cable is made of Nb-Ti and copper and is 10-meter long. We consider a case of an unprotected quench, i.e., the power converter with initial current $I_0 = 10$ kA is turned off and the current follows an RL exponential decay with a constant inductance $L_{\text{magnet}} = 100$ mH and time-varying resistance R_{field}; see Fig. 3.16 (left). For the sake of simplicity, the crowbar switch is modelled as a time-varying resistance. The co-simulation time is equal to $t = 0.2$ s. The electrical circuit and the 1D thermal models are solved with ORCAD PSpice and COMSOL, respectively. The absolute tolerance of the former one is equal to 10^{-3} K and of the latter one is 10^{-10} A. Both models are solved with the Newton-Raphson method. The considered superconducting cable is divided into $n_{\text{N}} = 10^4$ nodes. The 1D model is initialized with an initial temperature distribution represented by a Gaussian profile as shown in Fig. 3.16 (right). The peak temperature is above the critical temperature for Nb-Ti and as a result some fraction of a cable is in the normal conducting state already at the beginning of the simulation.

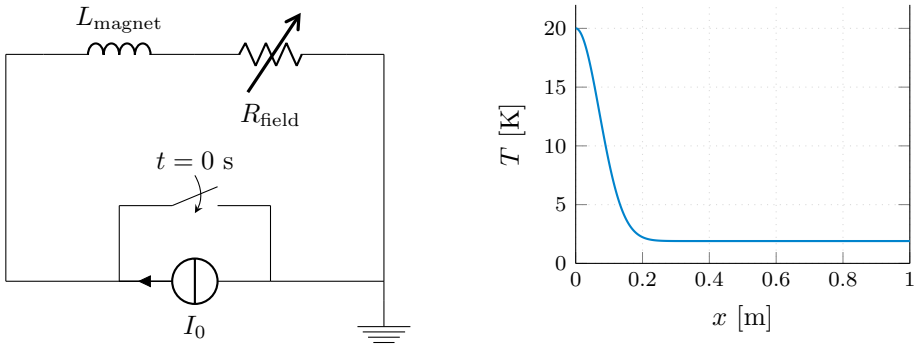

Figure 3.16: Left: Schematic of the circuit with a crowbar in parallel to the power converter, an inductance of the magnet and a time-varying resistance representing quench propagation in a turn. Right: Initial temperature profile for the first meter of the cable as for 1 m $< x <$ 10 m the initial temperature is equal to 1.9 K.

In this study we compare results obtained with waveform relaxation and weak coupling algorithms. In both cases, the maximum time step for field and circuit models is 10 µs and 100 µs, respectively. The waveform relaxation algorithm is solved with four time windows $H = 50$ ms and a relative tolerance of 10^{-5} for the circuit model is calculated according to (3.38) and used to stop iterations for each time window. The weak coupling scheme is solved for four time windows $\mathcal{J} = \begin{bmatrix} 1 & 5 & 10 & 50 \end{bmatrix}$ ms. The application of the weak coupling algorithm is justified as a current decay that is solely due to the resistance growth after a quench is characterized by relatively slow dynamics in the order of 50 A/s.

Fig. 3.17 shows the comparison of current and resistance profiles obtained with the two studied algorithms. As one can notice, for the weak coupling algorithm the decrease of the time window results in the current very slowly approaching the solution of the waveform relaxation algorithm. For each window, the waveform relaxation algorithm required three iterations to reach the prescribed relative tolerance of 10^{-5}.

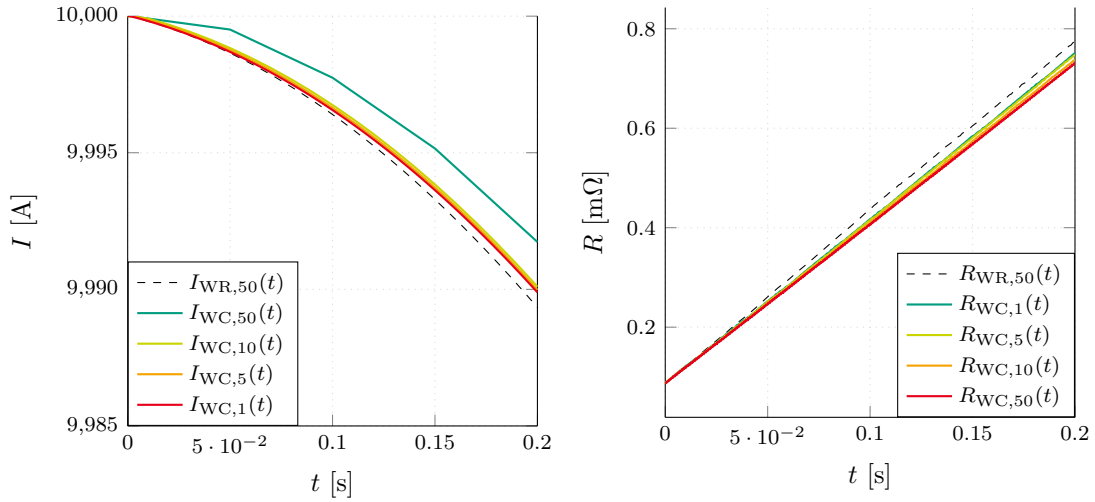

Figure 3.17: Left: Comparison of the current evolution during the co-simulation for the waveform relaxation and the weak coupling schemes. Right: Comparison of the resistance profiles.

Even though the current dynamics is relatively low, the solution of the weak coupling scheme was different from the solution of the waveform relaxation scheme. The differences between the solutions obtained with waveform relaxation and weak coupling for several time window sizes stems from the characteristics of these algorithms: Firstly, the weak coupling relies on exchange of data points with an arbitrary extrapolation (in this case constant extrapolation) while waveform relaxation exchanges actual waveforms containing the dynamic behavior of respective systems. Secondly, the weak coupling scheme performs exchange only once for a given communication point whereas for the waveform relaxation algorithm the signal exchange is carried out until the desired tolerance is reached. These differences accumulate over time and result in a growing discrepancy between the output signals.

Table 3.3 summarizes computation times for each of the studied cases. The fastest case was the weak coupling with a time window equal to $H = 50$ ms which required less time to complete than the waveform relaxation algorithm with the same window size. This is due to the fact that the waveform relaxation algorithm required three iterations for each window to reach the desired accuracy. The smaller the time window size for the weak coupling scheme, the longer it takes to compute the co-simulation scenario. This is due to the overhead of setting up and terminating simulations of models representing field and circuit subproblems.

Table 3.3: Comparison of computation time needed to solve the coupled problem with waveform relaxation (WR) and weak coupling (WC) algorithms.

Case	t_{comp} [s]
WR $H = 50$ ms	114
WC $H = 50$ ms	75
WC $H = 10$ ms	128
WC $H = 5$ ms	200
WC $H = 1$ ms	869

3.3.3 2D Magneto-Thermal Field/Circuit Coupling

The Finite Element Method (FEM) allows performing accurate and consistent modeling of superconducting magnets including: (i) optimization and design of magnetic field; (ii) estimation of the peak temperature and the maximum voltage to ground in the magnet during quench protection studies; (iii) mechanical design and optimization. Relevant quench protection scenarios of superconducting circuits are simulated with network solvers. A superconducting magnet and its powering circuit are intrinsically coupled. In particular, the coupling has to be accurately resolved for the quench protection studies involving the resistance growth and the inductive voltage variation in the distributed model and the voltage waves traveling across a chain of magnets.

For the purpose of consistently simulating both domains and their reciprocal influence, field/circuit coupling has been extensively studied [49], [60]. In [44], a magneto-thermal magnet model is represented by an equivalent network and solved monolithically with a superconducting circuit involving over a hundred magnets [61]. However, this approach features limited accuracy as the field model is initialized with a static magnetic field map. There are also approaches based on co-simulation which involve the application of the weak coupling scheme [60] and waveform relaxation [16].

In the following we will use term pre-conditioner to denote an equivalent, lumped representation of the distributed field model on the circuit side. The goal of the pre-conditioner is to introduce elements acting as the first order approximation of the distributed model. Note that even though the pre-conditioner is present in the circuit model, both models are solved independently (unlike in [44], where a sophisticated preconditioner was employed) and coupled through the waveform relaxation method. An equivalent circuital representation of a field model facilitates the coupling, so that the circuit solution after certain number of iterations with the waveform relaxation scheme converges to a solution as if a field model was present in the circuit even though they are solved independently and coupled via selected variables. In [16] it was demonstrated that the presence of pre-conditioners improves convergence w.r.t. schemes based on exchange of voltage and current.

Several equivalent circuital representations were studied. Among others there are approaches based on exchange of voltage and current as well as voltage and current enriched by a lumped inductance approximating the magnetic model around the operating point and acting as a preconditioner for the co-simulation scheme. Hereunder we report an equivalent field representation of the field model on the circuit side accounting for the magnetoquasistatic and thermal systems of a superconducting magnet distributed model [51]. In this setting, the field model is current-driven. Then, we will find a dual representation based on a voltage-driven field model. A comparison will be made for a trivial case of coupling two linear ordinary differential equations (one being a circuit model and the other mimicking a field model) as well as a network model coupled with a distributed field model.

The more accurate the equivalent field model is in reproducing the field model behavior, the less iterations are required to reach convergence or equivalently the larger time windows can be

chosen. Eventually, we will consider two options for enhancing equivalent circuit models and we will report preliminary results.

Current-Driven Mode

In [51] an equivalent circuital representation for a field model excited with an external current was formally stated and proved. The circuital representation consists of differential inductance and compensation voltage to account for nonlinearities on the field side. In the following we will recall the very representation and formulation of the coupling scheme.

2D Magneto-Thermal Model

The field model comprises strongly coupled magnetoquasistatic (MQS) and thermal systems as discussed in Chapter 2. First, we recall the MQS model and its governing equation given in (2.96). We constraint our analysis by neglecting the eddy current term, i.e., $\kappa = 0$ as well as the persistent magnetization currents. Furthermore, we only consider inter-filament coupling currents. Note that these simplifications do not affect the causality of the Stokes-Dirac structure and therefore the storage element. From (2.96) with $H = *_\nu B = *_\nu \mathrm{d}A$ we obtain the so-called curl-curl equation

$$\mathrm{d}(*_\nu \mathrm{d}A) + \mathrm{d}(*_{\nu\tau} \mathrm{d}\partial_t A) = \chi I_\mathrm{s} = \jmath_\mathrm{s}. \tag{3.39}$$

The curl-curl equation is driven by an external current density obtained from the current I_s of an electrical circuit to which the field model is coupled and the winding density function χ. It shall be noted that there could be a vector of multiple currents on the right hand side of (3.39). From the solution of (3.39) we find that the dynamic voltage U_dyn is given as

$$U_\mathrm{dyn} = \int_\Omega \chi^\top \partial_t A, \tag{3.40}$$

which in fact is a time derivative of the flux linkage $\varphi = \chi^\top A$.

The MQS model is solved in the monolithic sense coupled with the thermal model due to the dependence of governing equations and material properties on both, temperature and magnetic field. The thermal model is represented in terms of the heat balance equation (2.107). The external heat source q_0 comprises contributions from the Ohmic loss and cable eddy currents

$$q_0 = T\sigma_\rho + T\sigma_{\nu\tau} = *_\rho \jmath_\mathrm{s} \wedge \jmath_\mathrm{s} + \partial_t A \wedge \mathrm{d} *_{\nu\tau} \mathrm{d}\partial_t A. \tag{3.41}$$

From the solution of (2.107) and (3.39), the resistance R is extracted in post-processing as

$$R = \int_\Omega \chi^\top f_\mathrm{q} \rho \chi. \tag{3.42}$$

The finite element model composed of (3.39) and (2.107) is reformulated into an abstract differential-algebraic initial-value problem as

$$F_\mathrm{field}(x_1, \partial_t x_1, y_1, x_2, \partial_t x_2, y_2, u_1(t)) = 0 \tag{3.43}$$

with appropriate initial values $\begin{bmatrix} x_1(t_0) & x_2(t_0) \end{bmatrix}^\top$ and unknowns $\begin{bmatrix} x_1 & x_2 \end{bmatrix}^\top = \begin{bmatrix} A & T \end{bmatrix}^\top$. The output variables y_1 and y_2 are the dynamic voltage U_dyn and the resistance R, respectively. The input vector u_1 is the source current I_s.

Network Model

For a circuit model we consider a current/voltage-oriented MNA presented in Section 2.7.1. A superconducting circuit model comprises voltage and current sources, time-varying resistors, inductors, capacitors as well as equivalent field models. An equivalent field model is given by a differential inductance, a compensation voltage source, and a time-varying resistance. The

differential inductance is extracted, by means of a quotient of the finite differences of the flux linkage and current, at the operating current I_0 prior to the field/circuit coupling

$$L_{\text{diff}} = \left.\frac{\Delta\varphi}{\Delta I}\right|_{I_0}. \tag{3.44}$$

Due to the nonlinear characteristics of an iron yoke and transient effects occurring in superconducting magnets, the differential inductance is insufficient to capture magnetic transient phenomena. Therefore, the differential inductance is assisted with a compensation voltage given as

$$\Delta U = U_{\text{field}} - U_{L_{\text{diff}}}, \tag{3.45}$$

where U_{field} and $U_{L_{\text{diff}}}$ are, respectively, voltages across the field model (3.40) and the corresponding differential inductance obtained from previous iterate of the field/circuit coupling algorithm [51]. The goal of ΔU is to compensate the voltages across the differential inductance so that only the induced voltage across the magnet from the field model is present in the circuit. The last component of the equivalent model is the resistance of the magnet extracted according to (3.42). Schematic of the circuital equivalence of a field model composed of a single electrical part is depicted in Fig. 3.18. Since both voltage waveforms have independent time step distributions, in order to avoid introducing interpolation we keep them separate and let the circuit solver resolve the differences.

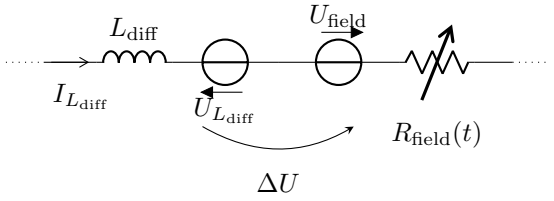

Figure 3.18: Schematic of the equivalent magnet model on the circuit side for the field/circuit coupling with a current-driven field model.

In case of multiple currents flowing through separate regions of the distributed model (as a result of e.g., multiple power converters or a CLIQ-based protection), the circuit model contains a differential inductance matrix and several assemblies of the type shown in Fig. 3.18. To conclude, the differential inductance L_{diff} is either a scalar or matrix, and acts as a pre-conditioner for the circuital equivalent field model. L_{diff} is kept constant during a time window, while nonlinear transient effects resulting in a variation of the effective differential inductance and resistance are accounted for as time-varying voltage sources and resistors, respectively.

In analogy to (3.43), the network model is also characterized in terms of an initial value problem as

$$F_{\text{circuit}}(x_3, \partial_t x_3, y_3, x_4, \partial_t x_4, y_4, u_2(t)) = 0 \tag{3.46}$$

with initial values $\begin{bmatrix} x_3(t_0) & x_4(t_0) \end{bmatrix}^\top$. The unknowns x_3 and x_4 are, respectively, the currents through the inductors and voltage sources, and nodal voltages. The output variables y_3 and y_4 are currents through differential inductances extracted from the field model $I_{L_{\text{diff}}}$ and the voltages across these inductors $U_{L_{\text{diff}}}$, respectively. The input vector u_2 comprises the field resistance R_{field}, the dynamic voltage from the field model U_{field} and the voltage across the differential inductance $U_{L_{\text{diff}}}$ in the circuit. Note that the voltage $U_{L_{\text{diff}}}$ acts as a self-reference, i.e., output signal from the previous iteration becomes an input to the current iteration. The self-reference voltage is part of the voltage compensation aimed at cancelling out the voltage across the inductance L_{diff} such that only the field voltage U_{field} is present in the circuit (as expected for a field/circuit coupling case).

Waveform Relaxation

For the coupling of field and circuit models we follow the formulation presented in [51]. We employ a Gauss-Seidel-type scheme with waveform relaxation algorithm as given in Section 3.1.4. The circuit model is solved as the first subsystem

$$F_{\text{circuit}}\left(x_3^{k+1}, \partial_t x_3^{k+1}, y_3^{k+1}, x_4^{k+1}, \partial_t x_4^{k+1}, y_4^{k+1}, u_2^k(t)\right) = 0 \tag{3.47}$$

with the following coupling conditions

$$\begin{aligned} U_{\text{field}}^{k+1} &= U_{\text{dyn}}^k, \\ R_{\text{field}}^{k+1} &= R^k, \\ U_{L_{\text{diff}}}^{k+1} &= U_{L_{\text{diff}}}^k = L_{\text{diff}} \partial_t I_{L_{\text{diff}}}^k. \end{aligned} \tag{3.48}$$

The second subsystem is the field model (3.43) represented as

$$F_{\text{field}}\left(x_1^{k+1}, \partial_t x_1^{k+1}, y_1^{k+1}, x_2^{k+1}, \partial_t x_2^{k+1}, y_2^{k+1}, u_1^{k+1}(t)\right) = 0 \tag{3.49}$$

with a coupling condition given as

$$I_{\text{s}}^{k+1} = I_{L_{\text{diff}}}^{k+1}. \tag{3.50}$$

The termination criterion of the convergence loop is given as follows

$$c_m(k) = \left(\max_{t \in \mathcal{T}_j} |y_m^k(t) - y_m^{k-1}(t)| < \text{absTol}\right) \vee \left(\max_{t \in \mathcal{T}_j} \frac{|y_m^k(t) - y_m^{k-1}(t)|}{|y_m^k(t)|} < \text{relTol}\right), \tag{3.51}$$

The termination criteria are chosen in order to cover a typical application of field/circuit coupling for superconducting magnets, namely a quench protection scenario. A quench protection scenario starts at relatively high current (for some cases even above 20 kA) for which the relative tolerance is effective. At the end of a current discharge, at low current levels as the current approaches 0 A, the relative tolerance may fail and therefore the absolute tolerance is put in place.

In order to verify the consistency of the proposed scheme, we calculate the power balance for an equivalent circuital representation of the field model

$$P_{\text{circuit}} = I_{L_{\text{diff}}}^{k+1}\left(L_{\text{diff}} \partial_t I_{L_{\text{diff}}}^{k+1} - L_{\text{diff}} \partial_t I_{L_{\text{diff}}}^k + U_{\text{field}}^k + I_{L_{\text{diff}}}^{k+1} R_{\text{field}}^k\right) \tag{3.52}$$

and the field model itself as the product of flow and effort variables

$$P_{\text{field}} = I_{\text{s}}^{k+1}\left(U_{\text{dyn}}^{k+1} + I_{\text{s}}^{k+1} R^{k+1}\right). \tag{3.53}$$

Considering an ideal case of perfect convergence, i.e., $I_{L_{\text{diff}}}^{k+1} = I_{L_{\text{diff}}}^k$, we note that the voltage across the differential inductance is entirely compensated by its value from the previous iterate. As a result, the circuit contains only the field dynamic and resistive voltages. Furthermore, the power on the circuit and field sides are equal up to sign.

Since the waveform relaxation algorithm is terminated after a finite number of iterations while the currents through the differential inductance from two consecutive iterates are below a certain tolerance, there is a loss of power due to the coupling. However, the error is bounded by the prescribed tolerance. In fact, the error can be made arbitrarily small by reducing either of the tolerances.

Voltage-Driven Mode

The voltage-driven mode for the considered field/circuit coupling is obtained by finding a dual circuit representation to the current-driven case. As it will be outlined, the dual circuital model consists of a differential inductance and two current sources for compensation to represent the field model and a resistance to account for both, the magnetic field and the temperature distribution from the field model. In order to obtain a monolithic simulation of a field model with an additional network equation certain enhancements to the field model are required, i.e., the network equations have to be embedded with the field model.

2D Magneto-Thermal Model

In order to excite the curl-curl equation (3.39) with a voltage waveform, we introduce an additional ordinary differential equation (ODE) as depicted in Fig. 3.19. The ODE derived from the KVL reads

$$U_{\mathrm{mag}} - U_{\mathrm{dyn}} - RI_{\mathrm{s}} = 0, \tag{3.54}$$

where U_{mag} is the input port voltage obtained from the accompanying electrical circuit. Recall that U_{dyn} is calculated as the time derivative of the flux linkage (2.80). The extraction of the integral quantities as well as the heat balance equation remain unmodified. The input vector u_1 in the initial value problem (3.43) is given as a voltage waveform (for details see the following Section). The output signal y_1 in this case is current I_{s}, which is the solution of (3.54).

Network Model

Figure 3.19 (left) depicts an equivalent circuital representation of a field model excited with a voltage waveform. The equivalent model is composed of three parallel branches. The first one is a series connection of an inductor L_{diff} and resistor R_{field}, which have the same role as in the current-driven setting. The second branch is a current source with input waveform set to the current through L_{diff} from the previous iteration. The last branch is also a current source with a value equal to the current calculated by the field problem in the previous iteration.

The inductor and resistor serve as pre-conditioners of the field model on the circuit side. The differences between the field model and its circuital representation are accounted for by means of the current source compensation

$$\Delta I = I_{\mathrm{field}} - I_{L_{\mathrm{diff}}}. \tag{3.55}$$

The result of the compensation is to obtain a current equal to the current calculated by the field model in the output node of the equivalent model according to KCL.

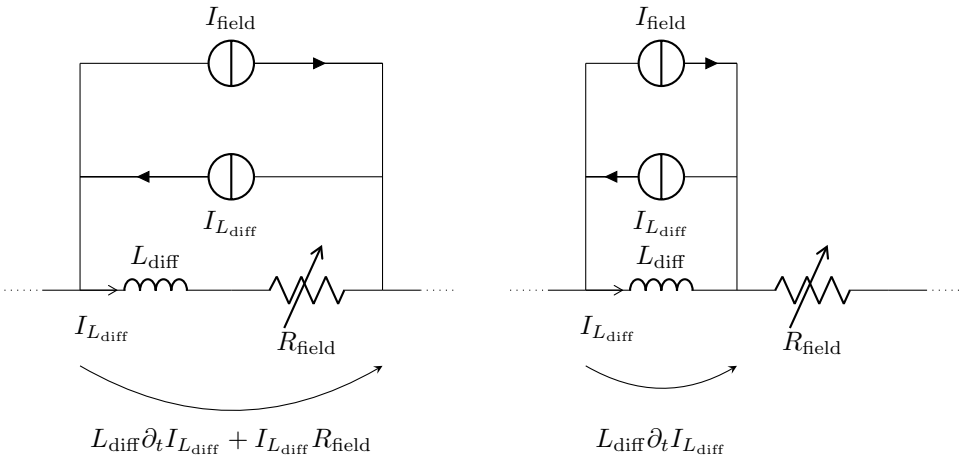

Figure 3.19: Schematic of the equivalent field model on the circuit side for the field/circuit coupling in a voltage-driven setting with (left) and without (right) time-varying resistance in the parallel branch with the inductance.

The discussed setting also supports magnet model subdivision into several electrical parts with distinct voltage excitations. In this case several equivalent models are added to a circuit and their mutual coupling is incorporated by means of a differential inductance matrix. The circuit model takes the same representation in terms of an initial value problem as for the current-driven case (3.46).

Another scheme with current sources forming compensation only in parallel to the inductor L_{diff} was also investigated (as shown in Fig. 3.19, right). With this setup, the current flowing

through resistor R_{field}, in case the convergence is reached, is equal to the field current. As a result, the voltage across the resistor on the field an circuit side are equal (up to the desired tolerance). However, numerical experiments presented in Section 3.3.3 dedicated to field/circuit coupling of a superconducting magnet indicated that both schemes have very similar performance. Further, theoretical investigation is required in order to draw conclusion on equality of both schemes.

Waveform Relaxation

Analogously to the current-driven case, we employ a Gauss-Seidel-type scheme with the waveform relaxation algorithm as given in Section 3.1.4. The termination criteria are the same as in the prior case. The first subsystem is the circuit model

$$F_{\text{circuit}}\left(x_3^{k+1}, \partial_t x_3^{k+1}, y_3^{k+1}, x_4^{k+1}, \partial_t x_4^{k+1}, y_4^{k+1}, u_2^k(t)\right) = 0 \tag{3.56}$$

with the following coupling conditions

$$\begin{aligned} I_{\text{field}}^{k+1} &= I_{\text{s}}^k, \\ R_{\text{field}}^{k+1} &= R^k, \\ I_{L_{\text{diff}}}^{k+1} &= I_{L_{\text{diff}}}^k. \end{aligned} \tag{3.57}$$

The field model (3.43) is again considered as the second subsystem

$$F_{\text{field}}\left(x_1^{k+1}, \partial_t x_1^{k+1}, y_1^{k+1}, x_2^{k+1}, \partial_t x_2^{k+1}, y_2^{k+1}, u_1^{k+1}(t)\right) = 0. \tag{3.58}$$

with a coupling condition given as

$$U_{\text{mag}}^{k+1} = L_{\text{diff}} \partial_t I_{L_{\text{diff}}}^{k+1} + I_{L_{\text{diff}}}^{k+1} R_{\text{field}}^k. \tag{3.59}$$

The power balance for an equivalent circuital representation of the field model reads

$$P_{\text{circuit}} = \left(L_{\text{diff}} \partial_t I_{L_{\text{diff}}}^{k+1} + I_{L_{\text{diff}}}^{k+1} R_{\text{field}}^k\right)\left(I_{L_{\text{diff}}}^{k+1} - I_{L_{\text{diff}}}^k + I_{\text{field}}^{k+1}\right). \tag{3.60}$$

The power of the field model is calculated from the input port yields

$$P_{\text{field}} = I_{\text{s}}^{k+1} U_{\text{mag}}^{k+1}. \tag{3.61}$$

Considering the perfect convergence, i.e., $I_{L_{\text{diff}}}^{k+1} = I_{L_{\text{diff}}}^k$, we note that the the currents flowing through the differential inductance and current source from two consecutive iterates cancel each other out. As a result, the output current of the compensation branch is exactly equal to the field current. The power on the circuit and field side are equal up to sign, which confirms the consistency of the proposed scheme.

Coupling of Two Lumped Element Models

As the first step in analyzing the field/circuit coupling algorithms, we will compare current- and voltage-driven modes considering co-simulation of two lumped element models. We will employ causality analysis of bond graphs representing the coupled models. Such an analysis is aimed at determining whether the "field" model has preferred or non-preferred causality on the storage element. Causality has direct implications on the stability of numerical schemes as integral causality is more stable than the differential one.

These considerations are illustrated with a numerical experiment. We consider an RL circuit with $L_{\text{diff}} = 0.1$ H and $R_{\text{circuit}} = 1\ \Omega$. The "field" model consists of an inductor $L_{\text{field}} = 0.09$ H connected to either a current or a voltage source. Hence, the equivalent circuital model overestimates the inductance of the "field" model. The overall simulation time $t \in [0, 0.4]$ s is divided into $N = 4$ time windows of equal length $H = 0.1$ s. Both models are implemented with ORCAD Cadence PSpice with maximum time step $h = 100$ µs and an absolute tolerance equal to 10^{-10} A. Models are co-simulated with the Gauss-Seidel type waveform relaxation algorithm; see Section 3.1.4. The convergence criteria are based on $I_{L_{\text{diff}}}$ with relTol $= 5 \cdot 10^{-5}$ and absTol $= 1$ mA. The expected solution is an exponential decay of the circuit current with a time constant $\tau_{\text{RL}} = L_{\text{field}}/R_{\text{circuit}}$.

Current-Driven Mode

Fig. 3.20 shows electrical schematics of the circuit and "field" models for the field/circuit coupling in the current-driven mode. Since the "field" model contains only a lumped inductor, the corresponding circuital equivalent model does not include time-varying resistance, i.e., $R_{\text{field}} = 0\ \Omega$.

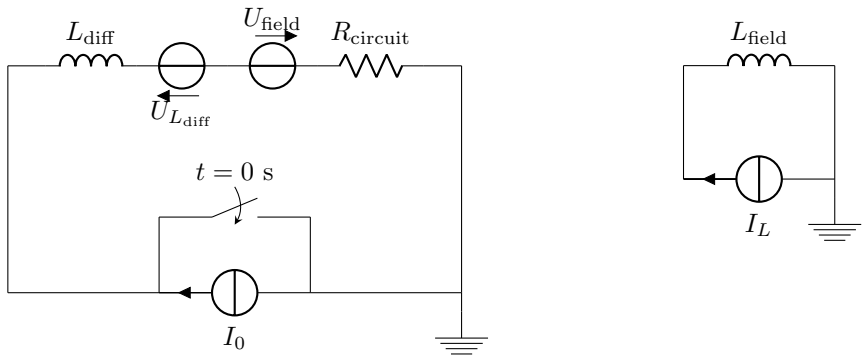

Figure 3.20: Left: Schematic of the RL circuit with an equivalent model for the current-driven case. Right: "Field" model with a lumped inductance L_{field} and a current source I_L.

A bond graph representing the considered circuit model for the current-driven mode is depicted in Fig. 3.21. The series connection of components is represented by means of a 1-junction. The sources of effort are setting effort and the circuit resistance also has an effort-out causality. The inductor L_{diff} with input effort has preferred, integral causality. A bond graph representation of the "field" model consists of a source of flow for I_{Lfield} and an I-type storage for L_{field}. As a result, the "field" inductor has non-preferred, differential causality and indicated by an orange bar in Fig. 3.21).

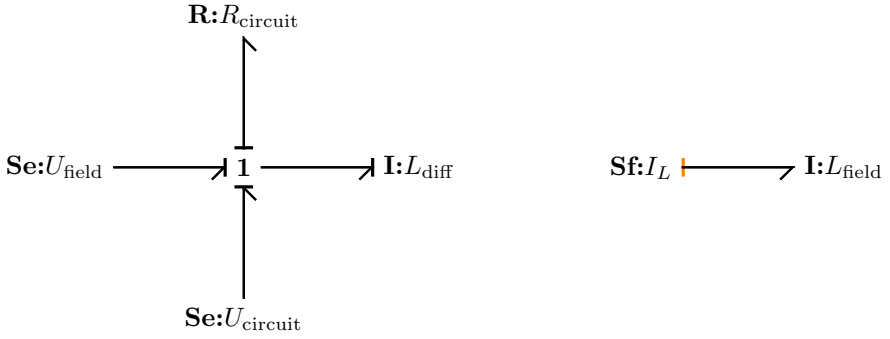

Figure 3.21: Bond graph of the circuit model (left). Bond graph of the "field" model with non-preferred differential causality denoted in orange (right).

Fig. 3.22 presents the current profile obtained from the co-simulation along with an analytical solution. The compensation voltage (3.45) accounting for the differences in the dynamic behavior of coupled models is also shown in Fig. 3.22.

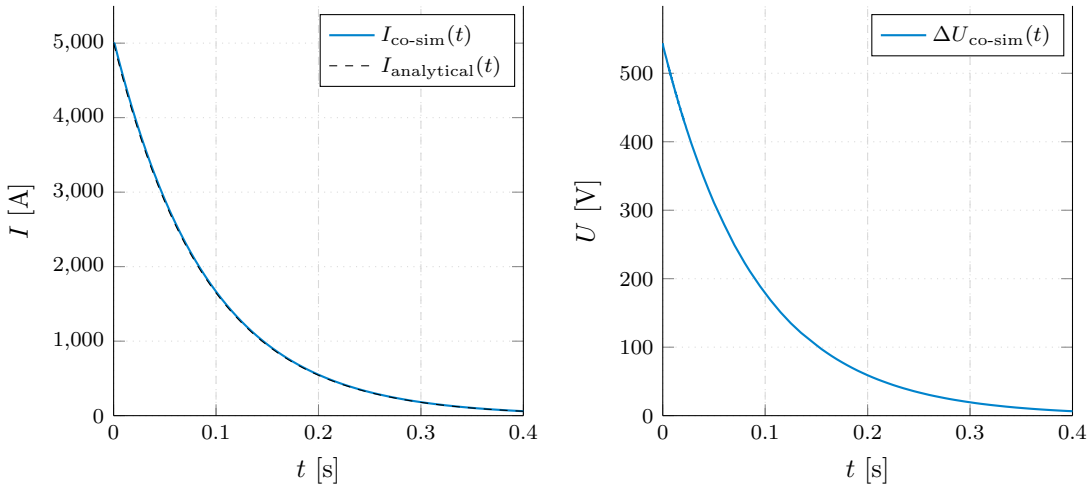

Figure 3.22: Current evolution during the co-simulation compared to analytical solution (left). Compensation voltage (right).

The current obtained with the field/circuit coupling is in a very good agreement with the expected analytical solution $I(t) = I_0 e^{-t/\tau_{\text{RL}}}$. The difference between "field" and circuit inductance was compensated by means of voltage sources (3.45). Since $L_{\text{diff}} > L_{\text{field}}$ for a given current profile, the induced voltage across the differential inductance on the circuit side is larger than the induced voltage of the "field" model. Thus, the compensation voltage is positive in order to reduce the steepness of the current profile as compared to a setup without any compensation.

Voltage-Driven Mode

A schematic representation of both coupled models is presented in Fig. 3.23. Similarly as for the previous case, the pre-conditioner is only composed of the differential inductance.

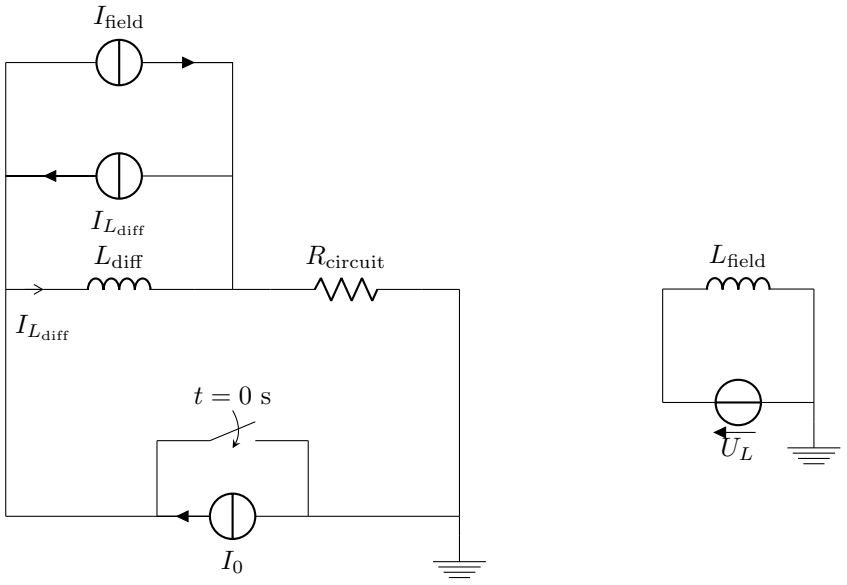

Figure 3.23: Left: Schematic of the RL circuit with an equivalent model for the voltage-driven case. Right: "Field" model with a lumped inductance L_{field} and a voltage source U_L.

Bond graph models representing the "field" and circuit models from Fig. 3.23 for a voltage-

driven mode are depicted in Fig. 3.24. The circuit model comprises a 0-junction and the storage element L_{diff} has preferred, integral causality. The "field" model, with a source of effort also has preferred, integral causality (see Fig. 3.24).

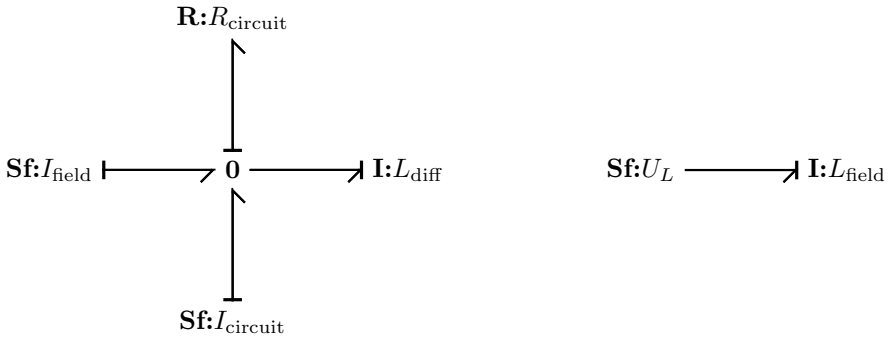

Figure 3.24: Bond graph of the circuit model with preferred, integral causality (left). Bond graph of the "field" model with preferred, integral causality (right).

A comparison of current calculated with the field/circuit coupling and the analytical solution are compared in Fig. 3.25 (left). Fig. 3.25 (right) shows the compensation current due to the estimation inaccuracy of the "field" inductance on the circuit side.

Also for the voltage-driven setting, the field/circuit coupling reproduced the analytical solution with the requested accuracy. The current compensation has a negative value indicating that the current calculated by the "field" model is larger than the current flowing through the differential inductance on the circuit side. This is due to the fact that the time constant of the circuit model is larger then the one of the "field" model.

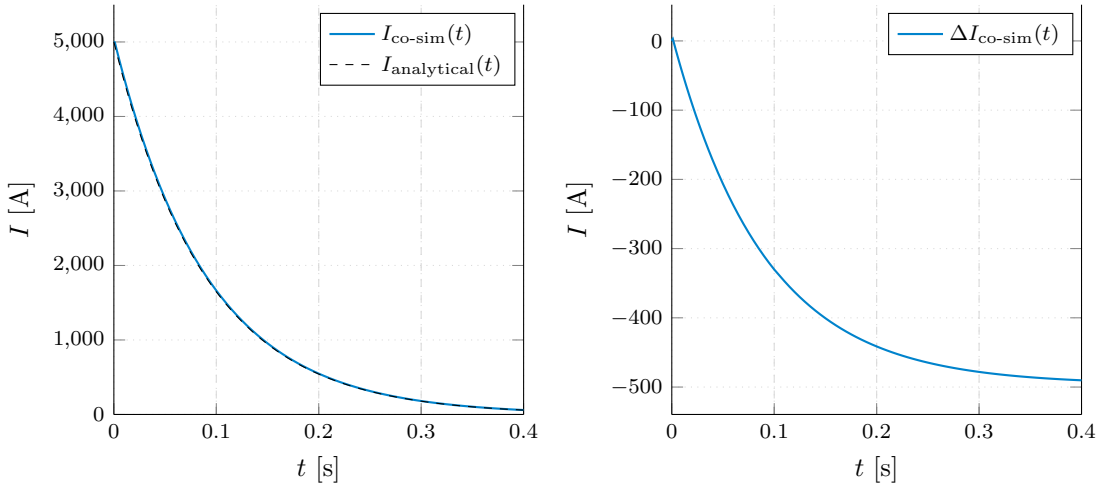

Figure 3.25: Left: Current evolution during the co-simulation compared to analytical solution. Right: Compensation current.

In both cases the results are in a very good agreement with the analytical solution, which verifies the consistency of the coupling scheme. Now we compare the convergence of both operating modes. Fig. 3.26 denotes the number of iterations per time window needed to reach convergence. As one can notice, in the first time window, the current-driven mode required four iterations more as compared to the voltage-driven mode in order to adjust the compensation element to the desired accuracy. For the following three time windows the number of iterations was the same and equal to four (recall that the iterations are 0-based).

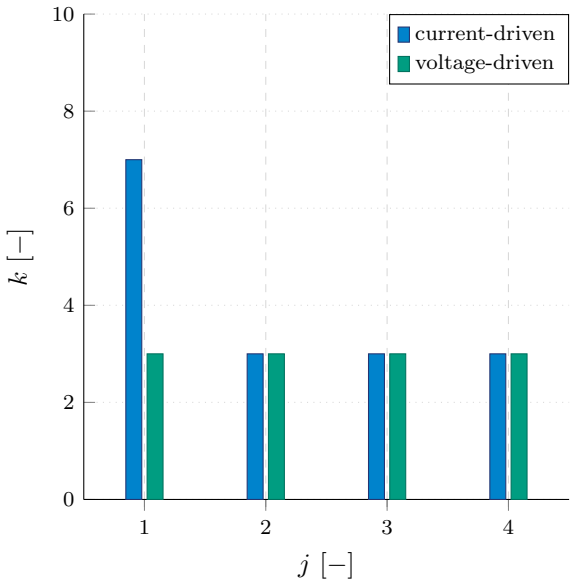

Figure 3.26: Comparison of number of convergence iterations per time window for both, current- and voltage driven modes.

Comparison of relative and absolute tolerance calculated according to the convergence criterion (3.51) are presented in Fig. 3.27.

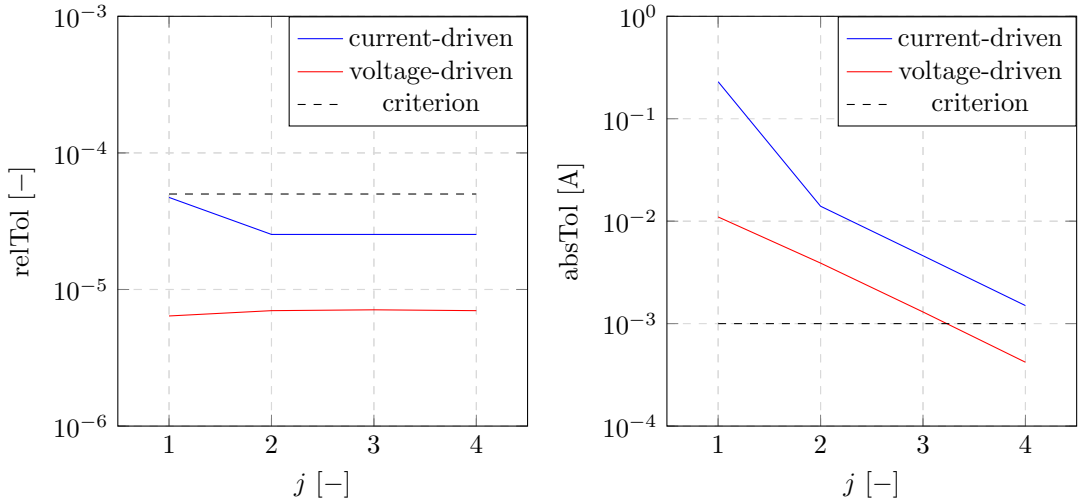

Figure 3.27: Comparison of relative (left) and absolute (right) tolerance per time window

Despite fewer iterations in the first window, the voltage-driven mode converged to a solution with smaller by an order of magnitude relative and absolute tolerances. For the following time windows, with equal number of iterations, the difference is maintained.

For the given setup, the current-driven mode could not achieve a relative tolerance below 10^{-5}, while the voltage-driven mode converged to a relative tolerance below 10^{-7}. This study confirms that integral causality for both, "field" and circuit models leads to better numerical stability and smaller errors. A similar conclusion for the voltage-driven mode can be drawn on the basis of index analysis as discussed in [16]. To conclude, the voltage-driven case is more stable and, therefore, less expensive numerically.

Coupling of a Distributed and Lumped Element Model

In this Section the field/circuit coupling algorithm is illustrated with a realistic case of a standalone dipole magnet protected by a CLIQ system. The electrical circuit is represented in Fig. 3.28 and comprises two equivalent models with mutually coupled inductors representing the field model. The field model is a single aperture separation dipole magnet D1. The magnet is 6.27-meter long and other parameters relevant for the simulation are taken from [62]. The electrical circuit is simulated with ORCAD Cadence PSpice and an absolute tolerance of the Newton-Raphson method equal to 10^{-10} A. We employ a 2D magneto-thermal model developed in COMSOL with an absolute tolerance for the Newton-Raphson scheme set to 10^{-3} Wb, 10^{-3} K. The solver tolerances of both field and circuit models are a trade off between the numerical accuracy and the computation time and are based on experience. Details on the FEM formulation and implementation are reported in [48]. Due to the symmetry of the MQS model, we only consider a half of the geometry as shown in Fig. 3.28.

The initial current of the power converter I_0 is equal to 11 kA. At $t = 0$ s the power converter is switched off and a CLIQ unit is triggered. The CLIQ unit consists of a capacitor bank of capacitance $C_{\text{CLIQ}} = 50$ mF charged to an initial voltage of $V_{\text{CLIQ}}(t = 0\text{ s}) = 1000$ V with resistance of leads equal to $R_{\text{CLIQ}} = 20$ mΩ. The circuital model of the magnet consists of two equal self-inductances $L_1 = L_2 = 8.69$ mH corresponding to the upper and lower pole, respectively, with a mutual inductance $M_{12} = M_{21} = 3.74$ mH calculated at I_0. Hence, the total differential inductance is equal to 24.85 mH. With the presence of an iron yoke, the differential inductance varies with the source current as shown in Fig. 3.35.

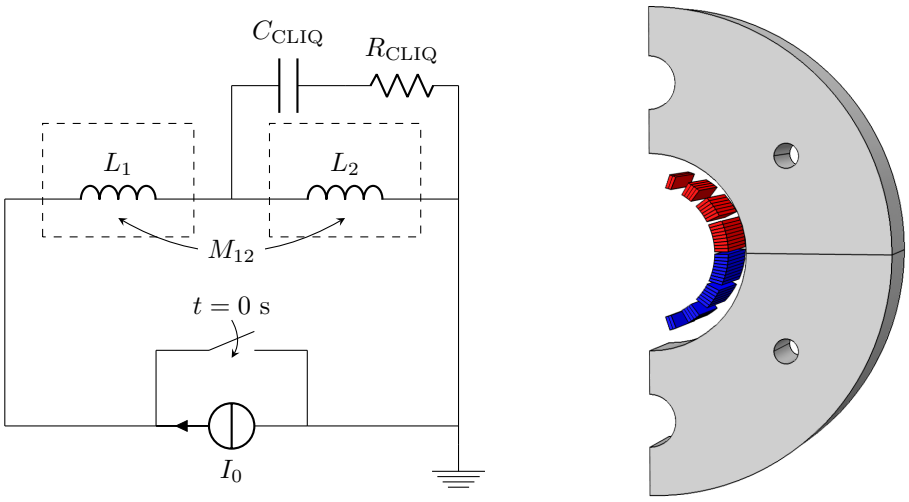

Figure 3.28: Schematic of a circuit with two mutually coupled electrical parts protected by a CLIQ unit and a power converter with initial current I_0 switched off at $t = 0$ s (left). Geometry of the D1 magnet with the upper coil L_1 in red, the lower coil L_2 in blue and the iron yoke in gray (right).

The total co-simulation time is equal to 0.5 s and is divided into $N = 8$ time windows. The first time window is very short in order to accurately resolve the commutation of the CLIQ unit. The size of following windows is relaxed as the current transient is being damped. The time window definition and maximum time steps for field and circuit models are reported in Table 3.4 and are based on experience.

Table 3.4: Definition of time window sizes and maximum time steps for circuit and field models.

j	0	1	2	3	4	5	6	7
H	$[0{,}5 \cdot 10^{-4}]$	$[5 \cdot 10^{-4}{,}0.01]$	[0.025,0.05]	[0.05,0.1]	[0.1,0.2]	[0.2	0.35]	[0.35,0.5]
$h_{\text{max,circuit}}$	10^{-6}	10^{-5}	$2 \cdot 10^{-5}$	$4 \cdot 10^{-5}$	10^{-4}	$2 \cdot 10^{-4}$	$5 \cdot 10^{-4}$	$5 \cdot 10^{-4}$
$h_{\text{max,field}}$	$5 \cdot 10^{-6}$	$5 \cdot 10^{-5}$	10^{-4}	$2 \cdot 10^{-4}$	$5 \cdot 10^{-4}$	10^{-3}	10^{-3}	10^{-3}

The aim of this study is to compare current- and voltage-driven modes, which requires to change library components of inductors surrounded by dashed rectangles (see Fig. 3.28), *IOPort* array definition, and the field model. Co-simulation results are compared to the solution of a monolithic field model with integrated equations of the electric circuit shown in Fig. 3.28. The circuit equations are implemented in a similar fashion as for the voltage-driven mode (3.54). The KVL and KCL yield the following set of differential equations

$$\begin{aligned} U_{\text{dyn},1} + R_1 I_{\text{s},1} + U_{\text{dyn},2} + R_2 I_{\text{s},2} + R_{\text{crow}} I_{\text{s},1} = 0, \\ R_{\text{CLIQ}} \left(I_{\text{s},2} - I_{\text{s},1} \right) + V_{\text{CLIQ}} + U_{\text{dyn},2} + R_2 I_{\text{s},2} = 0, \\ C_{\text{CLIQ}} \partial_t V_{\text{CLIQ}} + I_{\text{s},1} - I_{\text{s},2} = 0, \end{aligned} \tag{3.62}$$

where R_i and $U_{\text{dyn},i}$ are, respectively, the resistance and the induced voltage of a coil section i, for $i = 1, 2$. We do not consider the CLIQ switch commutation and assume that the power converter crowbar resistance has constant value during the discharge $R_{\text{crow}} = 100$ µΩ.

Causality Analysis Based on the Bond-Graph Model

The analysis of computational causality for the field/circuit coupling is carried out on the basis of the bond graph model of a superconducting magnet (Fig. 2.39). In order to simplify the analysis, hereunder, we neglect the thermal domain as well as the eddy, coupling, and persistent currents, which does not impact the causality analysis for the storage element. This is motivated by the fixed causality of the Stokes-Dirac structure representing the interconnection of the magnetic domain (2.90). In addition, recall that the injection structures (2.80) distributing lumped inductive and dynamic voltage as well as current in the coil domain also have fixed causalities (flow-in, effort-out). In the following we keep fixed causality of the injection components and check the causality assignment. For both excitation modes, there is a causal conflict for the bond linking the injection and the Stokes-Dirac structure as both have fixed causalities (see red stroke in Fig. 3.29 and 3.30). This is expected for the magnetoquasistatic system, for which the right hand side of the system of equation has to be inverted; in fact, the inversion occurs after the injection element. Moreover, in both cases there is a preferred, integral causality on the storage.

For the current-driven case, the input port has the flow-out causality. This results in no causal conflicts on the 1-junction representing the input voltage divider. As a result, the input current can be directly applied to the coil domain.

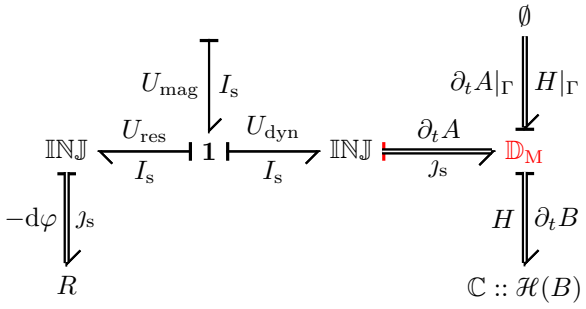

Figure 3.29: Current-driven case (flow-out causality).

For the voltage-driven case, however, the input port is characterized by the effort-out causality. This inevitably leads to a causal conflict for the 1-junction (marked by a red causal stroke). Since, the causality can be easily flipped for the input port, we mark the conflict by red strokes on bonds connected from the 1-junction to both injections. The conflict is resolved with the additional ODE to which the distributed model is coupled. The solution of the ODE is current that is then distributed in a similar fashion as for the current-driven case, i.e., the current is applied to the coil domain.

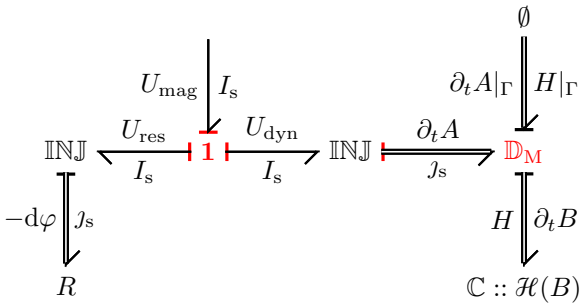

Figure 3.30: Voltage-driven case (effort-out causality).

Results for the Current-Driven Mode

A comparison of current and resistance profiles during the discharge for both electrical parts are shown in Fig. 3.31 (left). Fig. 3.31 (right) presents the evolution of the compensation voltage.

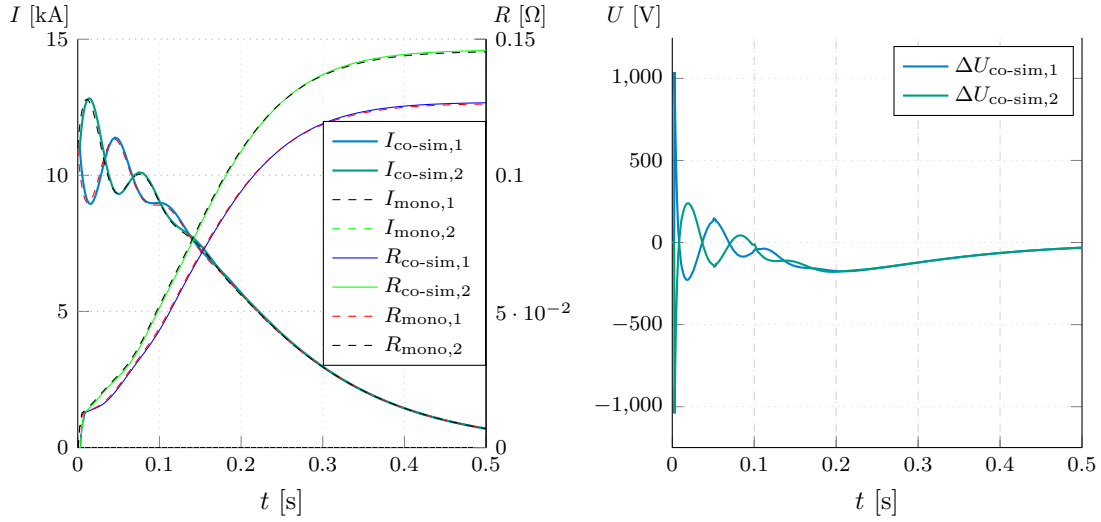

Figure 3.31: Left: Current evolution during the co-simulation compared to a monolithic solution. Right: Evolution of compensation voltages.

Discharge of the capacitor to the magnet results in current oscillations, which induce inter-filament coupling losses. These losses are capable of transforming a large volume of the magnet to the normal conducting state. The resistance, growing after a quench, damps the oscillations and decreases the current. Both, the current and resistance are in a good agreement with the reference profiles. The compensation voltage is initially equal to 1000 V, which is the CLIQ charging voltage, and afterwards its magnitude decreases and oscillates with the frequency of the current profile.

Results for the Voltage-Driven Mode

As one can notice in Fig. 3.32 (left), a comparison of current and resistance evolution also reproduced monolithic results with an acceptable accuracy. The compensation current confirms that, initially, the differential inductance on the circuit side is underestimated, while for $t > 0.2$ s, as the current decreases the differential inductance is overestimated.

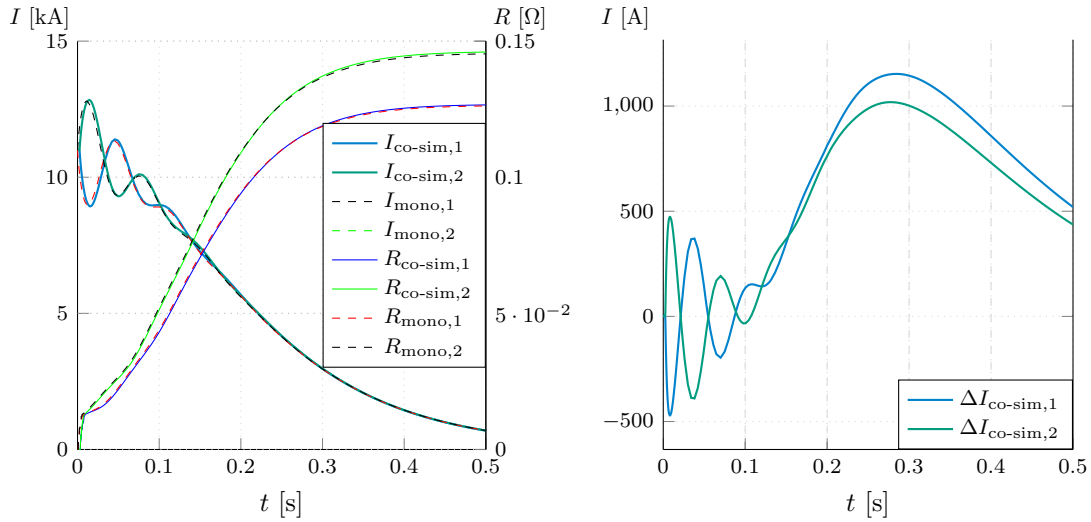

Figure 3.32: Left: Current evolution during the co-simulation compared to a monolithic solution. Right: Waveforms of compensation currents.

The number of iterations per time window is compared and reported in Fig. 3.33. The performance of the voltage-driven mode, expressed in terms of iterations, was at least as good as for the current-driven mode. For several windows ($j = \{2, 3, 4, 5, 7, 8\}$) the former mode performed better and required fewer iterations. This difference is reflected on the computation time as the current-driven mode required 9891 s and the voltage-driven one required 6837 s. The monolithic simulation was solved in 643 s. In terms of the computation time, the monolithic study outperformed the field/circuit coupling for the case of a standalone magnet. However, monolithic approach is not suited to simulation of large superconducting circuit models and distributed magnet models due to large number of elements in the circuit.

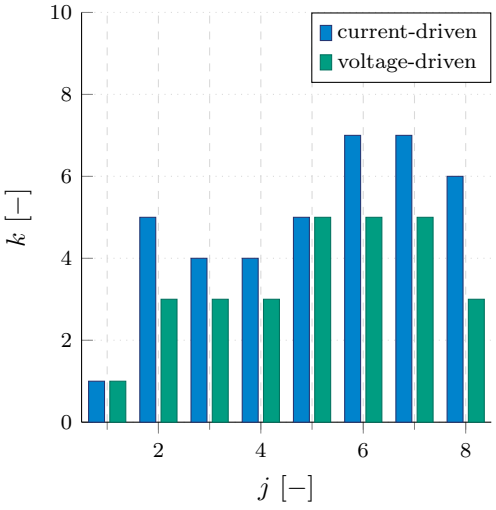

Figure 3.33: Comparison of number of iterations per time window.

Comparison of relative and absolute convergence is presented in Fig. 3.34. For all the windows the relative tolerance was below 10^{-3} and the absolute tolerance below 10 A.

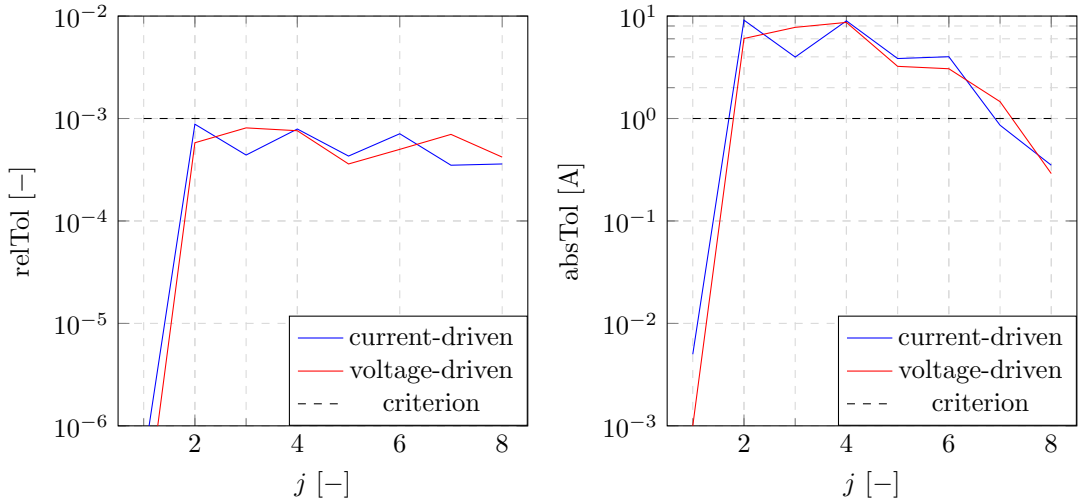

Figure 3.34: Comparison of relative (left) and absolute (right) tolerance per time window.

The study confirmed hints provided by the causality analysis of the bond graph model: a change of the causality of the input port does not change the causality of the storage element, and both operating modes result in a similar numerical scheme. However, unlike for the lumped element systems for which the integral causality yields better convergence, for the distributed parameter systems, the integral causality does not bring the same conclusion. In particular, the distributed systems are not only discretized in time, but also in space, which has to be considered in the analysis of the numerical stability. Better convergence of the voltage-driven mode can be explained by the presence of the resistance pre-conditioner on the field side (3.54). However, further numerical and theoretical investigation is necessary in order to quantify the differences between both numerical schemes.

Note on Optimization of Field/Circuit Coupling

In the presented case, almost all time windows required more than two iterations in order to reach the desired convergence rate. One of the reasons is inaccuracy of the pre-conditioner element in the circuit model for which iterations allow to adjust the compensation component (either voltage or current) in the equivalent model. Thus, there is certain potential to improve the computational performance. We present two potential concepts for performance improvements. The first one is to update the pre-conditioner element on the circuit side at the operating point of the field model. The second one aims at improving convergence in periods of large current variations. These periods are characterized by a decrease of the differential inductance of the field model. As a consequence the compensation component in the equivalent models has to be adjusted accordingly and this process might require a large number of convergence iterations.

Updating Differential Inductance at Each Time Window

Due to the nonlinear characteristics of the iron yoke, the differential inductance can vary during the current discharge from the nominal value to 0 A as shown in Fig. 3.35. Even though the inductance is kept constant during each time window, its value can be updated at the communication points with a value corresponding to the operating current. As a result the amplitude of the compensation element (either a voltage or a current source) should be decreased and the algorithm would require fewer iterations to converge.

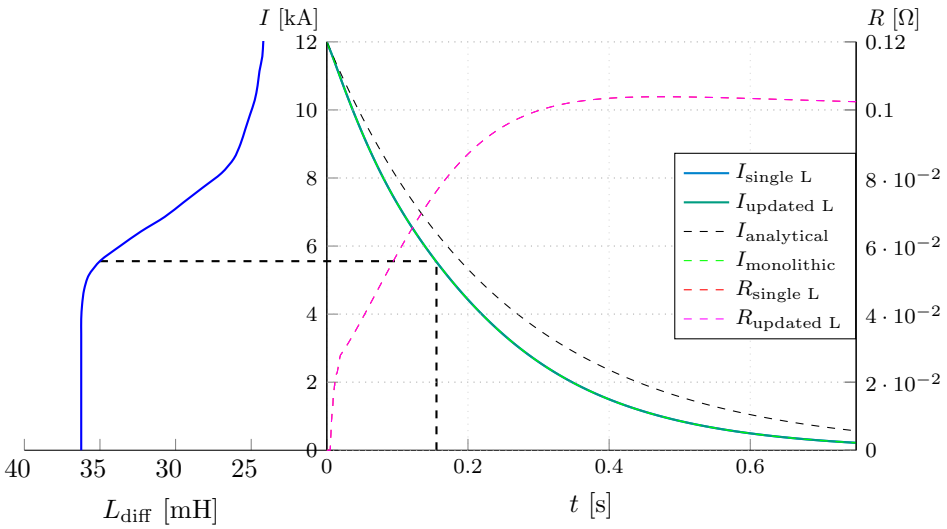

Figure 3.35: Left: Differential inductance of the D1 magnet as a function of the transport current. Right: Comparison of the current discharge for an analytical (constant differential inductance and no internal magnet resistance), monolithic, and co-simulated solutions. The monolithic and co-simulated solutions feature resistance growth due to the fast decay of current, which induces inter-filament coupling current losses capable of quenching the magnet (so-called quench-back).

This concept is illustrated by means of a current-discharge of the D1 magnet in series with a dump resistor $R_{\text{dump}} = 0.1\ \Omega$. The initial current of the magnet is equal to 12 kA and at $t = 0$ s, the power converter is shut down and bypassed with a crowbar. The electrical circuit is solved with the ORCAD Cadence PSpice and the field model is simulated with COMSOL. The setting of the absolute tolerances for both solvers is the same as for the CLIQ discharge of the D1 magnet.

The co-simulation time is equal to 0.74 s and is divided into $N = 37$ windows of equal length $H = 20$ ms. The maximum time step of the circuit model is equal to 100 µs and the field model equal to 1 ms and are kept constant for all the windows. We employ the current-driven mode since the interpretation of the voltage compensation is more intuitive as compared to the voltage-driven one. Two cases are considered: (i) the differential inductance is extracted from the field model only prior execution of the first time window; (ii) the differential inductance is calculated prior execution of each time window.

The obtained current discharge is depicted in Fig. 3.31 and compared to a monolithic solution. An analytic solution with a constant value of the differential inductance ($L = 36$ mH) is reported in order to highlight differences due to the differential inductance variation and resistance growth.

The compensation voltage for both considered scenarios is reported in Fig. 3.36. For the case of the differential inductance updates a saw-tooth profile is obtained as the compensation is not needed at the beginning of each time window. The compensation voltage profile for the case of the single differential inductance calculation features small spikes at the boundaries of several windows. This phenomena is due to the calculation of the induced field voltage as a time derivative of the spline interpolation of the flux linkage in a post-processing step. This is due to the fact that COMSOL does not provide a direct access to the time derivative of the flux linkage from the solution of the field model.

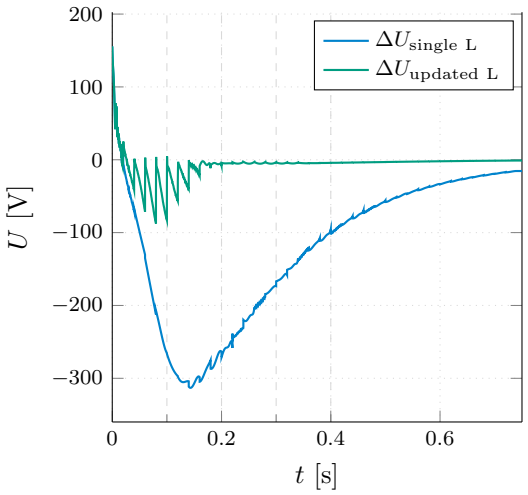

Figure 3.36: Voltage compensation during the co-simulation compared to analytical solution.

For the sake of readability, in Fig. 3.37 we present the number of iterations for the first 20 time windows as for the following 17 only two iterations were required ($k = 1$). For the considered scenario, three regions can be identified: (i) for $0 \leq j \leq 10$ biggest variations of the differential inductance; (ii) for $11 < j \leq 18$ the differential inductance changes according to the $L_{\text{diff}}(I)$ characteristics in Fig. 3.35; (iii) for $j > 19$ the dynamic effects are decaying and the differential inductance reaches a constant value for low currents ($I < 1$ kA).

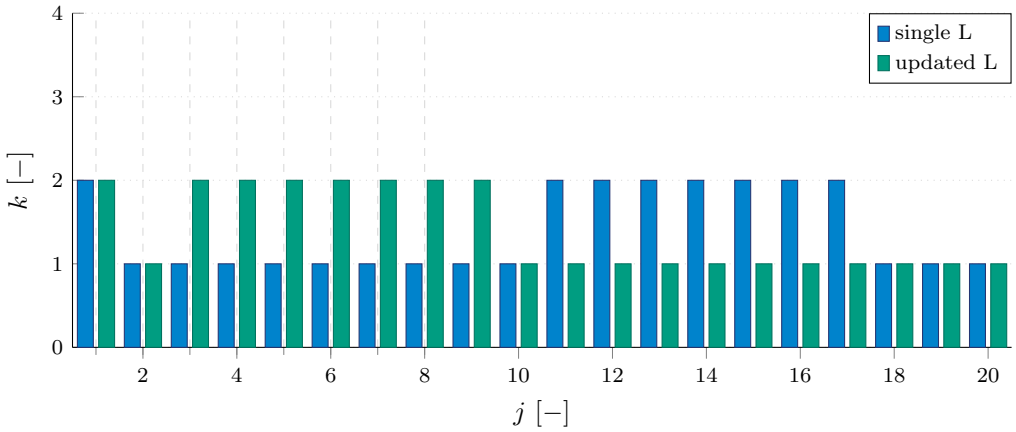

Figure 3.37: Comparison of number of convergence iterations per time window.

Overall, the number of iterations is the same. However, the updates of the differential inductance led to the relative tolerance an order of magnitude lower, which stems from better approximating the field model on the circuit side as indicated in Fig. 3.38. As shown in Fig. 3.36, the updates result in decrease of the amplitude of the compensation voltage. Lower amplitude translates into fewer iterations needed to reach that value. Comparing both cases for $t > 0.2$ s we note that the updates of differential inductance translate into fewer iterations. Since the relative tolerance is lower with updates of the differential inductance, larger time windows can be afforded. For current below 5 kA the differential inductance remains constant as the iron yoke operates in the linear part of its magnetization characteristics.

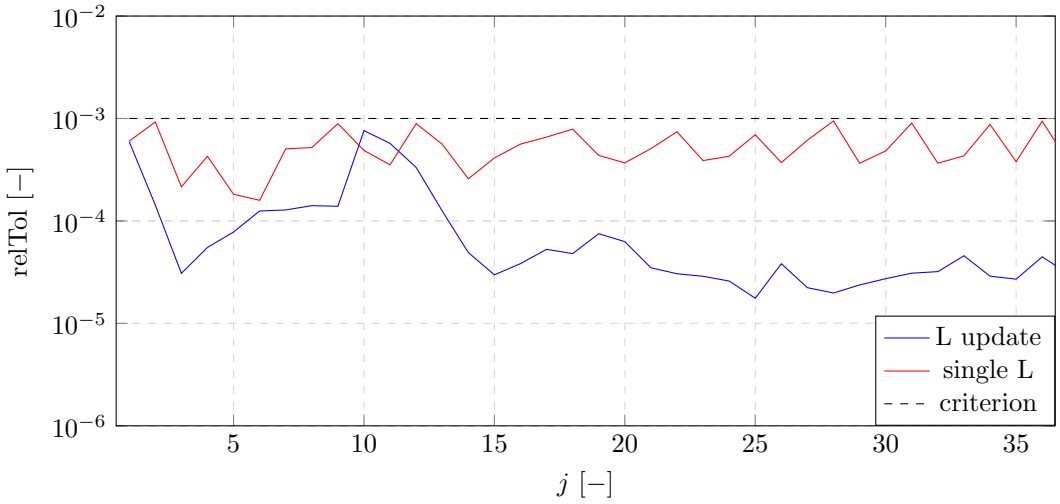

Figure 3.38: Comparison of relative tolerance per time window

Despite a mere estimation of the differential inductance during the entire current discharge, the compensation voltage is still required in order to account for transient effects occurring in the field model.

Scaling of the Differential Inductance on the Circuit Side

The current variation during a discharge results in a magnetic field change that in turn causes coupling losses. These losses result in a decrease of the apparent differential inductance, especially in the initial phase of a discharge. In [51] it was indeed shown that an empirical decrease of the pre-conditioner differential inductance reduced the number of iterations in the first time window and effectively reduced the computational effort. A further decrease of the differential inductance deteriorated performance.

The highly nonlinear behavior of the coupled problem makes it impossible to analytically determine the value of the scaling factor. Nonetheless, results of a given co-simulation can be utilized to perform an optimization of the scaling factor in order to find its suitable value. Furthermore, the solution obtained from the first iteration could be helpful to estimate the value of the scaling factor. Such an approach could be profitable for parametric sweep studies for which parameters do not vary drastically from simulation to simulation.

3.3.4 2D Magneto-Thermal Field/Mechanical Field Coupling

In this Section we present a one-way coupling algorithm for distributed magneto-thermal and mechanical models of superconducting accelerator magnets. The latter models are typically used in the design of the mechanical structure and the optimization of the magnetic field quality in nominal conditions. Furthermore, analysis of mechanical response of quenching magnets, which experience variation of the Lorentz force and temperature, is important in case of superconducting coils composed of a brittle material such as Nb_3Sn. Additionally, protection of these coils with a CLIQ [63], [8] system brings to mind a question on the mechanical response of the magnet structure to the current overshoot during a CLIQ discharge.

The field/circuit coupling algorithm discussed in Section 3.3.3 was employed to determine the temperature and magnetic field distribution in the magnet cross-section during the CLIQ discharge. Then, the temperature and the Lorentz force were set as a load to an existing mechanical model by means of a one-way coupling algorithm. Since the models are typically discretized with different meshes, we apply a mesh-based interpolation technique to transfer coupled quantities.

There have been already several approaches to analysis of the Lorentz force impact on the superconducting accelerator magnet structure. Milanese has proposed a method for the interpolation of electromagnetic forces calculated with the electromagnetic ROXIE model [14] to a mechanical model developed in ANSYS [64]. Caspi et al. have developed an integrated workflow to electrical, thermal, and mechanical analysis of the magnet-design process [15]. In contrary to already presented coupling schemes, we use existing, magneto-thermal and mechanical models which are typically computed out with COMSOL Multiphysics [65] and ANSYS APDL [66], respectively. For the mesh-based interpolation, we employ the MpCCI (Multi-physics Code Coupling Interface) environment [67] providing a generic coupling mechanism. MpCCI was used to solve coupled problems involving mesh-based interpolation in other fields [68], [69].

2D Magneto-Thermal Model

We employ the 2D magneto-thermal distributed model presented already for the field/circuit coupling (cf. Section 3.3.3) [48]. The coil is composed of half-turns with homogenized material properties and physical laws.

The strongly coupled curl-curl (3.39) and heat balance equations (2.107) are represented in terms of a differential-algebraic initial-value problem

$$F_{\mathrm{mag-th}}(x_1, \partial_t x_1, y_1, x_2, \partial_t x_2, y_2, u_1(t)) = 0 \tag{3.63}$$

with unknowns $\begin{bmatrix} x_1 & x_2 \end{bmatrix}^\top = \begin{bmatrix} A & T \end{bmatrix}^\top$. The output variables y_1 and y_2 are the Lorentz force $F_{\mathrm{L}} = \jmath_{\mathrm{s}} \times (\nabla \times A)$ with $\jmath_{\mathrm{s}} = \chi I_{\mathrm{s}}$ being the current density and temperature T, respectively. The input vector u_1 is the source current I_{s} obtained with the field/circuit coupling.

The temperature distribution T in the coil and the Lorentz force F_{L} are provided as a load for the mechanical model.

2D Mechanical Model

A 2D mechanical model of a superconducting magnet allows replicating the magnet-assembly operations. This approach is employed to find proper dimensions as well as materials for the structural components. The goal of this analysis is to ensure that, once the magnet is assembled and cooled down, the structural elements remain in good contact and after powering the coil windings are still compressed. In this quench protection study we consider the impact of not only the Lorentz force but also the temperature evolution in the magnet cross-section.

The mechanical model is characterized by a static linear elastic equation (Navier-Cauchy equation [70], [71])

$$\mu \Delta u + (\lambda + \mu) \nabla (\nabla \cdot u) + F_T(T) + F_{\mathrm{L}}(\jmath_{\mathrm{s}}, A) = 0, \tag{3.64}$$

where u denotes the displacement vector, μ and λ are the Lamé parameters given as

$$\mu = \frac{E}{2(1+\nu)}, \quad \lambda = \frac{E\nu}{(1+\nu)(1-2\nu)} \tag{3.65}$$

with E and ν being the Young modulus and Poisson ratio, respectively. Neglecting the anisotropy of the materials, the thermal force is given as

$$F_T(T) = \nabla \cdot C\alpha \nabla T \tag{3.66}$$

with C and α being the elasticity matrix and the thermal expansion coefficient, respectively. Strain and stress are obtained from the mechanical model solution allowing for an estimation of the mechanical load on the coil. The linear elastic equation (3.64) is represented in terms of a differential-algebraic initial-value problem as

$$F_{\mathrm{mech}}(x_3, \partial_t x_3, y_3, u_3(t)) = 0 \tag{3.67}$$

with unknown $x_1 = u$. The vector of output variables y_3 consists of the strain and stress tensors [71]. The input vector u_3 is composed of the distribution of the Lorentz force and the temperature of the windings.

One-Way Coupling with Mesh-Based Interpolation

A co-simulation with mesh-based interpolation involves two or more coupled models discretized with distinct mesh definitions. A mesh definition consists of a vector containing mesh nodal positions along with a matrix of connectivity mapping mesh nodes into mesh elements. In case of difference in mesh definitions, the exchange of coupled quantities can not be performed directly. For this reason, the solutions obtained at mesh entities have to be accurately interpolated according to the mesh definitions as well as the element interpolation functions. To this end, we employ the MpCCI coupling environment. The MpCCI environment already provides a code adapter for ANSYS APDL models capable of automatically reading their mesh definition. In case of COMSOL a dedicated Java code adapter was developed following the MpCCI API. The COMSOL code adapter reads mesh definition and quantities calculated at the mesh nodes (for the temperature) and element barycenters (for the Lorentz force). The considered magneto-thermal (3.39, 2.107) and mechanical (3.64) models are discretized with a low-order finite element mesh on a quadrilateral and triangular grid.

With the one-way coupling algorithm the overall simulation time $\mathcal{I}$ is divided into N time windows $\mathcal{I}_j = (t_j, t_{j+1}]$ with $j = 0, ..., N-1$. We follow the algorithm outlined in Section 3.1.1 with a difference that the first subsystem is already solved for $t \in (t_0, t_N]$ before executing the algorithm. The first subsystem is the magneto-thermal model given as

$$F_{\mathrm{mag-th}}(x_1, \partial_t x_1, y_{1,j}, x_2, \partial_t x_2, y_{2,j}, u_1(t)) = 0. \tag{3.68}$$

The second subsystem is the mechanical model described as

$$F_{\mathrm{mech}}(x_3^{(j)}, \partial_t x_{3,j}, y_{3,j}, u_{3,j}(t)) = 0. \tag{3.69}$$

The computed magneto-thermal field solution $T(t_j)$ and $F_{\mathrm{L}}(t_j)$ is read at discrete time instants t_j and set as a load for a static mechanical analysis. The mechanical study is initialized with two static studies, i.e., pre-stress and cool-down. Then the model is computed at the communication points t_j.

One-way coupling of the electro-thermal and mechanical models with mesh-based interpolation is illustrated with a case study of an individually powered, single-aperture, 5.5-meter long, 11-T dipole magnet. Parameters of the magnet are reported in [72]. We model the magnet at the circuit side by means of two equal self-inductances $L_1 = L_2 = 14$ mH corresponding to the upper and lower pole, with a mutual inductance $M_{12} = M_{21} = 7.1$ mH. The magnet is powered by a power converter (PC) and protected by a CLIQ system as shown in Fig. 3.39. The CLIQ unit consists of a 60 mF capacitor bank with an initial voltage equal to 500 V. The operating current equals 11850 A. At $t = 0$ s the PC is switched off and a parallel crowbar represented by a non-linear resistance is closed. In addition, a CLIQ unit is also triggered. Note that this remains an academic example and the numeric results may not correspond to an actual operational scenario of the 11 T magnet.

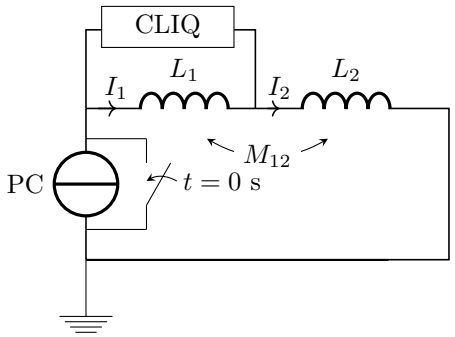

Figure 3.39: Schematic of the standalone circuit with an 11 T dipole magnet powered by a power converter with a parallel crowbar. Magnet is protected by a CLIQ unit composed of a charged capacitor bank and a switch triggered at $t = 0$ s.

The electrical circuit is implemented in ORCAD Cadence PSpice whereas the magneto-thermal distributed model (3.39-2.107) is calculated with COMSOL Multiphysics. For the magneto-thermal model, we assume homogeneous initial temperature of $T(t_0) = 1.9$ K and the initial distribution of the magnetic vector potential corresponding to the solution of the magnetostatic study at the nominal current I_0. In addition, the high-field inner layer turn is assumed to be in the normal conducting state 25 ms before the triggering of the CLIQ unit at $t = 0$ ms to analyze the thermal stress due to the quench initiation. The model is made of two quadrants with appropriate boundary conditions due to the model symmetry as well as the presence of current oscillations and resulting imbalance in the upper and lower coils. The coupling region for both models is constrained to the coil domain composed of half-turns. The solution of (3.64) is obtained with a 2D mechanical model in ANSYS APDL. The model is also represented with two quadrants and consists of all the main structural elements, i.e., the coil with half-turns made of Nb_3Sn, copper, insulation, and resin as well as the copper wedges, steel collar, iron yoke, and outer shell. In addition, the model contains dedicated contact elements representing connections between the structural elements. The model was created during the initial design phase of the 11 T magnet [73]. Fig. 3.40 shows the current profile obtained from a field/circuit coupling in the current-driven mode.

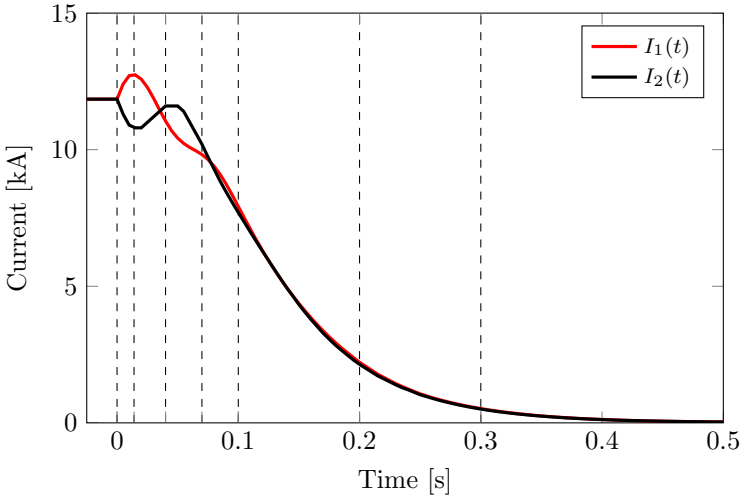

Figure 3.40: Current evolution in two poles of the magnet during the CLIQ discharge. Dashed lines indicate the time points for which the results of mechanical analysis are analysed.

The one-way coupling algorithm was executed for $t_N = 500$ ms with $N = 103$ communication points. To accurately resolve the initial current oscillations, for $t \in [0\text{ ms}, 30\text{ ms})$, the magneto-thermal field solution is transferred every 1 ms. For the rest of the discharge, $t \in [30\text{ ms}, 500\text{ ms}]$, the communication takes places every 10 ms. CLIQ discharge in the magnet introduces current oscillations in both poles. The current oscillations result in a change of the magnetic field which generates heat due to the coupling losses in the half-turns. The temperature increase provokes quench in large portions of the coil. Then, the temperature is increased further by the heat generation due to the Ohmic loss in the copper stabilizer.

The temperature is evaluated at the nodes of the magneto-thermal model, interpolated by the MpCCI server, and set to mesh nodes of the mechanical model. The Lorentz force density is evaluated at the element barycenters of the magneto-thermal model, interpolated, and set onto barycenters of the mesh elements of the ANSYS model. The current imbalance demonstrates itself as an asymmetry of the electrodynamic force distribution between the lower and the upper pole. As a result of the current discharge and temperature increase, the impact of the Lorentz force is superimposed with the thermal stress in the coil. The peak of the CLIQ current is observed at $t = 14$ ms. The corresponding temperature and Lorentz force distributions are

presented, respectively, in Fig. 3.41 and 3.42.

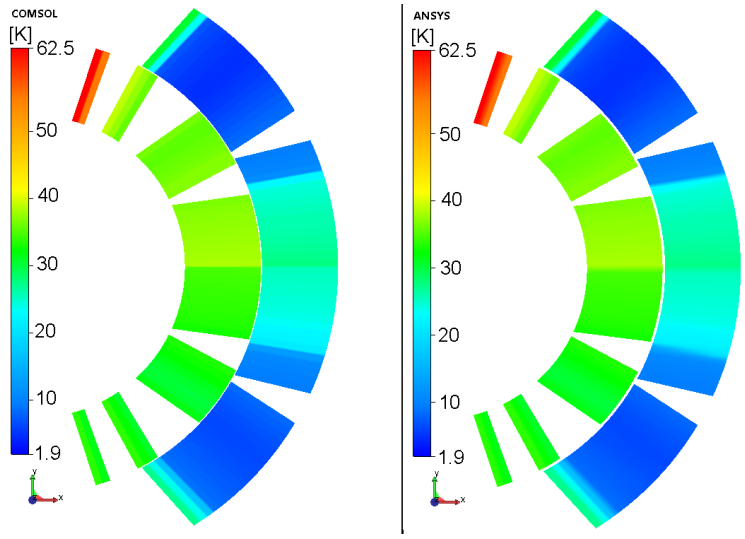

Figure 3.41: Comparison of the temperature distribution at $t = 14$ ms obtained from COMSOL (left) and interpolated on the ANSYS mesh (right). Note slight up-down asymmetry due to the CLIQ discharge and initial quench.

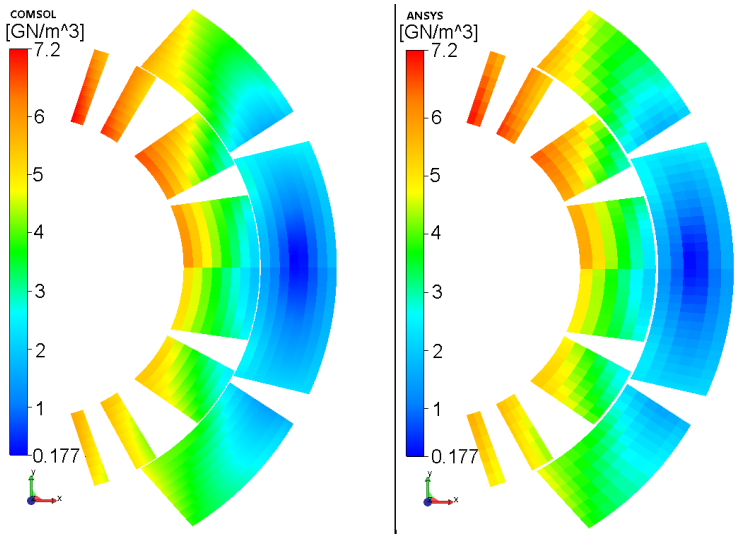

Figure 3.42: Comparison of the Lorentz force distribution at $t = 14$ ms obtained from COMSOL (left) and interpolated on the ANSYS mesh (right). Note the up-down asymmetry due to the CLIQ discharge.

Table 3.5 lists peak maximum stress in the half-turns for the time instants indicated in Fig. 3.40. The first four time points correspond to the initial current oscillations. In this period, the largest electrodynamic force is observed in the upper pole due to the current overshoot. The remaining three time points denote the middle and the final part of the current discharge when the temperature differences become significant.

Table 3.5: Maximum equivalent stress in the mechanical model.

t [ms]	max(σ_{eq}) [MPa]	Location
-25	102	2nd block of inner layer in the upper pole
0	102	2nd block of inner layer in the lower pole
14	108	2nd block of inner layer in the upper pole
40	95.7	1st block of inner layer in the upper pole
70	85.6	1st block of inner layer in the lower pole
100	93.1	3rd block of inner layer in the upper pole
200	122	3rd block of inner layer in the upper pole
300	124	3rd block of inner layer in the upper pole

In the beginning of the current discharge the maximum stress is dominated by the Lorentz force. Moreover, as a result of the CLIQ oscillations, the upper pole experiences the increase of the electrodynamic force above the nominal value. At the same time, since the CLIQ system is quenching large portions of the coil volume in a short time, the thermal stresses are also introduced. Fig. 3.43 shows the maximum stress corresponding to the peak CLIQ current at $t = 14$ ms. The maximum value equals 108 MPa and is located in the bottom-right corner of the second inner layer block of the upper pole. (The numbering of the blocks starts from the mid-plane.) The current decrease translates into the reduction of the electromagnetic force below the nominal value. Simultaneously, the temperature differences start to be dominating. In fact, at $t = 100$ ms the thermal stress is demonstrated by the increase of the peak equivalent stress. At $t = 300$ ms, the peak equivalent stress occurs in the block adjacent to the half-turn with the initial quench. The maximum temperature in the coil equals 145 K and is also positioned in that block of turns. In the considered scenario the peak equivalent stress in the coil during the discharge did not correspond to the maximum current in the upper pole (at $t = 14$ ms.) but to the thermal stress at the end of the discharge.

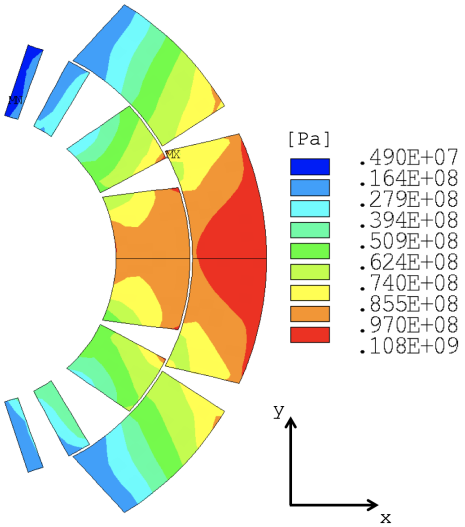

Figure 3.43: Distribution of the equivalent stress in the magnet cross-section at $t = 14$ ms.

We conclude that the effect of the Lorentz force superimposed with temperature difference in the magnet can either amplify or compensate each other in certain regions of a coil depending upon several factors such as, the magnet geometry, initial quench location, and CLIQ configuration. Thus, coupled magneto-thermal and mechanical analysis during the quench protection should be carried out in order to quantify the magnitude and location of the maximum stress in the coil.

Chapter 4

Hierarchical Co-Simulation

Nominal operation of a superconducting circuit is composed of a cycle that follows the operation of a particle accelerator, namely there is the ramp-up of the current (following the increase of the beam energy), the steady-state operation at the nominal current (period when collisions are taking place), and the current ramp-down (in case the beam quality has deteriorated below certain value and the beam has to be dumped). In case no faults occur, such a cycle is being repeated during the machine operation. For an analysis of such a scenario the controller/circuit coupling algorithm is sufficient to obtain meaningful results capturing the controller and circuit behavior (cf. Section 3.3.1). In some scenarios only a monolithic circuit model is sufficient [58]. In this case a lumped element model composed of inductors, capacitors, and resistors is sufficient to reproduce the transient behavior of a magnet.

However, in case of a malfunction of one of the subsystems, due to the complexity of an accelerator circuit, there is a large amount of failure scenarios that could take place. One of the more frequent events is a quench for which the operation of protection systems is governed by a dedicated sequence of steps. To consistently study quench initiation, propagation, and protection several models of a superconducting magnet shall be employed. As it was already mentioned, during the nominal operation of a circuit a lumped element circuital representation of a magnet is sufficient. In order to reproduce the resistance growth following a quench, at least a 1D thermal model has to be introduced (cf. Section 3.3.2). The growing resistance coupled to the electrical circuit model results in an increase of the resistive voltage. The evolution of the resistive voltage is monitored by a model of a quench detection system which, in case the voltage exceeds a detection threshold, triggers magnet and circuit protection systems. At this stage it is important to estimate the peak temperature and the maximum voltage to ground. Therefore, 2D finite element magneto-thermal models are introduced. This requires the application of the field/circuit coupling algorithm (cf. Section 3.3.3). The algorithm is executed as long as the current flowing through the magnet is above certain value. Afterwards, the study is continued until the circuit current is discharged (which could be different from the magnet current). Eventually, the mechanical response of the magnet's structure to the variation of the electrodynamic forces and temperature differences shall be studied (cf. Section 3.3.4).

In this context, an added value of the equivalent circuital representation of field models for the field/circuit coupling (cf. Section 3.3.3) is that it can be used for several purposes: (i) the controller/circuit coupling (pre-conditioner with differential inductance only); (ii) the 1D field/circuit coupling (with additional time-varying resistance); and (iii) the 2D field/circuit coupling (with additional compensation elements). As a result, the circuit topology can be kept intact and can accommodate several coupling schemes.

Depending on the state of the superconducting magnet operation it can be represented by one out of a hierarchy of available models (hierarchy can be determined by model accuracy, complexity, etc.). Selected models, representing a particular state of the operation, are coupled by means of a coupling algorithm. Once a state is executed it can transition to another one (switching of states). In order to obtain consistent results it is necessary to switch models and

coupling algorithms. Furthermore, to ensure the continuity of solutions and avoid inconsistencies, the switching should be automated and take place during the co-simulation run-time. Since physical domains can be introduced on demand we need to consider the so-called hierarchical co-simulation. A schematic representation of model activity during an execution of a hierarchical co-simulation scenario involving several coupled models and co-simulation algorithms is depicted in general terms in Fig. 4.1.

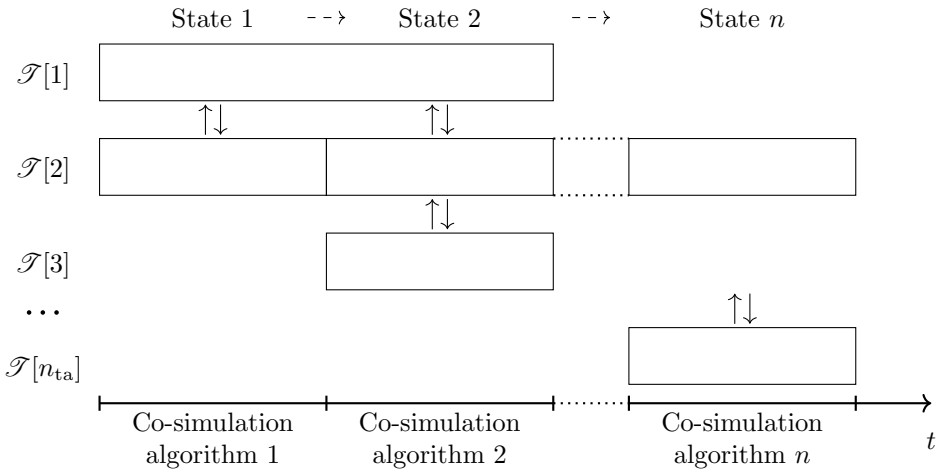

Figure 4.1: Schematic representation of a hierarchical co-simulation involving several models active at certain periods of the simulation time. Continuous arrows denote the signal exchange. Dashed arrows represent switching of states. Note that the state transition is not always unidirectional and may involve loops.

In order to enable switching of states we extend the co-simulation framework by introducing a state machine. Each state definition encodes a subset of active models, coupling variables, and a coupling algorithm in a given period of time. The transition between states is handled by a dedicated algorithm. The remainder of this Chapter discusses enhancements to the algorithms, data structures, and architecture presented in Chapter 3. Finally, the hierarchical co-simulation framework is illustrated by means of a co-simulation of a circuit composed of several high-field quadrupole magnets. The purpose of the co-simulation is to study the initial quench propagation, consecutive detection, trigerring of the protection system and the discharge of the energy stored in the magnetic field of the magnets.

4.1 Algorithms

In this section we present an application of the Deterministic Finite Automaton (DFA), also referred to as a state machine, to handle the switching of models and coupled variables as well as coupling algorithms. We rely on a formal definition of the DFA; for an introduction please refer to Appendix D or [74]. In the following, we discuss the main components of the hierarchical state machine, namely the state definition, the input alphabet, and the state transition function.

4.1.1 State Definition

The initialization procedure of the hierarchical co-simulation outlined hereunder concerns all tool adapters needed to execute all coupling algorithms foreseen for a given co-simulation scenario. A state for a hierarchical state machine describes a coupling algorithm, which involves at least one active tool adapter out of all available tool adapters. In case there are at least two coupled tool adapters, then an appropriate subset of coupling signals has to be selected as well. Thus, in order to switch between coupling algorithms, a state is characterized by

- a subset of active tool adapters out of all tool adapters initialized from the user input;
- a subset of active signals (inputs/outputs) out of all defined signals per each tool adapter;
- an array of signal types (either WAVEFORM or DATA_POINT), one per each active signal;
- the maximum number of iterations in order to distinguish between non-iterative ($k_{\max} = 1$) and iterative ($k_{\max} > 1$) algorithms.

Let n_S be the number of states. In addition, recall that n_P, n_I, n_O, and n_S denote the number of ports, input signals, and output signals, respectively (cf. Section 3.2.3). Then, Fig. 4.2 illustrates data structures needed to describe a state definition along with their cardinality. The *StateDefinition* object contains a one-dimensional array of indices of active tool adapters for each state. Moreover, there is also a two-dimensional array of hierarchical signal bundles for each tool adapter, and each port.

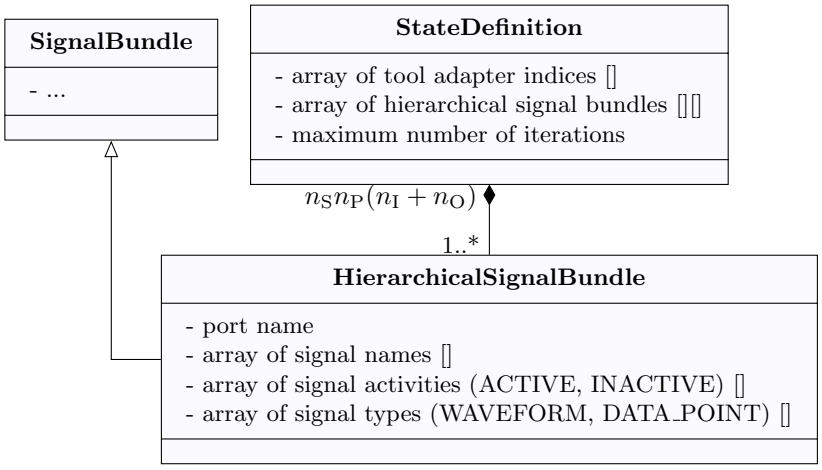

Figure 4.2: UML diagram of a class representing the state definition. For the definition of *SignalBundle* please refer to Fig. 3.7.

As a consequence of introducing the *HierarchicalSignalBundle* object, the signal definition (cf. *SignalBundle* class in Fig. 3.7) is extended by adding a state property (either ACTIVE or INACTIVE) to allow for signal activation and deactivation depending on whether or not for a given state of the co-simulation a particular signal is needed. Only active signals can participate in the signal exchange. With this extension, each active tool adapter has to have at least one active input or output signal.

The start state is fully determined by the user input, i.e., it consists of a subset of tool adapters and an array of the following signal extensions needed to execute the first coupling algorithm. The definitions of following states consist of a new state definition object. A typical final (accepting) state for a co-simulation of a superconducting circuit is the circuit discharge, which is followed by a dead state. The dead state is either the end of co-simulation time or a run-time error. An array Q, $\dim(Q) = n_S$ contains a set of all states describing a given co-simulation scenario.

4.1.2 Input Alphabet

The input alphabet is predefined upon launching a co-simulation and is based on a set of events. Events can be either implicit or explicit and take a form of assertions. The implicit events are based on internal variables of coupled models that can be exposed through signals stored in an *IOPort* object. Then, they are compared to a user-defined threshold (e.g., assert whether a

voltage across an element is greater than a prescribed threshold). The explicit events are based on the global co-simulation time (e.g., assert whether the co-simulation time reached a certain value). These events are the symbols of the input alphabet from which input strings for the state machine are constructed. We note, however, that the input symbols for the state machine are not known a priori and are obtained during the co-simulation run-time.

4.1.3 State Transition

The last component of the state machine description is the state transition function. The state transition function is a map from a current state and an input symbol to the next (output) state. Thus, for each state there is a two-dimensional array of transition functions.

For the sake of stability and simplicity, we assume that the state transition function is executed before starting an execution of a time window (cf. set initial conditions method in Alg. 5). As a result, each time window has a fixed set of active tool adapters and signals. In other words, a coupling algorithm can not change until the time window execution, including iterations, is completed. Note that the transition function can be also executed as a tool adapter study. This would allow for changing of coupling algorithms during a time window execution. However, this could lead to instabilities in case switching of states from an iteration to an iteration. A more robust solution is a posteriori shortening of the time window to the occurrence of an event in the last, converged iteration step; in this case the state machine is executed outside of the convergence loop.

For the start state, all tool adapters as well as required input and output signals have to be defined. The remaining states can be characterized in an incremental manner, i.e., only the tool adapters to be activated/deactivated have to be provided and the ones already defined remain intact.

Once the next step is determined, an activation algorithm is executed. The activation algorithm is summarized as a sequence of steps shown in Alg. 7. The outermost for-each loop steps over a subset of tool adapters given by the state definition (see Fig. 4.2). Then, another for-each loop goes through a subset of ports for the current tool adapter. Eventually, the innermost for-each loop is executed for each signal of the processed port according to the state definition and executes a sequence of methods: (i) set state; (ii) activate complementary signals; (iii) deactivate competing signals. The first method is rather trivial, while the other two aim at validating the state definition and require more description.

Algorithm 7 Tool adapter and signal activation algorithm

```
1: for each 𝒯_m ∈ 𝒯 do
2:     set state of 𝒯_m according to the state definition
3:     for each 𝒫_p ∈ 𝒫 do
4:         for each signal s in the signal definition do
5:             set state of signal s
6:             set type of signal s
7:             activate signals complementary to s
8:             deactivate competing signals with s
```

In order to perform the signal exchange, either an input or an output has to be defined. Thus, upon activating a signal (either input or output) its complementary one (either output or input) is found and activated as well. For that purpose, the signal search algorithm from Alg. 6 is employed. Once a complementary signal is found, its signal type also is set accordingly.

While switching coupling algorithms from a time window to another, a signal can be handed over from one model to another (e.g., resistance provided from 1D and 2D models). In order to avoid conflicts, there is a safeguard put in place. Once a certain signal is activated, the signal search algorithm from Alg. 6 finds other active signals of the same name and direction. If there is a signal returned, then it is deactivated. As a consequence, the user input with the state definitions can be reduced and include only one element of the pair of active signals.

In case a tool adapter is deactivated based on the state definition, and still has an active output signal then its simulation is not executed. However, the output signal, if requested, is extrapolated with a constant value in order to maintain the continuity of state variables at the communication point.

4.2 Architecture

In order to introduce a state machine for the hierarchical co-simulations, we extend the architecture described in Section 3.2. With the extension, the architecture accounts not only for tool adapters of numerical models but also for an additional tool adapter of a state machine. In fact, the state machine is implemented as another tool adapter. As a result, the state machine can be integrated with the main algorithm for the co-simulation management (cf. Alg. 5).

The aim of the proposed extension is to introduce as little changes as possible to the existing architecture, algorithms, and data structures. At the same time the extended framework shall be back-compatible, i.e., shall support both, hierarchical and regular co-simulation scenarios. Therefore, the state machine is implemented as a tool adapter which can be either present or not as described in the following Section.

4.3 State Machine Tool Adapter

In order to implement the functionality of the hierarchical state machine we introduce a *StateMachineToolAdapter* object. The object incorporates required properties and methods. Among the properties there is an array of references to all tool adapters, a one-dimensional array of state definitions, a one-dimensional array of input symbols (input alphabet), and a two-dimensional array of transition functions with output states for each state and input symbol. The methods include: (i) get input symbol; (ii) execute transition function; (iii) execute the algorithm for activation of tool adapters and signals. The UML diagram of the object is shown in Fig. 4.3.

The *StateMachineToolAdapter* class inherits from the *ToolAdapter* abstract class. As a result the state machine is equipped with the same properties and methods as all other tool adapters. Thus, the *StateMachineToolAdapter* object can participate in the signal exchange, which is essential to derive an input symbol (either implicit or explicit). In addition, the remaining methods, needed to prepare for and execute a time window, can be called. In particular, methods for setting initial conditions and executing a study can be used to call the state transition function before and during each execution of a time window, respectively. The execute study method is empty as we consider only state transition prior to the execution of a time window.

What is more, a *StateMachineToolAdapter* object can be stored in the tool adapter array $\mathcal{T}$. In fact it is the first element in order to allow for execution of the transition function before executing remaining tool adapters. Thus, the size of the tool adapter array is $\dim \mathcal{T} = n_{\mathrm{ta}} + 1$. The state machine is seamlessly integrated with the main algorithm orchestrating the co-simulation process (cf. Alg. 5). The only change in Alg. 5 is to extract a subarray of active tool adapters with the same execution index in line 8. Thus, only active tool adapters are executed in a given time window. A similar adjustment is required in the signal exchange algorithms. The inner for-each loop in Alg. 6 is executed for each active input signal. The signal search algorithm is also adjusted and returns only active output signals.

Note that the main co-simulation and the signal exchange algorithms, in case of a single state with all tool adapters and all signals being active, are equivalent to the algorithms discussed in Section 3.2.2 and 3.2.3, respectively. Thus, all tool adapters and all signals per each tool adapter are active by default. Provided the state machine is initialized, the state of all remaining tool adapters and their signals is set prior to the execution of the first time window. To conclude, the framework is back-compatible and depending on the user input, a co-simulation can be executed either as a standard (discussed in Chapter 3) or a hierarchical scenario.

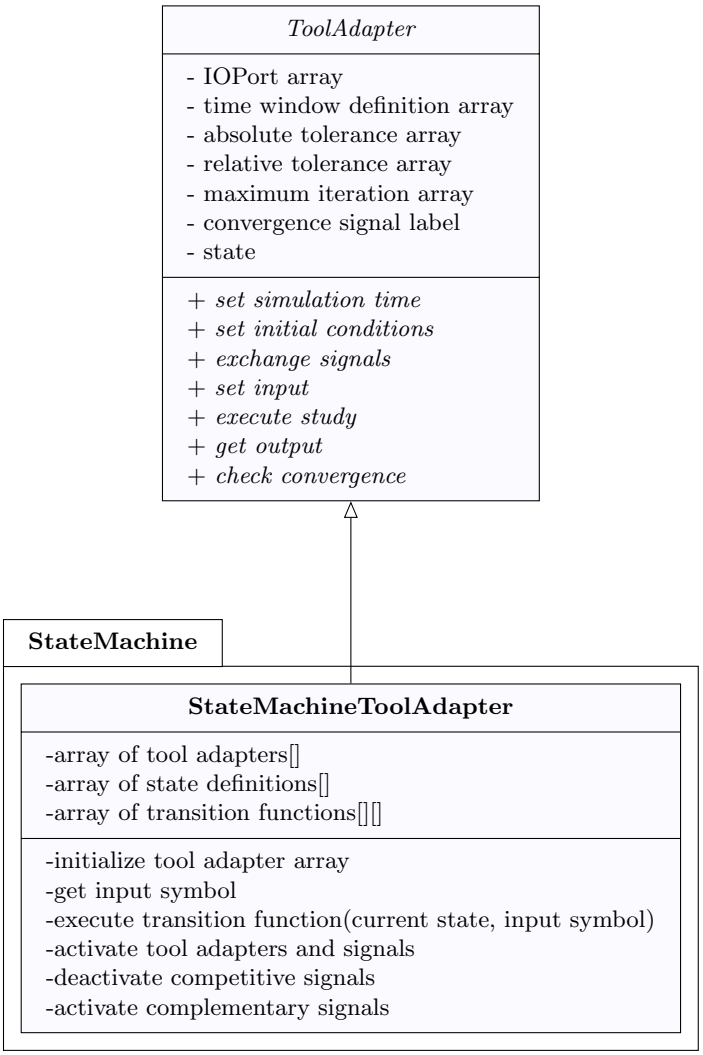

Figure 4.3: UML diagram with the inheritance structure for the state machine tool adapter. Note that the *ToolAdapter* abstract class is extended with the state property needed for hierarchical co-simulation.

4.4 Applications

We demonstrate the capabilities of the hierarchical co-simulation framework with a case study of the inner triplet circuit for the High-Luminosity LHC upgrade. The circuit is composed of six high-field superconducting quadrupole magnets with cables made of Nb_3Sn superconductor. A quadrupole magnet is focusing a beam of particles in one plane and defocusing in the other. Thus, the magnets are grouped into pairs in order to focus the beam in both directions. For the inner triplet circuit there are three pairs: Q1a and Q1b, Q2a and Q2b, Q3a and Q3b.

The magnets are powered by a main power converter supplying 16.47 kA in nominal conditions. In addition, there are two trim power converters for the first and third pairs of magnets which reduce the nominal current by 2 kA. The circuit protection consists of crowbars for power converters as well as diodes across Q2a and Q2b. For the sake of simplicity, the crowbar switch is modelled as a time-varying resistance. Each magnet is protected with a quench heater and CLIQ systems. The schematic representation of the circuit is shown in Fig. 4.5. Details on the design of the circuit and magnet protection can be found in [75].

We consider nominal conditions for the operating point of the circuit and several scenarios

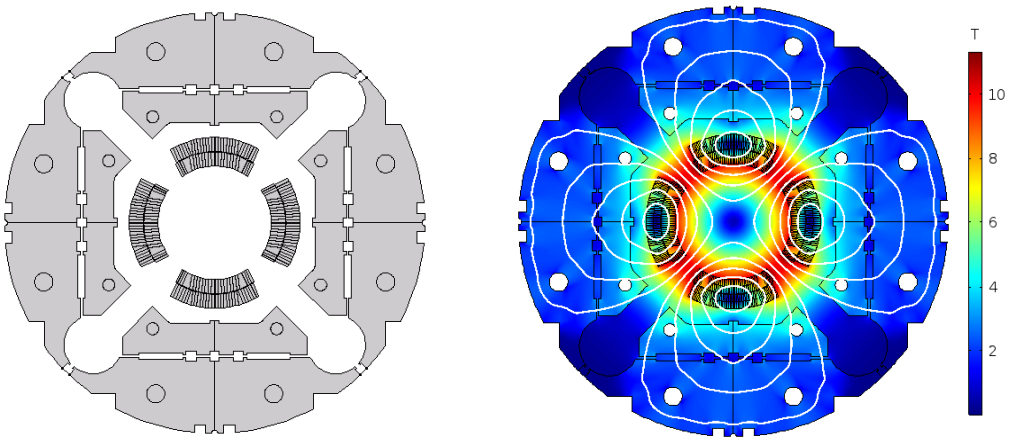

Figure 4.4: Cross-section of the quadrupole magnet (left) along with the magnetic field profile at the nominal current (right).

that could occur in the circuit. In particular we consider quench detection implemented as a voltage measurement across one magnet. During the simulation, the voltage across Q2a is continuously measured. With constant current, the voltage across the magnet should be equal to 0 V. However, if the voltage exceeds a threshold of 100 mV, due to the resistance growth after a quench, and/or failures in the circuit, quench protection systems are triggered in order to reduce the current in the circuit to 0 A. In order to avoid spurious triggering of the protection system, the threshold has to be exceeded for two consecutive sampling periods of the detection system. This process is also referred to as quench validation. In case a magnet recovers from a quench and/or a fault in the circuit disappears before the validation, then the circuit returns to the nominal operation. To conclude, depending on the evolution of the voltage across the magnet Q2a, the simulation can follow different execution paths. The considered scenario translates into a state machine presented in Section 4.1.3.

The hierarchical co-simulation of the inner triplet circuit involves 11 coupled models: a state machine implementing the switching of tool adapters and signals, a static function generator of control signals for the circuit, a model of the basic quench detection logic, a network model with equivalent field models for each magnet (each magnet is represented by four coupled inductors, one per coil), a 1D thermal model representing the longitudinal quench propagation, and six 2D magneto-thermal models of superconducting quadrupoles. The employed models and corresponding tool adapters with their execution index and description are given in Table 4.1.

Table 4.1: Description of models employed in the hierarchical co-simulation of the inner triplet circuit. For the sake of readability the suffix *ToolAdapter* is removed from the name of each tool adapter.

Model	Tool Adapter	e	Description
State machine	*StateMachine*	1	Implements state machine
Function generator	*FunctionGenerator*	2	Provides stimulus to the circuit
Quench detection	*QuenchDetection*	2	Measures voltage across Q2a
Electrical circuit	*PSpice*	3	Simulates circuit model
1D FEM	*Comsol*	4	Simulates longitudinal quench propagation
2D FEM	*Comsol*	5	Simulates 2D magneto-thermal response
5x 2D equivalent network	*LEDET*	5	Simulates 2D magneto-thermal response

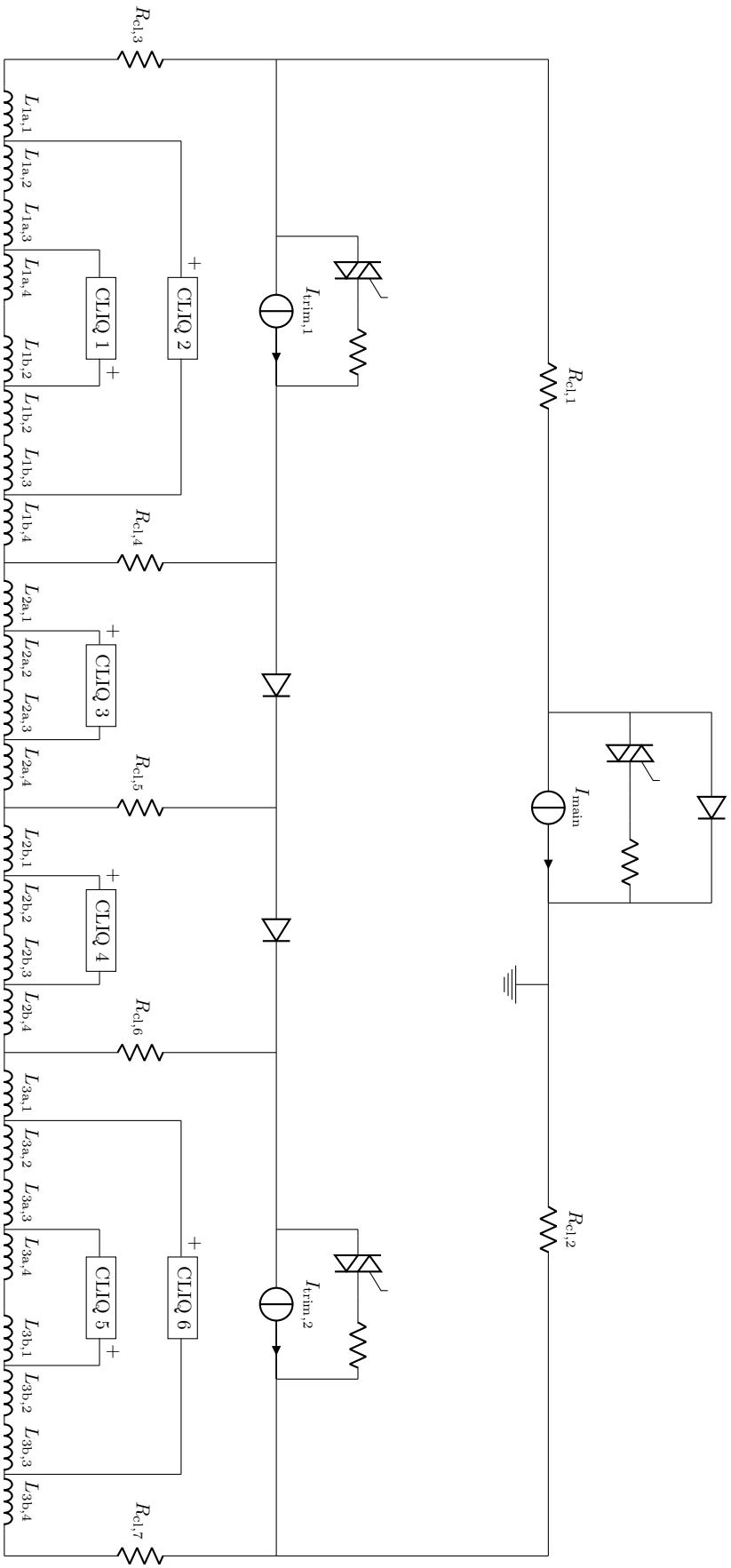

Figure 4.5: Schematic representation of the inner triplet circuit.

The execution order is assigned as follows: (i) the state machine model has always the execution index equal to 1; (ii) the function generator and quench detection models are independent and have the execution index set to 2; (iii) the execution order of the circuit model is equal to 3; (iv) the 1D thermal model is executed as the fourth one; (v) the 2D models are executed in parallel as the fifth ones. The execution index of the latter three is justified by the fact that they control the circuit behavior, while for the former two, the execution follows case studies of field/circuit coupling from Section 3.3.3.

In the following, we consider a case study of quench detection and protection of the inner triplet circuit also reported in [76]. Initially, the circuit is coupled to the function generator and quench detection system by means of the one-way coupling. Then, we assume one high-field turn of Q2a magnet to be artificially quenched at $t = 10$ ms. The longitudinal quench propagation results in the increase of the resistive voltage. This requires the application of the waveform relaxation algorithm to couple circuit and 1D thermal model. As long as the voltage does not exceed the threshold, the simulation remains in the quench propagation state. Depending on the initial current in the magnet, the quench can either propagate or recover. In case the resistive voltage is above the threshold of 100 mV, then the simulation transitions to the detection state. If the voltage remains above the threshold for another 10 ms, then the simulation goes to the quench protection state; otherwise, it will return to the quench propagation state. The quench protection state involves multi-field/circuit coupling in the current-driven mode.

The overall co-simulation time is equal to 450 ms and is divided into 45 windows of equal duration of 10 ms. This is one of the downsides of the fixed time window selection. Since it is not known a priori when the quench detection and validation would take place, the time window is selected according to the fastest state. For the considered scenario, the time windows are set according to the sampling frequency of the quench detection system. As a result, the performance of the field/circuit coupling might be limited by the communication overhead.

The absolute tolerance of the distributed models is set to 10^{-3} K (for 1D) and 10^{-3} K, 10^{-3} Wb (for 2D) while for the circuit model it is equal to 10^{-10} A. Since the remaining models implement discrete logic, there is no tolerance to be set. The maximum time step of the field models is equal to 10^{-4} s. The circuit model is solved with the maximum time step of 10^{-5} s. For the waveform relaxation algorithm, the relative and absolute tolerance are set to 10^{-3} and 10 A, respectively. The maximum number of iterations is equal to 10.

Note that this example does not reproduce the actual design and operation of the inner triplet circuit as well as the quench detection and protection systems for the High-Luminosity LHC upgrade. However, it can be used to carry out studies of the circuit behavior in nominal and failure conditions.

4.4.1 State Definition

In the presented hierarchical co-simulation scenario, five states are considered as summarized in Table 4.2. Thus, the set of states is given as $Q = \{S_0, S_1, S_2, S_3, S_4\}$.

Table 4.2: Description of states for a DFA representing hierarchical co-simulation.

State	Description	Coupling algorithm
$^{\rightarrow}S_0$	circuit operation at the nominal current	one-way coupling
S_1	longitudinal quench propagation	waveform relaxation
S_2	quench detected (validation pending)	waveform relaxation
S_3	magnet protection - current discharge	waveform relaxation
$^{*}S_4$	end of the simulation time	-

The start state, S_0, is a co-simulation of the function generator and the circuit. They are coupled by means of the one-way coupling. The function generator provides control signals for power converters and switches (for crowbars and CLIQ units).

The second state, S_1, introduces the 1D thermal model along with the quench detection system. The 1D model is initialized with a Gaussian temperature profile so that its fraction is in the normal conducting state. As a result, the quench propagates longitudinally. The quench detection system monitors the voltage across the magnet.

The third state, S_2, involves the same subset of models as in S_1. This state represents a detected quench for which the validation is required. During this state, the quench detection model is providing the control signals of the switches. The function generator is providing only the current profile of the power converters.

The fourth state, S_3, represents the field/circuit coupling of six 2D magneto-thermal models with the circuit model in the current-driven mode. In this state the 1D model and function generator are switched off. The resistance of the magnet Q2a provided by the 1D model is replaced by the one given by the 2D model. That results in the resistance discontinuity.

4.4.2 Input Alphabet

The input alphabet for the hierarchical state machine consists of five characters, $\Sigma = \{a, b, c, d, e\}$. Let t_{qi}, t_{qd}, and U_{Q2a} denote, respectively, the quench initiation time, the quench detection time, and the voltage across the magnet Q2a. Table 4.3 contains a summary of the input alphabet along with a description of corresponding activation conditions.

Table 4.3: Description of input characters.

Character	Description
a	if $t = t_{\mathrm{qi}}$, then initiate quench
b	if $U_{\mathrm{Q2a}} > 100$ mV, then quench detected
c	if $t = t_{\mathrm{qd}} + 10$ ms and $U_{\mathrm{Q2a}} < 100$ mV, then quench recovered
d	if $t = t_{\mathrm{qd}} + 10$ ms and $U_{\mathrm{Q2a}} \geq 100$ mV, then quench is detected and validated
e	if $t = t_{\mathrm{end}}$, then the simulation is completed

Characters a, e correspond to the explicit events as they are known before starting the co-simulation. The remaining characters are implicit events, whose occurence is determined during the co-simulation execution. The language L consists of strings of any length that end with character e as it is shown in the following.

4.4.3 Transition Function

The state transition function encodes information of the next state of the state machine for a given current state and an input character. With the states and input characters, the considered hierarchical co-simulation is represented as a graph in Fig. 4.6.

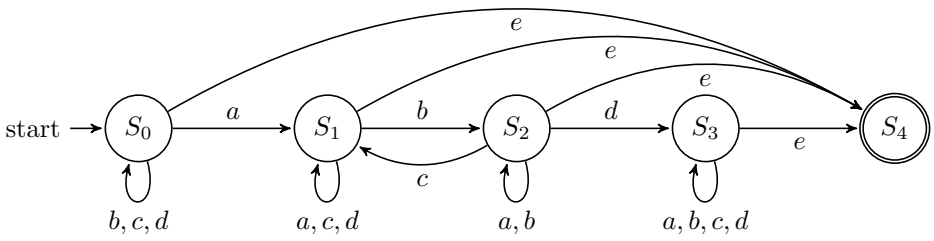

Figure 4.6: Graph representing transitions between states for the inner triplet hierarchical co-simulation.

From the graph one can indeed read that the state machine is accepting strings composed of characters from the input alphabet Σ as long as they end with character e. Note that e takes precedence over the remaining characters in case they occur simultaneously.

Another, equivalent representation of the state transition function is a table (see Table 4.4). The rows of the table contain the current state and the input characters are in the column headers. The entries of the table are the output of the transition function, i.e., the next state for the state machine.

Table 4.4: State transition table for the inner triplet hierarchical co-simulation.

	a	b	c	d	e
$^{\rightarrow}S_0$	S_1	S_2	S_0	S_0	S_4
S_1	S_1	S_2	S_1	S_1	S_4
S_2	S_2	S_2	S_1	S_3	S_4
S_3	S_3	S_3	S_3	S_3	S_4
$^{*}S_4$					

The state machine is scalable w.r.t. both, the number of states and the input characters.

4.4.4 Results

In the following, we present results obtained for each state activated during the execution of the hierarchical co-simulation. Since the last state, S_4, does not execute any simulation we do not provide any description of thereof. In fact, the last state is a dead state, i.e., the state machine remains in this state.

Nominal Circuit Operation

The co-simulation begins with the first state, S_0, which covers the nominal operation of the circuit. This state consists of two tool adapters, namely the function generator and circuit. They are coupled by means of the one-way coupling (cf. Section 3.1.1) and exchange waveforms. That requires the maximum number of iterations equal to 1 ($k_{\max} = 1$) and the type of each signal is set to WAVEFORM. The function generator provides current profiles to each power converter as well as control signals to each crowbar and CLIQ unit. The quench detection system monitors the voltage across Q2a. The execution of this state spans over a single time window $\mathcal{I}_0 = [0, 0.01]$ s as at $t = 0.01$ s a quench is artificially introduced in the 1D model. Fig. 4.7 presents the current and voltage of Q2a during the first state.

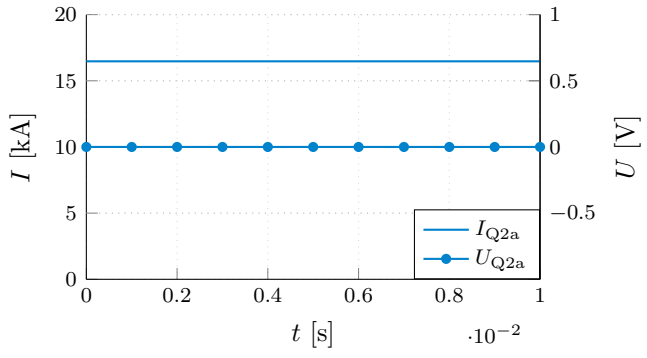

Figure 4.7: Evolution of the current through and voltage across Q2a during the nominal operation of the inner triplet.

Longitudinal Quench Propagation

Starting from the execution of the second time window, the 1D thermal model of Q2a is introduced to the subset of active models. The 1D model represents a high-field half-turn of $5.5-\mathrm{m}$ -long magnet. The half-turn is composed of copper (stabiliser) and Nb_3Sn (superconductor). The 1D model is initialized with a Gaussian profile with the same temperature distribution as in Fig. 3.16 (Right). The 1D model is coupled to the electrical circuit with the waveform relaxation algorithm. As a result, this algorithm is executed for each model during this state. Since the power converter is modelled as an ideal current source, the current flowing through the magnet remains constant during the time window. The initial temperature and operating current result in the longitudinal quench propagation and resistance growth. The evolution of current through and voltage across the 1D model is depicted in Fig. 4.8.

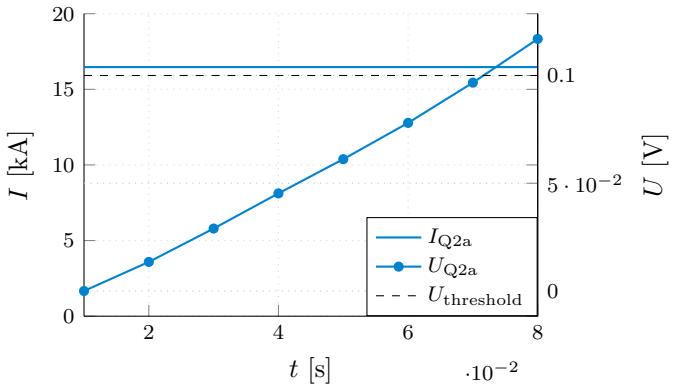

Figure 4.8: Current and voltage evolution during the longitudinal quench propagation state.

At $t = 0.08$ s, a quench is detected as the voltage across Q2a is above the threshold. As a result, the input character to the state machine is b and the transition function returns S_2 as the next state , i.e., $\delta(S_1, b) = S_2$.

Quench Detection and Validation

Once the quench is detected, the state machine transitions to the third state. Its purpose is to either validate or invalidate the detected quench. The third state consists of the same subset of active models as in S_2 coupled by means of the waveform relaxation algorithm. Similarly, as for the previous state, current and voltage profiles of Q2a are of interest (see Fig. 4.9).

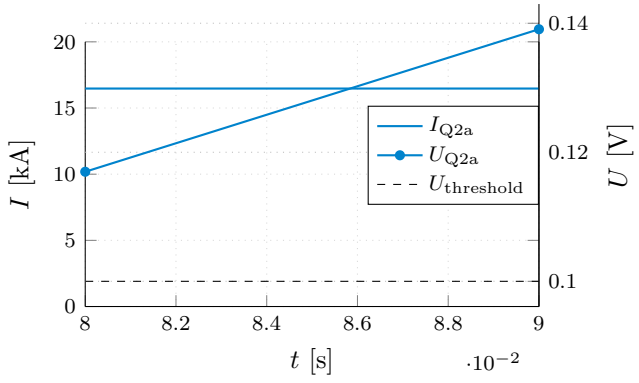

Figure 4.9: Current and voltage profiles of Q2a during the third state.

In fact, as one can notice in Fig. 4.9, the voltage across magnet Q2a remains above the threshold

of 100 mV for the validation period of 10 ms. This fulfils the condition of the input character d. In this case, the state transition function returns S_3, i.e., magnet protection, as the next state.

Magnet Protection

The third state is devoted to the study of the magnet and circuit protection. The quench detection system switches off the power converters and triggers crowbars and CLIQ units. Thus, the function generator is no longer needed and is deactivated. In addition, the 1D thermal model of Q2a is replaced with the 2D magneto-thermal model in COMSOL. The remaining five quadrupole magnets are represented with the equivalent electro-thermal network model implemented with LEDET (Lumped-Element Dynamic Electro-Thermal) software [45]. Unlike the 2D COMSOL model, the LEDET models contain outer-layer heater systems which are triggered once the models are activated. Each CLIQ unit is composed of a capacitor bank of capacitance $C_{\mathrm{CLIQ}} = 40$ mF charged to an initial voltage of $V_{\mathrm{CLIQ},0} = 1000$ V with resistance of leads equal to $R_{\mathrm{CLIQ}} = 50$ mΩ. We employ the field/circuit coupling algorithm discussed in Section 3.3.3 in the current-driven mode. Since all six electro-thermal models of quadrupole magnets have the same execution index, they are solved in parallel. Execution of the third state spans over $N = 35$ time windows, i.e., $t \in [0.09, 0.45]$ s. Fig. 4.10 shows current profiles obtained with the field/circuit coupling algorithm for Q1a and Q2a. Current oscillations due to a capacitive discharge result in generation of coupling losses in superconducting cables. These losses heat up the coil volume and bring the magnet into the normal conducting state. The growing resistance decreases current flowing through the magnet.

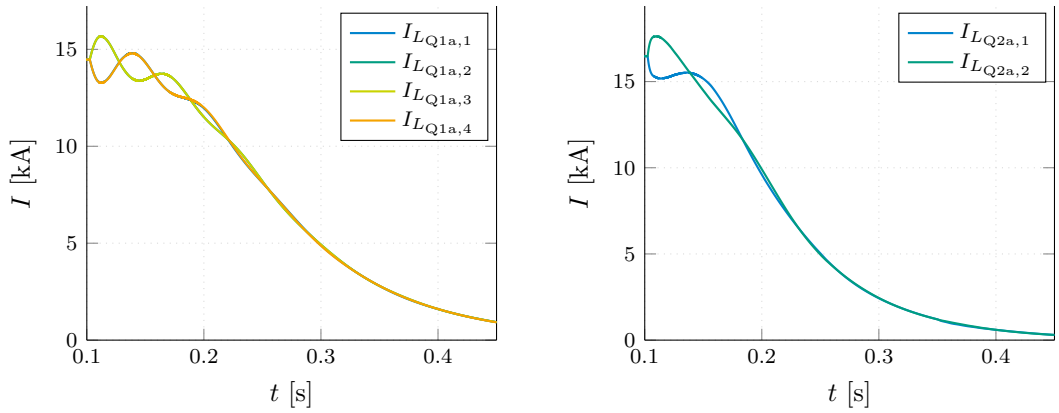

Figure 4.10: Current evolution during the magnet discharge for Q1a (left) and Q2a (right).

The simulation of the inner triplet circuit reproduced complex, nonlinear phenomena occuring at a broad range of temporal and spatial scales. Due to its complexity, the circuit can not be studied in a monolithic fashion and, with multiple coupled domains, the co-simulation is the only viable solution. In fact, the study involved a co-simulation of 11 tool adapters which were exchanging 142 signals. The state machine allowed for switching of states in order to reproduce a potential sequence of events that might occur in the circuit. We note that each state used only a subset of models needed to reproduce a particular scenario. That resulted in an efficient use of computational resources. Initially, the quadrupole magnets were represented as inductors in the circuit and as more details were required, higher fidelity models were introduced on demand (recall switching from the lumped inductance, to the 1D thermal model, and afterwards to the 2D magneto-thermal model). That creates a hierarchy of magnet models and solvers as 2D models can be solved with a fast, simplified LEDET model or a more demanding and accurate FEM COMSOL model.

The study highlighted two shortcomings of the framework to be addressed in the future development. The first one is related to the signal exchange. In case there is a hand over of signals, as it was the case for the resistance of Q2a, the initial conditions of the newly introduced

model have to be adjusted in order to maintain the continuity of solution at the communication point. Here, the 2D model should adjust the initial temperature of a given turn in order to match the final resistance of the 1D model. The second limitation is due to the fixed time window selection for the main algorithm. Since, the occurence of some events is not known a priori, the time windows have to be selected according to the fastest state. Thus, an adaptive time window selection algorithm and the state transition during window with a posteriori window shortening would decrease the computation time by reducing the comunication overhead.

As one can notice in Fig. 4.6, the first state can be modified in order to account for a quench detection in nominal condition. Should a fault occur in the circuit during the first state such that the voltage across the magnet is above the threshold, then the state machine should transition to state S_2. In this case, however, the state machine would turn into a nondeterministic finite automaton (NFA), i.e., for a given input character, the transition function returns a subset of states (from S_2 on input c, the state machine could transition either to S_1 or S_0). Once, an NFA is designed, it has to be converted to a DFA for a practical implementation by means of the subset construction algorithm [74].

Chapter 5

Conclusion and Outlook

The goal of this work was to develop a consistent representation of multi-domain, multi-physics, multi-rate, and multi-scale phenomena occurring in superconducting accelerator magnets. On the modeling side, the multi-domain and multi-physics challenge was captured by employing the energy-based modeling framework. On the algorithm side, the multi-scale and multi-rate behavior is harnessed by means of the co-simulation technique that allows to combine dedicated models of selected phenomena (e.g., fast vs. slow dynamics, 1D vs. 2D discretization). The port-Hamiltonian representation can provide a relevant perspective on the coupling process.

For the first time, the port-Hamiltonian formalism and bond graph modeling was applied in the field of superconducting accelerator electrical circuits modeling. In particular, we developed a distributed model of a superconducting magnet and a lumped model of a superconducting circuit. The former model consists of electromagnetic (distributed resistance after a quench, eddy currents, persistent magnetization) and thermal phenomena (heat conduction) coupled by means of the irreversible entropy creation and a common energy storage element. The common energy storage allowed to characterise the magneto-caloric effect. In addition, two distributed boundary ports along with a lumped one were identified. In fact, the variation of the internal energy of the system, i.e., power flow, is determined by the power flow through these ports. The port-Hamiltonian model provided an independent cross-check of the consistency of the existing FEM model [48]. For the superconducting circuit model we proposed application of a Kirchhoff-Dirac structure that represents the modified nodal analysis. The analysis of the underlying structure by means of the computational causality provides similar conclusions as the one obtained with the index analysis [49]. The port-based models of the electromagnetic and thermal domains as well as the electrical circuit can be further extended. In fact, the superconducting model is not yet complete and should account for fluid dynamics and mechanics. The port-Hamiltonian approach allows to extend the model due to its intrinsically modular and multi-physical nature.

In order to tackle the complexity of the multi-physics and multi-domain phenomena with multi-scale and multi-rate characteristics, the coupled problem is subdivided into subproblems. Each subproblem is represented with a dedicated numerical model solved independently. In order to restore the coupling between subproblems we employed the cooperative simulation approach with algorithms for information exchange between the subproblems. To this end, a co-simulation framework has been developed with an architecture and data structures allowing for implementation of the main four coupling algorithms (one-way coupling, weak coupling, strong coupling, waveform relaxation) along with a state machine for hierarchical scenarios. It is noteworthy that the framework is agnostic to the simulated case and can be applied to other co-simulation cases in other fields. The framework has been already employed to several relevant cases in the field of particle accelerators [76], [77], [78].

The controller/circuit coupling incorporated the weak-coupling and waveform relaxation algorithms. A model of a controller is solved with a fixed time stepping algorithm, while a network model of an electrical circuit is solved with an adaptive time stepping scheme. The digital imple-

mentation of a controller is an example of a weak coupling scheme. For the waveform relaxation we stated and proved two conditions for the minimum and maximum number of iterations. In addition, it was shown that in certain conditions, the waveform relaxation is more efficient then the weak coupling scheme.

The field/circuit coupling algorithm proved to be a suitable solution for studying complex superconducting circuits and magnets. The bond graph models were applied to study two excitation modes, namely, the current- and voltage-driven ones. The properties of both schemes were studied for a lumped and distributed setup. Due to the dependence of the differential inductance on the current (iron yoke saturation) and time derivative of current (eddy-currents) we observed large number of iterations in the first time window while the transient is initialised. Therefore, two strategies for the improvement of the performance for the field/circuit coupling were identified and evaluated: (i) scaling of the differential inductance; (ii) update of the differential inductance at the beginning of each time window. Application of both strategies proved to improve the convergence rate of the coupling algorithm.

Discharge of the energy stored in the magnetic field of a superconducting magnet results in a decay of the Lorentz force and simultaneous build up of the temperature difference. The resulting stress in the superconductor may result in material degradation and, therefore, has to be studied. To this end, dedicated mechanical models are developed and applied. Since magneto-thermal and mechanical models are typically developed with different simulation suites, we developed a one-way coupling algorithm. In order to account for differences in mesh definition in both models, we employed MpCCI, an existing mesh-based interpolation environment.

The aforementioned three types of co-simulation algorithms correspond to main operational states of a superconducting circuit in both, nominal and failure conditions. Integrated analysis of the entire operational cycle involves multiple coupled models active only in particular phases. Each phase involves a subset of available models in order to represent transient effects with desired accuracy. This translate into a need for switching of models and coupling schemes and is captured by means of a hierarchical co-simulation. The co-simulation framework provides this feature by implementing a deterministic state machine. The scalability and robustness of the framework was demonstrated with a hierarchical co-simulation of a high-field quadrupole circuit [76].

5.1 Outlook

The presented work on the energy-based modelling of multi-* problems provides a foundation for the analysis magneto-thermal and electrical phenomena occurring in superconducting accelerator magnets and circuits. As such, the modelling framework can be further extended in order to approach several relevant research avenues. The estimation of the coupling strength between the subsystems representing a superconducting circuit and in general multi-physics problems is of high importance. Power is a universal quantity characterising each physical system. Therefore, the power exchanged between coupled models could be used as a metric of coupling-strength. Firstly, such a metric would provide insights into the process of heterogeneous domain decomposition and indicate whether a multi-physics model could be decomposed into submodels (weak coupling), or it should be solved in a monolithic fashion (strong coupling). Secondly, for models decomposed into smaller units, the estimation of coupling strength could guide the choice of a coupling algorithm to obtain satisfactory results in a time-efficient way. Another interesting aspect is the assignment of the computational order. In particular, this process is non-trivial for multiple coupled models while there is a growing number of possible permutations.

One of the limitations of the presented framework is the use of fixed time windows for the co-simulation process. On one hand, too large time window may lead to divergent results. On the other hand, too small time windows may translate into large computational time due to the communication and model initialisation overhead. The amount of power flowing between two coupled physical models could be used as input for an adaptive time window selection algorithm [17]. Other criteria could be used like the initial convergence speed. Another concept that

promises performance improvements is a parareal algorithm, which allows for parallel execution of multiple consecutive time windows [79]. Each time window can be solved with the waveform relaxation algorithm. The main co-simulation algorithm can be extended in order to account for this type of computations. Currently, the STEAM co-simulation framework only supports scalar waveforms. A natural extension is to account for distributed variables and integrate the capabilities of the MpCCI environment for mesh-based interpolation and model coupling with the co-simulation framework.

There are also several potential improvements to the hierarchical co-simulations. Among others, one could consider energy-based model switching. The energy variation in a model can be used as an input character for the state machine. This would allow to determine what models should be activated as they experience significant energy variation. Similarly, models with negligible changes of internal energy can be deactivated. Such an approach would allow to use the computational resources more efficiently by simulating only the most significant phenomena. For instance, if the variation of a source current in the magneto-thermal model of a magnet results in the temperature variation exceeding a certain threshold, the very model should be introduced to the co-simulation. Similarly, if the power is not dissipated in a magnet anymore and a steady state is reached, it can be deactivated. Another relevant improvement to the hierarchical co-simulation is a posteriori shortening of a time window in order to provide an exact switching moment between states.

Appendix A

Differential Forms

The aim of this appendix is to provide a subset of vector analysis operators and operations that are used throughout the thesis. Thus, the appendix does not serve as a comprehensive introduction to the theory of the exterior differential forms. An interested reader is recommended to refer to [80] for more detailed discussion on the topic. An introduction oriented towards an application for port-Hamiltonian systems is given in Section 4.2.1 in [20].

We consider an n-dimensional smooth manifold Ω, which is C^∞ differentiable. The manifold is characterized by n independent coordinates $(x_1, ..., x_n)$. We introduce also a tangent manifold $T\Omega$ with tangent vectors $(\partial_{x_1}, ..., \partial_{x_n})$. The dual basis of cotangent vectors is given as $(\mathrm{d}x_1, ..., \mathrm{d}x_n)$. The set of p-forms on Ω is denoted by $\Lambda^p(\Omega)$.

For the sake of simplicity we consider an $\mathbb{R}^3$ space and introduce 0-, 1-, 2-, and 3-forms with $\mathrm{d}x$, $\mathrm{d}y$, $\mathrm{d}z$ as basis covectors (see Table A.1).

Table A.1: Differential Forms in $\mathbb{R}^3$.

Form order	Expression
0-form	$F = f$
1-form	$F = f_x\mathrm{d}x + f_y\mathrm{d}y + f_z\mathrm{d}z$
2-form	$F = f_x\mathrm{d}y \wedge \mathrm{d}z + f_y\mathrm{d}z \wedge \mathrm{d}x + f_z\mathrm{d}x \wedge \mathrm{d}y$
3-form	$F = f\mathrm{d}x \wedge \mathrm{d}y \wedge \mathrm{d}z$

We note that the integral of a 1-form F over an oriented line l has a notion of work (e.g., integration of a force $\vec{f}$ over a certain displacement)

$$\int_l (f_x\mathrm{d}x + f_y\mathrm{d}y + f_z\mathrm{d}z) = \int_l \vec{f}\mathrm{d}l.$$

Similarly, the integral of a 2-form J over an oriented surface S has a meaning of flux (e.g., integral of a current $\vec{\jmath}$ density over a surface)

$$\int_S (\jmath_x\mathrm{d}y \wedge \mathrm{d}z + \jmath_y\mathrm{d}z \wedge \mathrm{d}x + \jmath_z\mathrm{d}x \wedge \mathrm{d}y) = \int_S \vec{\jmath}\mathrm{d}S.$$

A.1 Exterior Product

The exterior product $\wedge$, also referred to as the wedge product, maps a p-form ω and a q-form η onto a $p+q$-form $\omega \wedge \eta$ (for $p+q > n$ the exterior product is equal to 0 by definition)

$$\wedge : \Lambda^p(\Omega) \times \Lambda^q(\Omega) \mapsto \Lambda^{p+q}(\Omega).$$

The exterior product is characterized by the following properties

1. is distributive, $\omega \wedge (\eta + \nu) = \omega \wedge \eta + \omega \wedge \nu$;
2. is associative $\omega \wedge (\eta \wedge \nu) = (\omega \wedge \eta) \wedge \nu$;
3. is graded anticommutative $\omega \wedge \eta = (-1)^{pq} \eta \wedge \omega$.

With these properties, we consider two relevant exterior products in a three-dimensional space. Let $\mathrm{d}x$, $\mathrm{d}y$, and $\mathrm{d}z$ be basis vectors in $\mathbb{R}^3$ space. Then, the exterior product of two 1-forms, $A = a_x \mathrm{d}x + a_y \mathrm{d}y + a_z \mathrm{d}z$ and $B = b_x \mathrm{d}x + b_y \mathrm{d}y + b_z \mathrm{d}z$ is a 2-form $A \wedge B$ given as

$$\begin{aligned} A \wedge B &= (a_x \mathrm{d}x + a_y \mathrm{d}y + a_z \mathrm{d}z) \wedge (b_x \mathrm{d}x + b_y \mathrm{d}y + b_z \mathrm{d}z) = \\ &= (a_x b_y - a_y b_x) \mathrm{d}x \wedge \mathrm{d}y + (a_y b_z - a_z b_y) \mathrm{d}y \wedge \mathrm{d}z + (a_z b_x - a_x b_z) \mathrm{d}z \wedge \mathrm{d}x. \end{aligned}$$

We note that the exterior product of two 1-forms is a cross product of two vectors.

Another meaningful exterior product in $\mathbb{R}^3$ space is the exterior product of a 1-form $A = a_x \mathrm{d}x + a_y \mathrm{d}y + a_z \mathrm{d}z$ and a 2-form $C = c_x \mathrm{d}y \wedge \mathrm{d}z + c_y \mathrm{d}z \wedge \mathrm{d}x + c_z \mathrm{d}x \wedge \mathrm{d}y$, $A \wedge C$ denoted as

$$\begin{aligned} A \wedge C &= (a_x \mathrm{d}x + a_y \mathrm{d}y + a_z \mathrm{d}z) \wedge (c_x \mathrm{d}y \wedge \mathrm{d}z + c_y \mathrm{d}z \wedge \mathrm{d}x + c_z \mathrm{d}x \wedge \mathrm{d}y) = \\ &= (a_x c_x + a_y c_y + a_z c_z) \mathrm{d}x \wedge \mathrm{d}y \wedge \mathrm{d}z. \end{aligned}$$

We find that the result of $A \wedge C$ is an inner product space.

A.2 Exterior Derivative

The exterior derivative d is a map of a p-form ω onto a $p+1$-form $\mathrm{d}\omega$

$$\mathrm{d} : \Lambda^p(\Omega) \mapsto \Lambda^{p+1}(\Omega).$$

Hereunder we report properties of the exterior derivative

1. $\mathrm{d}(\omega + \eta) = \mathrm{d}\omega + \mathrm{d}\eta$;
2. $\mathrm{d}(\omega \wedge \eta) = \mathrm{d}\omega \wedge \eta + (-1)^{\mathrm{deg}\omega} \omega \wedge \mathrm{d}\eta$;
3. For each ω, $\mathrm{d}(\mathrm{d}\omega) = 0$;
4. For each function f, $\mathrm{d}f = \sum \frac{\partial f}{\partial x^i} \mathrm{d}x^i$.

The second is equivalent to the product rules of the vector calculus, and the third property denotes the Poincaré Lemma. We note that, the exterior derivative in $\mathbb{R}^3$ space for a given form order is equivalent to the gradient, curl, and divergence operators in vector calculus

1. if a is a 0-form, then $\mathrm{d}a = \nabla a$;
2. if b is a 1-form, then $\mathrm{d}b = \nabla \times \vec{b}$;
3. if c is a 2-form, then $\mathrm{d}c = \nabla \cdot \vec{c}$.

Generalized Stokes' Theorem

Consider a smooth and oriented p-manifold Ω with consistently oriented smooth boundary $\Gamma = \partial\Omega$. Let ω be a $p-1$-form defined on an open set containing Ω. Then the Stokes' theorem can be written as

$$\int_\Omega \mathrm{d}\omega = \int_\Gamma \omega.$$

For $p = 1$ we obtain the Stokes' theorem, and for $p = 2$ we obtain the Gauss' theorem.

A.3 Hodge Operator

The (Hodge) star operator is a linear map on a p-form onto an $n-p$-form

$$* : \Lambda^p(\Omega) \mapsto \Lambda^{n-p}(\Omega).$$

Consider an oreiented p-manifold Ω endowed with an inner product $\langle ., . \rangle$, then the Hodge star of the p-form ω denoted by $*\omega$ is defined as

$$\langle \alpha, \omega \rangle = \int_\Omega \alpha \wedge (*\omega)$$

for any p-form α. This definition is particularly suited for the calculation of the energy density function [20].

Appendix B

Electromagnetic Domain

Phenomena occurring in the electromagnetic domain of a superconducting magnet are characterized by the Maxwell equations [81]. Hereunder we represent the partial differential equations in terms of the differential forms as given in [82].

B.1 Governing Equations

Table B.1 provides a summary of variables used to describe electromagnetic phenomena.

Table B.1: Description of variables in the electromagnetic domain

Symbol	Form order	Unit	Description
φ	$\Lambda^0(\Omega)$	V	Electric scalar potential
Ψ	$\Lambda^0(\Omega)$	A	Magnetic scalar potential
A	$\Lambda^1(\Omega)$	Wb	Magnetic vector potential
E	$\Lambda^1(\Omega)$	V	Electric field strength
H	$\Lambda^1(\Omega)$	A	Magnetic field strength
D	$\Lambda^2(\Omega)$	C	Electric flux density
B	$\Lambda^2(\Omega)$	Wb	Magnetic flux density
$\jmath$	$\Lambda^2(\Omega)$	A	Electric current density
ρ	$\Lambda^3(\Omega)$	C	Electric charge density

We note that all field quantities can be formulated in terms of the magnetic vector potential A and the electric scalar potential φ

$$E = -\mathrm{d}\varphi - \partial_t A$$

$$B = \mathrm{d}A$$

up to the gauging operation $\varphi' = \varphi - \partial_t \lambda$ and $\mathrm{A}' = \mathrm{A} - \mathrm{d}\lambda$.
Faraday law of induction describes the relation between the time variance of the magnetic field and the induced electric field

$$\mathrm{d}E = -\partial_t B.$$

Moreover, recall that there are no magnetic charges, as the magnetic induction is free of sources

The Ampère law relates the magnetic field around a closed loop to the electric current flowing through the loop

$$\mathrm{d}H - \partial_t D = \jmath.$$

The Gauss law states the relationship between the electric charge and the resulting electric flux density as

$$\mathrm{d}D = \rho.$$

Finally, the material laws are represented by means of the Hodge star operator and respective material properties

$$\jmath = *_\kappa E, \quad D = *_\epsilon E, \quad H = *_\nu B.$$

B.2 Topological Diagram

The Maxwell equations are conveniently reported in Fig. B.1 as a topological diagram. Equations (B.1)-(**??**) form the Faraday complex given on the left side of the diagram. The Ampère-Maxwell complex, on the right side, is constructed from equations (B.1) and (B.1). Both complexes are linked by means of the material laws (B.1).

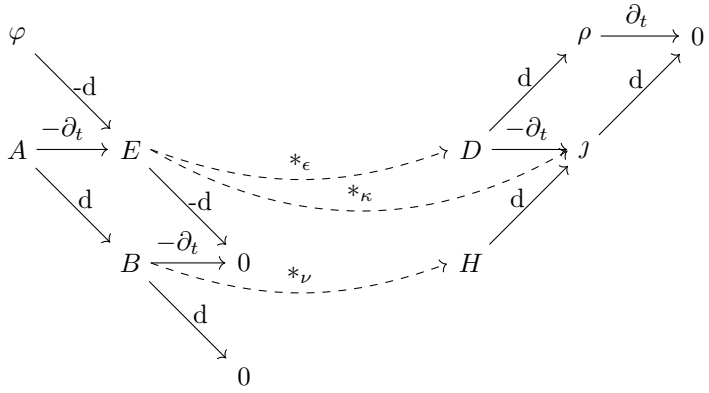

Figure B.1: Electromagnetic domain represented as a topological diagram with a Faraday (left) and Ampère-Maxwell (right) sides.

Rows of the diagram correspond to the differential form order, from 0- to 3- forms on the Faraday side and from 3- to 0- form on the Ampère-Maxwell side. It is noteworthy that the conjugate power pairs can be read-out from corresponding rows of the diagram, e.g., (A, D), $(E, \jmath)$, and (B, H).

Appendix C

Thermal Domain

Temperature in a superconducting magnet is obtained as a solution of the heat balance equation. The appendix provides a brief summary of the thermodynamic variables along with a set of governing equations given in [26].

C.1 Governing Equations

Table C.1 contains a summary of thermodynamic variables with their corresponding differential form order, unit, and description.

Table C.1: Description of quantities in the thermal domain

Symbol	Form order	Unit	Description
T	$\Lambda^0(\Omega)$	K	Temperature
$\jmath_{\mathrm{S}}$	$\Lambda^2(\Omega)$	W/K	Entropy flux
$\jmath_{\mathrm{Q}}$	$\Lambda^2(\Omega)$	W	Heat flux
$\mathcal{U}$	$\Lambda^3(\Omega)$	J	Internal energy density
s	$\Lambda^3(\Omega)$	J/K	Entropy density
σ	$\Lambda^3(\Omega)$	W/K	Irreversible entropy flow
f_{s}	$\Lambda^3(\Omega)$	W/K	Reversible entropy flow

Conservation of the internal energy in thermodynamic systems can be expressed as

$$\partial_t \mathcal{U} = -\mathrm{d}\jmath_{\mathrm{Q}}.$$

The Fourier law introduces the heat flux $\jmath_{\mathrm{Q}}$ as

Time variation of the internal energy $\mathrm{d}\mathcal{U} = T\mathrm{d}s$ yields an expression for the variation of the entropy density

$$\partial_t s = -\frac{1}{T}\mathrm{d}\jmath_{\mathrm{Q}}.$$

The entropy flux is defined by

$$\jmath_{\mathrm{S}} = \frac{\jmath_{\mathrm{Q}}}{T}.$$

The Jaumann's entropy balance [26] reads

$$\mathrm{d}\jmath_{\mathrm{Q}} = \mathrm{d}(T\jmath_{\mathrm{S}}) = T\mathrm{d}\jmath_{\mathrm{S}} + \mathrm{d}T \wedge \jmath_{\mathrm{S}}.$$

Eventually the time variation of entropy is given as

$$\partial_t s = -\frac{1}{T}\mathrm{d}T \wedge \jmath_{\mathrm{S}} - \mathrm{d}\jmath_{\mathrm{S}} + \sigma_{\mathrm{ext}} = \frac{*_{k(T)}}{T^2}\mathrm{d}T \wedge \mathrm{d}T\mathrm{d}\frac{*_{k(T)}}{T}\mathrm{d}T + \sigma_{\mathrm{ext}} = \sigma_{\mathrm{s}} - f_{\mathrm{s}} + \sigma_{\mathrm{ext}}.$$

C.2 Topological Diagram

Topological diagram of the thermodynamic domain shown in Fig. (C.1) depicts relations between the quantities describing thermodynamic domain given so far. The topological diagram is composed of three subgroups for entropy, temperature, and internal energy. The subdivision originates from the zeroth, first, and second law of thermodynamics introducing fundamental concepts of temperature, internal energy, and entropy, respectively [83].

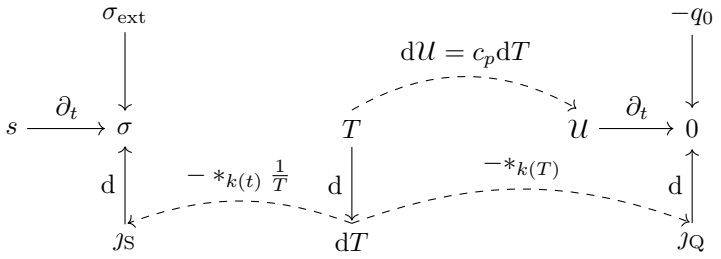

Figure C.1: Thermodynamic domain represented as a topological diagram with entropy (left), temperature (centre), and internal energy (right).

Appendix D

Deterministic Finite Automata

A hierarchical co-simulation in its nature is based on a certain set of states providing a set of active tool adapters representing a given state of the system under analysis. We follow the introduction from [74] covering a wide range of topics including but not limited to the Deterministic Finite Automata (DFA).

D.1 Definition

Let Σ be an alphabet composed of a finite set of symbols. A string S over an alphabet Σ is a list with entries being elements of Σ. The length of a string is given as the number of characters in the corresponding list. There is a special string ϵ representing an empty string. A set of all possible strings for an alphabet Σ is denoted as Σ^*. Then, a language L is a set of strings (either finite or infinite) defined over a certain alphabet Σ.

We consider a DFA as a formalism defining a certain language L. It defines an automaton with a finite set of states with a unique transition between two states for a given input. A DFA is a quintuple (Q, q_0, F, Σ, δ) with

1. Q is a finite set of states;
2. q_0 denotes the start state;
3. F is a finite set of final (accepting) states $F \subseteq Q$. Furthermore, we introduce a dead state to which a state machine transitions for any input;
4. An input alphabet Σ providing a list of allowable input symbols for the DFA;
5. A transition function δ which, on the basis of two input arguments: (i) a state; and (ii) an input symbol, determines a unique next state (e.g. $\delta(q, a)$ returns a state to which a DFA will transit from state q for an input a). The transition function can be extended to accept a state and an input string. We note, however, that the extended transition function $\hat{\delta}$ is in fact a recursive chain of transition functions, i.e. $\hat{\delta}(q, a_1a_2...a_n) = \delta(\hat{\delta}(a_1a_2...a_{n-1}), a_n)$ with the recursion terminated if the length of the input string is equal to 1.

The language L of a DFA is not empty if there exists an input string S for the start state q_0 for which the transition function δ returns a final state $q \in F$

$$L \neq \varnothing : \exists S \in L : \hat{\delta}(S, q_0) \in F.$$

D.2 Table and Graph Representations

There are two common equivalent representations of a DFA, namely a graph and a table.

These representations are introduced by means of an example of a state machine which detects strings without a triplet of characters sos. There are four states $Q = \{A, B, C, D\}$ with description given in Table D.1. We note that states A, B, C are final. The alphabet contains four symbols $\Sigma = \{s, o, \sim s, \sim o\}$. The tilde symbol is used to denote all characters other than the one which comes after the tilde.

Table D.1: Description of states for a DFA detecting strings without an sos substring.

State	Description
A	Input symbol different from s ($\sim s$)
B	Input symbol is s
C	Input symbol is o (previous symbol was s)
D	Input symbol is s (previous symbols were so)

The graph representation is composed of nodes and edges. Nodes are depicted by circles and represent states. The start state is indicated by an arrow and a label start. The final states are denoted by double circles. Edges represent transition functions from one state to another. The input symbol for the transition function is provided over an edge. A graph representation for the considered example is presented in Fig. D.1.

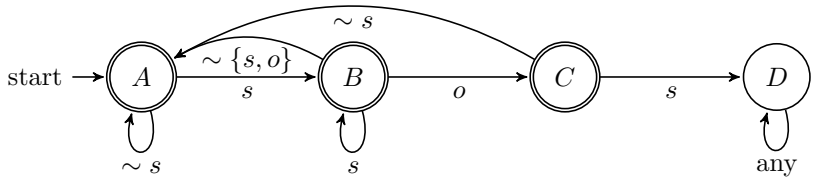

Figure D.1: Graph representation of the DFA.

For the table representation (see Table D.2), columns represent the alphabet and the rows contain states. An arrow in the left superscript indicates the start state while stars in the same position denote final states. An entry of the table is the output of the transition function for state and input signal corresponding to the row and column, respectively. Table D.2 represents the considered example and contains the same information as Fig. D.1.

Table D.2: Table representation of the DFA.

	s	o	$\sim s$	$\sim o$
$^{\rightarrow *}A$	B		A	
$^{*}B$	B	C	A	A
$^{*}C$	D		A	
D	D	D	D	D

The table contains several empty entries as for a given row the existing ones are sufficient to cover all possible inputs and provide a unique state as an output. In fact the example was a regular expression, which can be shown to be equivalent to a state machine. [74]

For relatively small state machines, the graph representation is suitable, however, for large state machines, the tabular representation is more convenient.

Bibliography

[1] (19.08.2018). LHC Schematic, [Online]. Available: http://cds.cern.ch/record/842611.

[2] (19.08.2018). CERN, [Online]. Available: http://home.cern/about.

[3] K. H. Mess, P. Schmüser, and S. Wolff, *Superconducting Accelerator Magnets*. Singapore: World Scientific, 1996.

[4] M. N. Wilson, *Superconducting magnets*. Clarendon Press Oxford, 1983.

[5] (19.08.2018). LHC Main Dipole Cross Section, [Online]. Available: http://cds.cern.ch/record/40524.

[6] (19.08.2018). Rutherford cable composed of multi-filamentary strands, [Online]. Available: https://lhc-machine-outreach.web.cern.ch/lhc-machine-outreach/components/cable.htm.

[7] K. Dahlerup Pettersen, R. Denz, J. L. Gomez-Costa, D. Hagedorn, P. Proudlock, F. Rodriguez-Mateos, R. Schmidt, and F. Sonnemann, "The protection system for the superconducting elements of the Large Hadron Collider at CERN," in *Proceedings of PAC, New York, 1999*.

[8] E. Ravaioli, "CLIQ. A new quench protection technology for superconducting magnets," PhD thesis, Universiteit Twente, 2015.

[9] A. Siemko, "Safeguarding the superconducting magnets," *CERN Courier*, 2013.

[10] V. Trang, "The port-hamiltonian approach for the modelling, reduction and control of plasma's dynamics in tokamaks," PhD thesis, University Grenoble Alpes, 2011.

[11] J. Garcia, G. Dauphin-Tanguy, and C. Rombaut, "Electrothermal bond graph model for semiconductor switching devices," in *Proceedings of Applied Power Electronics Conference. APEC '96*, vol. 1, Mar. 1996, 258–263 vol.1.

[12] J. van Dijk, H. J. Coelingh, and P. C. Breedveld, "Modeling three phase induction machines with rotor skin-effect," Proceedings of 2nd IMACS International Multiconference CESA'98, IEEE, Nabeul-Hammamet, Tunisia, 1998, pp. 535–540.

[13] K. Hamada, N. Mitchell, A. Foussat, S. McIntosh, A. Holmes, K. Cave-Ayland, A. Ash, F. Domptail, S. Zheng, E. Surrey, and N. Taylor, "Analysis of ITER Magnet in Safety-Related Fault Condition—Case Study for PF3," *IEEE Transactions on Applied Superconductivity*, vol. 26, no. 4, pp. 1–5, Jun. 2016.

[14] S. Russenschuck and A. Bernhard. (19.08.2018). ROXIE 10.2., [Online]. Available: http://cern.ch/roxie.

[15] S. Caspi and P. Ferracin, "Toward Integrated Design and Modeling of High Field Accelerator Magnets," *IEEE Transactions on Applied Superconductivity*, vol. 16, no. 2, pp. 1298–1303, Jun. 2006.

[16] S. Schöps, "Multiscale modeling and multirate time-integration of field/circuit coupled problems," PhD thesis, Katholieke Universiteit Leuven, 2011.

[17] S. Sadjina, L. T. Kyllingstad, S. Skjong, and E. Pedersen, "Energy conservation and power bonds in co-simulations: non-iterative adaptive step size control and error estimation," *Engineering with Computers*, vol. 33, no. 3, pp. 607–620, Jul. 2017.

[18] (19.08.2018). Functional Mock-up Interface 2.0, [Online]. Available: `https://fmi-standard.org`.

[19] M. Bagnasco, D. Bessette, L. Bottura, C. Marinucci, and C. Rosso, "Progress in the Integrated Simulation of Thermal-Hydraulic Operation of the ITER Magnet System," *IEEE Transactions on Applied Superconductivity*, vol. 20, no. 3, 2010.

[20] V. Duindam, A. Macchelli, S. Stramigioli, and H. Bruyninckx, *Modeling and Control of Complex Physical Systems, The Port-Hamiltonian Approach*. Springer Berlin, 2009.

[21] A. van der Schaft, "Implicit Hamiltonian Systems with Symmetry," *Reports on Mathematical Physics*, vol. 41, no. 2, pp. 203–221, 1998.

[22] H. M. Paynter, *Analysis and design of engineering systems*. Boston: MIT Press, 1961.

[23] D. Karnopp, D. Margolis, and R. Rosenberg, *System Dynamics: Modeling, Simulation, and Control of Mechatronic Systems*. Oxford: Wiley, 2012.

[24] S. Behzadipour and A. Khajepour, "Causality in vector bond graphs and its application to modeling of multi-body dynamic systems," *Simulation Modelling Practice and Theory*, vol. 14, no. 3, pp. 279–295, 2006.

[25] M. Dalsmo and A. van der Schaft, "On representations and integrability of mathematical structures in energy-conserving physical systems," *SIAM Journal on Control and Optimization*, 1998.

[26] D. Eberard and B. Maschke, "Port Hamiltonian Systems Extended to Irreversible Systems: The Example of Heat Conduction," in *IFAC Nonlinear Control Congress*, Elsevier, 2004.

[27] B. Maschke and A. van der Schaft, "From Conservation Laws to Port-Hamiltonian Representations of Distributed-Parameter Systems," in *16th IFAC World Congress*, Elsevier, 2005.

[28] A. van der Schaft and B. Maschke, "Hamiltonian formulation of distributed-parameter systems with boundary energy flow," *Journal of Geometry and Physics*, vol. 42, no. 1, pp. 166–194, 2002.

[29] A. van der Schaft, "Interconnections of input-output Hamiltonian systems with dissipation," in *2016 IEEE 55th Conference on Decision and Control (CDC)*, Dec. 2016, pp. 4686–4691.

[30] H. De Gersem and T. Weiland, "Finite-element models for superconductive cables with finite interwire resistance," *IEEE Trans. Magn.*, vol. 40, no. 2, pp. 667–670, 2004.

[31] S. Russenschuck, *Field computation for accelerator magnets: analytical and numerical methods for electromagnetic design and optimization*. John Wiley & Sons, 2011.

[32] R. R. Hake, "Thermodynamics of Type-I and Type-II Superconductors," *Journal of Applied Physics*, vol. 40, no. 13, pp. 5148–5160, 1969.

[33] M. Mentink and T. Salmi, "Quench absorption coils: a quench protection concept for high-field superconducting accelerator magnets," *Superconductor Science and Technology*, vol. 30, no. 6, 2017.

[34] G. Bozza, Z. M. Malecha, and R. V. Weelderen, "Development and application of a generic CFD toolkit covering the heat flows in combined solid–liquid systems with emphasis on the thermal design of HiLumi superconducting magnets," *Cryogenics*, vol. 80, no. Part 3, pp. 253–264, 2016.

[35] K. D. Pettersen, R. Denz, J. L. Gomez-Costa, D. Hagedorn, P. Proudlock, F. Rodriguez-Mateos, R. Schmidt, and F. Sonnemann, "The protection system for the superconducting elements of the Large Hadron Collider at CERN," in *PAC New York*, 1999.

[36] C.-W. Ho, A. E. Ruehli, and P. A. Brennan, "The Modified Nodal Approach to Network Analysis," *IEEE Transactions on Circuits and Systems*, vol. 22, no. 6, pp. 504–509, Jun. 1975.

[37] A. van der Schaft and B. Maschke, *Conservation Laws and Lumped System Dynamics*, P. M. Hof, C. Scherer, and P. S. Heuberger, Eds. Boston, MA: Springer US, 2009, pp. 31–48.

[38] P. Bamberg and S. Sternberg, *A course in mathematics for students of physics: 2*. Cambridge: Cambridge University Press, 1990.

[39] H. D. Gersem, K. Hameyer, and T. Weiland, "Field-circuit coupled models in electromagnetic simulation," *Journal of Computational and Applied Mathematics*, vol. 168, no. 1, pp. 125–133, 2004, Selected Papers from the Second International Conference on Advanced Computational Methods in Engineering (ACOMEN 2002).

[40] N. Hogan, "Impedance Control: An Approach to Manipulation: Part I Theory," *Journal of Dynamic Systems, Measurement, and Control*, 1985.

[41] A. Macchelli, "Energy-Based Control of Spatially-Discretized Distributed Port-Hamiltonian Systems," *IFAC Proceedings Volumes*, vol. 45, no. 2, pp. 786–791, 2012.

[42] E. F. Crawley, B. G. Cameron, and D. Selva, *System architecture: Strategy and product development for complex systems*. Pearson, 2016.

[43] K. Burrage, *Parallel and sequential methods for ordinary differential equations*. Oxford: Oxford University Press, 1995.

[44] M. Maciejewski, E. Ravaioli, B. Auchmann, A. Verweij, and A. Bartoszewicz, "Automated lumped-element simulation framework for modelling of transient effects in superconducting magnets," in *2015 20th International Conference on Methods and Models in Automation and Robotics (MMAR)*, Aug. 2015, pp. 840–845.

[45] E. Ravaioli, B. Auchmann, M. Maciejewski, H. ten Kate, and A. Verweij, "Lumped-element dynamic electro-thermal model of a superconducting magnet," *Cryogenics*, vol. 80, pp. 346–356, 2016.

[46] F. González, M. Á. Naya, A. Luaces, and M. González, "On the effect of multirate co-simulation techniques in the efficiency and accuracy of multibody system dynamics," *Multibody System Dynamics*, vol. 25, no. 4, pp. 461–483, Apr. 2011.

[47] M. Arnold, "Multi-Rate Time Integration for Large Scale Multibody System Models," in *Proceedings of IUTAM Symposium on Multiscale Problems in Multibody System Contacts*, P. Eberhard, Ed., Dordrecht: Springer Netherlands, 2007, pp. 1–10.

[48] L. Bortot, B. Auchmann, I. Cortes Garcia, A. Fernandez Navarro, M. Maciejewski, M. Prioli, S. Schöps, and A. Verweij, "A 2-D Finite-Element Model for Electro-Thermal Transients in Accelerator Magnets," *IEEE Transactions on Magnetics*, vol. 54, no. 3, Mar. 2018.

[49] S. Schöps, H. D. Gersem, and A. Bartel, "A Cosimulation Framework for Multirate Time Integration of Field/Circuit Coupled Problems," *IEEE Transactions on Magnetics*, vol. 46, no. 8, pp. 3233–3236, Aug. 2010.

[50] M. Maciejewski, I. C. Garcia, S. Schöps, B. Auchmann, L. Bortot, M. Prioli, and A. P. Verweij, "Application of the Waveform Relaxation Technique to the Co-Simulation of Power Converter Controller and Electrical Circuit Models," in *2017 22nd International Conference on Methods and Models in Automation and Robotics (MMAR)*, Aug. 2017, pp. 837–842.

[51] I. C. Garcia, S. Schöps, M. Maciejewski, L. Bortot, M. Prioli, B. Auchmann, and A. Verweij, "Optimized field/circuit coupling for the simulation of quenches in superconducting magnets," *IEEE Journal on Multiscale and Multiphysics Computational Techniques*, vol. 2, pp. 97–104, 2017.

[52] M. Maciejewski, P. Bayrasy, K. Wolf, M. Wilczek, B. Auchmann, T. Griesemer, L. Bortot, M. Prioli, A. M. F. Navarro, S. Schöps, I. C. Garcia, and A. P. Verweij, "Coupling of Magnetothermal and Mechanical Superconducting Magnet Models by Means of Mesh-Based Interpolation," *IEEE Transactions on Applied Superconductivity*, vol. 28, no. 3, pp. 1–5, Apr. 2018.

[53] E. Ravaioli, K. Dahlerup-Petersen, F. Formenti, J. Steckert, H. Thiesen, and A. Verweij, "Modeling of the Voltage Waves in the LHC Main Dipole Circuits," *IEEE Transactions on Applied Superconductivity*, vol. 22, no. 3, Jun. 2012.

[54] E. Lelarasmee, A. E. Ruehli, and A. L. Sangiovanni-Vincentelli, "The Waveform Relaxation Method for Time-Domain Analysis of Large Scale Integrated Circuits," *IEEE Transactions on Computer-Aided Design of Integrated Circuits and Systems*, vol. 1, no. 3, pp. 131–145, 1982.

[55] J. K. White, F. Odeh, A. L. Sangiovanni-Vincentelli, and A. E. Ruehli, "Waveform Relaxation: Theory and Practice," *Transactions of the Society for Computer Simulation*, vol. 2, no. 1, pp. 95–133, 1985.

[56] D. Estévez Schwarz and C. Tischendorf, "Mathematical Problems in Circuit Simulation," *Mathematical and Computer Modelling of Dynamical Systems*, vol. 7, no. 2, pp. 215–223, 2001.

[57] M. Günther and P. Rentrop, "Numerical Simulation of Electrical Circuits," *Proceedings of the GAMM Annual Meeting*, vol. 1-2, pp. 51–77, 2000.

[58] E. Ravaioli, K. Dahlerup-Petersen, F. Formenti, V. Montabonnet, M. Pojer, R. Schmidt, A. Siemko, M. S. Camillocci, J. Steckert, H. Thiesen, and A. Verweij, "Impact of the Voltage Transients After a Fast Power Abort on the Quench Detection System in the LHC Main Dipole Chain," *IEEE Transactions on Applied Superconductivity*, vol. 22, no. 3, Jun. 2012.

[59] D. Paudel, *Quench simulation of superconducting magnets with commercial multiphysics software*, Aalto University, Espoo, Master's thesis, 2015.

[60] E. Lange, F. Henrotte, and K. Hameyer, "An Efficient Field-Circuit Coupling Based on a Temporary Linearization of FE Electrical Machine Models," *IEEE Transactions on Magnetics*, vol. 45, no. 3, pp. 1258–1261, Mar. 2009.

[61] E. Ravaioli, V. I. Datskov, G. Kirby, M. Maciejewski, H. H. J. ten Kate, and A. P. Verweij, "CLIQ-Based Quench Protection of a Chain of High-Field Superconducting Magnets," *IEEE Transactions on Applied Superconductivity*, vol. 26, no. 4, pp. 1–5, Jun. 2016.

[62] T. Nakamoto, M. Sugano, Q. Xu, H. Kawamata, S. Enomoto, N. Higashi, A. Idesaki, M. Iio, Y. Ikemoto, R. Iwasaki, N. Kimura, T. Ogitsu, N. Okada, K. i. Sasaki, M. Yoshida, and E. Todesco, "Model Magnet Development of D1 Beam Separation Dipole for the HL-LHC Upgrade," *IEEE Transactions on Applied Superconductivity*, vol. 25, no. 3, pp. 1–5, Jun. 2015.

[63] E. Ravaioli, V. Datskov, C. Giloux, G. Kirby, H. ten Kate, and A. Verweij, "New, Coupling Loss Induced, Quench Protection System for Superconducting Accelerator Magnets," *IEEE Transactions on Applied Superconductivity*, vol. 24, no. 3, pp. 1–5, 2014.

[64] A. Milanese, "A method to transfer concentrated Lorentz forces to a finite element mechanical model," *EuCARD Publication*, pp. 667–670, 2010.

[65] (19.08.2018). COMSOL Multiphysics 5.2a, [Online]. Available: `http://comsol.com`.

[66] (19.08.2018). ANSYS APDL 16.2, [Online]. Available: `http://ansys.com`.

[67] Fraunhofer Institute SCAI. (19.08.2018). MpCCI Coupling Environment 4.5, [Online]. Available: `https://www.mpcci.de`.

[68] U. Schreiber and U. van Rienen, "Coupled Calculation of Electromagnetic Fields and Mechanical Deformation," in *Scientific Computing in Electrical Engineering SCEE 2004*, A. M. Anile, G. Alì, and G. Mascali, Eds., ser. Mathematics in Industry, Berlin, Germany: Springer, 2006.

[69] P. Bayrasy, "Coupled simulations of electric arcs for switching devices with MpCCI and ANSYS," in *Proceedings of NAFEMS European Conference "Multiphysics Simulation" 2016*, IEEE, 2016, pp. 39–41.

[70] L. D. Logan, *A First Course in the Finite Element Method*. Cengage Learning, 2012.

[71] O. Steinbach, *Numerical approximation methods for elliptic boundary value problems. finite and boundary elements*. Springer, 2008.

[72] E. Nilsson, S. I. Bermudez, A. Ballarino, B. Bordini, L. Bottura, J. Fleiter, F. Lackner, C. Loffler, J. C. Perez, H. Prin, G. DeRijk, D. Smekens, and F. Savary, "Design Optimization of the Nb $_3$Sn 11 T Dipole for the High Luminosity LHC," *IEEE Transactions on Applied Superconductivity*, vol. 27, no. 4, Jun. 2017.

[73] M. Karppinen, N. Andreev, G. Apollinari, B. Auchmann, E. Barzi, R. Bossert, V. V. Kashikhin, A. Nobrega, I. Novitski, L. Rossi, D. Smekens, and A. V. Zlobin, "Design of 11 T Twin-Aperture Nb $_3$Sn Dipole Demonstrator Magnet for LHC Upgrades," *IEEE Transactions on Applied Superconductivity*, vol. 22, no. 3, Jun. 2012.

[74] J. E. Hopcroft, R. Motwani, and J. D. Ulman, *Introduction to automata theory, languages, and computation*. Pearson Addison Wesley, 2007.

[75] E. Ravaioli, G. Ambrosio, B. Auchmann, P. Ferracin, M. Maciejewski, F. Rodriguez-Mateos, G. Sabbi, E. Todesco, and A. P. Verweij, "Quench Protection System Optimization for the High Luminosity LHC Nb $_3$Sn Quadrupoles," *IEEE Transactions on Applied Superconductivity*, vol. 27, no. 4, Jun. 2017.

[76] L. Bortot, B. Auchmann, I. C. Garcia, A. M. F. Navarro, M. Maciejewski, M. Mentink, M. Prioli, E. Ravaioli, S. Schöps, and A. P. Verweij, "STEAM: A Hierarchical Cosimulation Framework for Superconducting Accelerator Magnet Circuits," *IEEE Transactions on Applied Superconductivity*, vol. 28, no. 3, pp. 1–6, Apr. 2018.

[77] L. Bortot, M. Maciejewski, M. Prioli, A. Fernandez Navarro, J. B. Ghini, B. Auchmann, and A. P. Verweij, "A Consistent Simulation of Electro-thermal Transients in Accelerator Circuits," *IEEE Transactions on Applied Superconductivity*, vol. 27, no. 4, Jun. 2017.

[78] A. M. Fernandez Navarro, M. Maciejewski, A. Verweij, L. Bortot, M. Mentink, M. Prioli, B. Auchmann, S. Izquierdo Bermudez, E. Ravaioli, and S. Yammine, "Simulation of a Quench Event in the Upgraded High-Luminosity LHC Main Dipole Circuit Including the 11 T Nb $_3$Sn Dipole Magnets," *IEEE Transactions on Applied Superconductivity*, vol. 28, no. 4, 2018.

[79] M. J. Gander, Y.-L. Jiang, and R.-J. Li, "Parareal schwarz waveform relaxation methods," in *DOMAIN DECOMPOSITION METHODS IN SCIENCE AND ENGINEERING XX*, 2013.

[80] H. Flanders, Ed., *Differential Forms with Applications to the Physical Sciences*, ser. Mathematics in Science and Engineering. Elsevier, 1963, vol. 11.

[81] J. C. Maxwell, "A Dynamical Theory of the Electromagnetic Field," *Royal Society Transactions CLV*, vol. 23, pp. 459–512, 1864.

[82] R. Ingarden and A. Jamiolkowski, *Classical Electrodynamics*. PWN-Polish Sc. Publ. Elsevier, Warszawa, 1985.

[83] P. Atkins, *The Laws of Thermodynamics: A Very Short Introduction*. Oxford: Oxford University Press, 2013.